2015

# Small signal stability analysis for a turbine-generator unit connected to an HVDC system

Yin Chin Choo
*University fof Wollongong*

# Small Signal Stability Analysis for a Turbine-Generator Unit Connected to an HVDC System

A thesis submitted in fulfilment of the
requirements for the award of the degree

**Doctor of Philosophy**

from

**University of Wollongong**

**by**

**Yin Chin Choo, BE(Hons)**

**School of Electrical, Computer and Telecommunications Engineering**

**March 2015**

Dedicated to my daughters, Melody Jia Ai Tan and Harmony Jia Yue Tan, my husband, my brother and my beloved parents...

## Acknowledgements

This thesis would not have become a realisation without the contributions of many people and institutions.

First and foremost, I wish to express my utmost gratitude to my principal supervisor, Associate Professor Kashem M. Muttaqi, for providing me an opportunity to pursue postgraduate studies at the University of Wollongong (UOW) and support throughout my candidature. I would also like to thank my co-supervisor, Dr. Ashish Agalgaonkar, for his invaluable assistance and time throughout the project. I am also grateful to have Professor Sarath Perera as my co-supervisor and his invaluable guidance and moral support. Also, I'm thankful for Professor Michael Negnevitsky from University of Tasmania (UTAS) for his guidance and support. I really appreciate all of your patience, motivation, knowledge, experience and moral support provided throughout the research and writing of this thesis.

This research project was financially supported by the Australian Research Council (ARC) under ARC Discovery Grant DP0666431. The financial support is greatly appreciated.

Many thanks go to Roslyn Causer-Temby of the School of Electrical, Computer and Telecommunications Engineering (SECTE) at UOW and former staff, Esperanza Riley of Australian Power Quality & Reliability Centre (APQRC), formerly known as Integral Energy Power Quality and Reliability Centre (IEPQRC) in providing assistance in administrative related issue.

The support and accompaniment of my fellow friends, Dr. Kai Zou, Dr. Nishad Mendis and Dr. Prabodha Paranavithana are very much appreciated. Thanks for all your support and encouragement during my postgraduate studies at the University of Wollongong and this makes my postgraduate studies memorable.

Special thanks to my family, which include my daughters, Melody Jia Ai Tan and Harmony Jia Yue Tan for bringing laughter and happiness in my life, my husband, Wei Turk Tan for being supportive and understanding, and my brother, Xiang Yung Choo, for his encouragement and support.

Last but not least, I am very thankful for my parents for their unconditional and unfailing love and support throughout my life. Thank you so much for your love, encouragement, guidance, understanding and support which sustain and make me come this far. I love you all.

## Certification

I, Yin Chin Choo, declare that this thesis, submitted in fulfilment of the requirements for the award of Doctor of Philosophy, in the School of Electrical, Computer and Telecommunications Engineering, University of Wollongong, is entirely my own work unless otherwise referenced or acknowledged. This manuscript has not been submitted for qualifications at any other academic institute.

Yin Chin Choo

Date: $27^{th}$ March 2015

## Abstract

The rapidly growing complexity and increasing size of power system networks with a large number of interconnections have exposed the system to various contingencies that may lead the system to steady-state, dynamic or transient instability. It is thus vital for a power system to be able to maintain the load-generation balance under normal operating conditions and to regain an acceptable state of equilibrium after being subjected to a disturbance such that the system frequency remains within its operating range. Conventional methodologies in assessing power system transient or small-signal stabilities, such as Time Domain Approach, Extended Equal Area Criterion, Direct method of Lyapunov Function and Transient Energy Function are employed. Eigenvalues analysis, participation factor analysis and transient security assessment using transient security index have been used as the assessment tools in this thesis for evaluating the power system stability.

In achieving satisfactory operation of the power system, it is important to control and maintain the overall system frequency at all the time. System frequency relies greatly on the generation-load balance; any frequency variation resulted from active power imbalance will initiate the response of the generator governing system to restore the frequency. Power system performance can also be affected by dynamic characteristics of hydraulic governor-turbines during and following any disturbance. Accurate modelling of hydraulic governor-turbines is essential to characterise and analyse the system response during an emergency situation.

Classical ideal lossless representation of the hydraulic turbine, used extensively in the past for governor stability studies, is only appropriate for small perturbations around the initial operating condition and approximates to the practical turbine characteristics at low frequencies. This thesis has developed a detailed modelling of hydraulic turbine-penstock, considering the water hammer effects and friction, for stability studies of turbine-generator governing system to capture and describe the essential dynamic performances for wide variety of system analyses. The stability criterion to govern an isolated hydraulic system as well as relative stability of the hydraulic system utilising frequency response methods

have been presented together with a guideline to adjust system gain to improve the relative stability of the system.

Subsynchronous torsional interaction (SSTI) phenomenon is commonly seen associated with turbine-generator (TG), whose rotor is generally a complicated mechanical system, due to close interaction with the constant current controllers at HVDC rectifier stations. The controllers of HVDC system and the outer loops which set the reference to the current controller have potential to introduce negative damping on the nearby generating units. The interaction of hydroelectric TG unit with power system controls or ac transmission system has not been a concern due to the inherently large value of the generator rotor inertia and viscous waterwheel damping, which provides considerably large damping of torsional oscillations for hydroelectric unit. As a result, a limited number of research studies have been conducted for hydroelectric TG units, especially in the close vicinity of HVDC systems.

This thesis has aimed to explore the interaction of HVDC system with the hydroelectric TG units under different system conditions. It is observed that the torsional frequency of a hydroelectric TG unit may fall well-within the frequency range of the negative damping introduced by the HVDC current controller. The modal torsional damping may be sufficient to diminish the negative damping effect posed by the HVDC current controller with a relatively high value of generator-to-turbine inertia ratio. Damping torque analysis has been carried out to determine the degree of sensitivity of system parameters towards electrical damping. Perturbation analysis is conducted to assess the dynamic response of a hydroelectric unit with different generator-to-turbine ratios. The case studies have indicated that hydroelectric TG units could possibly experience unstable SSTI in the close vicinity of an HVDC system under certain operating conditions; the SSTI phenomenon is predominant especially when a hydroelectric unit with low generator-to-turbine inertia ratio connected to an HVDC system due to deficiency in modal damping.

The thesis has also investigated the SSTI bahaviour of a fixed-speed induction machine based wind turbine-generator (WTG) unit. Growing torque oscillations have been observed if the modulated frequency is close to the mechanical torsional mode of a WTG unit and the

combined electromechanical system suffers from a lack of sufficient damping. The resulting oscillatory fluctuations in the blade-hub torque of a WTG unit are substantially high in comparison with the one in the hub-generator torque for the specified electrical disturbances. The torsional torques may eventually settle down after a certain time interval, however, the sustained torsional oscillations may result in fatigue damage and reduce the fatigue life of the mechanical shaft system.

Small signal stability analysis, utilising linear methodologies, has been powerful in providing valuable insights on the power system dynamic characteristics. Small signal stability usually concerns with the sufficiency of the system electromechanical oscillations damping. To investigate the SSTI and HVDC interactions, the dynamic behaviours of each power system components need to be carefully modelled. This research focuses on the electrical and electromechanical behaviours of hydroelectric TG units. Stator transients have been included in the formulation of the synchronous machine for detailed analysis. The dynamics of all AC network elements, including transmission lines, transformers, loads and filters, have also been taken into account for detailed analysis, especially when HVDC and SSTI are of interest.

This thesis proposes a small signal dynamic model, which is developed based on frequency response modelling, for the SSTI analysis of turbine-generator with HVDC system. The proposed small signal dynamic model allows the formulation of the state-space model and transfer function representation of power system components individually and offers a more straightforward execution for various network configurations.

In this thesis, a subsynchronous damping controller (SSDC), constituting of a washout filter, a gain block and a lead-lag phase compensator has been designed and incorporated to the current controller of the rectifier to overcome and mitigate the torsional interaction between the TG unit and the HVDC system.

## Publications

This thesis includes chapters that have been written as the following journal and conference articles:

**Chapter 2:** Y.C. Choo, M.A. Kashem, M. Negnevitsky, "Transient Stabilty Assessment of a Small Power System Subjected to Large Disturbances", *Proceedings of Australasian Universities Power Engineering Conference (AUPEC 2006)*, Melbourne, Victoria, 10–13 December 2006.

**Chapter 3:** Y.C. Choo, K.M. Muttaqi, M. Negnevitsky, "Evaluation of small signal stability of a power system", *Australian Journal of Electrical and Electronics Engineering (AJEEE)*, Vol. 4, No. 3, 2008.

**Chapter 4:** Y.C. Choo, K.M. Muttaqi, M. Negnevitsky, "Stability of a Hydraulic Governor Turbine System for Isolated Operation", *Proceedings of Australasian Universities Power Engineering Conference (AUPEC 2007)*, Perth, Western Australia, 9–12 December 2007.

**Chapter 5:** Y.C. Choo, K.M. Muttaqi, M. Negnevitsky, "Modelling of Hydraulic Turbine for Dynamic Studies and Performance Analysis", *Proceedings of Australasian Universities Power Engineering Conference (AUPEC 2007)*, Perth, Western Australia, 9–12 December 2007.

**Chapter 6:** Y.C. Choo, K.M. Muttaqi, M. Negnevitsky, "Modelling of Hydraulic Governor-Turbine for Control Stabilisation", *Australian and New Zealand Industrial and Applied Mathematics Journal (ANZIAMJ)*, Vol. 49, 2007.

**Chapter 7:** Y.C. Choo, A.P. Agalgaonkar, K.M. Muttaqi, S. Perera, M. Negnevitsky, "Subsynchronous Torsional Behaviour of a Hydraulic Turbine-Generator Unit Connected to a HVDC System", *Proceedings of Australasian Universities Power Engineering Conference (AUPEC 2008)*, Sydney, New South Wales, 14–17 December 2008.

**Chapter 8:** Y.C. Choo, A.P. Agalgaonkar, K.M. Muttaqi, S. Perera, M. Negnevitsky, "Dynamic Modelling of Hydroelectric Turbine-Generator Unit connected to a HVDC System for Small Signal Stability Analysis", *Proceedings of Australasian Universities Power Engineering Conference (AUPEC 2009)*, Adelaide, Southern Australia, 27–30 September 2009.

**Chapter 9:** Y.C. Choo, A.P. Agalgaonkar, K.M. Muttaqi, S. Perera, M. Negnevitsky, "Subsynchronous Torsional Interaction Behaviour of Wind Turbine-Generator Unit Connected to an HVDC System", *the 36th Annual Conference of the IEEE Industrial Electronics Society (IECON 2010)*, Glendale, AZ, USA, 7–10 November 2010.

**Chapter 10:** Y.C. Choo, A.P. Agalgaonkar, K.M. Muttaqi, S. Perera, M. Negnevitsky, "Analysis of Subsynchronous Torsional Interaction of HVDC System Integrated Hydro Units with Small Generator-to-Turbine Inertia Ratios", *IEEE Trans. Power Syst.*, Vol. 29, No. 3, pp. 1064-1076, 2014.

As the primary supervisor, I, Associate Professor Kashem M. Muttaqi, declare that the greater part of the work in each article listed above is attributed to the candidate, Yin Chin Choo. In each of the above manuscripts, Yin Chin contributed to study design and was primarily responsible for data collection, data analysis and data interpretation. The first draft of each manuscript was written by the candidate and Yin Chin was then responsible for responding to the editing suggestions of her co-authors. The co-authors, Associate Professor Kashem Muttaqi (Chapters 2−10), Dr. Ashish P. Agalgaonkar (Chapters 7−10), Professor Sarath Perera (Chapters 7−10) and Professor Michael Negnevitsky (Chapters 2−10) were responsible for assisting in study design, interpreting data and editing all the manuscripts. Yin Chin has been solely responsible for submitting each manuscript for publication to the relevant journals and conferences, and she has been in charge of responding to reviewers' comments, with assistance from her co-authors.

Yin Chin Choo
Candidate
$27^{th}$ March 2015

Associate Professor Kashem M. Muttaqi
Principal Supervisor
$27^{th}$ March 2015

## Table of Contents

## List of Figures

## List of Tables

# Chapter 1

# Introduction

## 1.1 Problem Statement

High voltage direct current (HVDC) technology is used to transmit electricity over long distances by overhead transmission lines or submarine cables. It is also used to interconnect separate power systems, where traditional alternating current (AC) connections cannot be used. The development of the HVDC technology started in the late 1920s, where Dr. Uno Lamm and ASEA were granted a patent on the discovery [1]. The first world's commercial commissioning of the HVDC technology with mercury-arc valves was in 1954. This was a link between the Swedish mainland and the island Gotland in the Baltic sea. The power rating was 20 MW at the transmission voltage of 100 kV [1, 2]. HVDC transmission of power has been widely applied throughout the world after since [3]. HVDC power transmission systems constitute an important application of power electronics technology today.

Subsynchronous torsional interaction (SSTI) between a steam turbine-generator (TG) unit and an HVDC system received deliberate attention especially after the field tests at Square Butte, North Dakota, USA revealed the undesirable interactions between the HVDC terminal and the 11.5 Hz torsional mode of an electrically-close TG unit [4]. Subsequently, it was revealed that the HVDC rectifier stations with constant current control may introduce negative damping on the nearby generating units [4]. The outer loops which set the

reference to the current controller also have potential to introduce negative damping on the nearby generating units. A current-controlled Voltage Sourced Converter (VSC), located electrically close to the generator may also introduce negative damping in the certain frequency range and proper design of current controller may nullify the possibility of negative damping [5]. The increasing complexity of the electrical network as well as the stressed system conditions under various contingencies demand dynamic interaction studies from stability perspective.

To date, various research aspects associated with SSTI behavior of turbogenerators have been reported in the literature. However, limited number of research studies has been conducted for hydroelectric TG units, especially in the close vicinity of HVDC systems, due to the fact that the high inherent generator-to-turbine inertia (GTI) ratios of hydro units enhance the modal damping at torsional frequencies, thereby minimising the risk of sustained torsional oscillations [6]. However, it is believed that hydroelectric TG units with low GTI ratios at certain network conditions could possibly experience SSTI instability, where the turbine modal damping may not be sufficient to counteract the negative damping introduced by the HVDC current controller. Thus, this thesis is aiming to investigate the possible interactions of HVDC system with the hydroelectric TG units. The study has indicated that the torsional interaction could possibly be excited on a hydroelectric system when the complement of the system network resonance frequency $f_{comp}$ coincides with the torsional mechanical frequency $f_n$.

Subsynchronous damping controller (SSDC), constituting a washout filter, a SSDC gain block and a lead-lag phase compensator can be designed and incorporated to the current controller of the rectifier to overcome and mitigate the torsional interaction between the TG unit and the HVDC system. The phase characteristics of SSDC can be designed properly to compensate any phase lead/lag between the current controller input and the generator electrical torque, so as to provide positive damping at the required frequency range [8, 9]. The frequency response between the constant current controller input and the generator electrical torque, to determine the phase compensation required, can be obtained with the

assumption that the generator angle is maintained constant. A washout filter, which is a high pass filter, is also included to remove the steady speed variations [9].

Notably, in Australia, Basslink is a 400 kV DC electricity interconnector that connects the 500 kV transmission system in the State of Victoria across Bass Strait to the 220 kV transmission system in the State of Tasmania. Tasmania is mainly dominated by hydro generation. It is thus important for the system planners and designers to examine the damping contribution by the hydro units at torsional frequency. The methodologies developed in this thesis, can be used for damping torque analysis and to assess the SSTI of hydro units of different GTI ratio connected to an HVDC system.

Small signal stability is the ability of the power system to maintain synchronism when subjected to small disturbances. A disturbance is considered to be small if the equations that describe the resulting response of the system may be linearised for the purpose of analysis [3, 10, 11]. Linear analysis techniques have been widely applied in studying the dynamic performance of power systems since early 1970s [12]. Instability may result from either (i) a lack of synchronising torque, causing a steady increase in generator rotor angle, or (ii) a lack of sufficient damping torque, resulting in rotor oscillations of growing amplitude [3].

In reality, small disturbances always occur in a power system, such as small variations in loads and generation [3]. Some other forms of small disturbances could be transformer tap changing and switching operation of power system equipment, such as condenser/capacitor. The ability of the system to operate satisfactorily under small disturbance conditions ensures successful delivery of the maximum power to the system.

The dynamic characteristic of a power system is usually represented by a set of first order nonlinear differential-algebraic equations (DAEs). This thesis has presented the analytical technique in linearising the dynamic behaviours of each power system components individually, which can be performed using Taylor's series expansion at an equilibrium point, transforming the input-output variables into common reference frames, and interconnecting the components to form the overall state-space model for small signal stability analysis.

Integration of the subsystems can be carried out as the input-output of a subsystem can be the output-input of another subsystem. This thesis has particularly considered the power system components, such as synchronous generator, torsional shaft system, AC network system and HVDC system, for small signal stability analysis.

Small signal stability of the power system can be assessed using eigenvalues analysis, participation factors analysis. System oscillatory modes can be examined through investigation of eigenproperties. Participation factor analysis can be carried out to identify the optimal site for the installation of power system stabiliser (PSS) for Hopf bifurcation control in the critical mode.

Eigenvalue analysis provides invaluable insights into the dynamic interactions among all power system components in an electrical network by characterising the system modes damping ratio and oscillation frequency. However, the drawback of this technique is that it requires the overall system to be represented as a state-space model. The higher-order dynamic representation of the turbine-generator unit and the electrical network increases the order of overall state-space model, as well as the computational complexity.

Therefore, frequency response modelling, which allows the formulation of the state-space model and transfer function representation of power system components individually, would be beneficial for SSTI analysis with HVDC system. This frequency response modelling offers a more straightforward execution for various network configurations. Application of frequency response analysis on investigating SSTI of hydro and wind TGs in the close vicinity of HVDC system overcomes the limitations of eigenvalue analysis (the overall system will need to be modelled as a single state-space system) and complex torque analysis (only applicable to torsional dynamics of one TG set at a time and not to interactions of multiple TG sets, also only applicable to synchronous machine and not to induction machine).

## 1.2 Research Objectives and Methodologies

The main aim of the work presented in this thesis is to analyse the interactions of HVDC system with the TG unit, particularly SSTI between a hydroelectric TG unit and an HVDC

system, using small-signal stability analysis technique. The goals of this thesis are achieved through the following:

- Application of various conventional methodologies in assessing power system transient and small-signal stabilities.
- Assessment of system stability by applying stability analysis methodologies, including frequency response methods, for isolated and interconnected systems dominated by a hydroelectric system, considering the influence of HVDC system.
- Detailed modelling of hydraulic turbine-penstock, considering the water hammer effects and friction, for governing stability studies.
- The formulation of the linearised small-signal state space model of the integrated AC-DC systems by linearising each power system components individually, transforming input-output variables into common reference frames, and establishing interaction relationship between different power system components.
- Application of the developed linearised dynamic model to analyse the interaction behaviour between the hydroelectric unit and HVDC link using eigenvalue analysis.
- Application of analytical techniques, such as damping torque analysis and sensitivity analysis, in assessing the SSTI stability between hydroelectric TG and wind turbine-generator (WTG) connected to an HVDC system through analysing frequency perturbation and oscillatory damping.
- The establishment of theoretical analysis to investigate the impacts of different GTI ratios on the SSTI between the hydroelectric units and HVDC system.
- The development of a generic SSDC to overcome and mitigate the torsional interaction between the TG unit and the HVDC system by designing the phase characteristics of SSDC properly to compensate any phase lead/lag between the current controller

input and the generator electrical torque, so as to provide positive damping at the required frequency range.

The dynamic behaviour of each power system components, which includes synchronous or induction generator, torsional shaft system, AC network system, HVDC system, are linearised at an equilibrium point individually. This research is interested in the electrical and electromechanical behaviours of the TG units, and thus, stator transient have been included in the formulation of the synchronous machine for detailed analysis with torsional shaft system represented based on a mass-spring-damping model. The dynamics of all AC network elements, including transmission lines, transformers, loads, filters and etc, will need to be encountered for detailed analysis, especially when HVDC and SSTI are of interest. The conventional steady-state representation of the system network only allows for the electromechanical oscillation analysis, but it will not be adequate for HVDC and SSTI analysis. The analytical modelling of an HVDC system has been demanding due to the inherently nonlinear characteristics of the DC converter. The complexity of the HVDC system modelling involves modelling of the 12-pulse Graetz converter bridge, phase locked oscillator (PLO), firing and valve blocking controls and firing angle and extinction angle measurements, as well as the RC snubber circuits for each thyristor. Some assumptions are made to represent the linearised HVDC system for small-signal stability analysis. The three-phase ac systems are assumed to be balanced at fundamental frequency and higher order harmonics have been neglected.

## 1.3 Outline of the Thesis

A brief description on the contents of the remaining chapters is given below:

Chapter 2 presents a literature review on the transient stability of the power system when subjected to large disturbances. It provides a brief overview on the power system stability, the causes and effects of the power system instability. Various transient stability assessment is also described, such as Time Domain Approach, Extended Equal Area Crite-

rion, Direct Method of Lyapunov Function, Transient Energy Function in evaluating power system network's ability to withstand any disturbances. Comparative study of the different techniques in assessing transient stability has been demonstrated.

This Chapter has been published in Proceedings of Australasian Universities Power Engineering Conference (AUPEC 2006) in 2006.

Chapter 3 describes the background information on the small signal stability of the power system when subjected to small disturbances. It provides a brief overview on the application of the linear analysis technique in studying the dynamic performance of power systems. This Chapter establishes the fundamental understanding in the analytical techniques for the small-signal stability assessment, which includes time domain analysis, Eigenvalues analysis, participation factors analysis and transient security assessment using transient security index. This form the basis analytical technique that will be used at the later chapters for the stability studies.

This Chapter has been published in Australian Journal of Electrical and Electronics Engineering (AJEEE) in 2008.

Chapter 4 investigates the impact of the governor parameters selection onto the system stability by employing a simple radial network. The past developments in research related to governor tuning to determine the optimal governor parameters for speed control in a hydraulic system have been described. The stability of the transients depends upon the hydro turbine-penstock parameters, i.e. water starting time and mechanical starting time, and the selection of the parameters employed in the governing system, i.e. temporary speed droop and dashpot reset time for a mechanical-hydraulic governor and proportional-integral-derivative (PID) gains for a PID governor. The stability criterion to govern an isolated hydraulic system as well as relative stability of the hydraulic system has been demonstrated utilising frequency response methods. Proper selection of parameters used in the governing system is important to optimise the control operation in hydraulic system. It is thus vital to ensure that the governing system is stable, and is able to restore the generating unit to equilibrium at synchronous speed when subject to any load disturbances.

This Chapter has been published in Proceedings of Australasian Universities Power Engineering Conference (AUPEC 2007) in 2007.

Chapter 5 presents a detailed representation of turbine-penstock, accounting for the effects of water compressibility and pipe elasticity, as well as the friction, for the stability studies. The detailed representation of the hydraulic system allows the interpretation of the system dynamic behaviours to be more accurate and approximate to the practical cases closely and for a wide frequency range. Thus, more reliable stability analysis can be obtained.

This Chapter has been published in Proceedings of Australasian Universities Power Engineering Conference (AUPEC 2007) in 2007.

Detailed representation of the power system components is essential to determine the practical dynamic responses as accurately as possible for a wide variety of system studies. Extended from Chapter 5, Chapter 6 further investigates the detailed representation of the hydraulic systems governed by PID and porportional-integral (PI) controllers through simulation in MATLAB/Simulink.

This Chapter has been published in Australian and New Zealand Industrial and Applied Mathematics Journal (ANZIAMJ) in 2007.

Chapter 7 evaluates the SSTI behaviour of a hydroelectric turbine-generator unit connected in the close vicinity to an HVDC link. Torsional interaction is an important phenomenon of concern when a TG unit is connected to a series compensated line or an HVDC system. The SSTI may have significant impact on the hydraulic system due to the negative damping introduced by HVDC converter controls. When the complement frequency of the electrical resonance frequency is approximately equal to the mechanical torsional mode of the TG unit, while there is insufficient damping in the combined electro-mechanical systems, sustained shaft oscillations will appear. Investigations are carried out to examine the behaviour of an individual hydroelectric TG unit (with varying generator-to-turbine inertia ratio) interconnected with an HVDC system.

This Chapter has been published in Proceedings of Australasian Universities Power

Engineering Conference (AUPEC 2008) in 2008.

Chapter 8 presents the modelling techniques, which depict the dynamic characteristics of hydroelectric TG unit and HVDC systems using linearised state space models. This allows the investigation of the small-signal stability aspects associated with the control interaction between the hydroelectric unit and the HVDC system at higher frequencies, using eigen-analysis. Analytical technique in linearising the dynamic behaviours of each power system components individually, transformation of input-output variables into common reference frames and interconnecting the components to form the overall state-space model for small signal stability analysis is discussed thoroughly. The small-signal dynamic model developed in MATLAB/Simulink environment is compared and verified against with the PSCAD®/EMTDC™ simulated model in the electromagnetic transients (EMT) simulation environment in both time and frequency domains.

This Chapter has been published in Proceedings of Australasian Universities Power Engineering Conference (AUPEC 2009) in 2009.

Chapter 9 extends the investigations in Chapter 7 to examine the SSTI phenomenon of a fixed-speed induction machine based wind turbine-generator (WTG) unit connected to an HVDC system. WTG units typically feature high turbine inertia and low shaft stiffness between the turbine and generator rotor. These characteristics result in a lightly damped, low frequency torsional shaft mode oscillations, wherein the turbine swings coherently against the generator. The soft shaft mode can be excited by random wind variations, which results in large oscillatory fluctuations in the shaft torques and the electrical power. The SSTI behaviour of a WTG unit has been examined in PSCAD®/EMTDC© environment.

This Chapter has been published in the $36^{th}$ Annual Conference of the IEEE Industrial Electronics Society (IECON 2010) in 2010.

Chapter 10 extends the analysis in Chapter 8 to evaluate the SSTI behaviour of hydro units with small generator-to-turbine inertia (GTI) ratios under different system conditions. It is very important to investigate the hydroelectric TG response for network side perturbations and the effect of negative damping posed by an HVDC current controller and the

outer loops which set the reference to the current controller. Damping torque analysis has been carried out to determine the degree of sensitivity of system parameters. Perturbation analysis is conducted to assess the dynamic response of a hydroelectric unit with different GTI ratios. The resulting electromagnetic torque deviation and the electrical damping from the perturbation analysis from machine side as the mechanical system perturbation determine the system stability. The application of voltage perturbation at different modulated frequency at the terminal bus depicts the perturbation arising from HVDC system operation (network side perturbation). Dynamic characteristics of the power system components described by a first order non-linear differential-algebraic equations are also presented. It is observed that hydro units with low GTI ratios is more susceptible to SSTI instability due to deficiency in modal damping. Mitigation of SSTI between the hydroelectric unit and the HVDC system has been demonstrated at vulnerable torsional frequencies by incorporating a typical SSDC.

This Chapter has been published in IEEE Transactions on Power Systems.

Finally, Chapter 11 summarises the major outcomes of the work presented in the thesis, and presents recommendations and suggestions for future work.

## References


[1] W. Long, S. Nilsson, "HVDC transmission: yesterday and today," *IEEE Power and Energy Magazine*, Vol. 5, No. 2, pp. 22-31, 2007.

[2] H. Martensson, "History of High Voltage D.C. Transmission," *IEEE Power Engineering Review*, Vol. PER-4, No. 7, pp. 16-17, 1984.

[3] P. Kundur. *Power System Stability and Control.* McGraw-Hill, 1994.

[4] M. Bahrman, E.V. Larsen, R.J. Piwko, H.S. Patel, "Experience with HVDC - Turbine-Generator Torsional Interaction at Square Butte," *IEEE Trans. Power App. Syst.*, Vol. PAS-99, No. 3, May/June 1980.

[5] L. Harnefors, "Analysis of Subsynchronous Torsional Interaction With Power Electronic Converters," *IEEE Trans. Power Syst.*, Vol. 22, no. 1, pp. 305-313, Feb. 2007.

[6] K. Clark, "Overview of Subsynchronous Resonance Related Phenomena," in *Proc. 2012 IEEE PES Transmission and Distribution Conf. and Exposition (T&D)*, pp. 1-3, 2012.

[7] G. Andersson, R. Atmuri, R. Rosenqvist, S. Torseng, "Influence of Hydro Units' Generator-to-Turbine Inertia Ratio on Damping of Subsynchronous Oscillations," *IEEE Trans. Power App. Syst.*, Vol. PAS-103, No. 8, August 1984.

[8] D.J. Kim, H.K. Nam and Y.H. Moon, "A Practical Approach to HVDC System Control for Damping Subsynchronous Oscillation Using the Novel Eigenvalue Analysis Program," *IEEE Trans. Power Syst.*, Vol. 22, No. 4, November 2007.

[9] C. Karawita and U. D. Annakkage, "HVDC-Generator-Turbine Torsional Interaction Studies Using A Linearized Model With Dynamic Network Representation," in *Proc. Int. Conf. Power Systems Transients (IPST2009)*, 2009.

[10] P. M. Anderson, A. A. Fouad. *Power System Control and Stability.* John Wiley & Sons, Inc., 2003.

[11] Felix F. Wu, Chen-Ching Liu, "Characterization of Power System Small Disturbance Stability with Models Incorporating Voltage Variation," *IEEE Trans. Biomed. Circuits Syst.*, Vol. CAS-33, no. 4, April 1986.

[12] M. J. Gibbard, N. Martin, J. J. Sanchez-Gasca, N. Uchida, V. Vittal, L. Wang, "Recent Applications of Linear Analysis Techniques," *IEEE Trans. Power Syst.*, Vol. 16, no. 1, February 2001.

[13] IEEE Power System Engineering Committee, System Dynamic Performance Subcommittee, "Proposed terms and definitions for power system stability," *IEEE Trans. Power App. Syst."*, Vol. PAS-101, pp. 1894-1898, July 1982.

# Chapter 2

# Transient Stability Assessment of a Small Power System Subjected to Large Disturbances


### Abstract

The growth in size and complexity of power system networks with a large number of interconnections has exposed the system to various contingencies that would lead to system instability. Thus, it is important for a power system to be able to remain in a state of operating equilibrium under normal operating conditions and to regain an acceptable state of equilibrium after being subjected to a disturbance. Transient stability assessment of power systems involves the study of a set of non-linear differential equations following any large disturbance. Such analysis will aid both system planners and system operators in evaluating power system network's ability to withstand any disturbances. This chapter discusses time domain (TD) approach, Extended Equal Area Criterion (EEAC), Direct Method of Lyapunov Function and Transient Energy Function (TEF) in assessing the transient stability of a small power system when subjected to large disturbances. Simulations have been conducted on IEEE 14-bus system and results are presented in this chapter.

## 2.1 Introduction

Power system networks grow rapidly and continuously with a large number of interconnections. The complicated structure of such networks has exposed the system to various contingencies that could lead to system instabilities: steady-state, dynamic or transient. Transient stability analysis is important in evaluating the network's ability to regain an acceptable state of equilibrium after being subjected to either large or small disturbances [1]. The stability characteristic of a power system is analysed from the nature of the set of differential equations when subjected to disturbances [2].

A "disturbance" in a power system is defined as a sudden change or sequence if changes in one or more of the parameters of the system, or in one or more of the physical quantities [3]. Large disturbances often refer to severe disturbances, such as a fault on transmission network, loss of generation, or loss of a large load [1], and that the equations describing the power system cannot be linearised for analysis purpose when subjected to large disturbances [3]. The main factor contributing to the transient instability is the insufficient synchronising torque during the disturbance period in the system [3].

In the past, transient stability has been evaluated using TD approach. If the system could survive for the first swing, i.e., stable in the first swing, then it would generally remain stable in the following swings [3, 4]. TD approach is found to be time-consuming and inefficient for evaluating stability for a large system where the system components vary dynamically and yet, repeated simulations would need to be made. This has encouraged the expansion of various transient stability assessments, such as EEAC [5, 6], Direct Method of Lyapunov Function [2, 7, 8], TEF [8, 9, 10], Decision Tree Transient Stability Method [3] and Composite Electromechanical Distance (CED) Method [3].

A direct method of transient stability analysis of a multimachine power system using extension of the equal area criterion (EAC) has been proposed by Pavella [3]. [5, 6] have in-depth details on EEAC method for multimachine system transient stability. Direct method of Lyapunov function or TEF has been used by [2],[3],[7]-[11]. Pai [11] has provided further

explanations on the concepts of direct method of Lyapunov energy function.

The main purpose of this chapter is to investigate the transient stability of the power system when subjected to large disturbances. Section 2.2 evaluates the transient stability assessments used for both single machine infinite bus (SMIB) system and multimachine system. Section 2.3 shows the SMIB system and the IEEE 14 bus system used for transient stability assessment with simulations and results explained. The chapter is concluded in Section 2.4.

## 2.2 Transient Stability Assessments

Transient stability assessments using TD approach, EAC, direct method of Lyapunov function, EEAC and TEF have been examined on both SMIB system and multimachine system.

### 2.2.1 Single Machine Infinite Bus

A SMIB system shown in Fig. 2.1 is used to demonstrate the fundamental concepts and principles of transient stability when subjected to large disturbances.

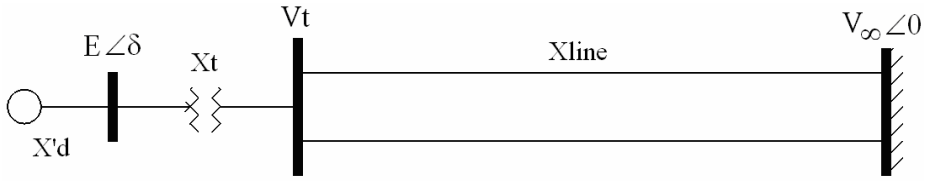


Figure 2.1: A single-machine infinite bus (SMIB) system

To simplify the assessment on transient stability, a classical model of the machines is used. The assumptions made are as follow [4]:

1. All mechanical power inputs are constant.

2. Damping or asynchronous power is negligible.

3. Voltage $E$ behind the transient reactance $X'_d$, i.e., generator bus voltage, is constant.

4. Loads are represented as constant impedances.

The equation of motion or the swing equation describing the SMIB system is as below [11]:

$$\frac{2H}{\omega_0}\frac{d^2\delta}{dt^2} = P_a = P_m - P_e;\ \frac{d\delta}{dt} = \omega \tag{2.1}$$

where $H$ is the inertia constant, $\delta$ is the angular position of the rotor, $\omega$ is the electrical frequency in rad/s, $P_a$ is the accelerating power, $P_m$ is the constant mechanical power input, $P_e$ is the generator's electrical power output and subscript 0 denotes the initial operating condition.

#### 2.2.1.1 Equal Area Criterion

The three conditions: pre-fault, during-fault and post-fault conditions are illustrated in the power-angle plot as shown in Fig. 2.2. Fault occurrence on one of the transmission lines reduces the electrical power output and accelerates the rotor angle. System kinetic energy eventually builds up until it arrives at the clearing angle $\delta_{cl}$, with acceleration area $A_{acc}$ accumulated. At this instant, the excess of electrical power output decelerates the rotor angle until it reaches a point where the previously stored kinetic energy is totally converted into potential energy, i.e., when the deceleration area $A_{dec}$ is equal to area $A_{acc}$.

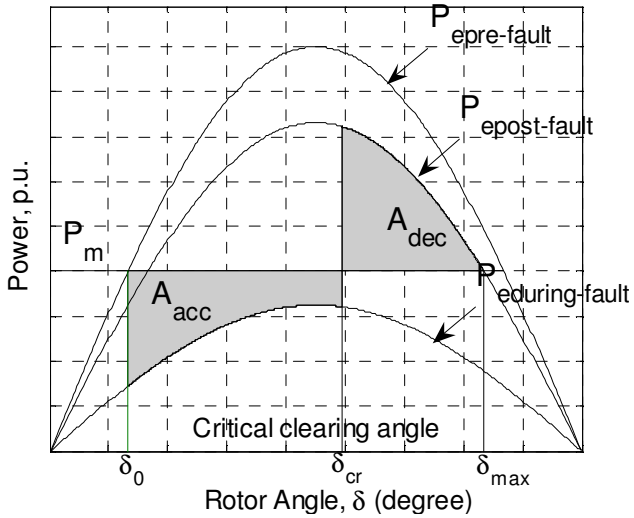


Figure 2.2: Power - angle relationship

#### 2.2.1.2 Direct Method of Lyapunov Function

*Lyapunov's stability theorem* [1, 11] states that:
The equilibrium point of a dynamic system $\frac{dx}{dt} = f(x)$ is stable if there exists a continuously differentiable positive definite function $V(x)$ such that $\frac{dV}{dt} \leq 0$. If the total derivative is negative definite, $\frac{dV}{dt} < 0$, then the equilibrium point is said to be asymptotically stable.

Direct method of Lyapunov function only requires the knowledge at the instant when the last operation is carried out [7]. Any previous knowledge on the occurrences of the faults or switching operations is not of concern.

The function $V(x,t)$ is known as a Lyapunov function with the characteristics as follows [7]:

- The Lyapunov function $V(x,t)$ is positive definite.
- It is a function of the time $t$ and the $n$ variables $x_1$, $x_2$, ..., $x_n$ of the system which is described by $\frac{dx}{dt} = f(x,t)$.
- The total derivative $\frac{dV}{dt}$ along the system trajectories is not positive.

Terms involving $\frac{dx_1}{dt}$, $\frac{dx_2}{dt}$, ..., $\frac{dx_n}{dt}$ are resulted when the total time derivative of the Lyapunov function $V(x,t)$ is taken. Thus, the differential equations describing the system, $\frac{dx}{dt} = f(x,t)$ is incorporated into the total derivative $\frac{dV}{dt}$. For a non-positive $\frac{dV}{dt}$, the stability of the equilibrium is promised [7].

Post-fault equation of a simple system is:

$$M\frac{d\omega}{dt} = P_m - P_{e_{postfault}} = P_m - P_{max_{postfault}} \sin\delta \tag{2.2}$$

where, $M$ = moment of inertia and $P_{max}$ = maximum power.

Integrating both sides give the system energy:

$$V = \frac{1}{2}M\omega^2 - P_m\left(\delta - \delta_{SEP}\right) - P_{max_{postfault}}\left(\cos\delta - \cos\delta_{SEP}\right) \tag{2.3}$$

The critical energy $V_{cr}$ is evaluated where $\delta = \delta_{UEP}$, $\omega$=0 as indicated in equation (2.4).

$$V_{cr} = -P_m \left(\delta_{UEP} - \delta_{SEP}\right) - P_{max_{postfault}} \left(\cos \delta_{UEP} - \cos \delta_{SEP}\right) \tag{2.4}$$

where, subscripts $SEP$ and $UEP$ denote stable equilibrium point and unstable equilibrium point respectively.

The stability of the system could be assured if $\delta \leq \delta_{UEP}$ or the system's total energy $V$ is less than the critical energy $V_{cr}$ for $\delta_{SEP} < \delta < \delta_{UEP}$. If system exceeds the unstable equilibrium point $\delta_{UEP}$, the system would continue to build-up the kinetic energy, which gives rise to the velocity. As a result, the rotor angle would accelerate and machine would lose synchronism [7].

### 2.2.2 Multimachine System

This section elaborates on extending the transient stability assessment to the multimachine system. A classical model of the machines is used in the system with $M_i$, $P_{mi}$, $E_i$ assumed to be constant throughout the transient, and all loads are modelled as constant impedance. The conductances and subsceptances vary from pre-, during-, to post-fault system configurations. The transient stability analysis reported in the next section neglects the conductances assuming lossless transmissions lines in the system.

The motion of the $i$-th machine of an $n$-machine system reduced to generator internal nodes is described by [3, 5, 6]:

$$\frac{d\delta_i}{dt} = \omega_i; \; M_i \frac{d\omega_i}{dt} = P_{mi} - P_{ei} \; i = 1, 2, \ldots, n \tag{2.5}$$

where

$$P_{ei} = E_i^2 G_{ii} + \sum E_i E_j Y_{ij} \cos(\delta_i - \delta_j - \theta_{ij})$$
$$P_{mi} = E_i^2 G_{ii} + \sum E_i E_j Y_{ij} \cos(\delta_{0i} - \delta_{0j} - \theta_{ij})$$

for $j = 1, 2, \ldots, n$, $j \neq i$, $G$ = conductance, $Y$ = admittance, $\delta_{0i}$, $\delta_{0j}$ = initial operating rotor angle and $\theta$ = argument of $Y$.

#### 2.2.2.1 Time Domain Approach

By solving the non-linear swing equation (2.1), the transient stability of a power system could be determined. However, due to the non-linearity of the differential equations, the solution process is tedious and complicated. Thus, numerical integration methods have been applied to examine stability of the system. Rotor angle plot is obtained to determine the transient stability. Numerical integration methods, such as Runge-Kutta methods, are used iteratively to approximate the solution of ordinary differential equations.

#### 2.2.2.2 Extended Equal Area Criterion

EEAC reduces the multimachine transient stability assessment to the EAC by decomposing-aggregating the multimachine system into a two-machine equivalent, and further into a SMIB equivalent [3, 5, 6]. In this study, only a single critical machine, presumed to move apart from the rest, is considered for simplicity.

The multimachine system is decomposed into a critical machine and ($n$-1) of the remaining machines. The expression of relative motion of the critical machine with respect to the remaining machines in the system is developed in this section [3, 5].

The following denotations are made:

$cr$: "critical machine"

$a$: its equivalent, aggregated machine

$A$: the set of all remaining machines

The equivalent inertia coefficients:

$M_{cr}$ = inertia coefficients of the critical machine

$$M_a = \sum_{l \in A} M_l; \;\; M_{total} = \sum_{i=1}^{n} M_i; \;\; M = \frac{M_a M_{cr}}{M_{total}} \tag{2.6}$$

Centre of angles (COA) concept is used to model the equivalent machines and their motions [3]:

$\delta_{cr}$ = rotor angle of a critical machine

$$\delta_a = M_a^{-1} \sum_{l \in A} M_l \delta_l \tag{2.7}$$

The motions of the critical machine and the $(n-1)$ remaining machines are described as [5]:

$$\begin{aligned} M_{cr} \frac{d^2 \delta_{cr}}{dt^2} &= P_{mcr} - P_{ecr} \\ M_l \frac{d^2 \delta_l}{dt^2} &= P_{ml} - P_{el} for l \in A \end{aligned} \tag{2.8}$$

The motion of the remaining system $A$ is illustrated by the total sum of all the motion of each remaining machines, which gives the following [5]:

$$M_a \frac{d^2 \delta_a}{dt^2} = \sum (P_{ml} - P_{el}) for l \in A \tag{2.9}$$

For further simplification, rotor angle of the remaining machines $\delta_j$ are made equivalent to $\delta_a$ for $j \in A$. Hence,

$$\delta_{cr} - \delta_l = \delta_{cr} - \delta_a; \delta_j - \delta_l = 0 for l, j \in A \tag{2.10}$$

The electrical powers contributed by each system are described as [5, 6]:

$$P_{ecr} = E_{cr}^2 Y_{crcr} cos(\theta_{crcr}) + \sum_{j \in A, j \neq cr} E_{cr} E_j Y_{crj} cos(\theta_{cr} - \theta_a - \theta_{crj}) \tag{2.11}$$

$$P_{el} = E_l^2 Y_{ll} cos(\theta_{ll}) + E_l E_{cr} Y_{lcr} cos(\theta_a - \theta_{cr} - \theta_{lcr}) + \sum_{j \in A, j \neq l} E_l E_j Y_{lj} cos(\theta_{lj}) \tag{2.12}$$

To model equivalent SMIB system, the rotor angle is defined as $\delta = \delta_{cr} - \delta_a$ [5].

The motion of the equivalent SMIB system is

$$M\frac{d^2\delta}{dt^2} = P_m - P_e \tag{2.13}$$

where

$$\begin{aligned} P_m &= M_{total}^{-1}\left(M_a P_{mcr} - M_{cr}\sum_{l\in A} P_{ml}\right); \\ P_e &= M_{total}^{-1}\left(M_a P_{ecr} - M_{cr}\sum_{l\in A} P_{el}\right) \end{aligned}$$

Now, the equivalent SMIB equation of motion is modelled as follow [5]:

$$M\frac{d^2\delta}{dt^2} = P_m - P_e = P_m - [P_c + P_{max}sin(\delta - v)] \tag{2.14}$$

where

$$P_e = P_c + P_{max}sin(\delta - v) = M_{total}^{-1}\left(M_a P_{ecr} - M_{cr}\sum P_{el}\right) \tag{2.15}$$

for $l \in A$

$$\begin{aligned} P_c &= M_{total}^{-1}\left[M_a E_{cr}^2 G_{crcr} - M_{cr}\left(\sum_{l\in A} E_l^2 G_{ll} + \sum_{l,j\in A; j\neq l} E_l E_j G_{lj}\right)\right] \\ P_{max} &= M_{total}^{-1}\left[\sum_{l\in A} E_{cr}E_l Y_{crl}\sqrt{M_{cr}^2 + M_a^2 + 2M_{cr}M_a cos(2\theta_{crl})}\right] \\ v &= tan^{-1}\left(\frac{M_{total}}{M_a - M_{cr}}tan(\theta_{cra}) - \frac{\pi}{2}\right) \\ tan(\theta_{cra}) &= \frac{\sum_{l\in A} B_{crl}}{\sum_{l\in A} G_{crl}} = \frac{\sum_{l\in A} Y_{crl}sin(\theta_{crl})}{\sum_{l\in A} Y_{crl}cos(\theta_{crl})} \end{aligned}$$

The technique in identifying the critical machine for a given contingency involves the following [12]:

- Listing a number of the candidate critical machines;

- Considering candidate critical machines comprised of 1, 2, $\cdots$ machines and consecutively combining these candidate critical machines;
- Computing the corresponding candidate critical clearing times (CCT) consecutively: the smallest value of the clearing time is the CCT and the machine with this CCT is the critical machine.

The selection of critical machines may depend on the "initial acceleration criterion"; this includes [12]:

- Categorising the machines with their initial accelerations in a decreasing sequence;
- Selecting those machines which have accelerations similar to that of the machine with the highest initial acceleration.

#### 2.2.2.3 Transient Energy Function

A direct method has been developed in the past few decades [8, 9] to analyse the transient stability where the stability characteristics of system's post disturbance equilibrium point is examined [10]. Such method is named as 'Transient Energy Function' (TEF).

The Lyapunov or energy function $V$ describing the total system transient energy for the post disturbance system is as follow [8, 10]:

$$V_i = V_{KEi} + V_{PEi} \tag{2.16}$$

$$= \sum_{i=1}^{n} \frac{1}{2} M_i \omega_i^2 + \sum_{i=1}^{n} -P_i(\theta_i - \theta_{SEPi}) - \sum_{i=1}^{n-1} \sum_{j=i+1}^{n} [C_{ij} \left(cos\theta_{ij} - cos\theta_{SEPij}\right) + \int_{\theta_{SEPi}-\theta_{SEPj}}^{\theta_i-\theta_j} D_{ij} cos\theta_{ij} d\left(\theta_i - \theta_j\right)] \tag{2.17}$$

where $P_i = P_{mi} - E_i^2 G_{ii}$; $C_{ij} = E_i E_j B_{ij}$; $D_{ij} = E_i E_j G_{ij}$; $B$ = susceptance, $\theta_{ij} = \theta_i - \theta_j$; $\theta_i$ = stable equilibrium point for generator $i$.

The first term is 'Kinetic Energy ($V_{KE}$)'; the remaining three terms are 'Position Energy', 'Magnetic Energy' and 'Dissipation Energy' respectively. Dissipation energy is the

energy dissipated in the network transfer conductances, which includes part of the load impedances. The incorporation of the last three energies gives "Potential Energy ($V_{PE}$)" as in literature [8, 10].

The last term in energy equation, i.e., dissipation energy, can be calculated only if the system trajectory is known [8]. In this chapter, dissipation energy is neglected assuming a lossless transmission line.

The excess energy built-up when the system subjected to a disturbance is referred to transient energy, and would need to be absorbed by the system and convert it into potential energy totally for system's synchronism to be retained.

In TEF, system stability is assured if the transient energy at the instant of fault clearing is less than the critical energy, $V(\delta_{cl}, \omega_{cl}) < V_{cr}$, i.e. the system has positive stability index; otherwise it is unstable with negative stability index [8, 10]. Stability index is indicated as $V_{index} = V_{cr} - V_{cl}$, where $V_{cl}$ is the clearing energy.

At the instant of fault clearing, $\theta = \theta_{cl}$, $\omega = \omega_{cl}$; the transient energy with respect to the pre-fault equilibrium point $\theta_{SEP}$ is [8]:

$$\begin{aligned} V_{cl} &= V_{KEi} + V_{PEi} \\ &= \sum_{i=1}^{n} \frac{1}{2} M_i \omega_{cli}^2 - \sum_{i=1}^{n} P_i \left(\theta_{cli} - \theta_{SEPi}\right) - \\ &\quad \sum_{i=1}^{n-1} \sum_{j=i+1}^{n} \left[C_{ij} \left(cos\theta_{clij} - cos\theta_{SEPij}\right)\right] \end{aligned} \tag{2.18}$$

For a given contingency, the critical transient energy is equivalent to the system potential energy at the post-disturbance unstable equilibrium point (UEP), $\theta_{UEP}$, calculated with respect to the post-disturbance stable equilibrium point (SEP), $\theta_{SEP}$ [8]. Calculation of the critical transient energy evaluates the ability of the system to convert the build-up energy

at the instant of fault clearance.

$$\begin{aligned} V_{cr} &= V_{KEi} + V_{PEi} \\ &= \sum_{i=1}^{n} P_i \left(\theta_{UEPi} - \theta_{SEPi}\right) - \sum_{i=1}^{n-1} \sum_{j=i+1}^{n} \left[C_{ij} \left(cos\theta_{UEPij} - cos\theta_{SEPij}\right)\right] \end{aligned} \quad (2.19)$$

It is important to determine the UEP accurately for a direct method to be used effectively [8]. There are three basic methods in determining the critical energy $V_{cr}$ [10]: 1. Lowest energy UEP method, 2. Potential Energy Boundary Surface (PEBS) method, and 3. Controlling UEP method.

The procedure for transient stability assessment using transient energy of the machines is as follow [8, 9]:

1. Determine the post-disturbance network's SEP and its bus admittance.

2. Determine the system controlling UEP for a given disturbance and compute the critical energy $V_{cr}$ using the UEP determined.

3. The operating conditions at each clearing time $t_{cl}$, i.e., $\theta_{cl}$, $\omega_{cl}$ are computed to determine the transient energy $V_{cl}$ at clearing.

4. Transient stability is assured if clearing energy $V_{cl} \leq$ critical energy $V_{cr}$; else it is unstable.

5. Critical clearing time $t_{cr}$ could be determined when $V_{cl}$ is equal to $V_{cr}$.

Complex modes of instability are always encountered in power system, which makes the identification of the UEP more difficult. To confirm with the correct determination of the UEP, swing curves are obtained for cases where $t_{cl}$ slightly lower and slightly higher than the critical clearing time. The machine's UEP, where $\theta_{UEPi} > \frac{\pi}{2}$ indicates that the machine tends to swing away, and separate from the remaining system for a given disturbance [8].

Recent research reflects that part of the transient energy does not contribute to the system separation, and thus, correction should be made [8]. In this chapter, system's

post-disturbance SEPs are assumed to be equal to the pre-disturbances SEP. In practice, post-disturbance SEP is different from the initial operating condition depending on the post-fault network configurations. On the other hand, both clearing energy and critical energy are not calculated with respect to the same references, i.e., they are computed with respect to pre-disturbance SEP and post-disturbance SEP respectively. Thus, a correction term $V_{correction} = V|_{\theta_{SEP_{prefault}}}^{\theta_{SEP_{postfault}}}$ must be introduced such that both system clearing and critical energies are calculated with respect to the same reference [8]. The correction energy is the energy calculated at $\theta_{SEP_{postfault}}$ with respect to $\theta_{SEP_{prefault}}$.

## 2.3 Simulations and Results

Simulations have been conducted on both, SMIB and multimachine system. In this chapter, the IEEE 14 bus system shown in Fig. 2.6 is used as the multimachine system. TD approach, EAC and direct method of Lyapunov function have been applied on SMIB system whilst TD approach, EEAC and TEF have been applied on IEEE 14 bus system for transient stability assessment. A three-phase fault occurs on one of the double circuit lines in SMIB system and at bus 2 for multimachine system with line 2 - 4 cleared.

### 2.3.1 Single Machine Infinite Bus System

A SMIB system shown in Fig. 2.1 is used to conduct transient stability analysis when one of the double circuit lines is tripped. System parameters used for the analysis are shown in Table 2.1.

Table 2.1: System Parameters for SMIB

| $H$ | $P_m$ | $E$ | $V_\infty$ | $X_t$ | $X'_d$ | $X_{line}$ |
|---|---|---|---|---|---|---|
| 0.1 | 1.2 | 1.5 | 1.0 | 0.2 | 0.3 | 0.3 |

#### 2.3.1.1 Time Domain Approach

Single machine swing curve is plotted at clearing times of 0.04 sec and 0.05 sec as shown in Fig. 2.3(a) and (b). Fig. 2.3(a) shows a stable case where the rotor angle oscillates

with damping, and would eventually subside and reach steady-state towards the end of the transient. The system is critically stable with fault cleared at 0.04 sec, corresponding to a critical clearing angle $\delta_{cl}$ of 82.95 degrees. When the fault is cleared at 0.05 sec, system instability resulted as indicated in Fig. 2.3(b).

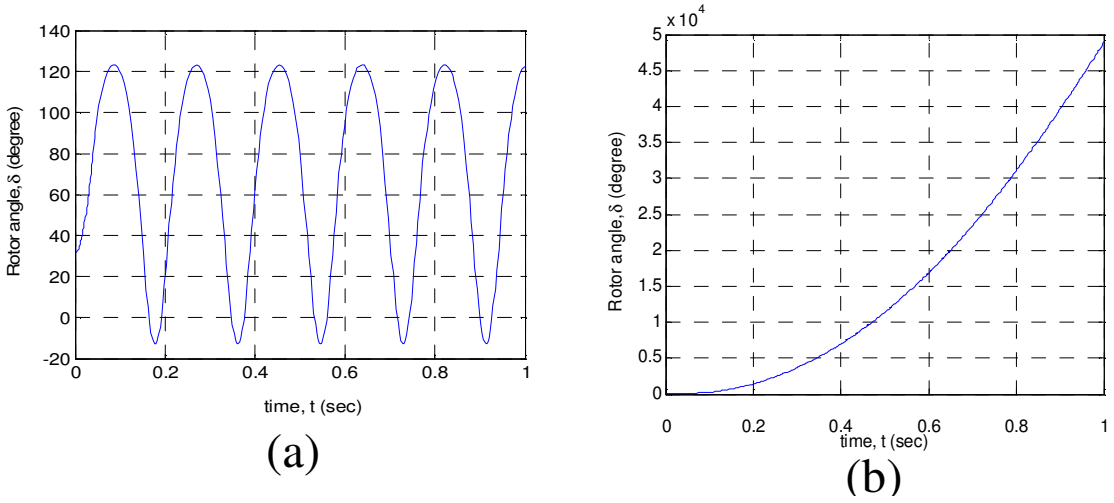


Figure 2.3: Time response of rotor angle with fault cleared at (a) 0.04 sec (b) 0.05 sec

#### 2.3.1.2 Equal Area Criterion

Transient stability analysis is investigated with one of the double lines in the SMIB system tripped. Fig. 2.4 shows the EAC plot for the SMIB system with pre-fault, during-fault and post-fault curves plotted. SMIB remains critically stable with the clearing angle $\delta_{cl}$ of 82.9535 degrees as shown in Fig. 2.4.

#### 2.3.1.3 Direct Method of Lyapunov Function

Fig. 2.5 shows the phase trajectories in $\omega$ - $\delta$ plot under post-fault condition. Each point on the phase trajectories plotted described a particular state of phase of the system. Critical energy $V_{cr}$ for the system investigated is 0.7783, which is shown to be the maximum trajectory, or separatrix in Fig. 2.5.

Stability could be assured if the transient energy at clearing conditions $\delta_{cl}$ and $\omega_{cl}$ remains in the separatrix or alternatively, $V(\delta_{cl}, \omega_{cl}) < V_{cr}$; otherwise it is unstable. The

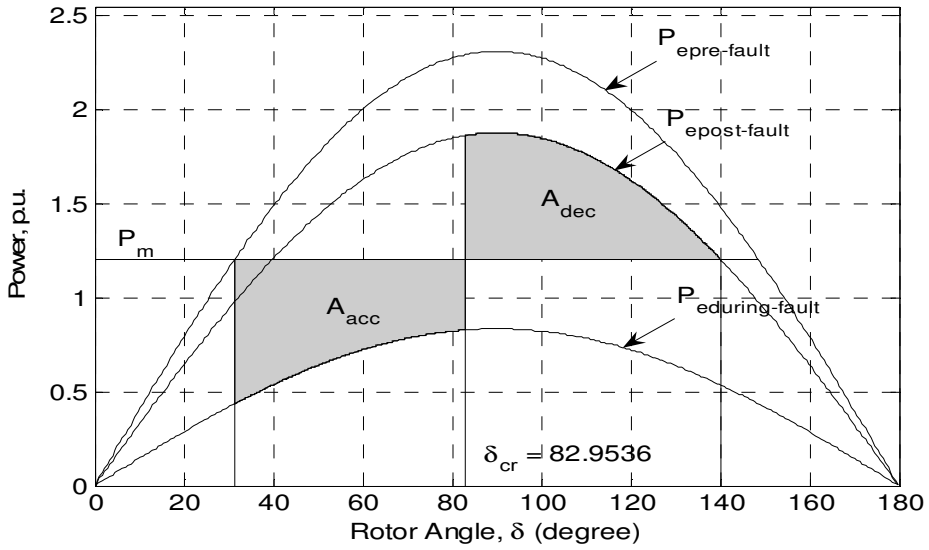


Figure 2.4: Equal Area Criterion (EAC) plot

phase trajectory plotted is deformed from the ellipse due to the non-linearity of the system's motion [7].

### 2.3.2 Multimachine System

In this chapter, the IEEE 14 bus system shown in Fig. 2.6 is used to conduct case studies. The IEEE 14 bus system represents a simple approximation of the American Electric Power System [13]. It consists of 5 synchronous machines, where 3 of them are synchronous compensators for reactive power support, 14 buses and 11 loads. The complete data for this system can be found in [14]. TD approach, EEAC and TEF have been applied on IEEE 14-bus system for transient stability assessment (TSA). A three-phase fault is assumed to occur at bus 2 and line 2 - 4 would be cleared.

#### 2.3.2.1 Time Domain Approach

Different values of clearing time, $t_{cl}$ have been applied to examine the swing curves of the machines. Fig. 2.7 shows the rotor angle of all machines when fault is cleared at 0.052 sec. Fig. 2.7(a) indicates all phase angle differences whereas Fig. 2.7(b) shows that all machines are swinging together.

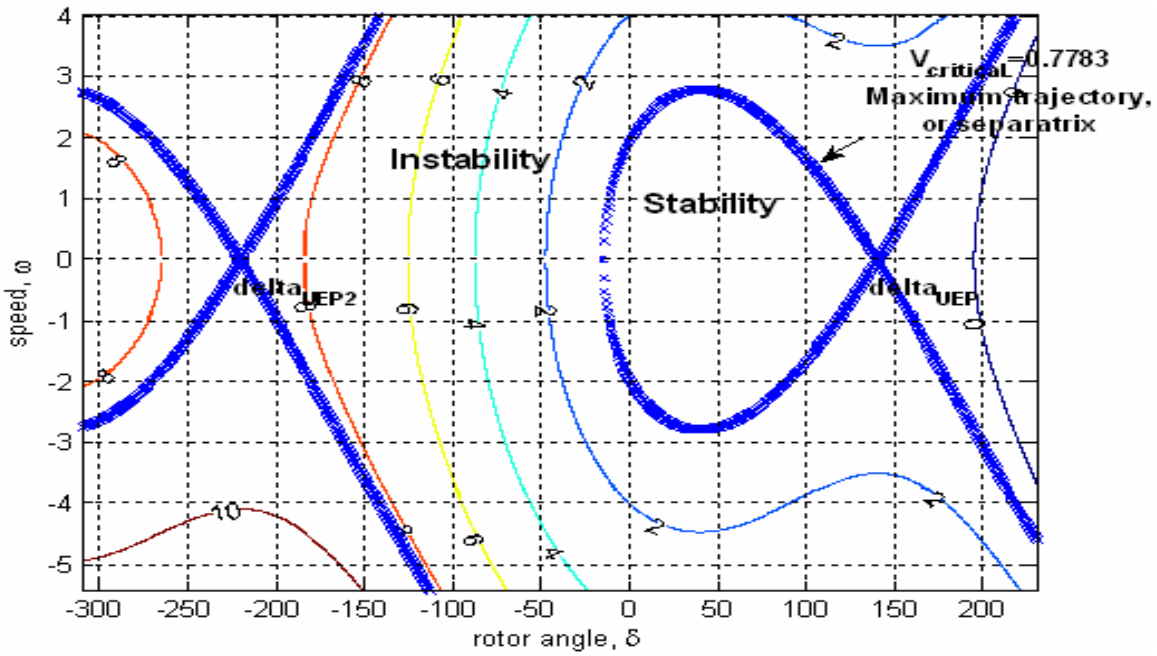


Figure 2.5: Constant V contour of the SMIB system

Simulations show that the system remains critically stable when the fault is cleared at 0.0903 sec. The system becomes unstable when the fault is cleared at 0.0905 sec as shown in Fig. 2.8. One of the machines moves apart from the remaining system as shown in Fig. 2.8(b). Fig. 2.8(a) shows the phase angle differences of all machines with respect to machine 1, which do not return after the maximum swings.

#### 2.3.2.2 Extended Equal Area Criterion

Generator 1 is presumed to be the critical machine to simplify the evaluation of transient stability assessment using EEAC approach. Fig. 2.9 indicates the power angle relationship of multimachine system when subjected to the three-phase fault.

It is highly unlikely for a swing bus to lose synchronism in reality, as it has the largest capacity. Any variations occur would not affect its voltage or frequency.

Figs. 2.10 and 2.11 show the power-angle relationship when generator 2 is presumed to be the critical machine that would move apart from the remaining system. The former with line 2 - 4 cleared whilst the latter with line 2 - 3 cleared.

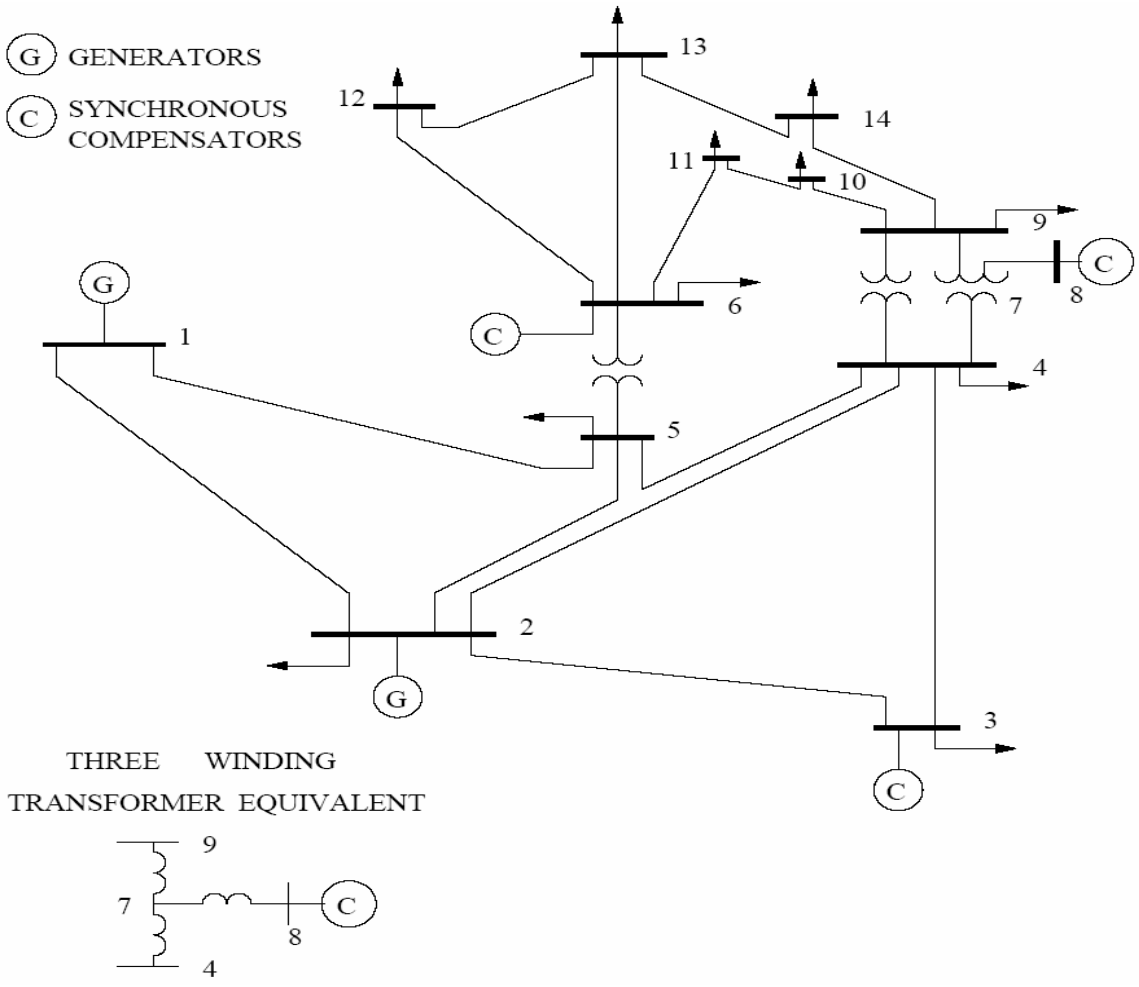


Figure 2.6: The IEEE 14 bus system [14]

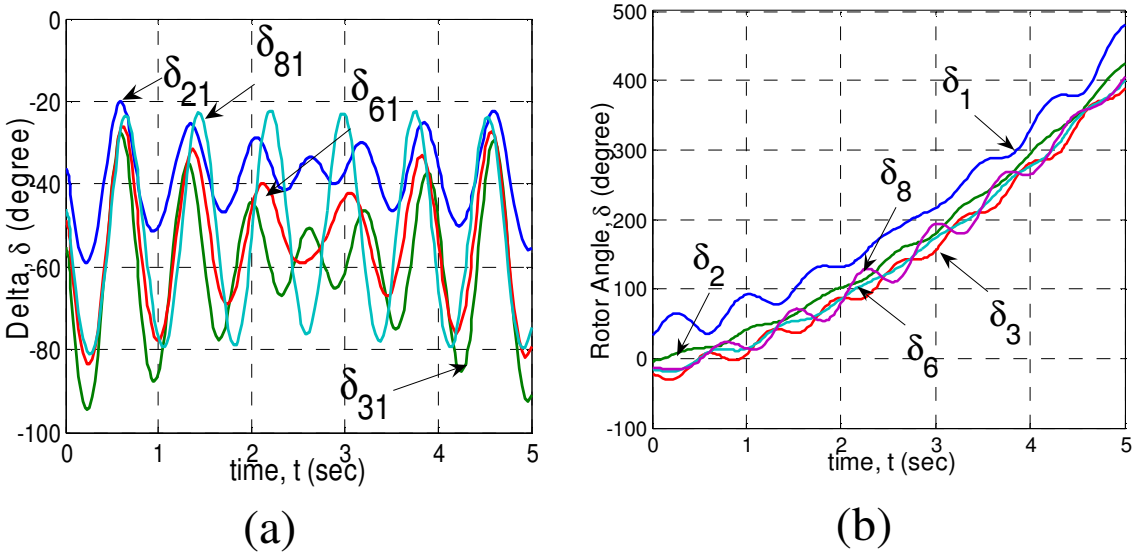


Figure 2.7: Fault cleared at $t = 0.052$ sec (a) Phase angle difference (b) Phase angle of each machine

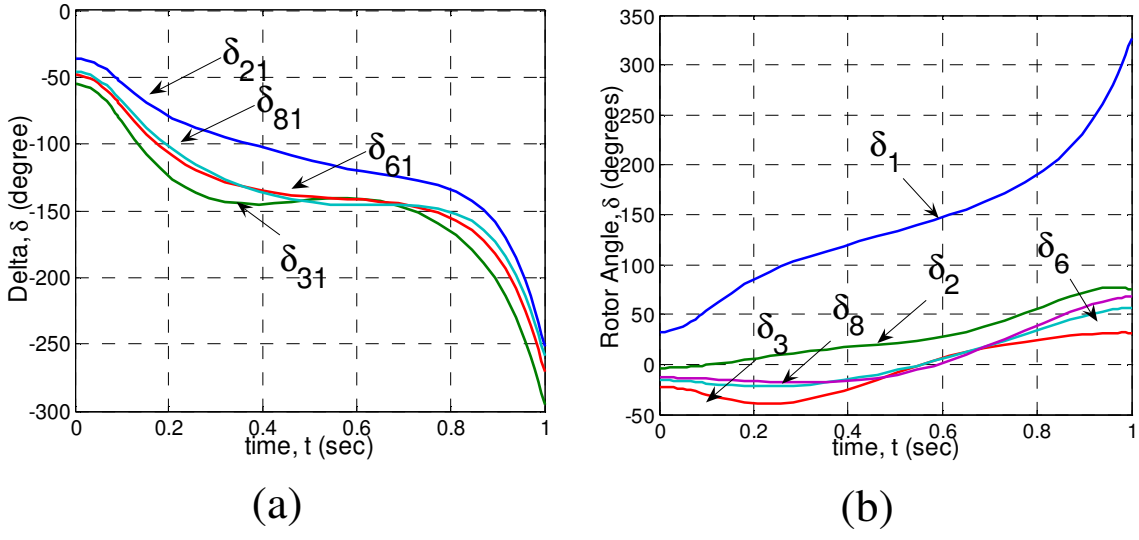


Figure 2.8: Fault cleared at $t = 0.0905$ sec (a) Phase angle difference (b) Phase angle of each machine

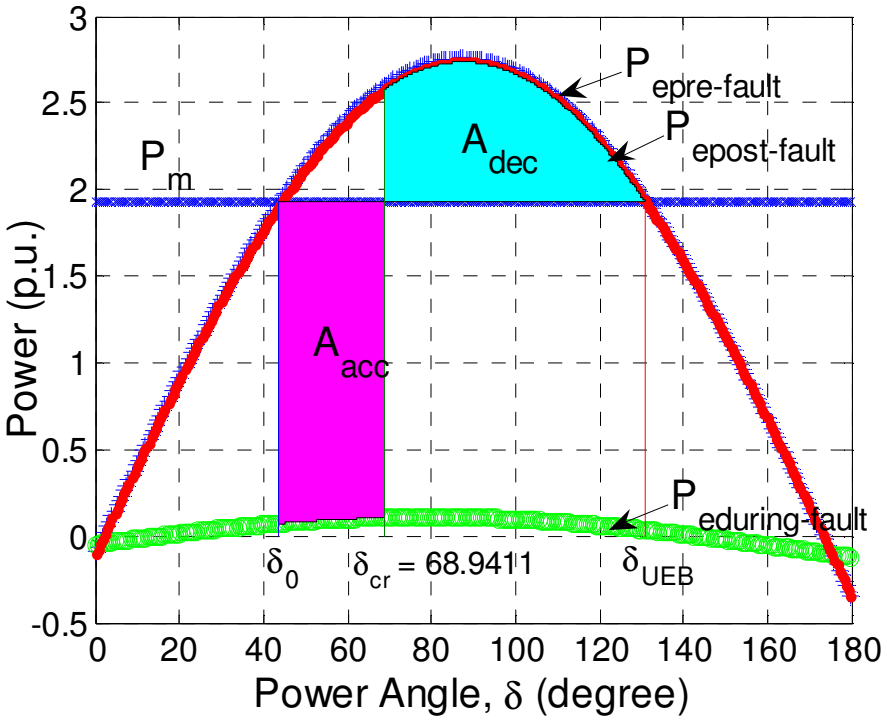


Figure 2.9: Power - angle relationship of multimachine system

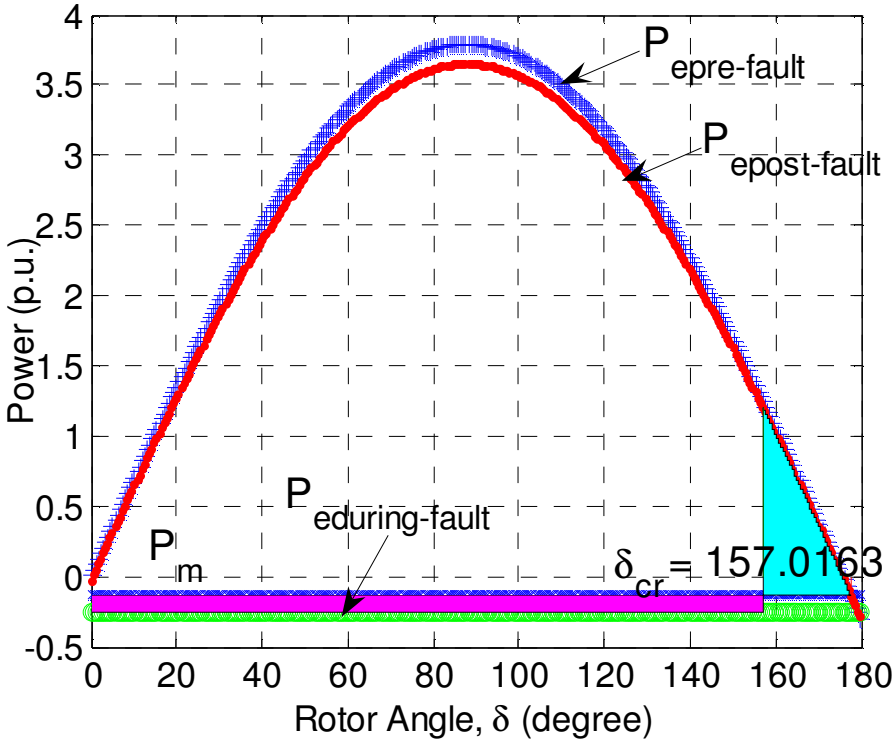


Figure 2.10: Clearance of line 2 - 4

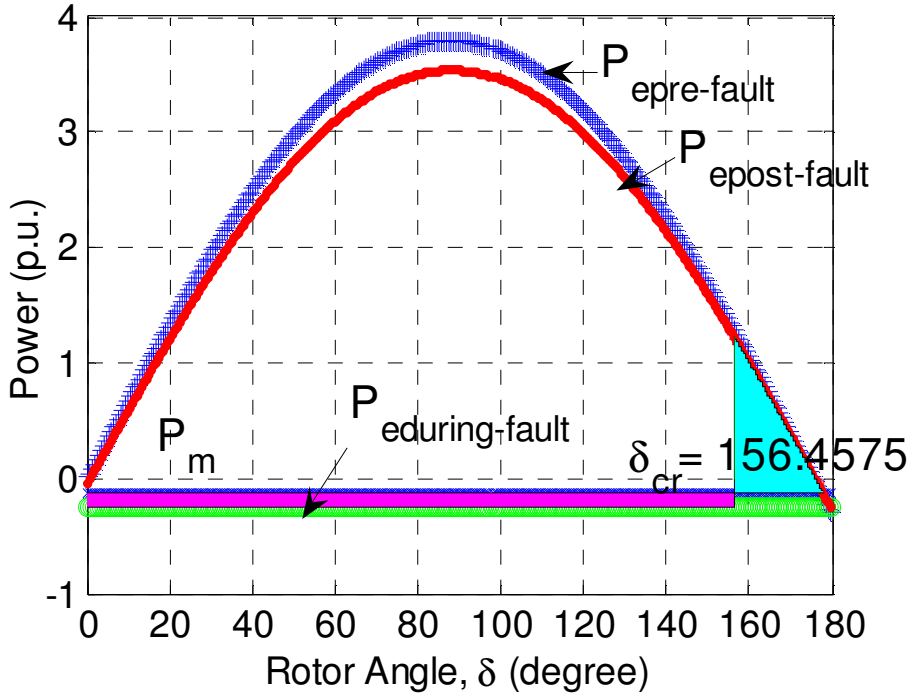


Figure 2.11: Clearance of line 2 - 3

$P_m$ is found to be negative in Figs. 2.10 and 2.11 because the total input power of the remaining system is much greater than the critical machine's input power as in (2.13). Fig. 2.11 indicates a more severe situation as it involves a smaller critical clearing angle. Thus, fault would need to be cleared quicker for the latter case to remain in stability.

#### 2.3.2.3 Transient Energy Function

At the instant of fault clearing, system kinetic energy started decreasing while potential energy started growing up. This indicates that the conversion of system kinetic energy into potential energy is taking place. The successful conversion of accumulated kinetic energy resulted from a particular disturbance into potential energy would result in a constant system energy towards the end of the transient.

## 2.4 Summary

This chapter has presented a comparative study of the different techniques in assessing transient stability. Here, the transient stability of a small power system subjected to large disturbances has been examined via application of TD approach, EEAC and direct method of Lyapunov function. These three methods are used to determine transient stability of a system. Studies have been carried out on the SMIB system and the IEEE 14 bus system and simulation results demonstrate that the transient stability assessment can be conducted on a small power system effectively. In using TD approach, several simulations are required to determine the critical clearing time. EEAC can determine critical clearing angle through a single simulation for any nature of fault, and hence, system's critical clearing time could be calculated. Direct method of Lyapunov function requires only the knowledge at the last instant of fault clearing to determine transient stability. This method is straightforward but computational requirements to determine the UEP are significant.

## References


[1] P. Kundur. *Power System Stability and Control.* McGraw-Hill, 1994.

[2] Ahmed H. El-Abiad and K. Nagappan, "Transient Stability Regions of Multimachine Power Systems," *IEEE Trans. Power App. Syst.*, Vol. PAS-85, no. 2, pp. 169-179, February 1966.

[3] M. Pavella and P. G. Murthy. *Transient Stability of Power Systems: Theory and Practice.* New York: John Wiley & Sons, Inc., 1994.

[4] P. M. Anderson, A. A. Fouad. *Power System Control and Stability.* John Wiley & Sons, Inc., 2003.

[5] Y. Xue, Th. Van Cutsem and M. Ribbens-Pavella, "A Simple Direct Method For Fast Transient Stability Assessment of Large Power Systems," *IEEE Trans. Power Syst.*, Vol. 3, no. 2, pp. 400-412, May 1988.

[6] Y. Xue, Th. Van Cutsem and M. Ribbens-Pavella, "Extended Equal Area Criterion Justifications, Generalizations, Applications," *IEEE Trans. Power Syst.*, Vol. 4, no. 1, pp. 44-52, February 1989.

[7] G. E. Gless, "Direct Method of Liapunov Applied to Transient Power System Stability," *IEEE Trans. Power App. Syst.*, Vol. PAS-85, no. 2, pp. 159-168, February 1966.

[8] A. A. Fouad and S. E. Stanton, "Transient Stability of a Multimachine Power System. Part I: Investigation of System Trajectories; and Part II: Critical Transient Energy," *IEEE Trans. Power App. Syst.*, Vol. PAS-100, no. 7, pp. 3408-3424, July 1981.

[9] A. N. Michel, A. A. Fouad and V. Vittal, "Power system transient stability using individual machine energy functions," *IEEE Trans. Circuits Syst.*, Vol. CAS-30, no. 5, pp. 266-276, May 1983.

[10] M. K. Khedkar, G. M. Dhole and V. G. Neve, "Transient Stability Analysis by Transient Energy Function Method: Closest and Controlling Unstable Equilibrium Point Approach", *IE(I) Journal - EL*, Vol. 85, pp. 83-88, September 2004.

[11] M. A. Pai. *Power System Stability: Analysis by the Direct Method of Lyapunov*. North-Holland Systems and Control Series, Vol. 3, North-Holland Publishing Company, 1981.

[12] Y. Xue, L. Wehenkel, R. Belhomme, P. Rousseaux, M. Pavella, E. Euxibie, B. Heilbronn, J. F. Lesigne, "Extended equal area criterion revisited," *IEEE Trans. Power Syst.*, Vol. 7, No. 3, pp. 1012 1022, August 1992.

[13] Power Systems Test Case Archive, accessed 12 October 2015. URL `http://www.ee.washington.edu/research/pstca/pf14/pg_tca14bus.htm`

[14] F. Milano, "Power System Analysis Toolbox: Documentation for PSAT version 1.3.4," 14 July, 2005.

# Chapter 3

# Evaluation of Small Signal Stability of a Power System


### Abstract

In reality, a power system is never in steady-state, as there are persistent fluctuations in load levels with associated adjustments in generation. The growing complexity of power systems as well as the system exposition to various contingencies have exacerbated the system's steady-state condition. Small disturbances that are always present in the power system networks include small variations in loads and generation and switching operation of power system equipment. It is important to maintain the load-generation balance such that the system frequency remains nominal. Multiple severe contingencies with complex interaction would cause system instabilities, and thus deteriorate the system condition. This chapter explores transient stability of a power system subjected to small disturbances using TD analysis, Eigenvalues analysis, participation factors analysis and transient security assessment using transient security index. Simulations have been conducted on IEEE 14-bus system and the results presented.

## 3.1 Introduction

Linear analysis techniques have been widely applied in studying the dynamic performance of power systems since early 1970s [1]. A disturbance is considered to be small if the equations that describe the resulting response of the system may be linearised for the purpose of analysis [2, 3, 4]. Instability may result from either (i) a lack of synchronizing torque, causing a steady increase in generator rotor angle, or (ii) a lack of sufficient damping torque, resulting in rotor oscillations of growing amplitude [2].

In reality, small disturbances always occur in a power system, such as small variations in loads and generation [2]. Some other forms of small disturbances could be transformer tap changing, switching operation of power system equipment, such as condenser and capacitor. The ability of the system to operate satisfactorily under small disturbance conditions ensures successful delivery of the maximum power to the system.

A system is said to be steady-state stable if, when subjected to small disturbances, it reaches a steady-state operating point which is identical, or close to the pre-disturbance condition [3, 4, 5]. The system parameters would not change significantly [3].

In this chapter, transient stability of a power system subjected to small disturbances has been examined using Power System Analysis Toolbox (PSAT). PSAT is a Matlab toolbox for static and dynamic analysis and control of electric power system [6, 7].

The main purpose of this chapter is to investigate the transient stability and responses of a power system responding to small disturbances. The chapter is structured as follows. Section 3.2 evaluates the linear analysis applied to a dynamic system. Section 3.3 describes the models used for the excitation system and turbine-governor (TG) control. This is followed by Section 3.4 which evaluates the transient stability assessments and their mathematical description on a multimachine system. The algorithm for transient stability determination is illustrated in Section 3.5. Section 3.6 shows the IEEE 14 bus system used for transient stability assessments, and presents the simulation results when small disturbances are applied. The chapter is concluded in Section 3.7.

## 3.2 Linear Analysis

In general, the behaviour of a power system is described by a set of first order non-linear differential-algebraic equations, DAEs, as follow [2], [3], [7] - [12]:

$$\begin{aligned} \dot{x} &= f(x, y) \\ 0 &= g(x, y) \end{aligned} \tag{3.1}$$

where $x$ is the vector of $n$ state variables comprised of the dynamic states of generators, excitation system, TG controller and others; $y$ is the vector of algebraic variables; $f$ is a vector of $n$ first order non-linear ordinary differential equations and $g$ is a vector of $m$ non-linear algebraic equations.

Linearisation of the DAE set in (3.1) at an equilibrium point $(x_0, y_0)$ gives the system Jacobian and state matrix [9] as shown in (3.2). The system's response to small variations in the input or state variables could then be investigated at the equilibrium point [2, 10].

$$\begin{bmatrix} \Delta\dot{x} \\ 0 \end{bmatrix} = \begin{bmatrix} f_x & f_y \\ g_x & g_y \end{bmatrix} \begin{bmatrix} \Delta x \\ \Delta y \end{bmatrix} = \begin{bmatrix} J \end{bmatrix} \begin{bmatrix} \Delta x \\ \Delta y \end{bmatrix} \tag{3.2}$$

where $J$ is the system Jacobian matrix, comprised of the submatrices of $f_x = \frac{\partial f}{\partial x}$; $f_y = \frac{\partial f}{\partial y}$; $g_x = \frac{\partial g}{\partial x}$; $g_y = \frac{\partial g}{\partial y}$.

Assuming $g_y$ is non-singular, system $A$ matrix, $A_{sys}$, can be readily obtained with the stator algebraic variables $y$ been eliminated [7, 8, 11, 12]. The matrix $A_{sys}$, which is a reduced Jacobian matrix, can be derived from the load flow solution.

$$A_{sys} = f_x - f_y g_y^{-1} g_x \tag{3.3}$$

## 3.3 Machine Models

Figs. 3.1 and 3.2 show block diagrams of the IEEE-Type 1 excitation system and TG Type II controller, respectively. The machine, exciter and TG models have been adopted from [6].

First block of the exciter model $\frac{K_A}{1+sT_A}$ in Fig. 3.1 is the system amplifier model. Second block $\frac{1}{K_E+sT_E}$ is the exciter block. The derivative feedback block $\frac{sK_F}{1+sT_F}$ is the compensation block; it is included to minimise the phase shift introduced by the time delays over a selected frequency range [2]. The output voltage $E_{fd}$ of a dc exciter is related to the field of the synchronous machine directly. Magnetic saturation of the exciter is represented by the non-linear function $S_E$. A commonly applied expression for saturation, i.e. an exponential function [2]:

$$V_X = E_{fd} S_E\left(E_{fd}\right) = A_{EX} e^{B_{EX} E_X} \tag{3.4}$$

where, $S_E\left(E_{fd}\right)$ is the saturation function, $E_X$ is the exciter output voltage, $A_{EX}$ and $B_{EX}$ are derived from exciter data.

The parameters $T_1$ and $T_2$ used for TG in Fig. 3.2 represent the time constant for transient gain and governor respectively [6]. Here, $R$ is the speed droop.

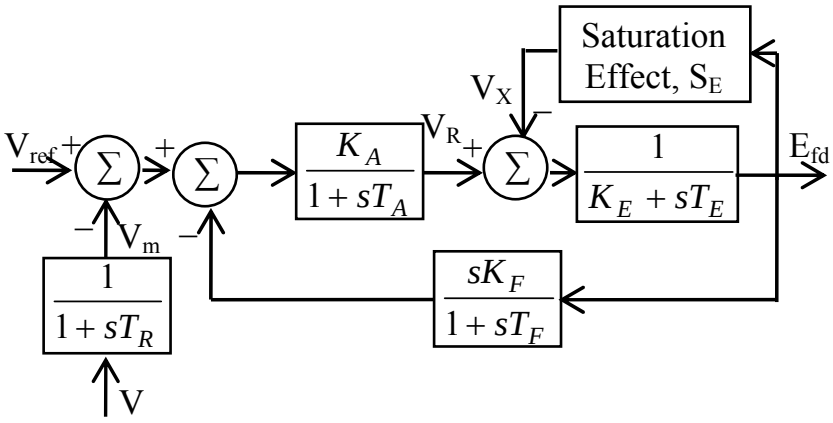


Figure 3.1: IEEE-Type 1 exciter model [6, 8]

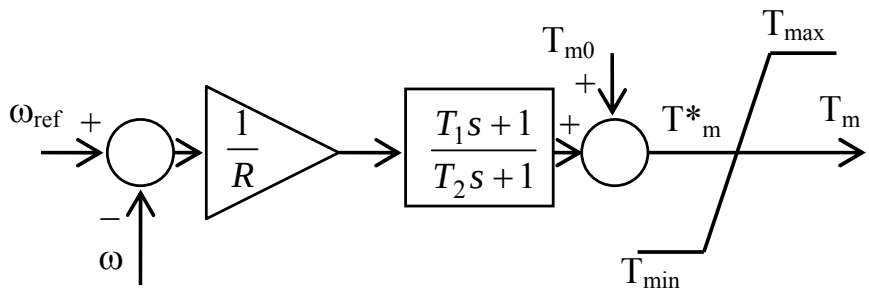


Figure 3.2: Turbine-governor Type II [6]

## 3.4 Transient Stability Assessments and Mathematical Description

The following subsections discuss the evaluation of the transient stability in multimachine system when subjected to small disturbances. Methods used to determine the transient stability are time domain analysis, Eigenvalues analysis and participation factors analysis. Eigen-properties such as damping ratio and oscillation frequency associated with system modes are studied as well. Transient security assessment is examined to determine the security status and the stability limit of the power system using a transient security index.

### 3.4.1 Time Domain Analysis

In this chapter, time domain is used to verify the results obtained from the frequency domain analysis. The system stability is assured if the oscillations are damped and reach steady-state towards the end of the transient. If the oscillations continue to grow, or are sustained indefinitely, the system is unstable [3].

### 3.4.2 Eigenvalues Analysis

The values of $s$ which satisfy the characteristic equation of matrix $A_{sys}$, given in (3.5), are the eigenvalues of the system:

$$det\,(sI - A_{sys}) = 0 \tag{3.5}$$

Analysis of the eigen-properties in matrix $A_{sys}$ provides important details on the system

stability characteristics [2].

A pair of eigenvalues is expressed as $s = \sigma \pm j\omega$. Both oscillation frequency and damping ratio could be determined as $f = \frac{\omega}{2\pi}$ and $\zeta = \frac{\sigma}{\sqrt{\sigma^2+\omega^2}}$ respectively [2]. In general, the system is stable if all the system eigenvalues lie onto left-half plane, i.e. $\Re(s_i) < 0$ for all $i$.

Interarea mode and local plant mode oscillations can be determined from the oscillation frequencies ranged between 0.1 Hz and 2.0 Hz [2]. Oscillation frequencies range from 0.1 Hz to 0.7 Hz are categorised as interarea mode of oscillation, whilst oscillation frequencies range from 0.7 Hz to 2.0 Hz are considered as local plant mode of oscillation [2, 13]. Interarea mode oscillation could be further categorised into low-frequency interarea mode and high-frequency interarea mode with oscillation frequencies of 0.1 Hz - 0.3 Hz and 0.3 Hz - 0.7 Hz, respectively [2].

The $n$-column vector $\phi_i$ is called the right eigenvector of $A$ associated with the eigenvalue $s_i$ if for any eigenvalue $s_i$, it satisfies the following equation [2]:

$$A\phi_i = s_i\phi_i \quad i = 1, 2, \cdots, n \tag{3.6}$$

where, the eigenvector $\phi_i$ has the following form

$$\phi_i = [\phi_{1i}\ \phi_2\ \cdots\ \phi_n i]^T$$

Likewise, the $n$-row vector $\psi_i$ is called the left eigenvector of $A$ associated with the eigenvalue $s_i$ if it satisfies the following equation [2]:

$$\psi_i A = s_i\psi_i \quad i = 1, 2, \cdots, n \tag{3.7}$$

The left and right eigenvectors corresponding to different eigenvalues are orthogonal, i.e. $\psi_j\phi_i = 0$ if $s_i$ is different to $s_j$. $\psi_i\phi_i = Z_i$ for the eigenvectors corresponding to the same eigenvalue, where $Z_i$ is a non-zero constant. These eigenvectors are generally been normalised such that $\psi_i\phi_i = 1$ as these vectors are established to within a scalar multiplier

only [2].

Differentiating (3.6), which describes the eigenvalues and eigenvectors, with respect to $a_{kj}$ yields the following:

$$\frac{\partial A}{\partial a_{kj}}\phi_i + A\frac{\partial \phi_i}{\partial a_{kj}} = \frac{\partial s_i}{\partial a_{kj}}\phi_i + s_i\frac{\partial \phi_i}{\partial a_{kj}} \tag{3.8}$$

Premultiplying (3.8) by $\psi_i$, this equation simplifies to the following with $\psi_i\phi_i = 1$ and $\psi_i(A - s_iI) = 0$:

$$\frac{\partial A}{\partial a_{kj}} = \frac{\partial s_i}{\partial a_{kj}} \tag{3.9}$$

All components of $\frac{\partial A}{\partial a_{kj}}$ are zero, excluding the component in the $k$th row and $j$th coloumn which is equal to 1. Thus,

$$\frac{\partial s_i}{\partial a_{kj}} = \psi_{ik}\phi_{ji} \tag{3.10}$$

Equation (3.10) has defined the sensitivity of the eigenvalue $s_i$ to the element $a_{kj}$ of the state matrix $A$, which is equivalent to the product of the left eigenvector component $\psi_{ik}$ and the right eigenvector component $\phi_{ji}$ [2].

### 3.4.3 Participation Factors Analysis

Participation matrix, which combines both left and right eigenvectors, is non-dimensional scalar that measures the association between the state variables and the modes of a linear system [2, 11, 12] and can be expressed as:

$$P = \begin{bmatrix} p_1 & p_2 & \cdots & p_n \end{bmatrix} \tag{3.11}$$

with $p_i = [p_{1i}\ p_{2i}\ \cdots\ p_{ni}]^T = [\phi_{1i}\psi_{i1}\ \phi_{2i}\psi_{i2}\ \cdots\ \phi_{ni}\psi_{in}]^T$ where $\phi_{ki} = k^{th}$ entry of the right eigenvector $\phi_i$; $\psi_{ik} = k^{th}$ entry of the left eigenvector $\psi_i$.

$\phi_{ki}$ measures the activity of the $k^{th}$ state variable in the $i^{th}$ mode whilst $\psi_{ik}$ weighs the contribution of this activity to the mode [2, 11]. The product $p_{ki}$, i.e. $\phi_{ki}\psi_{ik}$, evaluates the net participation. The sensitivity of eigenvalue $s_i$ to the diagonal component $a_{kk}$ of the state matrix $A$ as seen in (3.10) is equivalent to the participation factor $p_{ki}$, which are usually suggestions of the relative participations of the particular states in the corresponding modes [2]. Participation factors analysis can be used to determine the optimum sites for a power system stabiliser (PSS) [11]. Stabiliser coordination is applied to ensure that specified damping criteria for the rotor modes are achieved [1].

### 3.4.4 System Security Assessment

Transient security assessment determines the security status of a system at a particular operating condition using transient security index. The damping ratio of the critical mode in the system has been used as transient security index in this chapter [14]. This index identifies the critical modes for a particular operating condition, and the critical disturbances/contingencies for a particular system by ranking the index [14].

## 3.5 Algorithm for Transient Stability Determination

The determination of transient stability is important to ensure the satisfactory system operation under small disturbances. The flow chart in Fig. 3.3 shows an algorithm for determining transient stability of a power system subjected to various small disturbances. Simulation results provided in Section 3.6 further illustrate the algorithm.

## 3.6 Simulations and Results

Synchronous machine models used in IEEE 14 bus system shown in Fig. 3.4 are two-axis model including IEEE-Type 1 exciter.

In this chapter, small disturbances are modelled and applied to the IEEE 14 bus system to examine its transient stability; this includes small variations in loads and condenser switching. Time domain analysis is studied to validate the system stability as observed

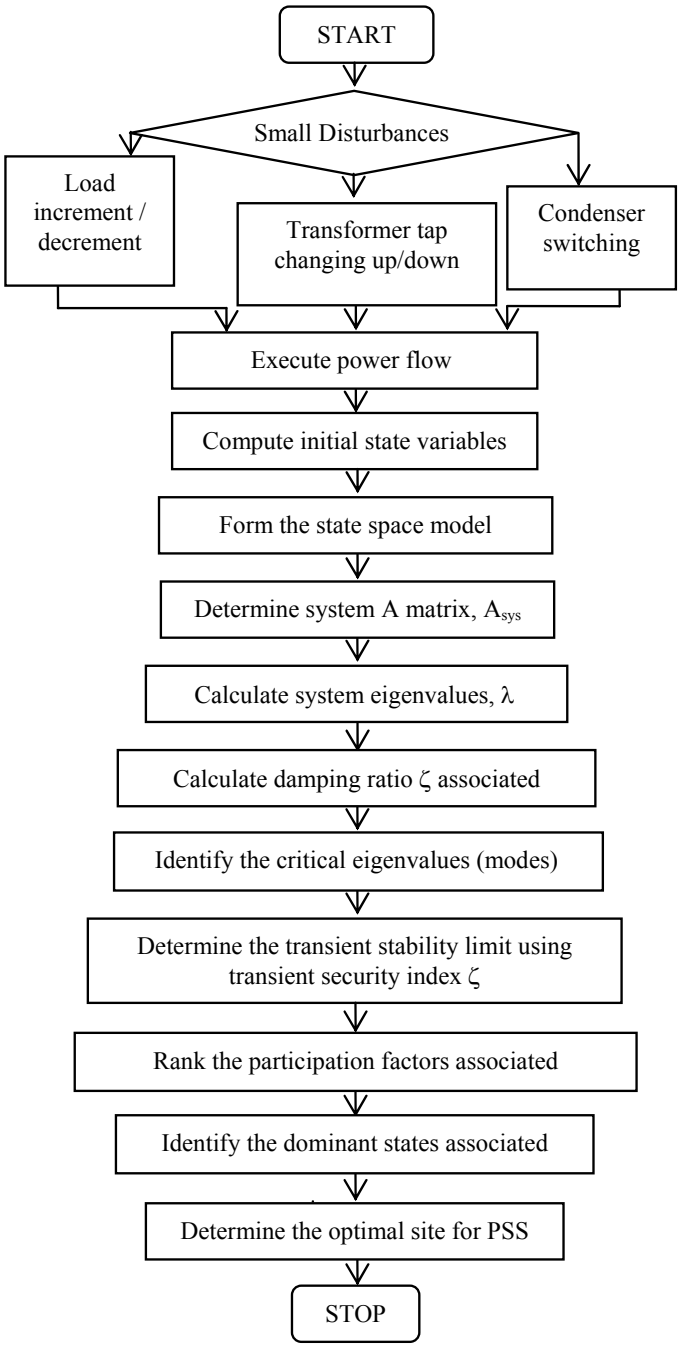


Figure 3.3: Transient stability determination algorithm

in the frequency domain analysis. Initial condition of the system, as indicated in the eigenvalues analysis in Fig. 3.5, shows all eigenvalues lie onto left-half plane, thus it is steady-state stable.

There are 54 eigenvalues computed. Table 3.1 shows only eigenvalues with oscillation frequencies between 0.1 Hz - 2.0 Hz for the system under normal operating conditions. The oscillation frequencies, damping ratios and dominant states associated are displayed as well. The first four oscillatory pairs represent the low-frequency interarea mode of oscillations with frequency ranges between 0.1 Hz to 0.3 Hz. These interarea mode oscillations have positive damping.

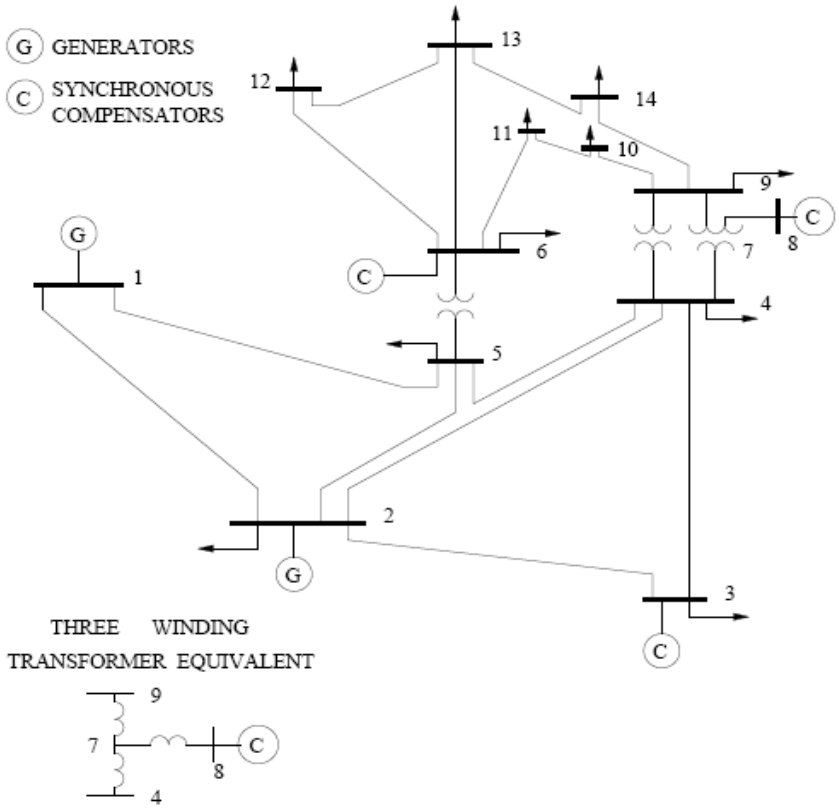


Figure 3.4: The IEEE 14-bus system [6]

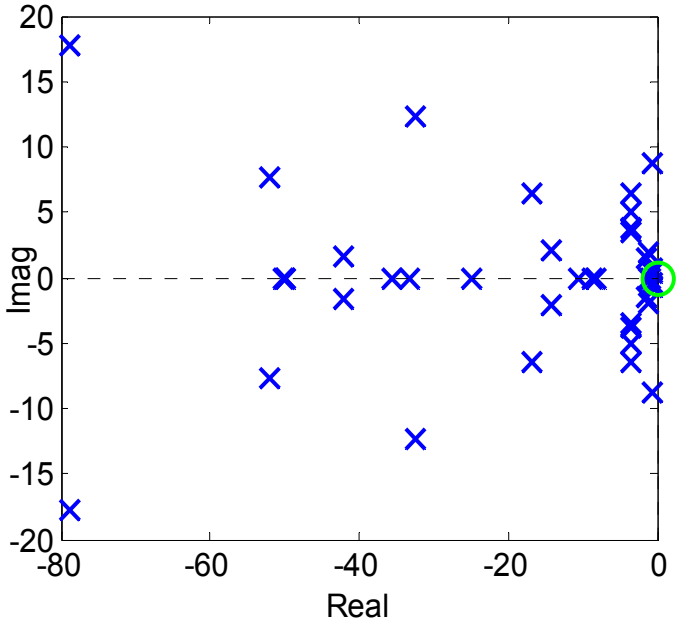


Figure 3.5: S-domain eigenvalues plot under normal condition

Table 3.1: Initial System Modes

| Mode | Eigenvalues $\lambda$ | Frequency (Hz) | Damping ratio $\zeta$ |
|---|---|---|---|
| 1 | -0.59 $\pm$ $j$0.76 | 0.1213 | 0.61 |
| 2 | -1.5373 $\pm$ $j$1.40 | 0.2234 | 0.74 |
| 3 | -42.03 $\pm$ $j$1.60 | 0.2545 | 1.00 |
| 4 | -1.21 $\pm$ $j$1.90 | 0.3018 | 0.54 |
| 5 | -14.21 $\pm$ $j$2.04 | 0.3250 | 0.99 |
| 6 | -3.45 $\pm$ $j$3.53 | 0.5624 | 0.70 |
| 7 | -3.45 $\pm$ $j$3.79 | 0.6036 | 0.67 |
| 8 | -3.44 $\pm$ $j$5.06 | 0.8047 | 0.56 |
| 9 | -16.87 $\pm$ $j$6.36 | 1.0123 | 0.94 |
| 10 | -3.55 $\pm$ $j$6.44 | 1.0242 | 0.48 |
| 11 | -52.02 $\pm$ $j$7.70 | 1.2256 | 0.99 |
| 12 | -0.59 $\pm$ $j$8.79 | 1.3985 | 0.07 |
| 13 | -32.49 $\pm$ $j$12.28 | 1.9541 | 0.94 |

### 3.6.1 Small Varitaions in Loads

This section evaluates the effect of loads changing onto the transient stability of the IEEE 14 bus system. Time responses of the machines' speed deviation and bus voltages are plotted to validate the system stability as observed in the eigenvalues analysis.

#### 3.6.1.1 A System Without Turbine-Governor Control

Before we look into the effect of load variations, we examine the system with and without TG controller subjected to 2% load increment on all load buses. This section evaluates the system without TG controller. Fig. 3.6 shows the eigenvalues plot when the system is subjected to 2% loads increase. A pair of the eigenvalues have crossed over the stability margin with the values of $0.02816 \pm j8.6183$, indicating instability. The active power generation is constant with no TG included. When the system is subjected to loads increment, the active power will become unbalanced as generation remains constant; hence it leads to instability.

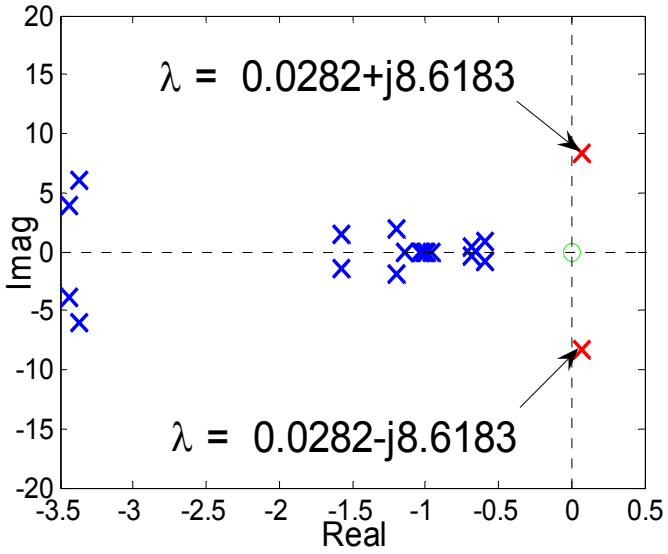


Figure 3.6: S-domain eigenvalues plot

#### 3.6.1.2 A System With Turbine-Governor Control

Obviously a power system without TG controllers is not realistic. Thus, TG controller is to be included. Any velocity differences resulted from disturbances would be corrected by the TG. It controls the generation to match the load variations and losses in the system.

Eigen-study is conducted when the system is subjected to 2% loads increase on all load buses. The pair of eigenvalues is $-0.55757 \pm j8.7644$, with a positive damping ratio $\zeta$ of 0.0635. The system is stable compared to the previous system without TG controller.

Now, the effect of loads changing onto the transient stability of the test system is examined. Test cases with total system loads increased by 30% and decreased by 30% are represented by Test Case (A) and Test Case (B) respectively. To identify the modes of the interarea and local plant modes, eigenvalues with frequencies in the range of 0.1 to 2.0 are displayed.

As interpreted in Table 3.2 and Fig. 3.7(a), the two local plant oscillatory modes (mode 12) as represented by $\lambda_{23}$ and $\lambda_{24}$ have oscillation frequency of 1.3289 Hz and negative damping $\zeta$ of $-0.0091$. The real parts of $\lambda_{23}$ and $\lambda_{24}$ are positive. This results instability. The dominant states associated are $E'_{q1}$ and $V_{f1}$.

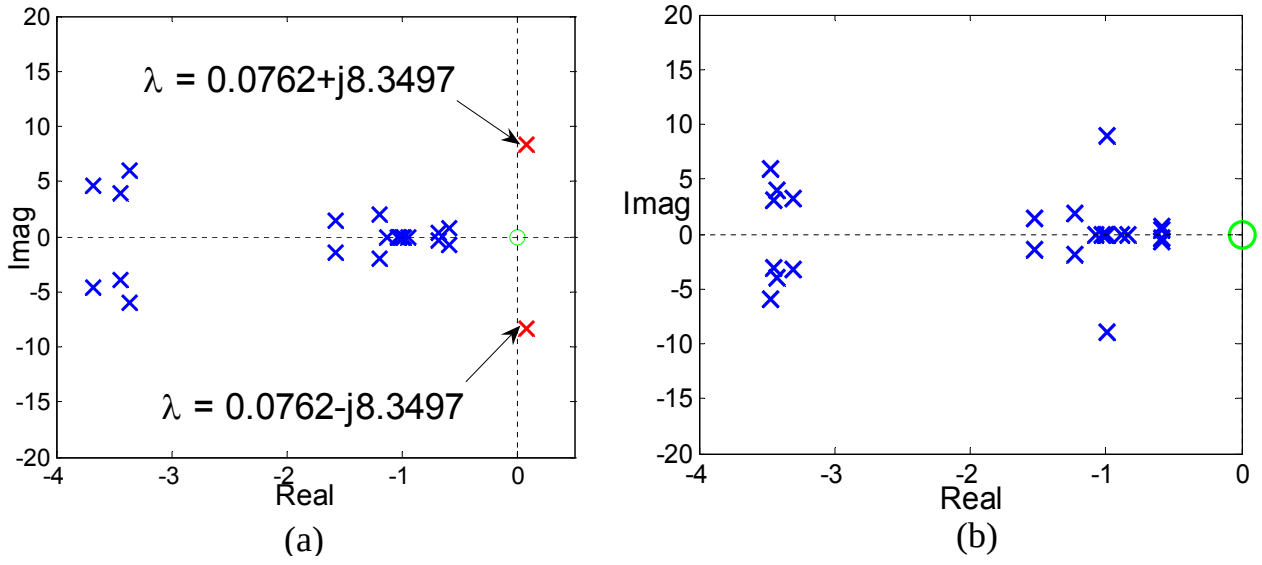


Figure 3.7: Eigenvalues plot - (a) Total system load increased by 30%; (b) Total system load decreased by 30%

Table 3.2: System Modes when Subjected to 30% Load Increase

| Mode | Eigenvalues $\lambda$ | Frequency (Hz) | Damping ratio $\zeta$ |
|---|---|---|---|
| 1 | -0.59 $\pm$ $j$0.79 | 0.1251 | 0.60 |
| 2 | -1.58 $\pm$ $j$1.42 | 0.2256 | 0.74 |
| 3 | -14.68 $\pm$ $j$1.81 | 0.2887 | 0.99 |
| 4 | -1.20 $\pm$ $j$1.94 | 0.3086 | 0.52 |
| 5 | -41.00 $\pm$ $j$2.45 | 0.3892 | 1.00 |
| 6 | -3.44 $\pm$ $j$3.89 | 0.6185 | 0.66 |
| 7 | -3.67 $\pm$ $j$4.56 | 0.7253 | 0.63 |
| 8 | -16.60 $\pm$ $j$5.71 | 0.9085 | 0.95 |
| 9 | -3.36 $\pm$ $j$6.06 | 0.9646 | 0.49 |
| 10 | -4.03 $\pm$ $j$7.41 | 1.1799 | 0.48 |
| 11 | -51.76 $\pm$ $j$7.85 | 1.2498 | 0.99 |
| 12 | 0.08 $\pm$ $j$8.35 | 1.3289 | -0.01 |
| 13 | -33.19 $\pm$ $j$11.23 | 1.7875 | 0.95 |

Fig. 3.8 shows the interarea mode and local plant mode oscillations. Local generator 1 mode has a period of $t \approx 0.75$ sec corresponding to a natural frequency of 1.3333 Hz. This value compares reasonably well with the result of eigenvalue analysis, which has an oscillation frequency of 1.3289 Hz.

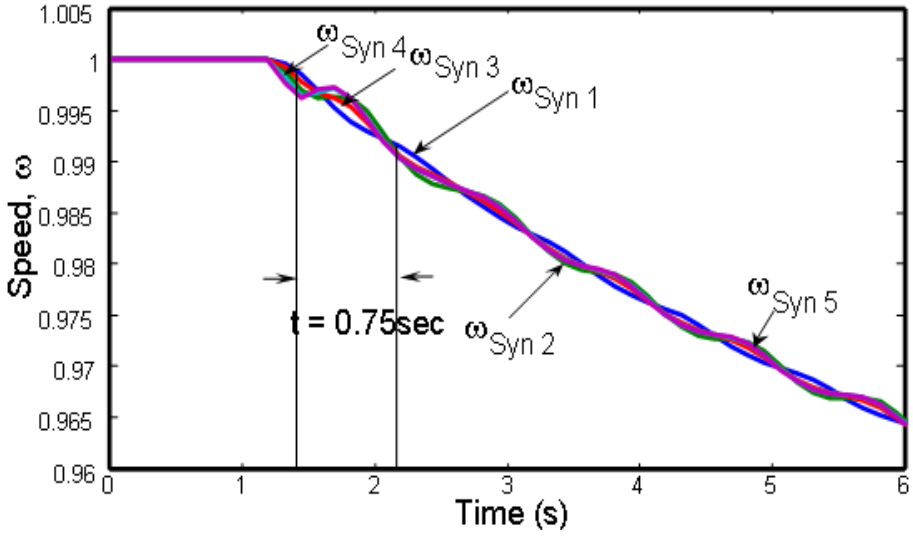


Figure 3.8: Time response of speed deviations

Fig. 3.9(a) shows the bus voltages of the system subjected to 30% increase of total loads at $t = 1.2$ sec. The bus voltages oscillate throughout the transient. The oscillations continue to grow, leading to instability.

When the system is subjected to 30% decrease of total loads at $t = 1.2$ sec, all eigenvalues lie onto the left half plane, as shown in $s$-domain plot in Fig. 3.7(b). There are four low-frequency interarea oscillation modes, with oscillation frequencies range between 0.1 Hz to 0.35 Hz. All eigenvalues obtained have positive damping, indicating a well-damped system under load decrement condition. The bus voltages shown in Fig. 3.9(b) indicates the voltages rise at $t = 1.2$ sec. The bus voltages oscillate throughout the transient, and eventually reach the steady-state towards the end of the transient, hence system is stable.

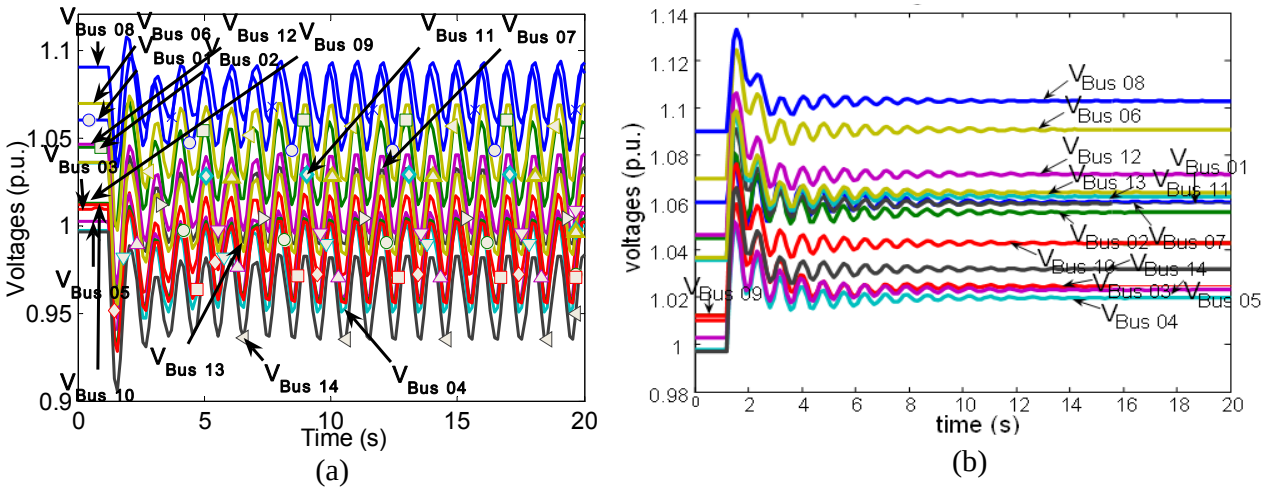


Figure 3.9: Bus voltages - (a) System subjected to 30% load increase; (b) System subjected to 30% load decrease

Fig. 3.10 shows the critical eigenvalue (mode) trajectory under different system load increment. The critical eigenvalues are the eigenvalues with least damping ratio or the rightmost eigenvalues which is close to being unstable. It is observed that the pair of eigenvalues crossed the imaginary axis, i.e., the stability limit (or Hopf bifurcation), when the total system loads are increased beyond 27%. When the total system loads are increased by 28%, the critical modes are $0.01639 \pm j8.3911$ with negative damping ratio $\zeta$ of $-0.0020$. The continuous increments on total system load result further reduction on damping, and eventually leads to the instability when the real value of $\lambda$, $\Re(\lambda)$, becomes positive. The associated damping ratio becomes negative, indicating growing amplitude with respect to time; leading to instability.

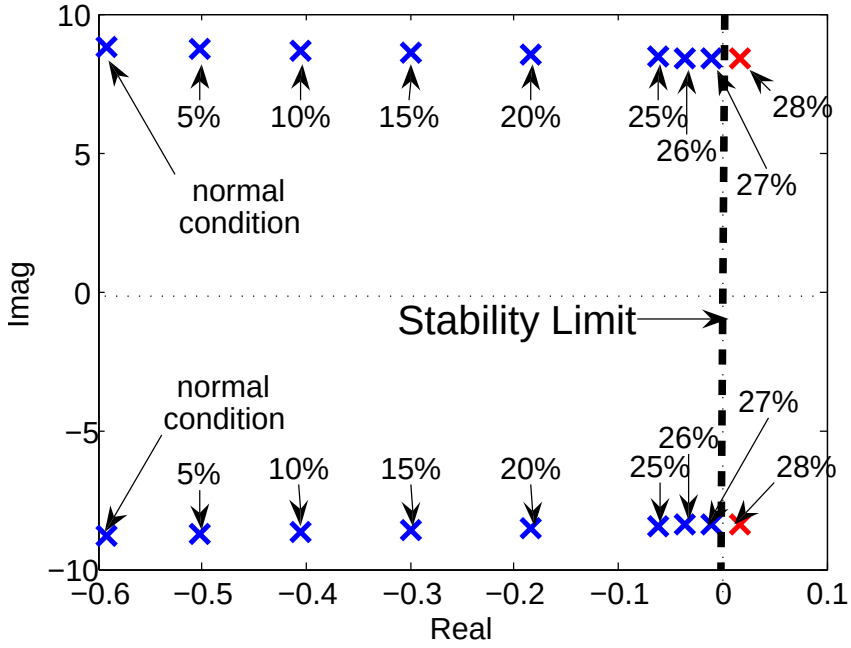


Figure 3.10: Eigenvalues trace with system load increment

Table 3.3 gives the critical pair of eigenvalues with the associated oscillation frequency and damping ratio subjected to total system load increment. The dominant state variables are $E'_{q1}$ and $V_{f1}$. Table 3.4 displays the six highest rank of participation factors associated with the critical eigenvalues and their magnitudes, which are the state variables related to generator at bus 1. This has suggested that bus 1 (where generator 1 is connected to) is the best site for the instalment of the PSS. Simulation shows that installation of a PSS at bus 1 allows the system loadings increase up to 30%.

Table 3.3: System Eigenvalues

| % | Eigenvalues $\lambda$ | Frequency (Hz) | Damping ratio $\zeta$ |
|---|---|---|---|
| 0 | -0.59 $\pm$ $j$8.79 | 1.3985 | 0.0673 |
| 5 | -0.50 $\pm$ $j$8.73 | 1.3892 | 0.0575 |
| 10 | -0.41 $\pm$ $j$8.66 | 1.3789 | 0.0467 |
| 15 | -0.30 $\pm$ $j$8.59 | 1.3678 | 0.0348 |
| 20 | -0.18 $\pm$ $j$8.52 | 1.3559 | 0.0217 |
| 25 | -0.06 $\pm$ $j$8.44 | 1.3433 | 0.0073 |
| 26 | -0.04 $\pm$ $j$8.42 | 1.3407 | 0.0043 |
| 27 | -0.01 $\pm$ $j$8.41 | 1.3381 | 0.0012 |
| 28 | 0.02 $\pm$ $j$8.39 | 1.3355 | -0.0020 |

Table 3.4: Participation Factor Analysis

| Gen | $E'_q$ | $V_f$ | $E''_q$ | $V_r$ | $\delta$ | $\omega$ |
|---|---|---|---|---|---|---|
| 1 | 0.320 | 0.248 | 0.059 | 0.048 | 0.044 | 0.043 |

The system load is scheduled to determine the transient stability limit. This has to be investigated to ensure that the system is secure for a given load increment. Stability limit could be determined when the security index goes across the threshold value, $\zeta_{threshold}$ [14]. If the difference between the last secure system load increment, $P_{load_{secure}}$, and the first insecure system load increment, $P_{load_{insecure}}$, is fairly small, the stability limit can be determined [14]. Fig. 3.11 shows transient stability limit determination for small disturbances.

Using transient stability index, the maximum total system load increment can be determined [14]. In this particular study system, if a damping criterion of 1% is to be considered to ensure the transient security (i.e. threshold value, $\zeta_{threshold}$ of 0.01), the maximum secure load increment would be 24%, where the damping ratio is 0.0103.

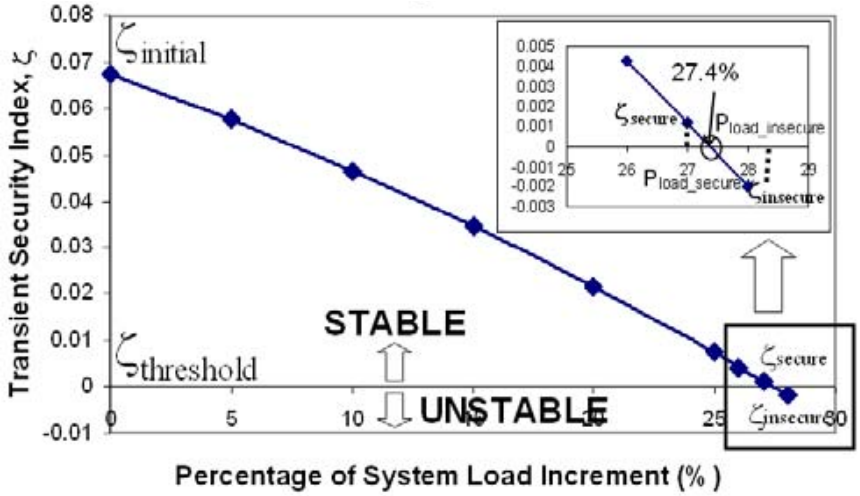


Figure 3.11: Transient stability subjected to small disturbances

### 3.6.2 Condenser Switching

Condenser located at bus 3 is disconnected at $t = 1.2$ sec to analyse its transient stability. Bus 15 is inserted into PSAT data file for which condenser is to be connected. A circuit breaker is inserted between bus 15 and bus 3 to allow the switching of the condenser. Figs.

3.13 - 3.16 show the time responses when condenser is to be switched off at $t = 1.2$ sec. Eigenvalue plot in Fig. 3.12 shows the system modes after condenser been switched off. All eigenvalues lie onto the left-half plane, which indicates that the transient stability of the system is retained after the switching operation. Eigenvalues analysis indicates that all modes have positive damping, hence the system is stable.

The time response of the bus voltages corresponding to the condenser switching off at $t = 1.2$ sec is observed. At that instant, all bus voltages oscillate and the system reaches steady-state.

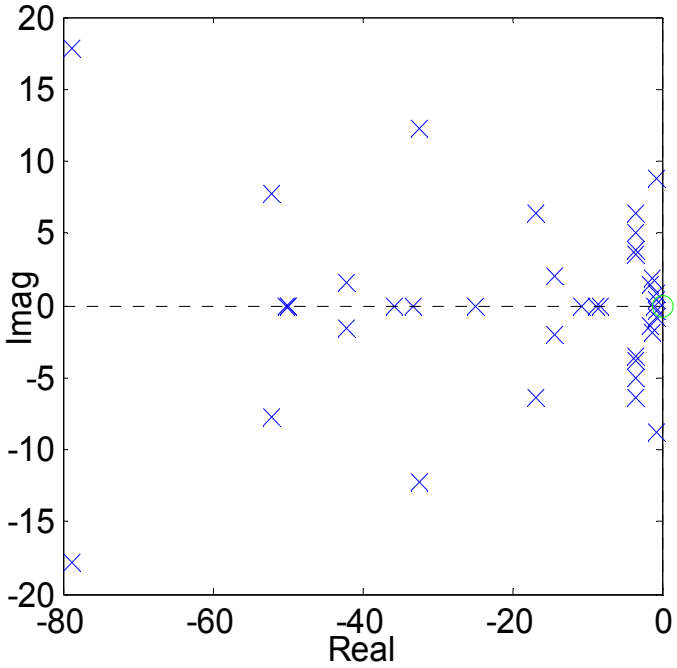


Figure 3.12: S-domain eigenvalues plot

Figs. 3.13(a) and (b) shows the machines' rotor angles and speeds respectively. At the instant when the condenser is switched-off, the machine starts to decelerate and the remaining machines start to accelerate to support the power impact. This power impact is shared by the remaining machines.

Figs. 3.14 and 3.15 show the time response of the exciter variables, $V_{fd}$ and $V_m$ respectively. Field voltage of exciter 3 increases as shown in Fig. 3.14 to compensate the reactive power dropped out from the condenser 3. $V_m$ of exciters 1, 2, 4 and 5 drops and oscillates

throughout the transient.

Fig. 3.16 shows the properties of the condenser connected to bus 15. The disconnection of condenser in the system causes both the reactive power supplied and the voltage at bus 15 to drop to zero. For the same reason, $V_m$ of the exciter 3 has dropped down to zero.

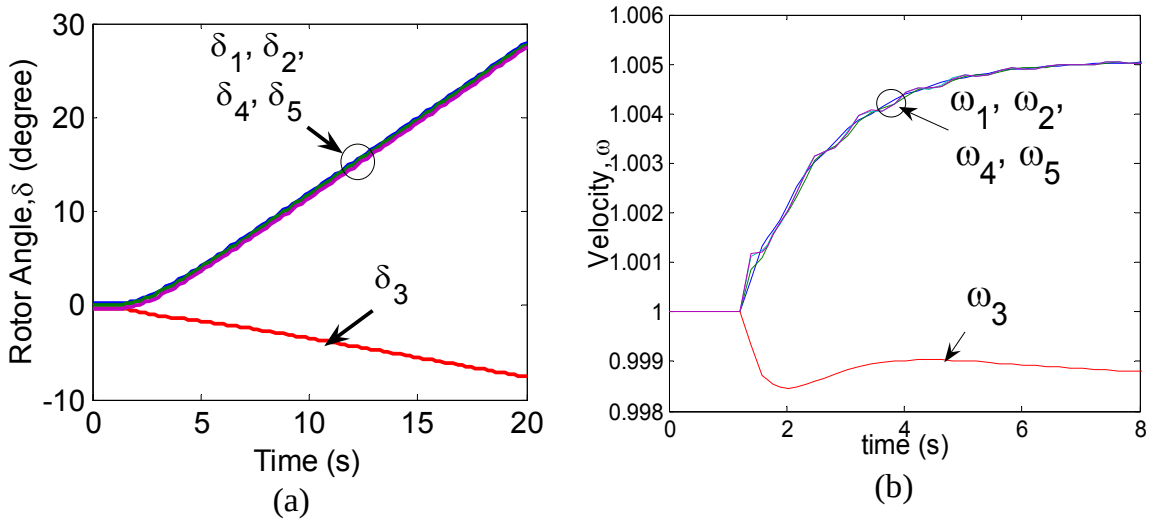


Figure 3.13: Time response of the machines' (a) Rotor angles and (b) Speeds

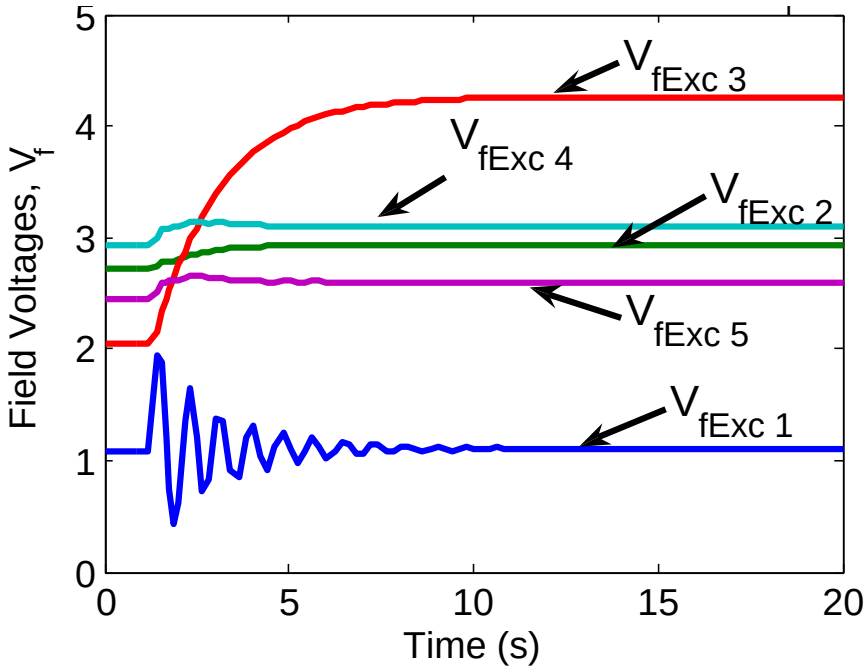


Figure 3.14: Time response of field voltage $V_{fd}$

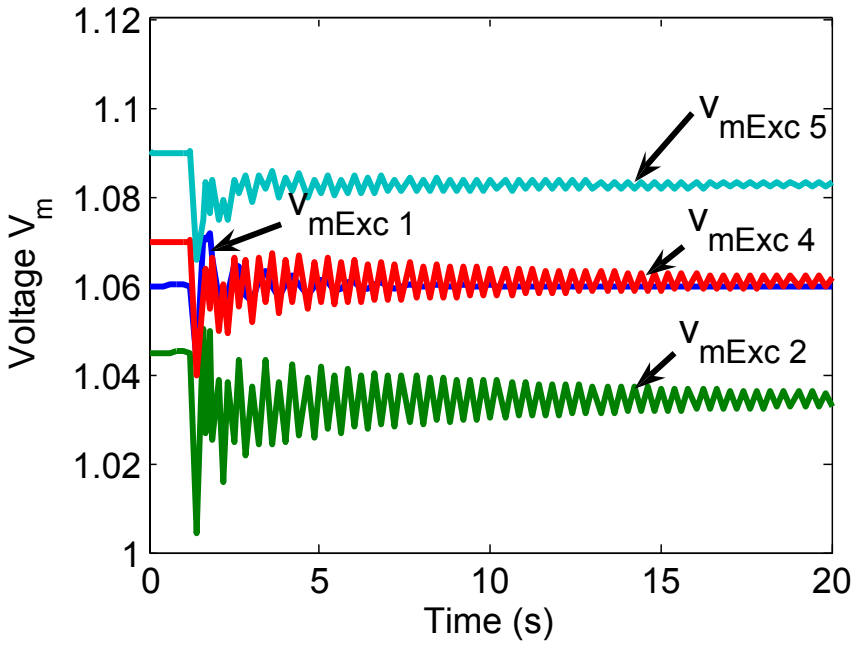


Figure 3.15: Time response of voltage $V_m$

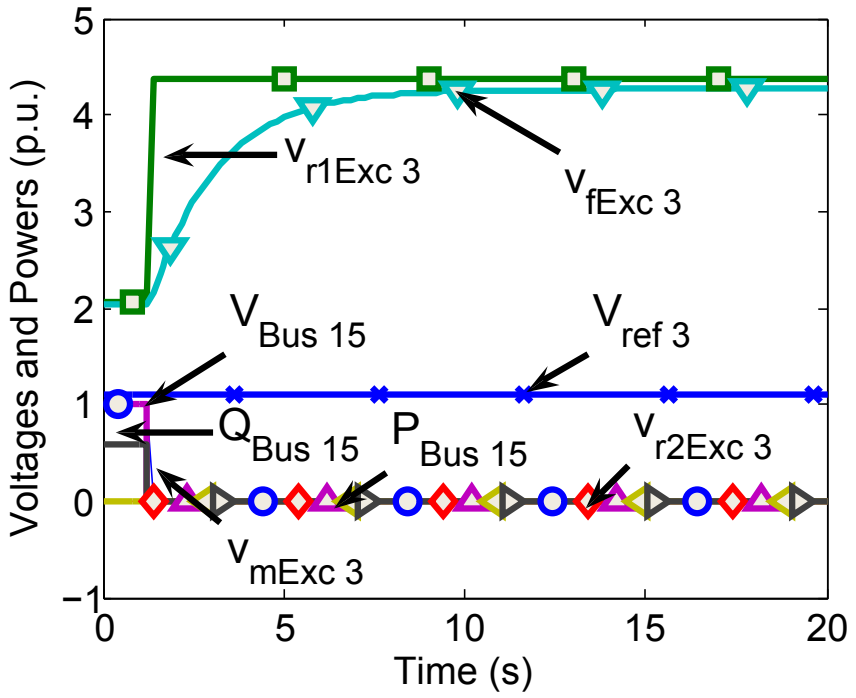


Figure 3.16: Voltage and power at the bus to which the associated condenser is located

## 3.7 Summary

In this chapter, the determination of transient stability of a power system subjected to small disturbances has been discussed using TD analysis, eigenvalue analysis and participation factors analysis. Studies have been conducted on the IEEE 14 bus system and simulation results using frequency analysis have been verified by TD analysis. Participation factors determine the dominant state variables associated with the mode (eigenvalues). This allows the determination of an optimal site to install a PSS for Hopf bifurcation control in the critical mode.

## References


[1] M. J. Gibbard, N. Martin, J. J. Sanchez-Gasca, N. Uchida, V. Vittal, L. Wang, "Recent Applications of Linear Analysis Techniques," *IEEE Trans. Power Syst.*, Vol. 16, no. 1, February 2001.

[2] P. Kundur. *Power System Stability and Control.* McGraw-Hill, 1994.

[3] P. M. Anderson, A. A. Fouad. *Power System Control and Stability.* John Wiley & Sons, Inc., 2003.

[4] Felix F. Wu, Chen-Ching Liu, "Characterization of Power System Small Disturbance Stability with Models Incorporating Voltage Variation," *IEEE Trans. Biomed. Circuits Syst.*, Vol. CAS-33, no. 4, April 1986.

[5] IEEE Power System Engineering Committee, System Dynamic Performance Subcommittee, "Proposed terms and definitions for power system stability," *IEEE Trans. Power App. Syst."*, Vol. PAS-101, pp. 1894-1898, July 1982.

[6] F. Milano, "Power System Analysis Toolbox: Documentation for PSAT version 1.3.4," 14 July, 2005.

[7] F. Milano, "An Open Source Power System Analysis Toolbox," *IEEE Trans. Power Syst.*, Vol. 20, no. 3, August 2005.

[8] P. W. Sauer, M. A. Pai. *Power System Dynamics and Stability.* Prentice-Hall, Inc., 1998.

[9] Y. V. Makarov, Z. Y. Dong, D. J. Hill, "A General Method for Small Signal Stability Analysis," *IEEE Trans. Power Syst.*, Vol. 13, no. 3, August 1998.

[10] J. G. Slootweg, J. Persson, A. M. can Voorden, G. C. Paap, W. L. Kling, "A Study of the Eigenvalue Analysis Capabilities of Power System Dynamics Simulation Software," *14th PSCC, Sevilla*, 24-28 June 2002.

[11] N. Mithulananthan, C. A. Canizares, J. Reeve, "Hopf Bifurcation Control in Power Systems Using Power System Stabilizers and Static Var Compensators," *North American Power Symposium (NAPS), San Luis Obispo, California*, October 1999.

[12] N. Mithulananthan, C. A. Canizares, J. Reeve, G. J. Rogers, "Comparison of PSS, SVC and STATCOM Controllers for Damping Power System Oscillations," *IEEE Trans. Power Syst.*, Vol. 18, no. 2, May 2003.

[13] M. Klein, G. J. Rogers, P. Kundur, "A Fundamental Study of Inter-Area Oscillations in Power Systems," *IEEE Trans. Power Syst.*, Vol. 6, no. 3, August 1991.

[14] L. Wang, F. Howell, P. Kundur, C. Y. Ching and W. Xu, "A tool for small-signal security assessment of power systems," *PICA 2001, Sydney, Australia*, 21-24 May 2001.

# Chapter 4

# Stability of a Hydraulic Governor Turbine System for Isolated Operation


### Abstract

It is important to control and maintain the overall system frequency to ensure satisfactory operation of the power system. System frequency relies heavily on the generation/load balance; any frequency deviation resulted from active power imbalance will initiate the response of the governor, to restore the frequency in accordance with the permanent speed droop settings of the units. A conventional approach in modelling the unit governing response is assuming the unit to be a single unit connected to a single load in an isolated system. An optimum setting for a governor will result in a desired transient response with least speed deviation and faster restoration to conventional speed when subject to a step load change. This chapter discusses the stability criterion to govern an isolated hydraulic system as well as relative stability of the hydraulic system utilising frequency response methods. Procedure to adjust system gains to improve the relative stability is presented.

## 4.1 Introduction

In a hydraulic power system, a governor is usually utilised to control the speed oscillations of the generator resulted from a load change. The stability of the transients depends upon the hydro turbine-penstock parameters, i.e., water starting time $T_w$ and mechanical starting time $T_m$, and the selection of the parameters employed in the governing system, i.e., temporary speed droop $\delta$ and dashpot reset time $T_r$ for a mechanical-hydraulic governor, and proportional-integral-derivative (PID) gains for a PID governor.

Governor tuning has been studied extensively in the past to determine the optimal governor parameters for speed control in a hydraulic system. Paynter [1] and Hovey [2, 3] investigated the stability of a hydraulic turbine unit controlled by a temporary droop governor and established the stability regions for the hydraulic system. Chaudhry [4] expanded Paynter and Hovey's works by introducing the permanent speed droop $\sigma$ and the self-regulation of turbine and load $D$ effects. Hagihara et al. [5] further expanded the research conducted by Paynter [1], Hovey [2, 3] and Chaudhry [4] to demonstrate the stability boundaries of a hydraulic system governed by a PID controller. The stability region can be expanded with the inclusion of the effect of the derivative gain $K_d$. Optimum adjustment of the governor parameters has been demonstrated in [1] - [5].

Proper selection of parameters used in the governing system is important to optimise the control operation in hydraulic system. Inadequate tuning of the governor would result system instability, and further deteriorate system performance. Thus, it is vital to ensure that the governing system is stable, and is able to restore the generating unit to equilibrium at synchronous speed when subject to any load disturbances. The optimum adjustment of governor parameters should be based on the following criterions [1]:

- Least speed deviation after load change
- Fast restoration to conventional speed
- Satisfactory stability of governing system

Tasmanian power system in Australia mainly consists of hydraulic turbines, which produce power of 2,255 MW, i.e., 92.4% of Tasmanian total generation. It is beneficial if the governor utilised can optimise Tasmanian system network operation with stability attained under all operating conditions.

This chapter uses frequency response methods to analyse hydraulic system's absolute and relative stability. These methods include the Routh-Hurwitz criterion, Bode diagram, Nyquist diagram and Nichols chart. Time response method is examined as well, where particular attention has been paid to the system overshoot and the settling time. Adjustment of system gains to obtain a desired response is established by employing a control theory. Governor parameter settings which will ensure stability can be determined from the stability limit curves. Frequency response methods allow the determination of the gain and phase margins before the system goes unstable. This determines the safe operating points that the governor can function before the system becomes critically unstable.

## 4.2 Hydraulic Governor Turbine System

The following assumptions are made to formulate the transfer function of the hydraulic turbine generating system:

- The water column is inelastic.
- The nonlinear relationships can be linearised as the changes of the hydraulic system, i.e., changes of turbine speed, head and gate opening, are relatively small.
- An isolated load is supplied by a single hydro plant.

Fig. 4.1 shows a typical hydraulic system governed by a PID governor. The open-loop transfer function of the hydraulic system is derived as follow:

$$G = \frac{K_p s + K_i + K_d s^2}{(\sigma K_p + 1)\, s + \sigma K_i + \sigma K_d s^2} \frac{1 - T_w s}{1 + 0.5 T_w s} \frac{1}{T_m s + D} \tag{4.1}$$

where $K_p$, $K_i$ and $K_d$ are proportional, integral and derivative gains, $s$ is the Laplace

transform variable, $\sigma$ represents the permanent speed droop, $T_w$ represents the water starting time, $T_m$ and $D$ are mechanical starting time and self-regulation of turbine and load respectively.

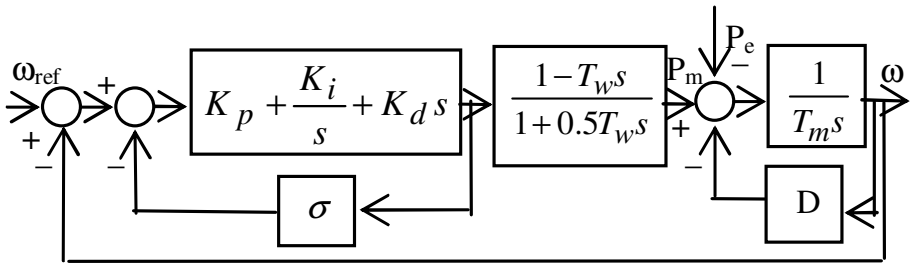


Figure 4.1: Hydraulic turbine generating system block diagram

This hydraulic system has the following characteristic equation:

$$\begin{aligned} 1 + GH &= 0 \\ 1 + \frac{\left(K_p s + K_i + K_d s^2\right)(1 - T_w s)}{(1 + 0.5T_w s)(T_m s + D)\left[s + \sigma\left(K_p s + K_i + K_d s^2\right)\right]} &= 0 \end{aligned} \tag{4.2}$$

The normalised expression of the characteristic equation is now developed as below:

$$1 + \frac{\lambda_1(1-n)(\lambda_2 + n + \lambda_5 n^2)}{(1 + 0.5n)(\lambda_3 + n)[\lambda_1\lambda_2\lambda_4 + (1 + \lambda_1\lambda_4)n + \lambda_1\lambda_4\lambda_5 n^2]} = 0 \tag{4.3}$$

where the non-dimensional parameters introduced are [5]:

$$\lambda_1 = \frac{K_p T_w}{T_m}, \quad \lambda_2 = \frac{K_i T_w}{K_p}, \quad \lambda_3 = \frac{D T_w}{T_m}, \quad \lambda_4 = \frac{\sigma T_m}{T_w}, \quad \lambda_5 = \frac{K_d}{K_p T_w}, \quad \tau = \frac{t}{T_w}, \quad n = \frac{d}{d\tau}$$

### 4.2.1 Stability Limit Curve

Stability limit of a hydraulic turbine governed by a PID governor (or a mechanical-hydraulic governor) can be determined from (4.3) which has the following forth-order form:

$$a_0 n^4 + a_1 n^3 + a_2 n^2 + a_3 n^1 + a_4 = 0 \tag{4.4}$$

By applying the Routh-Hurwitz criterion, the following stability criteria are derived:

$$
\begin{aligned}
a_0 > 0, \quad a_1 > 0, \quad a_2 > 0, \quad a_3 > 0, \quad a_4 > 0, \\
b_1 > 0 \Rightarrow \frac{a_1 a_2 - a_0 a_3}{a_1} > 0 \Rightarrow a_1 a_2 - a_0 a_3 > 0 \\
c_1 > 0 \Rightarrow \frac{b_1 a_3 - a_1 b_2}{b_1} > 0 \Rightarrow (a_1 a_2 - a_0 a_3) a_3 - a_1^2 a_4 > 0
\end{aligned} \tag{4.5}
$$

Stability limit curve can be obtained depending on the operating condition of the hydraulic system, i.e., self-regulation $D$ and permanent droop $\sigma$, and the hydro turbine-penstock parameters, i.e., water starting time $T_w$ and mechanical starting time $T_m$. $\lambda_1$ and $\lambda_2$ are selected to evaluate the systems stability as these parameters determine the proportional and integral gains, which could be adjusted to optimise the control operation in hydroelectric system. $\lambda_5$, which determine the derivative gain $K_d$ of the PID governor, will be chosen arbitrarily.

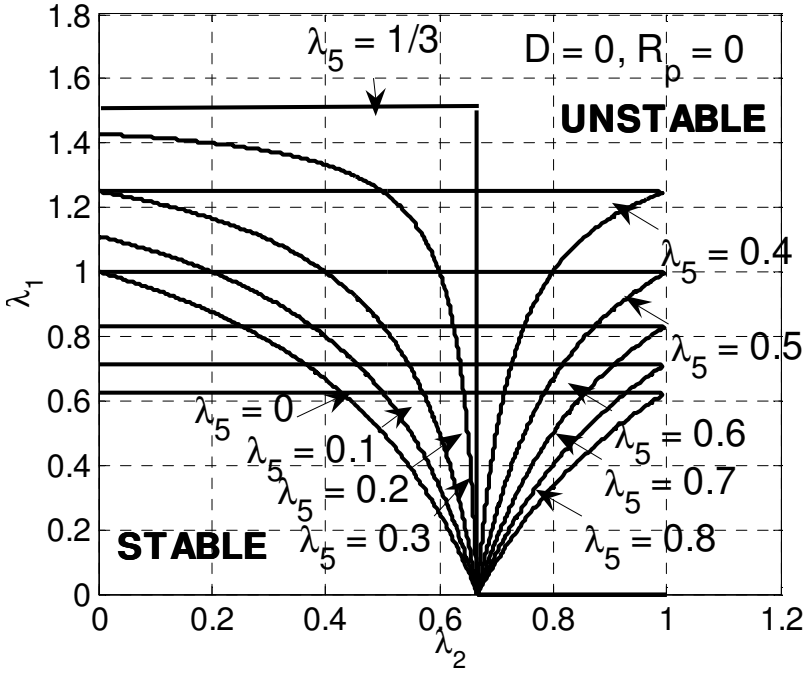


Figure 4.2: Stability limit curves for $D = 0$ and $\sigma = 0$

Fig. 4.2 shows the stability limit curves for system with no self-regulation $D$ and no permanent droop $\sigma$. Fig. 4.3 shows the stability limit curves of a system with self-regulation

$D = 1$ and permanent droop $\sigma = 0.05$ for various values of $\lambda_5$. System stability can be assured if the operating conditions $\lambda_1$ and $\lambda_2$ are within the boundaries of the stability limit curves.

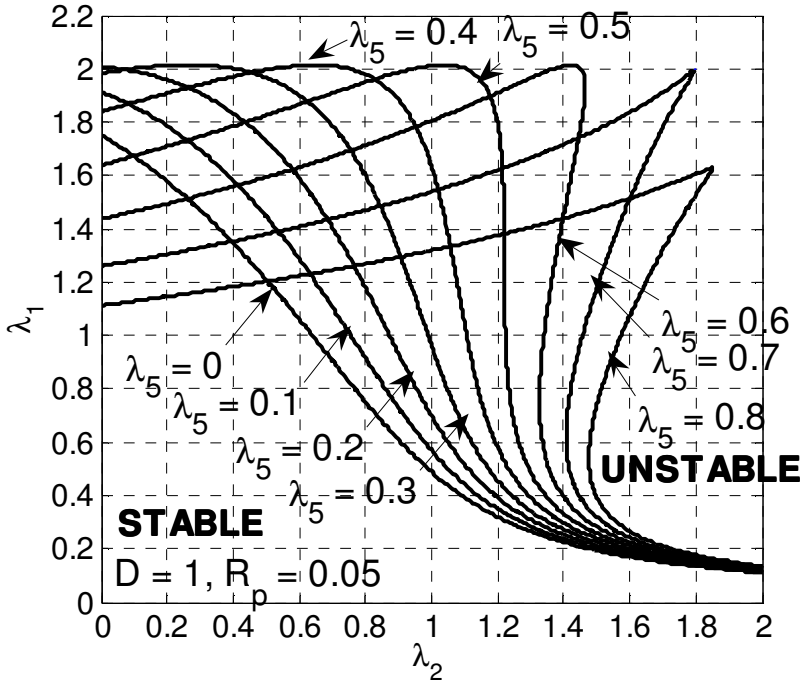


Figure 4.3: Stability limit curves for $D = 1$ and $\sigma = 0.05$

### 4.2.2 Frequency Response Methods

The absolute stability of a system has been determined with the application of the Routh-Hurwitz criterion presented in Section 4.2.1. It is desired to determine the relative stability of the system as well. The frequency response methods, namely Bode diagram, Nyquist diagram and Nichols chart will be employed in this section to examine the system's relative stability. Gain margin and phase margin will also be used to measure the closed-loop system's relative stability.

The gain margin is the increment of the system gain when the phase is -180° that will result in a critically stable system with the point (-1 + $j0$) intersected on the Nyquist diagram [6]. The phase margin is the quantity of phase shift of the $GH(j\omega)$ at unity

magnitude where a marginally stable system will yield with the (-1 + $j0$) point crossed on the Nyquist diagram. It evaluates the further phase lag required before the system becomes unstable [6].

#### 4.2.2.1 Bode Diagram

Bode diagram represents the frequency plot of the magnitude and phase of the open-loop frequency transfer function $G(j\omega)H(j\omega)$. The magnitude is plotted in dB on the log $\omega$ scale. The diagram provides relative stability in terms of gain margin and phase margin [6].

Gain margin and phase margin are the amount of gain and phase lag required respectively to make the system within the stability boundary. Gain margin is usually expressed in dB whilst phase margin is expressed in degrees [6].

The gain margin is measured at the phase-crossover frequency $\omega_p$, i.e.

$$Gain\ Margin = -20log_{10}\left|G(j\omega_p)H(j\omega_p)\right| dB \tag{4.6}$$

The phase margin is measured at the gain-crossover frequency $\omega_g$, i.e.

$$Phase\ Margin = 180^\circ + \angle GH(j\omega_g) \tag{4.7}$$

On the magnitude-versus-phase plot of the unity feedback system with open-loop transfer function $G(j\omega)$, the phase-crossover point is where the phase plot intersects the -180° axis and the gain-crossover point is where the magnitude plot intersects the 0 dB axis. Thus, gain crossover frequency is the frequency at which the magnitude curve intersects the 0 dB axis whilst phase crossover frequency is the frequency at which phase curve intersects the negative 180° axis in the bode diagram [6].

The relative stability measures, the gain and phase margins can be evaluated from the open-loop Bode diagram as shown in Fig. 4.4. A point representing a logarithmic magnitude of 0 dB and a phase angle of -180° (or -180°) on the Bode diagram is the critical point for stability.

Fig. 4.5 shows the closed-loop Bode diagram where the parameters of interest include the bandwidth $\omega_d$, the peak value $M_{p\omega}$ and the resonant frequency $\omega_r$ at which the peak amplitude occurs.

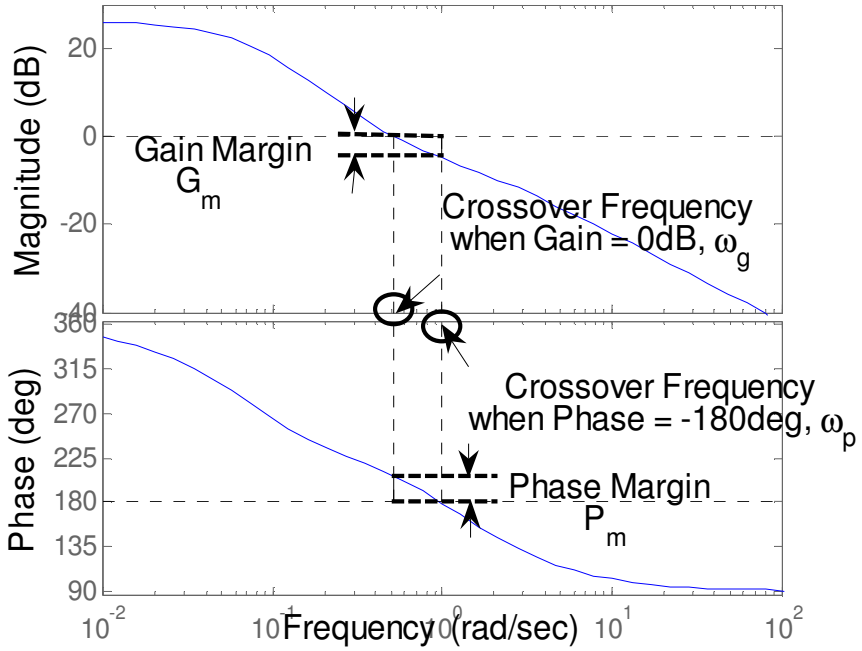


Figure 4.4: Open-loop bode diagram

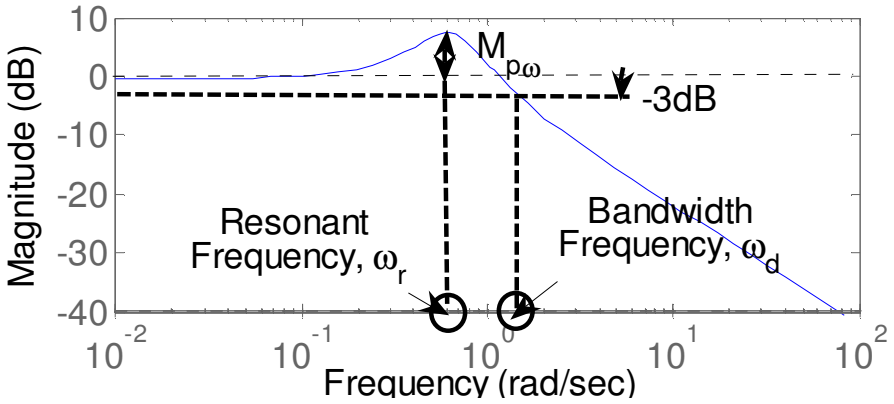


Figure 4.5: Closed-loop bode diagram

#### 4.2.2.2 Nyquist Diagram & Nichols Chart

Relative stability can be determined in Nyquist diagram, also known as polar plot. The critical point for stability is (-1, 0) point in the $GH(j\omega)$-plane, as shown in Fig. 4.6.

The stability criterion of a feedback control system is that the Nyquist diagram should not encircle the critical point (-1,0) [6, 7]. The increment of system gain required for the $GH(j\omega)$ locus to cross the (-1, 0) point on the real axis is defined as the gain margin. As for the phase margin, it is the phase angle required for the $GH(j\omega)$ at unity magnitude pass through the critical point (-1, 0) in the polar plot when the $GH(j\omega)$ is rotated [6]. These margins can be obtained as shown in Fig. 4.6.

Another frequency response method in evaluating the relative stability of the system is Nichols chart, the gain and phase margins are obtained as demonstrated in Fig. 4.7. The critical stability point in a Nichols chart is $(-180°, 0)$ point.

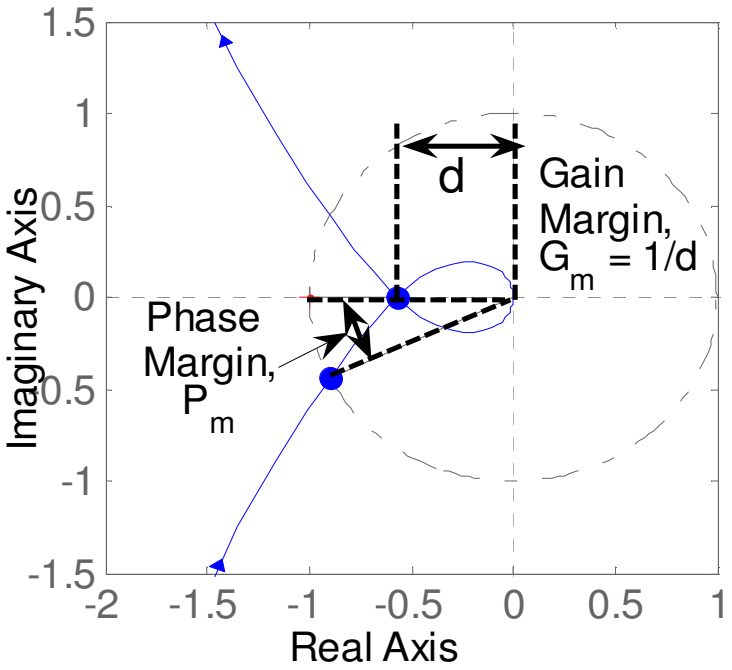


Figure 4.6: Nyquist diagram

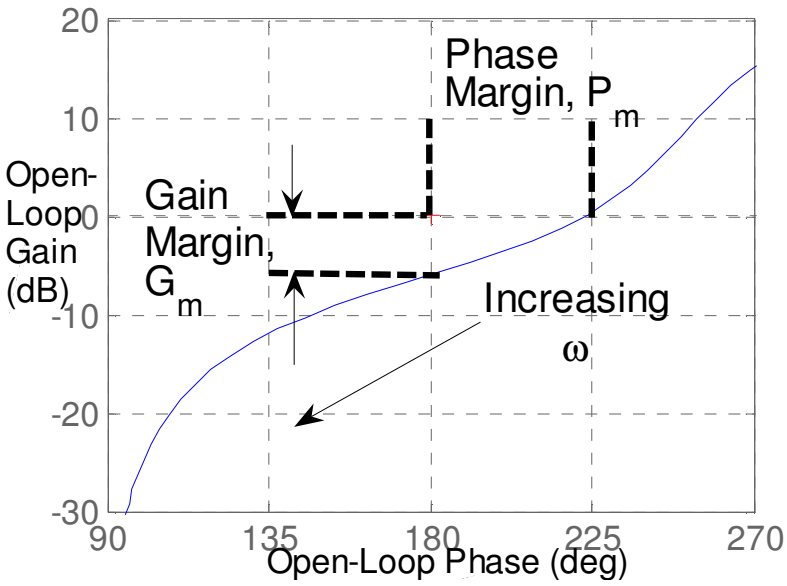


Figure 4.7: Nichols chart

### 4.2.3 Time Response Method

A small step load disturbance is applied to determine the governors' optimum settings with less overshoot and faster settling time. The transient response characteristics, such as percent overshoot P.O., settling time $T_s$, peak time $T_p$ and rise time $T_r$ are indicated in Fig. 4.8.

The time dependent characteristic of a mode corresponding to an eigenvalue $s_i$ is described by $e^{s_i t}$. Thus, the conclusion on the system stability can be drawn by the eigenvalues as below [8]:

- A real eigenvalue corresponds to a non-oscillatory mode.
- Complex eigenvalues arise in conjugate pairs, where each pair corresponds to an oscillatory mode.

A complex pair of eigenvalues, commonly expressed as in (4.8), has frequency of oscillation $f = \frac{\omega}{2\pi}$ and damping ratio $\zeta = \frac{-\sigma}{\sqrt{\sigma^2+\omega^2}}$ [8].

$$s = \sigma \pm j\omega \tag{4.8}$$

The real part of the eigenvalues provides the damping whilst the imaginary part presents the frequency of oscillation. A negative real part denotes a damped oscillation, resulting in a stable response while a positive real part implies a growing amplitude oscillation, i.e. an unstable response.

The damping ratio $\zeta$ decides the rate of decay of the oscillation amplitude. The time constant of amplitude decay is $\frac{1}{|\sigma|}$; this means that the amplitude decays to $\frac{1}{e}$ of the initial amplitude in $\frac{1}{|\sigma|}$ seconds or in $\frac{1}{2\pi\zeta}$ cycles of oscillation [8].

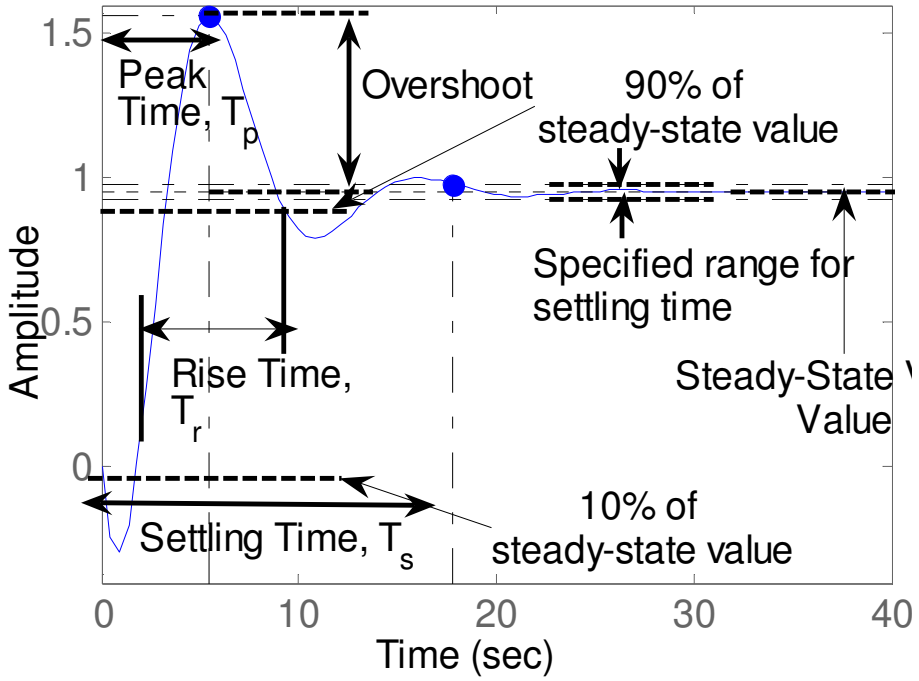


Figure 4.8: Time response specifications

### 4.2.4 System Stability Determination

The transfer function of the PID governor is derived as follows to allow the adjustments made on the integral gain $K_i$ as well as the proportional gain $K_d$ to improve system stability.

$$G_{PID} = \frac{K_p s + K_i + K_d s^2}{s + \sigma(K_p s + K_i + K_d s^2)} = \frac{K_i \left(1 + \frac{K_p}{K_i} s + \frac{K_d}{K_i} s^2\right)}{s + \sigma \left[K_i \left(1 + \frac{K_p}{K_i} s + \frac{K_d}{K_i} s^2\right)\right]} \tag{4.9}$$

Both self-regulation $D$ and permanent droop $\sigma$ are set accordingly to the system oper-

ating conditions. An arbitrarily value of $\lambda_5$ which determines the derivative gain $K_d$ is then selected. Now, two additional parameters are introduced as follow:

$$\frac{K_p}{K_i} = \frac{T_w}{\lambda_2}, \quad \frac{K_d}{K_i} = \frac{\lambda_5}{\lambda_2} T_w^2 \tag{4.10}$$

The transfer function of the PID governor then becomes:

$$G_{PID} = \frac{K_i \left(1 + \frac{T_w}{\lambda_2} s + \frac{\lambda_5}{\lambda_2} T_w^2 s^2\right)}{s + \sigma \left[K_i \left(1 + \frac{T_w}{\lambda_2} s + \frac{\lambda_5}{\lambda_2} T_w^2 s^2\right)\right]} \tag{4.11}$$

$\lambda_2$ is then selected arbitrarily according to the stability limit curve. For a value of $\lambda_2$ within the stability limit curve, system will be stable. The selection of $\lambda_2$ determines the ratios $\frac{K_p}{K_i}$ and $\frac{K_d}{K_i}$ as denoted in (4.10).

Various values of integral gain $K_i$ are selected, which will correspond to the proportional gain $K_p$ by the following expression:

$$K_p = \frac{T_w}{\lambda_2} K_i \tag{4.12}$$

These values of proportional gain $K_p$ are then related to $\lambda_1$ by the following expression:

$$\lambda_1 = \frac{K_p T_w}{T_m} \tag{4.13}$$

Generally, stability can be ascertained if ($\lambda_1$, $\lambda_2$) is within the boundaries of the stability limit curve.

#### 4.2.4.1 Improvement on System Stability with an Adjustment in System Gain

The frequency response may be undesirable due to the large overshoot depending on the selection of the integral gain $K_i$. To improve the frequency response, the integral gain $K_i$ can be adjusted to obtain a limitation of percent overshoot in the system. The procedure to adjust to the new integral gain $K_i$ is portrayed in the flowchart given in Fig. 4.9.

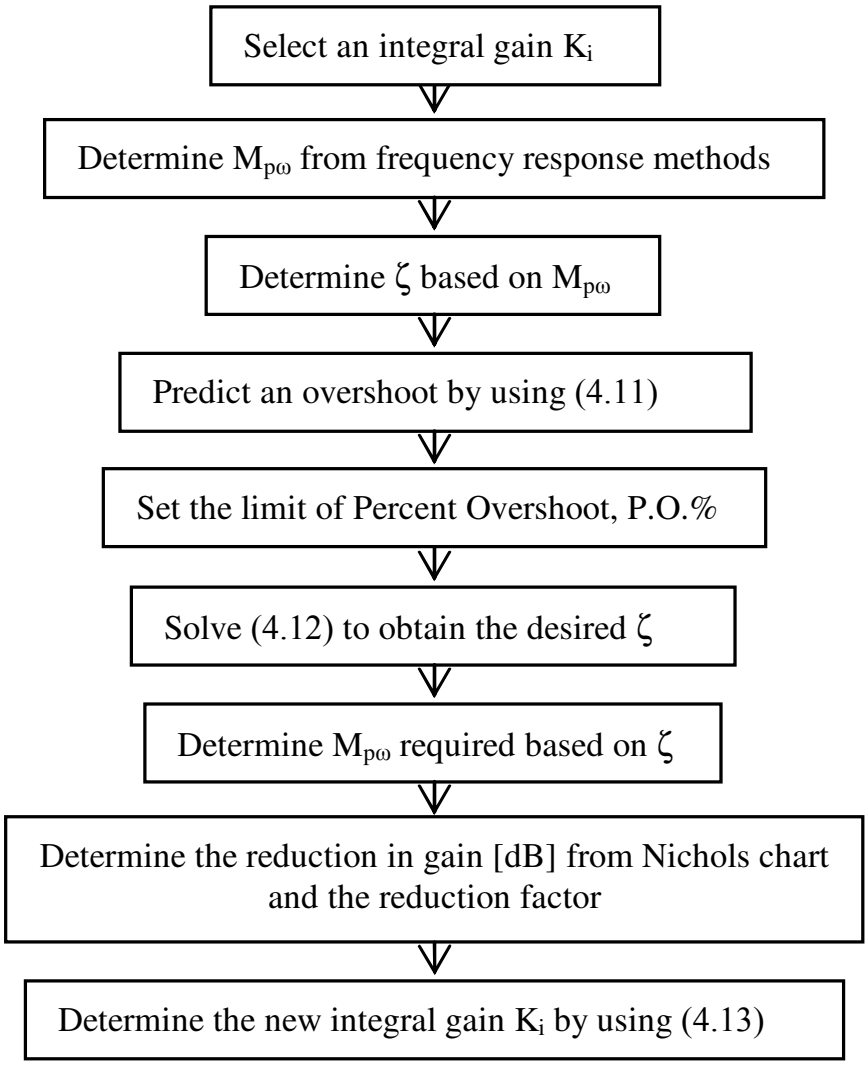


Figure 4.9: Flow chart on adjustment of integral gain $K_i$ to improve system stability

Equation (4.15) is then solved to obtain the desired damping ratio $\zeta$ [6]. Fig. 4.10 shows the maximum magnitude of the frequency response $M_{p\omega}$ with respect to the damping ratio $\zeta$. The percent overshoot P.O. is expressed as,

$$P.O. = 100exp^{-\frac{\zeta\pi}{\sqrt{1-\zeta^2}}} \tag{4.14}$$

where

$$\zeta = \sqrt{\frac{\left[log\left(\frac{P.O.}{100}\right)\right]^2}{\pi^2 + \left[log\left(\frac{P.O.}{100}\right)\right]^2}} \tag{4.15}$$

Note that the information extracted from Fig. 4.10 is only suitable for second-order systems; if the higher-order system is dominated by a pair of underdamped roots, it can be approximated by the second-order system [6]. In general, Fig. 4.10 acts as a reference guideline when applying to higher-order systems.

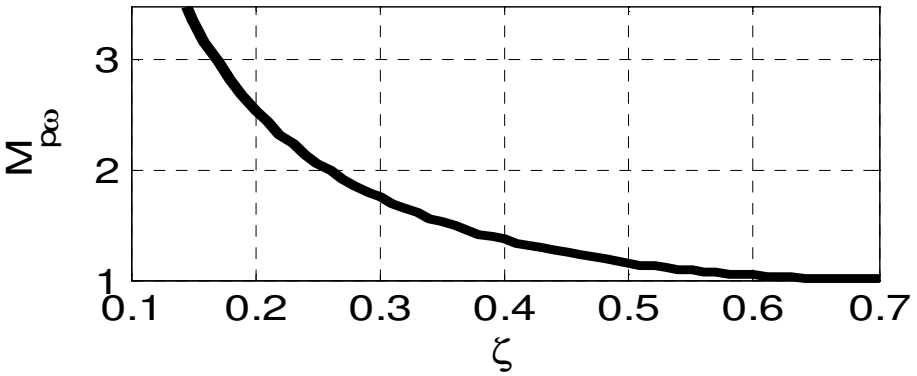


Figure 4.10: The maximum magnitude of frequency response $M_{p\omega}$ vs damping ratio $\zeta$ plot

The closed-loop characteristics can be determined from the Nichols chart. The intersection of the open-loop frequency response onto the $M_{p\omega}$ [dB] closed-loop curve indicates that the closed-loop system has a maximum magnitude of $M_{p\omega}$ at that crossover frequency $\omega$. Nichols chart is indeed useful in adjusting the system gain to improve the relative stability.

A reduction in system gain means that the open-loop frequency response is shifted vertically down on the Nichols chart to a certain point of frequency $\omega$, where the open-loop

frequency response intersects the closed-loop curve at the desired 20log($M_{p\omega}$) [dB]. This reduction in gain [dB] is equal to a reduction factor of $10^{\frac{gain[dB]}{20}}$. The desired integral gain $K_i$ required for the system will be

$$K_{i_{desired}} = \frac{K_{i_{initial}}}{reduction factor} \tag{4.16}$$

The closed-loop Bode diagram can be computed to verify the value of the maximum magnitude $M_{p\omega}$. Further investigation to include transient response subject to a step disturbance is still required to investigate the actual overshoot.

## 4.3 Simulation Results

Consider a hydro plant with water starting time $T_w = 1.24$ sec and mechanical starting time $T_m = 9.05$ sec. The system operates with motor type loading of self-regulation, $D = 1$ [5]. The plant is governed by a PI governor with no derivative gain (i.e., $\lambda_5$ is zero).

It can be observed from Fig. 4.3 that with derivative gain $K_d$ included, the stability region can be expanded. The study represents a base case with derivative gain $K_d$ neglected. The integral gain $K_i$ of the PI governor can be adjusted to improve the system's relative stability. This study will demonstrate the adjustment of the integral gain $K_i$, and thus, the proportional gain $K_p$ to give an optimum response by investigations utilising frequency response methods. The investigations are further evaluated by time response method, to examine the overshoot and the settling time when subject to a step disturbance. All analysis has been performed in MATLAB.

### 4.3.1 Results using Frequency Response Method

Frequency response methods are utilised to examine the system relative stability with the gain and phase margins measures. The methods used include Bode diagram, Nyquist diagram and Nichols chart.

Herein, $\lambda_2$ is selected as 0.6. As observed from Fig. 4.3, any values of $\lambda_1$ below 1.05

will result a stable system. $\lambda_1$ has to be a positive value. The hydraulic system has the following transfer function:

$$G = \frac{K_i(1 + 2.0667s)}{0.05K_i + (0.1033K_i + 1)s} \frac{1 - 1.24s}{1 + 0.62s} \frac{1}{9.05s + 1} \tag{4.17}$$

The integral gain $K_i$ chosen for the study are [0.1, 1, 2, 3]. These values are related to the proportional gain $K_p$ by (4.12) and the proportional gains are related to $\lambda_1$ by (4.13). $K_p$ and $\lambda_1$ resulted from the selection of integral gains $K_i$ are indicated in Table 4.1. All values of $\lambda_1$ are observed to be below 1.05, hence, the system is stable.

Table 4.1: System Properties

| $K_i$ | 0.1 | 1 | 2 | 3 |
|---|---|---|---|---|
| $K_p$ | 0.2067 | 2.0667 | 4.1333 | 6.2000 |
| $\lambda_1$ | 0.0283 | 0.2832 | 0.5663 | 0.8495 |

The system relative stability is evaluated to determine how much further the system gain can be increased before the instability is resulted. Measurement of the relative stability from Bode diagram, Nyquist diagram and Nichols chart has been explained in Section 4.2.2 and the plots are presented in Figs. 4.11, 4.12 and 4.14 respectively with the results presented in Table 4.2. The parameters of interest are the gain and phase margins, including the crossover frequencies when gain = 0 dB and phase = -180°. It is seen that the integral gain $K_i$ of 0.1 will provide the highest gain and phase margins.

The closed-loop characteristics can be determined from the open-loop frequency response plots. This is illustrated in Nichols chart plotted in Fig. 4.14, and the frequency responses are verified by the closed-loop Bode diagram in Fig. 4.13. The closed-loop characteristics, i.e., the maximum magnitude of the frequency response $M_{p\omega}$ and the resonant frequency $\omega_r$, are presented in Table 4.3.

Investigation on the adjustment of the integral gain $K_i$ has also been carried out to yield a better frequency response. When an initial value $K_i$ of 3 is selected, a large peak value, $M_{p\omega}$ of 21.1 dB is observed as shown in Fig. 4.14. As examined in transient step responses in Fig. 4.15 in the next section, it gives the highest overshoot of 140% and the

longest settling time of 68.65 sec which are undesirable.

To reduce the percent overshoot to 48%, this requires a damping ratio $\zeta$ of 0.2275 from (4.15). From Fig. 4.10, a damping ratio $\zeta$ of 0.2275 is obtained which corresponds to a maximum magnitude $M_{p\omega}$ of 2.257 or 7.071 dB. As illustrated in Fig. 4.14, the frequency response for $K_i = 1$ intersects the 7.37 dB closed-loop curve. To obtain such frequency response, the frequency response has to be lowered by a gain of 7.696 dB, which means the integral gain $K_i$ has to be reduced by a factor of 2.425 as determined by (4.16). This yields a new integral gain $K_i$ of 1.24, which is close to the correct integral gain $K_i$ of 1.

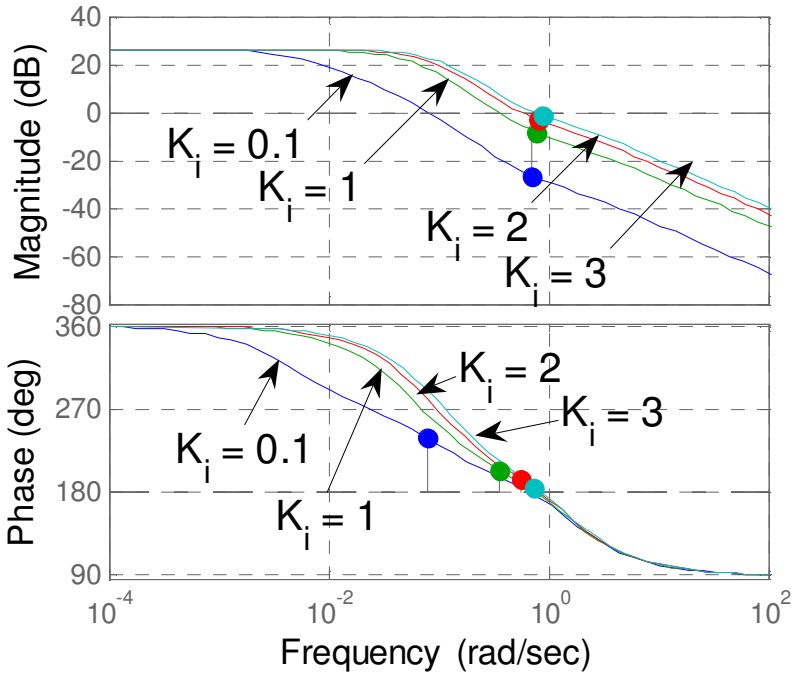


Figure 4.11: Open-loop bode diagram

Table 4.2: Relative Stability of Hydraulic System

| $K_i$ | 0.1 | 1 | 2 | 3 |
|---|---|---|---|---|
| 20 log($G_m$) [dB] | 26.62 | 8.19 | 3.55 | 1.18 |
| $P_m$ | 58.12 | 24.74 | 14.91 | 6.14 |
| $\omega_g$ | 0.71 | 0.77 | 0.83 | 0.87 |
| $\omega_p$ | 0.08 | 0.35 | 0.56 | 0.75 |

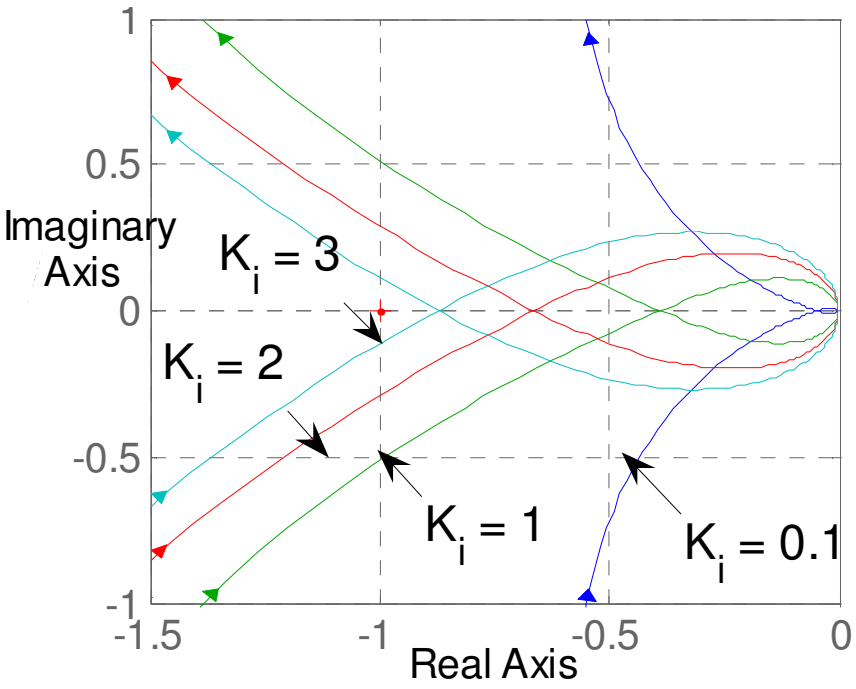


Figure 4.12: Nyquist diagram

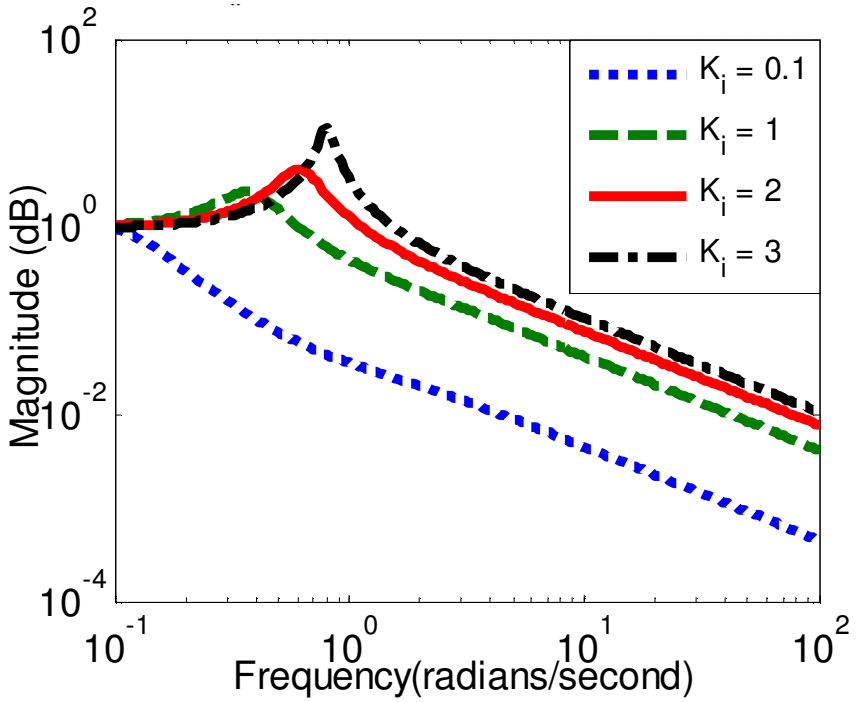


Figure 4.13: Closed-loop bode diagram

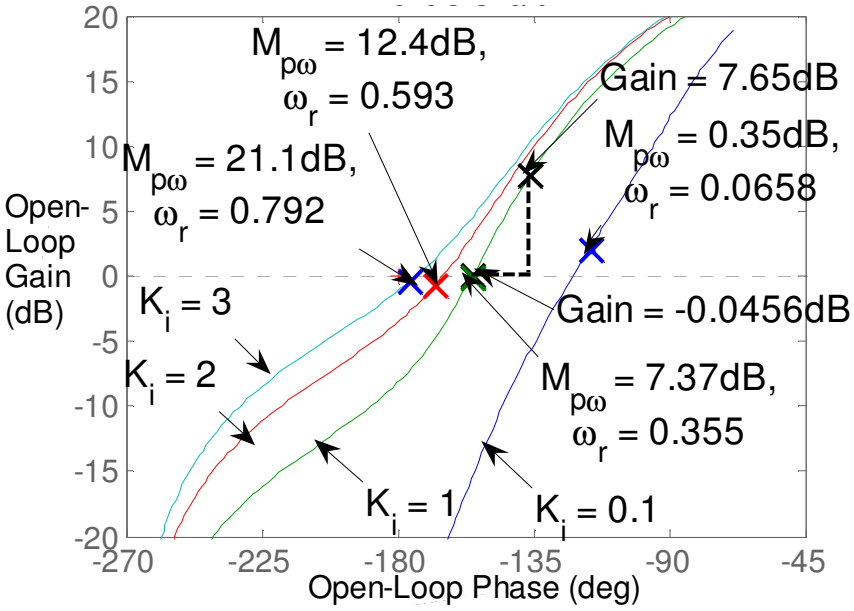


Figure 4.14: Nichols chart

Table 4.3: Closed-Loop Frequency Characteristics

| $K_i$ | 0.1 | 1 | 2 | 3 |
|---|---|---|---|---|
| $M_{p\omega}$ [dB] | 0.35 | 7.37 | 12.4 | 21.1 |
| $\omega_r$ | 0.0658 | 0.355 | 0.593 | 0.792 |

### 4.3.2 Results using Time Response Method

The frequency response methods are correlated with time response method. Herein, a transient step response will be examined to observe the system overshoot and settling time. A system with less overshoot and quicker settling time is considered as a good system.

The hydraulic system when subject to a step disturbance with the integral gain $K_i$ set to be 0.1, 1, 2 and 3 results in the transient responses as illustrated in Fig. 4.15. The associated performance characteristics, include rise time, peak time, settling time and overshoot, are presented in Table 4.4.

As determined in frequency response methods in the previous section, the integral gain $K_i$ of 0.1 will result in the highest gain and phase margins. This is further investigated using transient step response as shown in Fig. 4.15. It is observed that this system has the least overshoot among other values of $K_i$, however it has a longer settling time.

It is examined that system with integral gain $K_i$ of 1 yields a better response, with low overshoot and faster settling time. It has a percent overshoot of 57.26% and a settling time $T_s$ of 36.47sec. The percent overshoot obtained is different from that obtained in frequency response, due to the reason that this high-order hydraulic system is approximated by the second-order system.

The system subsides to a steady state value of (1-$e_{ss}$) where $e_{ss}$ is the steady state error derived as following:

$$e_{ss} = lim_{s \to 0} sE(s) = \frac{\sigma}{\sigma + 1} \tag{4.18}$$

where, $\sigma$ is permanent droop.

This shows that the system gains have no effects on determining the final steady-state value, but it is determined by system permanent droop $\sigma$. The steady-state error of this controller system is 5%.

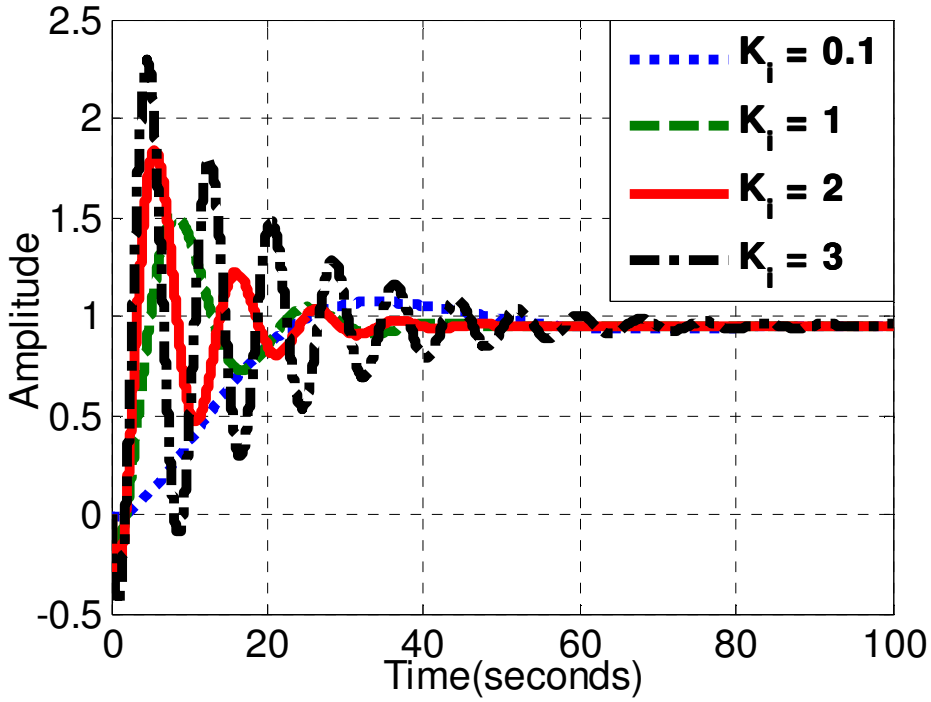


Figure 4.15: Transient step response

Table 4.4: Step Response Characteristics

| Integral Gain $K_i$ | 0.1 | 1 | 2 | 3 |
|---|---|---|---|---|
| Rise Time | 15.47 | 2.33 | 6.75 | 0.72 |
| Settling Time | 53.27 | 36.47 | 36.96 | 68.65 |
| Overshoot | 12.59 | 57.26 | 93.10 | 140.34 |
| Peak | 1.07 | 1.50 | 1.84 | 2.29 |
| Peak Time | 33.92 | 8.48 | 5.72 | 4.75 |

## 4.4 Summary

In conclusion, the stability of a hydraulic system governed by a PID controller is studied in this chapter. Relative stability has been analysed by utilising frequency response methods, namely Bode diagram, Nyquist diagram and Nichols chart. The analyses are further investigated using transient step responses. An optimum setting for a governor will result in a less overshoot and faster settling time in the transient response when subject to a step disturbance. An illustrative study case has been presented in adjusting the system gains utilising Nichols chart to reduce the percent overshoot, as well as to improve system relative stability.

## References


[1] H. M. Paynter. *Palimpsest on the Electronic Analog Art.* Geo, A. Philbrick Researches, Inc., Boston, Mass, 1955.

[2] L. M. Hovey, "Optimum Adjustment of Hydro Governors on Manitoba Hydro System," *The Engineering Journal*, November 1960.

[3] L. M. Hovey, "Optimum Adjustment of Hydro Governors on Manitoba Hydro System," *AIEE Transactions*, December 1962.

[4] M. H. Chaudhry, "Governing Stability of Hydroelectric Power Plant," *Water Power*, April 1970.

[5] S. Hagihara, H. Yokota, K. Goda, K. Isobe, "Stability of a Hydraulic Turbine Generating Unit Controlled by P.I.D. Governor," *IEEE Trans. Power App. Syst.*, Vol. PAS-98, no. 6, Nov/Dec 1979.

[6] R. C. Doft, R. H. Bishop. *Modern Control Systems.* 10th ed., Pearson Education, Inc., 2005.

[7] "IEEE Guide for the Application of Turbine Governing Systems for Hydroelectric Generating Units," *IEEE Std 1207-2004*, pp. 1-121, 2004.

[8] P. Kundur. *Power System Stability and Control.* McGraw-Hill, 1994.

# Chapter 5

# Modelling of Hydraulic Turbine for Dynamic Studies and Performance Analysis


### Abstract

Classical ideal lossless representation of the hydraulic turbine has been used widely in the past for governor stability studies. This model is suitable for small perturbations around the initial operating condition, and approximates to the practical turbine characteristics at low frequencies only. For satisfactory fast response and stable operation of governor studies, this classical model may not be adequate, rather a more accurate modelling of the turbine-penstock characteristics is desired to capture and depict the essential dynamic performances for wide variety of system analyses. In this chapter, a hydraulic turbine model with long penstock is represented where the water hammer effects and friction are taken in consideration. A detailed hydraulic turbine-penstock utilised for governing stability studies is used to analyse the transient response when subject to a load disturbance. Frequency response analysis as well as transient response analysis is performed to evaluate the effects of the detailed modelling of the turbine-penstock to the stability analyses and the dynamic

performances.

## 5.1 Introduction

The increasing complexity of the system network as well as the growing market and economics require more accurate and detailed representations of the power system components. This is to allow an adequate and accurate prediction of the system dynamic responses and performances to be obtained when system stability is analysed through simulation.

In the past, a classical ideal lossless turbine-penstock has been used widely to examine the stability as well as to obtain the optimum parameters for the hydraulic governing system [1] - [4]. This simple representation of the hydraulic governor turbine system has eased the computational requirements in establishing the stability boundaries and the transient responses subject to a step load disturbance. However, this simple linearised turbine-penstock model represented in the studies has neglected the effects of water compressibility and pipe elasticity which are usually encountered in reality; hence the accuracy is in doubt.

Detailed representation of the hydraulic system will assure a greater accuracy in the governor stability analysis. In a power network, system stability is vital to ensure satisfactory system operation, thus a faster response of the governor in returning the system frequency to nominal when subject to load disturbances is desired. This in turn requires a more detailed representation of the turbine-penstock model where the inherent nonlinear characteristics such as the effects of the water velocity in the penstock, acceleration of water column, hydraulic head and gate should be accounted for. This is to interpret the system dynamic behaviours as accurately as possible and to approximate to the practical cases closely and for a wide frequency range. Thus, of greater importance is to model the hydraulic system carefully to approximate the practical turbine model at all frequencies such that reliable stability analysis can be obtained.

Authors in [5] developed more detailed models of hydraulic prime mover/energy supply for system stability studies. Woodward [6] discussed the achievable enhancements in the hydraulic turbines representation as prime movers in power system analysis. Sanathanan [7]

illustrated a method for obtaining accurate reduced-order models for hydro turbines with long penstocks and demonstrated the inadequacy of the first order model.

In this chapter, a detailed representation of turbine-penstock, accounting for the effects of water compressibility and pipe elasticity, as well as the friction, is considered for the stability studies.

## 5.2 Hydraulic Turbine Model

Fig. 5.1 shows the block diagram of a hydraulic turbine generating system governed by a proportional-integral-derivative (PID) governing system.

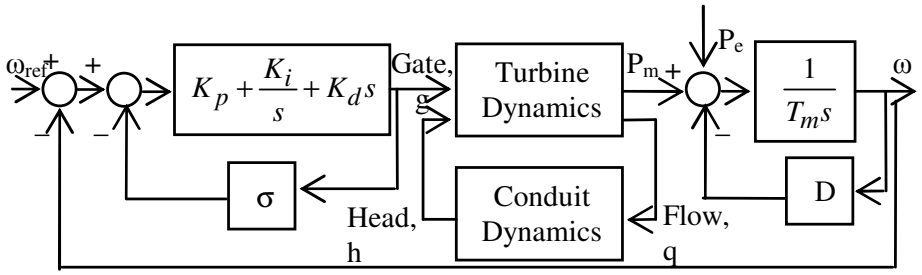


Figure 5.1: Hydraulic turbine generating system

The hydraulic governor turbine system as shown in Fig. 5.1 has the general open-loop transfer function as derived in the following:

$$G = \frac{K_p + \frac{K_i}{s} + K_d s}{1 + \sigma\left(K_p + \frac{K_i}{s} + K_d s\right)} \frac{1 - T_w s}{1 + 0.5 T_w s} \frac{1}{T_m s + D} \tag{5.1}$$

where $K_p$, $K_i$ and $K_d$ are proportional, integral and derivative gains, $s$ is the Laplace transform variable, $\sigma$ represents the permanent speed droop, $T_w$ represents the water starting time, $T_m$ and $D$ are mechanical starting time and self-regulation of turbine and load respectively. The mid-term of the open-loop transfer function as in (5.1) represents an ideal lossless turbine model. The following studies involve detailed representations of the turbine-penstock model as described in Section 5.2.1.

### 5.2.1 Turbine-Penstock Model

This paper will be concentrating on the representation of the turbine-penstock model for system stability studies. The linearised hydraulic turbine model can be represented for small perturbation about an initial operating condition as follows [6, 8]:

$$\begin{aligned} q &= a_{11}h + a_{12}\omega + a_{13}g \\ P_m &= a_{21}h + a_{22}\omega + a_{23}g \end{aligned} \tag{5.2}$$

where $q$ = water flow, $P_m$ = mechanical power, $h$ = hydraulic head, $\omega$ = speed/frequency, $g$ = gate,

$$a_{11} = \frac{\partial q}{\partial h}, \quad a_{12} = \frac{\partial q}{\partial \omega}, \quad a_{13} = \frac{\partial q}{\partial g}, \quad a_{21} = \frac{\partial P_m}{\partial h}, \quad a_{22} = \frac{\partial P_m}{\partial \omega}, \quad a_{23} = \frac{\partial P_m}{\partial g}.$$

Usually, the partial derivatives with respect to speed are insignificant.

To account for the dynamic interaction between the hydraulic system and the power system accurately, a detailed hydraulic system model is necessary which should account for the effects of water compressibility and pipe elasticity. Head and flow at the turbine end are related by the transfer function as follows [9]:

$$\frac{H(s)}{Q(s)} = -F - \frac{T_w}{T_e}\tanh(T_e s) \tag{5.3}$$

where $F$ = friction coefficient, $T_e$ = elastic time.

Combining (5.2) and (5.3) yields the following:

$$\frac{P_m}{g} = \frac{a_{23} + (a_{23}a_{11} - a_{21}a_{13})\,F + (a_{23}a_{11} - a_{21}a_{13})\,\frac{T_w}{T_e}\tanh(T_e s)}{1 + a_{11}F + a_{11}\frac{T_w}{T_e}\tanh(T_e s)} \tag{5.4}$$

Equation (5.4) represents a hydraulic turbine-penstock model where the effects of the pressure wave stretching the water conduit and the friction are taken into consideration.

The '$a$' coefficients vary depending on the turbine operating condition. For an ideal

turbine operating at rated speed and head, the $a$ coefficients are $a_{11} = 0.5$, $a_{13} = 1.0$, $a_{21} = 1.5$ and $a_{23} = 1.0$ [6, 8].

For an ideal turbine, (5.4) can be simplified to the following general representation:

$$\frac{P_m}{g} = \frac{1 - F - \frac{T_w}{T_e}\tanh(T_e s)}{1 + \frac{1}{2}F + \frac{1}{2}\frac{T_w}{T_e}\tanh(T_e s)} \tag{5.5}$$

### 5.2.2 Lumped-Parameter Approximation

The infinite product expansion of the transcendental functions involved in the transfer functions for distributed system developed by Goodson [10] has provided significant advantages for simulation as the system eigenvalues are mostly preserved. Both system poles and zeros are retained with the utilisation of the product expansion for any order approximation. It is crucial to keep the zeros and poles of the characteristic equation in the system as in a dynamic response, the zeros are of primary importance whilst the poles yield accurate oscillation frequencies and damping [10].

In [10], Taylor series expansion is demonstrated to have less preservations of the system zeros over the product expansion for any order approximation. Moreover, the product expansion has the ability to approximate the response with the extremum amplitude obtained [10]. These advantages illustrated allow a more precise description of the transient dynamic response with low-order ordinary differential equations.

The hyperbolic function involved in (5.4) and (5.5) can be approximated by a lumped-parameter equivalent with a sufficient number of the expansions terms, based on the analysis objective and the essential precision [9].

$$\tanh(T_e s) = \frac{sT_e \prod_{i=1}^{i=\infty}\left[1 + \left(\frac{sT_e}{i\pi}\right)^2\right]}{\prod_{i=1}^{i=\infty}\left[1 + \left(\frac{2sT_e}{(2i-1)\pi}\right)^2\right]} \tag{5.6}$$

When the hyperbolic function is approximated to $\tanh(T_e s) \approx sT_e$ for $i = 0$, the con-

ventional ideal lossless turbine assuming an inelastic water column is represented as follows:

$$\frac{P_m}{g} = \frac{1 - T_w s}{1 + \frac{1}{2} T_w s} \tag{5.7}$$

With the consideration of water hammer effects, the turbine-penstock representations corresponding to $i = 1$ and $i = 2$ are as follows:

for $i = 1$

$$\frac{P_m}{g} = \frac{a_{23}\left[1 + \left(\frac{2sT_e}{\pi}\right)^2\right] + \left(\frac{a_{23}}{2} - a_{21}\right) sT_w \left[1 + \left(\frac{sT_e}{\pi}\right)^2\right]}{\left[1 + \left(\frac{2sT_e}{\pi}\right)^2\right] + \frac{sT_w}{2}\left[1 + \left(\frac{sT_e}{\pi}\right)^2\right]} \tag{5.8}$$

for $i = 2$

$$\frac{P_m}{g} = \frac{a_{23}\left[1 + \left(\frac{2sT_e}{\pi}\right)^2\right]\left[1 + \left(\frac{2sT_e}{3\pi}\right)^2\right] + \left(\frac{a_{23}}{2} - a_{21}\right) sT_w \left[1 + \left(\frac{sT_e}{\pi}\right)^2\right]\left[1 + \left(\frac{sT_e}{2\pi}\right)^2\right]}{\left[1 + \left(\frac{2sT_e}{\pi}\right)^2\right]\left[1 + \left(\frac{2sT_e}{3\pi}\right)^2\right] + \frac{sT_w}{2}\left[1 + \left(\frac{sT_e}{\pi}\right)^2\right]\left[1 + \left(\frac{sT_e}{2\pi}\right)^2\right]} \tag{5.9}$$

As observed in (5.8) and (5.9), a more complicated and higher-order of the turbine-penstock representation is resulted when approximated with a higher expansion term of $i$. The magnitude and phase diagrams of the hydraulic turbine transfer functions as shown in (5.7), (5.8) and (5.9) are plotted in Figs. 5.2 and 5.3 respectively with arbitrary selections of $T_w = 2.0$ sec and $T_e = 1.0$ sec.

As interpreted in the bode diagrams shown in Figs. 5.2 and 5.3, the classical ideal lossless turbine (model with $i = 0$) agrees with the detailed representation models (i.e. models with $i = 1$, and $i = 2$) up to frequency 0.6 rad/sec only. As for the model with elementary component of the water column preserved (i.e. $i = 1$), it agrees with model including more components of the water column represented, (i.e. $i = 2$) up to a higher frequency of 4 rad/sec.

This means that the classical ideal lossless turbine approximates to the practical turbine

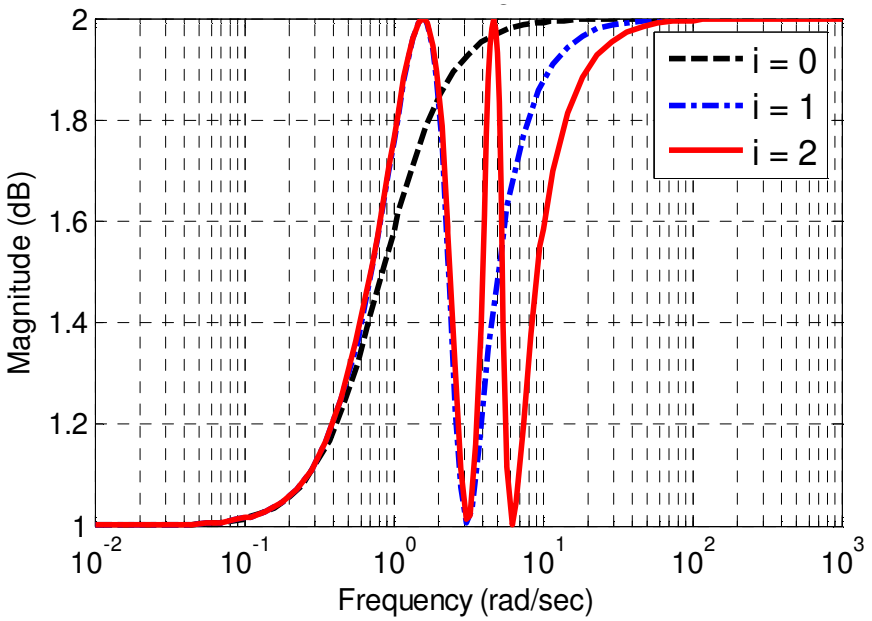


Figure 5.2: Magnitude plots of turbine-penstock models

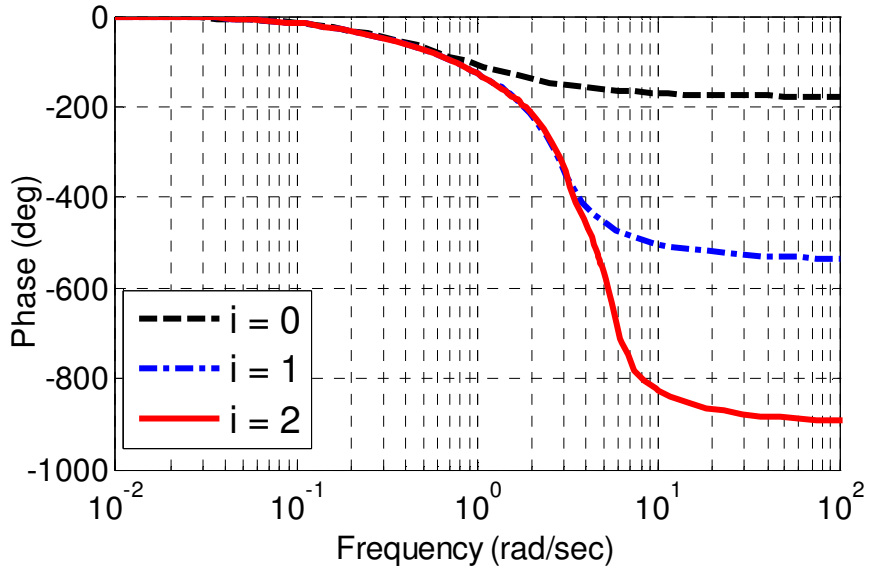


Figure 5.3: Phase plots of turbine-penstock models

at very low frequencies only. If the classical ideal lossless turbine is used for stability analysis at very high frequencies, the simulation responses may become erroneous. This classical representation is said to be very inaccurate in practical cases. Thus, a more detailed representation of turbine-penstock model is desired to predict the practical responses more precisely.

### 5.2.3 Stability of Hydraulic Turbine Generating Unit

Hagihara et al. [4] demonstrated the stability boundaries of a hydraulic system governed by a PID controller, but with the turbine-penstock model represented by a simple first-order transfer function as obtained in (5.7). With a more accurate turbine-penstock representation utilised for stability studies, the optimum parameters obtained in [4] are no longer resulting an optimum transient response when subject to load disturbances.

The optimum parameters suggested in [4] are:

$$\lambda_1 = 0.8, \quad \lambda_2 = 0.3, \quad \lambda_5 = \frac{1}{3} \tag{5.10}$$

The corresponding proportional-integral-derivative gains, $K_p$, $K_i$ and $K_d$ obtained from these $\lambda$ values are expressed as follows:

$$K_p = 0.8\frac{T_m}{T_w}, \quad K_i = 0.24\frac{T_m}{T_w^2}, \quad K_d = 0.27T_m \tag{5.11}$$

Now, the transient responses of the hydraulic system subject to a step load disturbance are investigated with the optimum parameters as expressed in (5.11) utilised. It is shown in Fig. 5.4 that for an ideal lossless turbine assuming an inelastic water column, the transient step response is optimum, with less overshoot and quicker settling time. However, when the fundamental component of the water column is represented (i.e., $i = 1$), the resulting response is oscillatory with higher overshoot and longer settling time.

If a higher-order representation of the turbine-penstock is employed, in this case, a turbine-penstock model with $i = 2$ (i.e., more components of the water column preserved)

yields an unstable response as seen in Fig. 5.5. Thus, this has concluded that the optimum parameters for PID governor recommended in [4] do not result in an optimum response when a higher-order turbine-penstock is modelled.

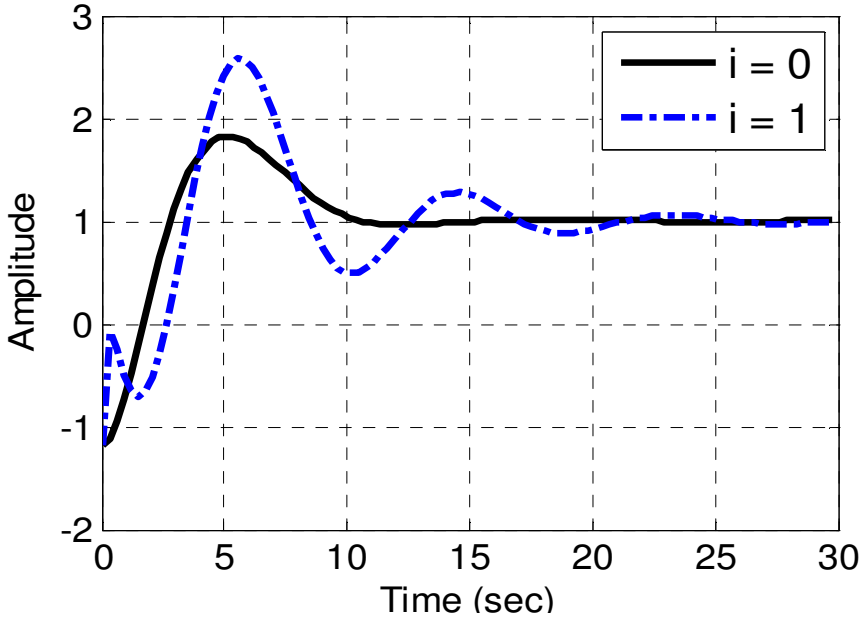


Figure 5.4: Step responses of ideal lossless turbine and turbine with elastic water column

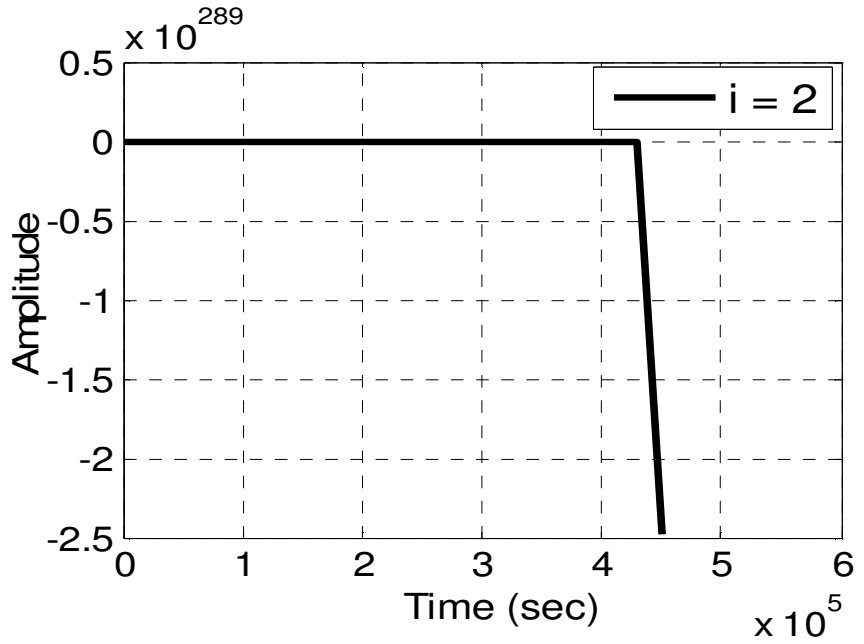


Figure 5.5: Unstable step response of higher-order turbine-penstock model

Murty et al. [11] extended Hagihara et al works by considering the influence of water column elasticity on the stability boundaries of the hydraulic unit with long penstock operating on an isolated load with an additional parameter $\lambda_6 = \frac{T_e}{T_w}$ introduced. This parameter is non-dimensional and has been introduced to accommodate $T_e$, which designates water reflection time constant [11]. The impact of water column elasticity can be demonstrated with $\lambda_6$, which significantly reduces the stability margins. For hydro systems with long penstocks, the value of $\lambda_6$ can be higher than 1.0. The stability margins are reduced significantly with the presence of long penstocks [11]. The derivation of the stability limit curves for hydro-turbine generating unit with elastic water column, in the non-dimensional representation, could function as a guide in adjusting the governor parameters optimally [11]. However, the optimum parameters for the PID governor are not included for the studies.

## 5.3 Simulation Results

A hydraulic unit with water starting time $T_w = 2.0$ sec, mechanical starting time $T_m = 8.0$ sec and elastic time, $T_e = 1.0$ sec is considered for the stability studies. Worse case scenario where purely resistive load with instantaneous voltage regulation is considered, thus, self-regulation of turbine and load, $D$ is neglected. The permanent speed droop, $\sigma$ associated with the governor is not considered in this study as well.

Herein, the stability of the hydraulic system is investigated to demonstrate the effects of detailed representations of the turbine-penstock models onto the transient responses. A base case with an ideal lossless turbine-penstock model utilised is compared with the study cases where detailed representations of the turbine-penstock are considered. These detailed models include the effects of the water hammer, i.e. the compressibility of the water column and the elasticity of the penstock, and may include the effects of friction as well.

To simplify the stability analysis, an ideal turbine is assumed with a coefficients $a_{11} = 0.5$, $a_{13} = 1.0$, $a_{21} = 1.5$ and $a_{23} = 1.0$ used.

In this stability analysis, three hydraulic turbine-penstock representations, i.e., a classical ideal lossless turbine assuming an inelastic water column, a turbine with fundamental

component of water column preserved (i.e., $i = 1$) and a turbine with more components of water column preserved (i.e., $i = 2$) are used. These three models are then compared to those models with friction included; herein frictions of 0.1 and 0.5 are considered.

The magnitude and phase plots of the hydraulic turbine-penstock models are shown in Figs. 5.6 and 5.7 respectively. As observed in Fig. 5.7, the friction has little effects on the phase. However, significant difference is observed in the magnitude plots as in Fig. 5.6 even at very low frequencies. When friction is encountered, it results a lower gain at the early frequency ranges but slowly agree with the model without friction when the magnitude reaches a higher peak. However, for a more detailed representation of the turbine-penstock, significant difference resulted when the peak returns to a lower peak. The lower peak of the model with friction included has a smaller value of magnitude compared to that without friction. This has illustrated that for a higher-order representation of turbine-penstock model, the model with friction included does not agree with the model without friction for a wide range of frequencies. Thus, the study is mostly erroneous if a classical ideal lossless turbine ($i = 0$, $F = 0$) is used to predict the response of a practical turbine-penstock with friction.

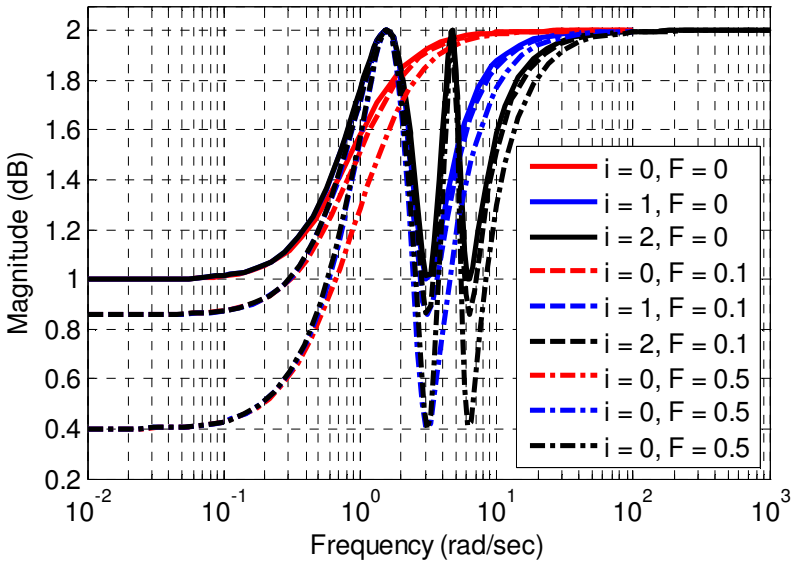


Figure 5.6: Magnitude plots of turbine-penstock models with and without friction

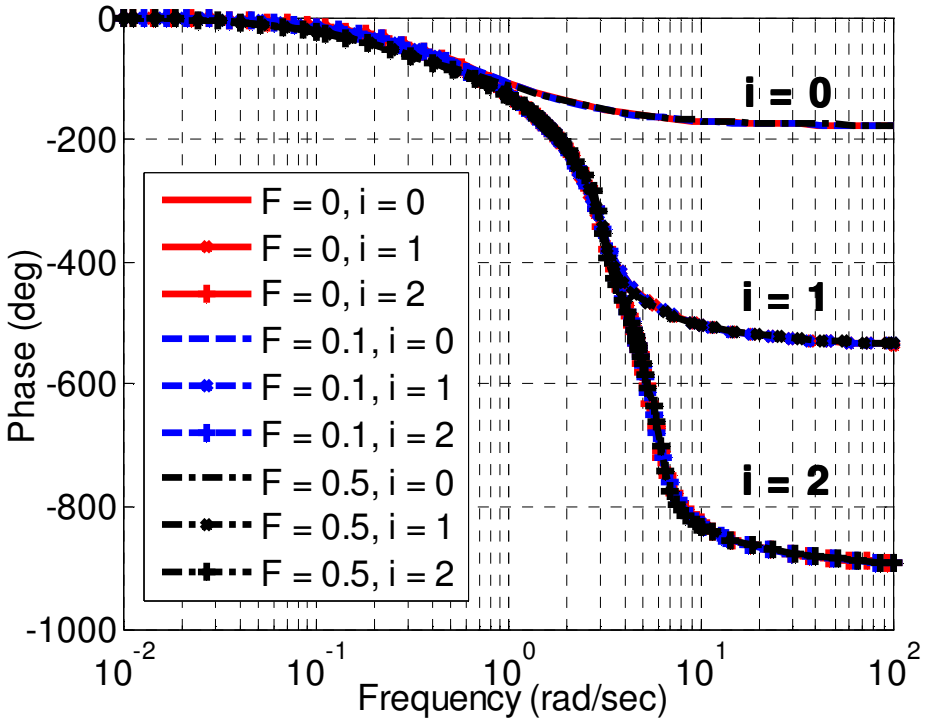


Figure 5.7: Phase plots of turbine-penstock models with and without friction

Frequency response loci for various hydraulic turbine-penstock models are included in the study as portrayed in Fig. 5.8. The frequency response loci in Fig. 5.8 agree with the bode diagram as shown in Fig. 5.6. The apparent drop in gain at low frequencies when friction is included may lead to misleading results.

The crosses marked on the frequency response loci are the response at frequency of 0.6 rad/sec. When a classical ideal lossless turbine model with no water column effect is considered, the response is differed from that detailed models with $i = 1$ and 2 at higher frequencies. This ideal lossless turbine has a lower gain at frequency of 0.6 rad/sec compared to the detailed models. However, with higher-order representations of turbine-penstock utilised ($i = 1$ and 2), the responses between both models are the same at frequency of 0.6 rad/sec. With a detailed turbine-penstock model utilised, the dynamic behaviours can be predicted more accurately to the practical responses for a wider range of frequencies.

With the effects of friction considered, the frequency response loci have significant difference at most of the frequency ranges as seen in Fig. 5.8. This is true as observed in

magnitude plots previously. Hence, the detailed modelling of turbine-penstock is important to allow a more precise description on the practical cases.

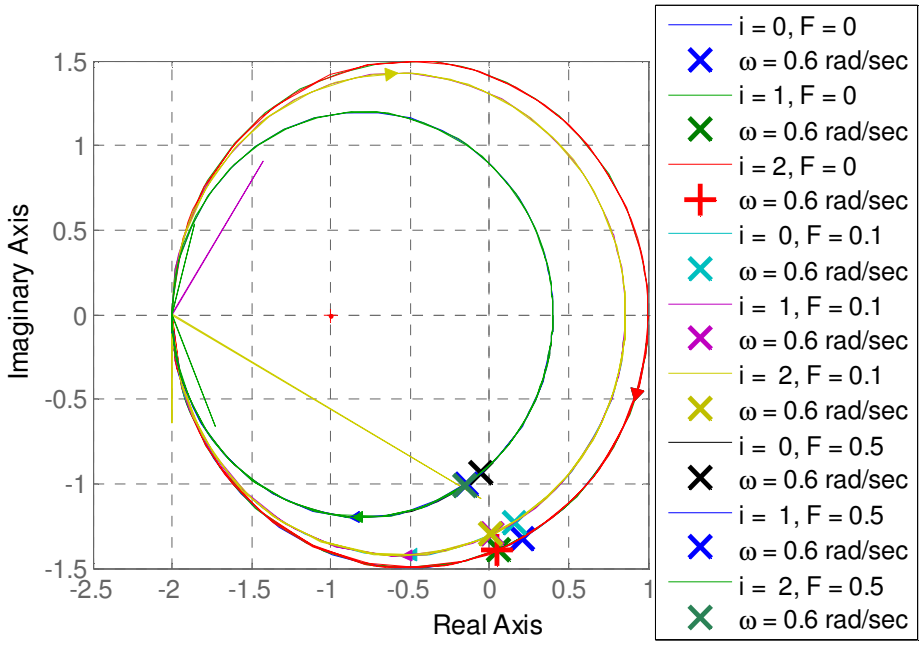


Figure 5.8: Frequency response loci for hydraulic turbine-penstock models

Now, the transient responses of the hydraulic system with different turbine-penstock models utilised are examined for a step load disturbance. The proportional-integral-derivative gains, $K_p$, $K_i$ and $K_d$ used are those suggested by Hagihara et al. as in (5.11). The resulted transient responses are shown in Fig. 5.9.

The classical ideal lossless turbine with no water column effects yields the optimum transient response as agreed in [4]. With elementary component of water column preserved (i.e., $i = 1$) but no friction included, the resulted response is oscillatory with a higher overshoot.

The ideal lossless turbine (i.e., $i = 0$) but with friction of 0.1 included results a response with a slightly longer settling time than the optimum response. If a higher friction is considered, $F = 0.5$, the transient response is obviously oscillatory and with significant settling time.

An additional study has been included to compare with the turbine-penstock model

approximated by Sanathanan [7]. Sanathanan employed Maclaurin series to approximate the turbine-penstock transfer function and claimed that the similar precision is obtained by a reduced second-order transfer function provided that the coefficients are selected properly.

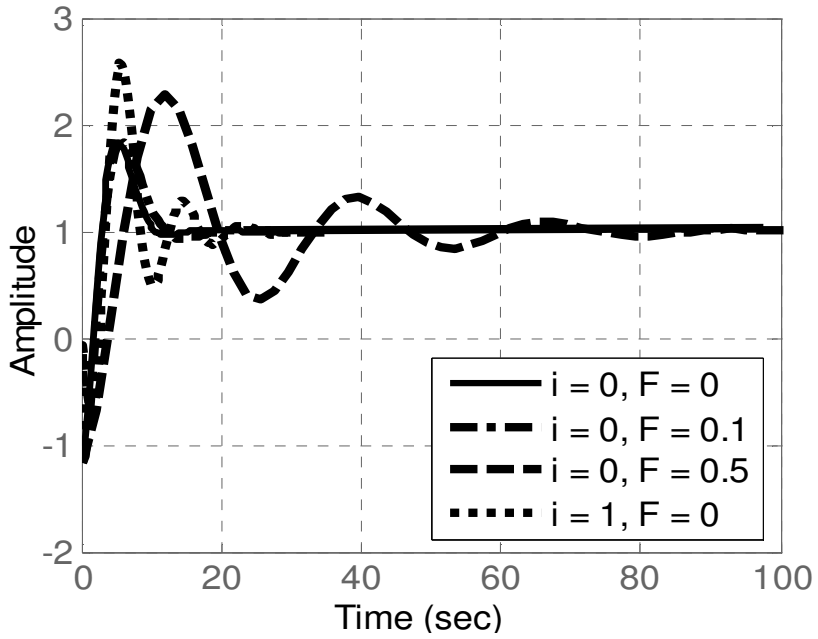


Figure 5.9: Step responses of turbine-penstock models

Now, Sanathanan's turbine-penstock models are compared against the models approximated by the product expansions with $i = 1$ and 2 in this chapter. Comparison between the magnitude and phase plots can be examined in Figs. 5.10 and 5.11 respectively. A model with friction of 0.05 is included in the study as well. The transfer function with the fundamental component of the water column retained ($i = 1$) is of fifth-order expression whilst the transfer function with $i = 2$ is of ninth-order.

The reduced second-order transfer function of Sanathanan's model, as observed in Figs. 5.10 and 5.11, agrees with the detailed forth-order model in the frequency range of 0 and 1.6 rad/sec. The reduced model approximates to the models approximated by the product expansions up to 1.6 rad/sec as well. As for the forth-order of Sanathanan's model, it approximates to the models used in this study up to 2.1 rad/sec.

A hydraulic turbine-penstock model approximated by the product expansions in this study with the fundamental water column component retained (i.e., $i = 1$) is generally adequate for the dynamic response and the performance analysis of the power system.

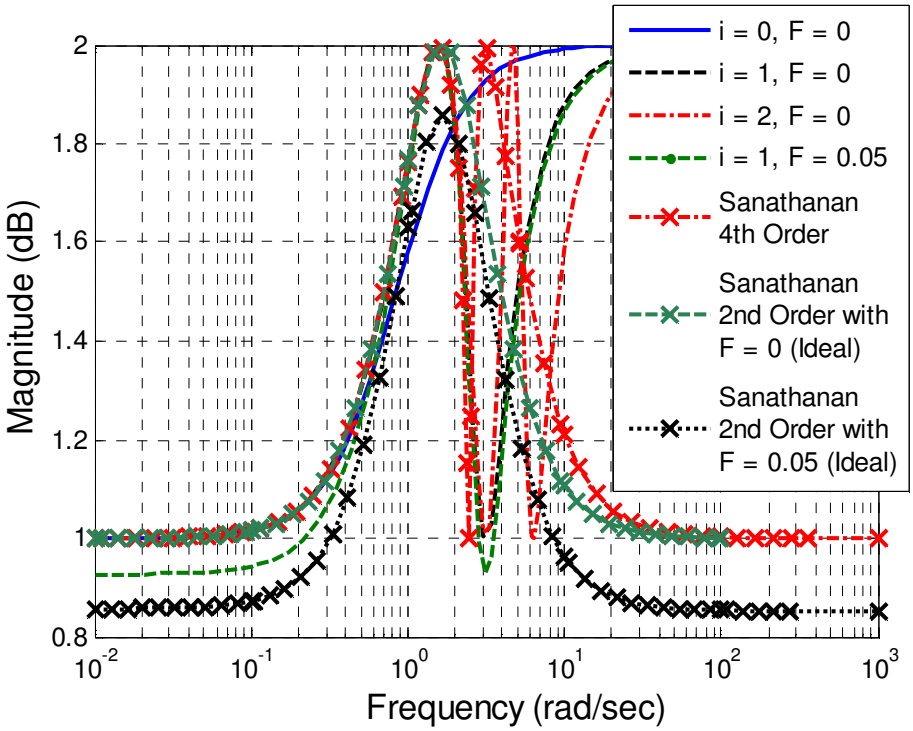


Figure 5.10: Comparisons of magnitude plots

The transient responses subject to a step load disturbance are examined and compared among Sanathanan's models and model approximated by product expansions (with $i = 1$, $F = 0$) as portrayed in Fig. 5.12. It is seen that with a detailed turbine-penstock represented, the resulted responses are oscillatory with longer settling time. The resulting response of a turbine-penstock model with fundamental water column component retained and with no friction is similar to Sanathanan's forth-order and reduced second-order responses. This has further ensured that the hydraulic turbine-penstock with fundamental component preserved is adequate for the stability studies.

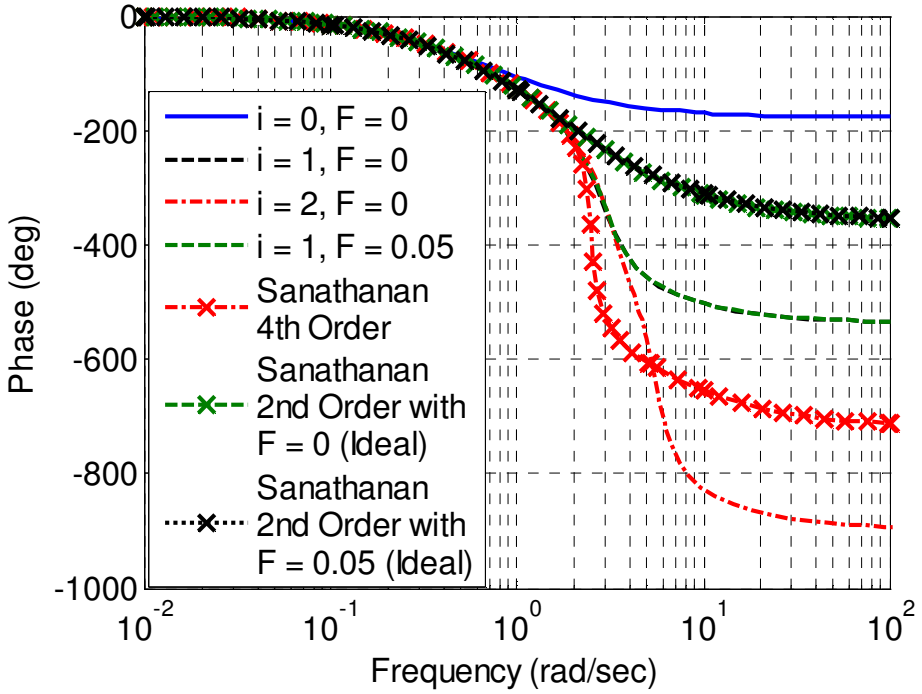


Figure 5.11: Comparisons of phase plots

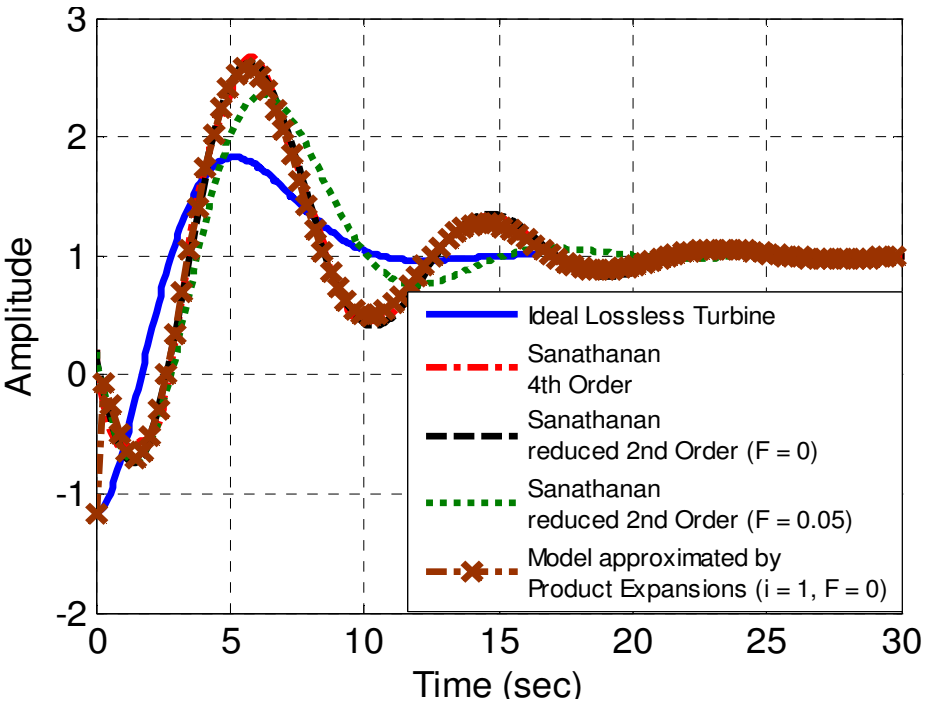


Figure 5.12: Comparisons of transient responses

## 5.4 Summary

In conclusion, the modelling of the hydraulic turbine-penstock is vital in evaluating the system stability. An ideal lossless turbine assuming an inelastic water column may not depict the practical behaviours at higher frequencies and may lead to erroneous results. To be able to capture and depict the practical system dynamic responses more precisely, a detailed representation of the water conduit and penstock is desired. This chapter demonstrates that the optimum parameters suggested for the PID governor based on the conventional turbine-penstock model do not result in an optimum response when applied to a system with a more detailed turbine-penstock represented. This further portrays that the conventionally-used turbine-penstock model is not adequate to depict the practical system dynamic responses and performances especially when a turbine with long penstock is used. Thus, the water hammer effects as well as the friction effects have to be modelled carefully to allow a more accurate and reliable analysis in system dynamics to be performed.

## References


[1] H. M. Paynter. *Palimpsest on the Electronic Analog Art.* Geo, A. Philbrick Researches, Inc., Boston, Mass, 1955.

[2] L. M. Hovey, "Optimum Adjustment of Hydro Governors on Manitoba Hydro System," *The Engineering Journal*, November 1960.

[3] M. H. Chaudhry, "Governing Stability of Hydroelectric Power Plant," *Water Power*, April 1970.

[4] S. Hagihara, H. Yokota, K. Goda, K. Isobe, "Stability of a Hydraulic Turbine Generating Unit Controlled by P.I.D. Governor," *IEEE Trans. Power App. Syst.*, Vol. PAS-98, no. 6, Nov/Dec 1979.

[5] IEEE Working Group Report, "Hydraulic turbine and turbine control models for system dynamic studies," *IEEE Trans. Power Syst.*, Vol. PWRS-7, no. 1, pp. 167-179, February 1992.

[6] J. L. Woodward, "Hydraulic-Turbine Transfer Function for Use in Governing Studies," *Proceedings IEE*, Vol. 115, no. 3, March 1968.

[7] C. K. Sanathanan, "Accurate Low Order Model for Hydraulic Turbine-Penstock," *IEEE Trans. Energy Convers.*, Vol. EC-2, no. 2, June 1987.

[8] D. G. Ramey, J. W. Skooglund, "Detailed Hydrogovernor Representation for System Stability Studies," *IEEE Trans. Power App. Syst.*, Vol. PAS-89, no. 1, January 1970.

[9] P. Kundur. *Power System Stability and Control.* McGraw-Hill, 1994.

[10] R. E. Goodson, "Distributed System Simulation Using Infinite Product Expansions," *Simulation*, Vol. 15, no. 6, pp. 255-263, December 1970.

[11] M. S. R. Murty, M. V. Hariharan, "Analysis and Improvement of the Stability of a Hydro-Turbine Generating Unit with Long Penstock," *IEEE Trans. Power App. Syst.*, Vol. PAS-103, no. 2, February 1984.

# Chapter 6

# Modelling of Hydraulic Governor-turbine for Control Stabilisation


### Abstract

Power system performance can be affected by dynamic characteristics of hydraulic governor-turbines during and following any disturbance, such as occurrence of a fault, loss of a transmission line or a rapid change of load. Accurate modelling of hydraulic governor-turbines is essential to characterise and diagnose the system response during an emergency situation. In this chapter, both detailed and simplified hydraulic systems governed by proportional-integral-derivative (PID) and proportional-integral (PI) controllers have been modelled. Their transient responses to disturbances are examined through simulation in MATLAB/Simulink. The dynamic performance of an isolated hydraulic system is investigated through evaluating stability margins, eigenvalues, root loci and frequency deviation time responses of the system and results are reported.

## 6.1 Introduction

Since 1973, the demand on modelling requirements for power system components has become more onerous due to the increasing complexity of power system networks [1]. Power system components such as governor, turbine and generator need to be represented by a detailed model. Classical representations of a hydraulic system, which assume an ideal lossless turbine, are limited to small perturbations around an initial operating point. They depict the actual characteristics at only very low frequencies. For large signal stability studies, the classical model may not capture the dynamic behaviour accurately and can lead to erroneous responses. Moreover, conventional governor tuning is performed based on the classical model, hence the optimal and stable governor settings obtained by the classical model may differ substantially from the settings obtained from comprehensive models. It is thus vital to represent the hydraulic model in detail in order to determine the practical dynamic responses as accurately as possible for a wide variety of system studies.

This chapter presents a detailed mathematical representation of the hydraulic turbine-penstock. The dynamic performance of the hydraulic system is studied using time domain and frequency domain methods.

## 6.2 Mathematical representations of hydraulic system

In this section, a mathematical representation of a hydraulic system, including both turbine-penstock and the governing system, is introduced. Figure 6.1 shows a block diagram of the hydraulic governor-turbine system connected to a power system network. The primary source for the electrical power provided by utilities is the kinetic energy of water which is converted into mechanical energy by the prime movers. The electrical energy to be supplied to the end users is then transformed from mechanical energy by the synchronous generators. The speed governing system adjusts the generator speed based on the input signals of the deviations of both system frequency and interchanged power with respect to the reference settings. This is to ensure that the generator will operate at or near nominal speed at all

times.

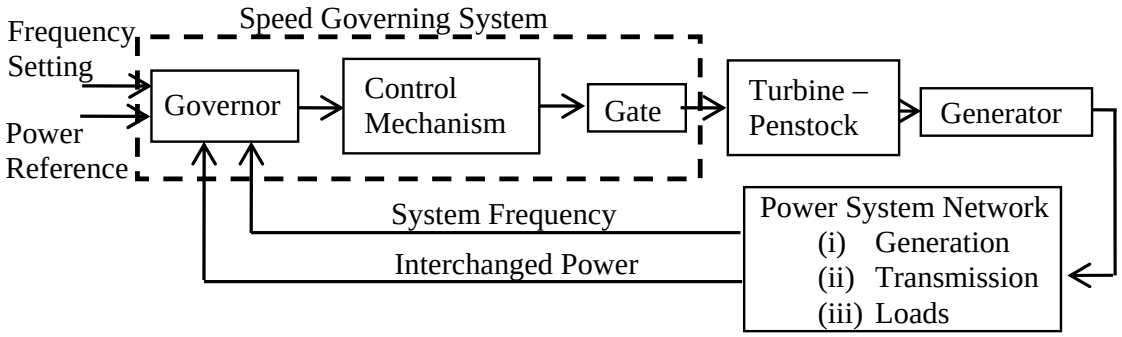


Figure 6.1: Functional block diagram of hydraulic governor-turbine system interconnected with a power system network

### 6.2.1 Hydraulic Turbine Model

The dynamic performance of a hydraulic system is affected by the turbine-penstock characteristics which are determined by water inertia, water compressibility, and pipe wall elasticity in the penstock. The effects of each component need to be modelled carefully to study their impact on the system dynamic performance. For example, the water inertia will cause changes in turbine flow to lag behind changes in turbine gate opening, and the travelling waves of pressure and flow involving a compressible fluid in an elastic pipe lead to the water hammer phenomenon.

#### 6.2.1.1 Realistic Nonlinear Turbine-penstock Model

IEEE working group [1] and Kundur [2] have discussed the model for a detailed representation of hydraulic dynamics in the penstock. The hydraulic unit characteristic of a single penstock is expressed as [2]:

$$\frac{dq}{dt} = \frac{(h_0 - h - h_l)a_{gravity}A}{L}, \tag{6.1}$$

$$\bar{q} = \bar{G}\sqrt{\bar{h}}. \tag{6.2}$$

where, $q$ = turbine flow, $t$ = time [sec], $h_0$ = initial steady-state head, $h$ = hydraulic head at gate, $h_l$ = head losses due to friction in the conduit, $a_{gravity}$ = gravity acceleration, $A$ = penstock cross section area, $L$ = conduit length, $G$ = ideal gate opening based on the change from the no load to full load being equal to 1 per unit [pu] and $^-$ denotes normalised value [pu].

The terms for the physical design of the plant describe the water starting time constant for rated conditions when (6.1) is normalised using the per unit system [3]:

$$\frac{d\bar{q}}{dt} = \frac{1 - \bar{h} - \bar{h}_l}{T_{w\_rated}}, \tag{6.3}$$

where $T_{w\_rated} = \frac{Lq_{base}}{a_{gravity}Ah_{base}}$, $T_{w\_rated}$ = water starting time constant at rated load [sec], $q_{base}$ = base value of water flow, $h_{base}$ = base value of hydraulic head.

The turbine representation is based on steady-state measurements related to output power and water flow. It can be expressed as follows [3]:

$$\bar{P}_m = A_t \bar{h} \left( \bar{q} - \bar{q}_{noload} \right), \tag{6.4}$$

where $P_m$ = mechanical power, $\bar{q}_{noload}$ = per unit no load water flow and turbine gain $A_t$ is a proportionality factor and is assumed to be constant. It is expressed as $A_t = \frac{1}{\bar{g}_{FullLoad} - \bar{g}_{NoLoad}}$, where, $\bar{g}_{FullLoad}$ = per-unit full-load gate opening and $\bar{g}_{NoLoad}$ = per-unit no-load gate opening.

In practice, it is common for governor-turbine manufacturers to indicate the speed ring position by arranging the gate position sensing device to give readings as a fraction of the gate stroke from the fully closed to the fully opened setting. In reality, the gates will not be fully closed at no load and they may not be completely opened at rated load. Hence, it is assumed that the turbine torque at rated speed and rated head is linearly related to the gate position sensor reading [4].

The combination of (6.2), (6.3) and (6.4) yields the general dynamic characteristics of a hydraulic turbine with a penstock, unrestricted head and tail race as shown in the block

diagram in Figure 6.2. A supplementary term, $GD\Delta\omega$ is subtracted from the output of the turbine model to represent speed deviation damping due to gate opening [1], where, $D$ = Self-regulation of load. The speed deviation $\Delta\omega$ is the deviation of the actual turbine-generator speed from the nominal speed.

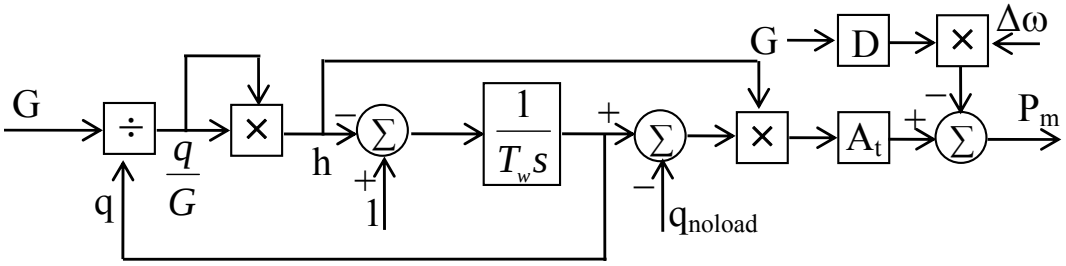


Figure 6.2: Hydraulic turbine block diagram assuming an inelastic water column

### 6.2.1.2 Linearised Turbine-penstock Models

The dynamic characteristics of the power system components are normally represented mathematically by differential equations. The technique of linear system analysis is employed to investigate the dynamic behaviour of the power system assuming small-signal conditions. The Laplace transform method is used herein to solve the linear differential equations; this method replaces the more complicated differential equations with relatively easily solved algebraic equations.

For a small variation about an equilibrium condition, the turbine is represented by the linearised equations, normalised based on initial steady-state values, as [1, 2, 5]:

$$\Delta\bar{q} = a_{11}\Delta\bar{h} + a_{12}\Delta\bar{\omega} + a_{13}\Delta\bar{g}, \tag{6.5}$$

$$\Delta\bar{P}_m = a_{21}\Delta\bar{h} + a_{22}\Delta\bar{\omega} + a_{23}\Delta\bar{g}. \tag{6.6}$$

where, $\omega$ = shaft speed, $g$ = movement of wicket gate or the amount of gate opening/closing [pu], $a_{11} = \partial q/\partial h$, $a_{12} = \partial q/\partial\omega$, $a_{13} = \partial q/\partial g$, $a_{21} = \partial P_m/\partial h$, $a_{22} = \partial P_m/\partial\omega$ and $a_{23} = \partial P_m/\partial g$.

Both the water flow and the mechanical power of the turbine are functions of head $h$,

machine speed $\omega$ and gate opening $g$. The partial derivatives represented by coefficients $a_{1i}$ and $a_{2i}$ ($i$ = 1,2,3) can be obtained from Thorne and Hill [5] for three different operating points.

In an interconnected power system, the hydraulic units are synchronised to the system network. As a result, speed variations $\Delta\omega$ are fairly small and usually neglected.

Consequently, the mechanical power output of the turbine can be obtained, with the inclusion of water inertia effect, as [5]:

$$\frac{\Delta\hat{\bar{P}}_m}{\Delta\hat{\bar{g}}} = \frac{a_{23}\frac{a_{23}a_{11}-a_{21}a_{13}}{a_{23}}\hat{T}_w s + 1}{a_{11}\hat{T}_w s + 1}. \tag{6.7}$$

where, $T_w$ = Water starting time constant [sec], $\hat{}$ denotes Laplace notation and $s$ denotes Laplace Transform variable.

Equation (6.7) is a conventional expression for a classical non-ideal hydraulic turbine. The superhat $\hat{}$ denotes the notation of the Laplace transform parameters. The typical values of the coefficients for an ideal lossless turbine are $a_{11} = 0.5$, $a_{13} = 1.0$, $a_{21} = 1.5$, $a_{23}$ = 1.0. The ideal lossless turbine used in system stability studies can be represented as [5]:

$$\frac{\Delta\hat{\bar{P}}_m}{\Delta\hat{\bar{g}}} = \frac{-\hat{T}_w s + 1}{0.5\hat{T}_w s + 1}. \tag{6.8}$$

The water starting time constant used for the linearised turbine-penstock model corresponds to the hydro unit's operating condition, i.e. $T_w$ is calculated with the current operating flow and head. For the nonlinear model described in Subsection 6.2.1.1, $T_{w\_rated}$ is obtained at rated conditions using rated head and rated flow as the bases. The application of the nonlinear model for simulation analysis will be beneficial as it allows one data base to denote the dynamic models for the system independent of dispatch. This is true if there are no common flow paths for more than one unit at the plant, for example a shared penstock. This is not the case for a linearised model where different values of $T_w$ are required as the dispatch of the hydro units is varied in the initial state load flows [3].

### 6.2.2 Hydraulic Governor Model

The fundamental function of a governor is to control the speed and/or load through the feedback signal of the speed error and/or power variation to control the gate position, which regulates the water flow through the penstock [2]. This is to ensure the active power balance in the system as well as to maintain grid frequency within nominal value under electrical load variations.

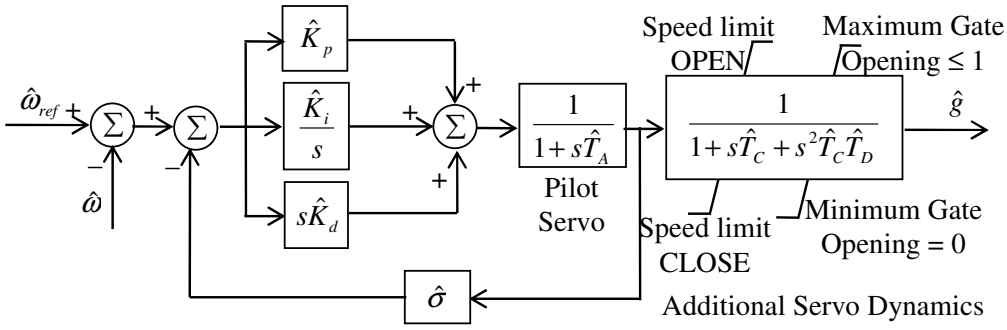


Figure 6.3: PID governor system

An electrohydraulic governor provided with PIDcontrollers is shown in Figure 6.3. The speed deviation is processed by the PID terms into a command signal to a series of hydraulic valves and servos to produce a change in throttle valve or gate position of the prime mover. The time constants $T_A$, $T_C$, $T_D$ of these hydraulic actuators are established by the pressure/flow characteristics of the gate and its servos, where, $T_A$ = pilot servomotor time constant [sec], $T_C$ = gate servo gain [sec] and $T_D$ = gate servomotor time constant [sec].

. However, the servomotor time constants have been neglected in deriving the governor response as their effects are substantial only if their poles occur before or near crossover frequency [1]. For security reasons, the speed of the gate stroke is restricted; it is represented by a simple rate-limit, which is sufficient for analysis. The gate opening is limited before it reaches its physical limits. Speed sensing, permanent droop, other measuring and computing operations are performed electrically. The electrical components provide better flexibility and enhanced execution with regard to dead bands and time lags [2]. The proportional term generates an instantaneous response to a speed error input, and it has a significant impact

on the system stability. The integral term performs together with the proportional term to determine the stability. Its ability to reduce the speed error to a zero value is known as "reset". The derivative term allows the expansion of the stability limits with larger values of proportional and integral gains whilst retaining the system stability [6].

The occurrence of a power system fault, which is reflected in the frequency deviation ($\omega_{ref}$ - $\omega$), will result in compensation operated by the PID governor. The correction executed depends on the droop, the dynamic settings and the characteristics of the PID governor. The permanent droop determines the speed regulation under steady-state operating conditions. It is described as the percentage or per unit speed drop needed to drive the gate from minimum to maximum opening without varying the speed reference [1]. Given the turbine characteristics, PID gains act to give stable gate position control and follow command signals in increasing or decreasing power generation.

The PID governor is represented as follows [2]:

$$\frac{\hat{g}}{\hat{\omega}_{ref} - \hat{\omega}} = \frac{s^2\hat{K}_d + s\hat{K}_p + \hat{K}_i}{s^2\hat{\sigma}\hat{K}_d + s\left(\hat{\sigma}\hat{K}_p + 1\right) + \hat{\sigma}\hat{K}_i}. \tag{6.9}$$

where, $\omega_{ref}$ = reference/nominal speed, $K_d$ = derivative gain, $K_p$ = proportional gain, $K_i$ = integral gain and $\sigma$ = permanent speed droop.

With derivative gain excluded, it yields the PI governor, which is represented as:

$$\frac{\hat{g}}{\hat{\omega}_{ref} - \hat{\omega}} = \frac{s\hat{K}_p + \hat{K}_i}{s\left(\hat{\sigma}\hat{K}_p + 1\right) + \hat{\sigma}\hat{K}_i}. \tag{6.10}$$

Small signal analysis is considered in the studies. The perturbations applied to the system are not significant such that neither the limits of the gate position nor the maximum gate opening/closing rates are reached. Thus, the windup effects have not been accounted for in the equations.

### 6.2.3 Combined electrical system

The differential equation of speed $\omega$ is derived and solved utilising water acceleration of the turbine and governor response described in Subsections 6.2.1 and 6.2.2 respectively, together with the swing equation depicting the machine acceleration expressed as $\frac{d\omega}{dt} = \frac{P_m - P_e - D\omega}{T_m}$ [2], $P_e$ = electrical power. This equation is used to determine the network system stability.

The differential equation is now transformed in Laplace space as

$$0.5\frac{\hat{\sigma}\hat{K}_d}{\hat{T}_w}s^4\hat{\omega} + \left(\frac{\hat{\sigma}\hat{K}_d}{\hat{T}_w} + 0.5\frac{\hat{K}_d\hat{D}\hat{\sigma}}{\hat{T}_m} + 0.5 + 0.5\hat{K}_p\hat{\sigma} - \frac{\hat{K}_d}{\hat{T}_m}\right)s^3\hat{\omega} + \left(\frac{\hat{D}\hat{\sigma}\hat{K}_d}{\hat{T}_m} + 1 + \hat{K}_p\hat{\sigma} + 0.5\frac{\hat{D}\hat{T}_w}{\hat{T}_m} + 0.5\frac{\hat{K}_p\hat{T}_w\hat{D}\hat{\sigma}}{\hat{T}_m} + 0.5\frac{\hat{K}_p\hat{K}_i\hat{\sigma}\hat{T}_m}{\hat{T}_w} + \frac{\hat{K}_d}{\hat{T}_m} - \frac{\hat{K}_p\hat{T}_w}{\hat{T}_m}\right)s^2\hat{\omega} + \left(\frac{\hat{D}\hat{T}_w}{\hat{T}_m} + \frac{\hat{K}_p\hat{T}_w\hat{D}\hat{\sigma}}{\hat{T}_m} + \frac{\hat{K}_p\hat{K}_i\hat{\sigma}\hat{T}_m}{\hat{T}_w} + 0.5\hat{K}_p\hat{K}_i\hat{D}\hat{\sigma} + \frac{\hat{K}_p\hat{T}_w}{\hat{T}_m} - \hat{K}_p\hat{K}_i\right)s\hat{\omega} + \left(\hat{K}_p\hat{K}_i + \hat{K}_p\hat{K}_i\hat{D}\hat{\sigma}\right)\hat{\omega} = 0. \tag{6.11}$$

This has fourth-order representation in the form of $a_0s^4 + a_1s^3 + a_2s^2 + a_3s^1 + a_4 = 0$, and it yields the stability limit if $(a_1a_2 - a_0a_3)a_3 - a_{12}a_4 = 0$ by Routh-Hurwitz criterion. In control theory, the system is considered to be stable when all roots of the characteristic equation lie in the left half of the $s$-plane. Moreover, to ensure stability, all the coefficients of the polynomial need to have the same sign and must be nonzero [7].

## 6.3 Simulation Results

Isolated operation of the hydraulic system is used for the case studies. A hydraulic turbine with water starting time, $T_w = 2$ sec, and mechanical starting time, $T_m = 8$ sec, is considered. A purely resistive electrical load with immediate voltage regulation is assumed with self-regulation $D = 0$. This is a worse case scenario as the power is independent of the speed and the inverse relationship between torque and speed makes it adverse for system stability. MATLAB/Simulink is used as a software tool for simulation studies.

The unit impulse involved in the hydraulic turbine-governor transfer functions has the

value of infinity at $t = 0$ and zero for all other times. However, this does not appear in physical systems. In reality, there is a very high finite value for a short period of time. Hydro turbines typically have initial inverse response characteristics of power to gate changes. They require provision of transient droop features in the speed controls for stable control operation, i.e., the governor should exhibit high regulation (low gain) for rapid changes in the frequency and vice versa [1]. Thus, the impulse functions involved in the turbine-governor equations are the natural response of the hydraulic system and the existing system transients. Practical systems are normally operating under steady-state condition with an operating point. If any fault occurs, the system will be perturbed with reference to this operating point.

From a simulation perspective, the system will be initialised to avoid any unexpected response or instability due to the impulse functions as well as to restore the system operating conditions to a steady state level. These initial transients last for a short time only and are usually ignored as they do not represent the true behaviour of the system. Also, any inherently unstable responses and transients in the dynamic systems will be damped out by the amortisseurs winding of the machine rotors and the interconnected system. The huge inertia of the machine aids in the damping process as well.

Figure 6.4 shows the stability limit curves of the hydraulic system where a classical turbine model is utilised. For governor settings bounded within the stability limit curve, a stable system will result. Governor settings on the stability limit will result in an undamped oscillatory response. It is observed that the inclusion of the derivative gain $K_d$ extends the stability boundary. With $K_d = 0.5$, the governor settings with $K_p = 3.0$ and $K_i = 0.7$ result in a stable response. Instability will result if the derivative gain is neglected.

Figure 6.5 shows the frequency response loci of different linearised hydraulic turbine-penstock models. The response for the classical model differs significantly from the linearised models operating at full load and no load for all frequency ranges. The linearised models agree well at fairly low frequencies. At a frequency of 0.3 rad/sec, the linearised models operating at no load and full load share similar characteristics. However, their characteristics

differ substantially with that of the classical model due to the fact that the water column effect is not considered in the classical model.

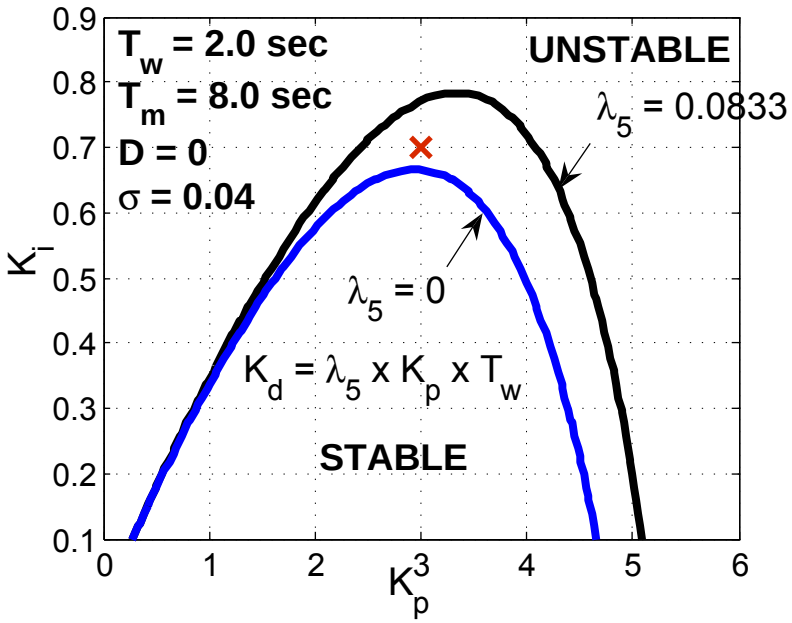


Figure 6.4: Stability limit of the hydraulic governor system

Figure 6.6 shows the eigenvalues for the closed-loop hydraulic governor-turbine systems. The oscillatory mode represented by a pair of complex conjugate eigenvalues is of primary interest, as the real part of the eigenvalues is the amount of the associated damping, whilst the imaginary part measures the frequency of oscillations. The classical hydraulic system with $K_d$ neglected is unstable as a pair of the eigenvalues crosses over the stability limit. However, with the consideration of a detailed turbine model, both systems (with or without $K_d$) become stable. These results are verified by the frequency deviation time responses as shown in Figures 6.7 and 6.8, when a small amount of load is applied at time, $t =$ 2 sec. An oscillatory but stable response for the classical turbine governed by the PID controller is observed in Figure 6.7. With a detailed turbine model, the responses reach steady-state faster with less oscillation, and the deviations resulting are smaller as well. This comprehensive model incorporates the general dynamic characteristics of a hydraulic turbine with due consideration of the penstock, unrestricted head and tail race effects, and

is suitable for most power system analysis.

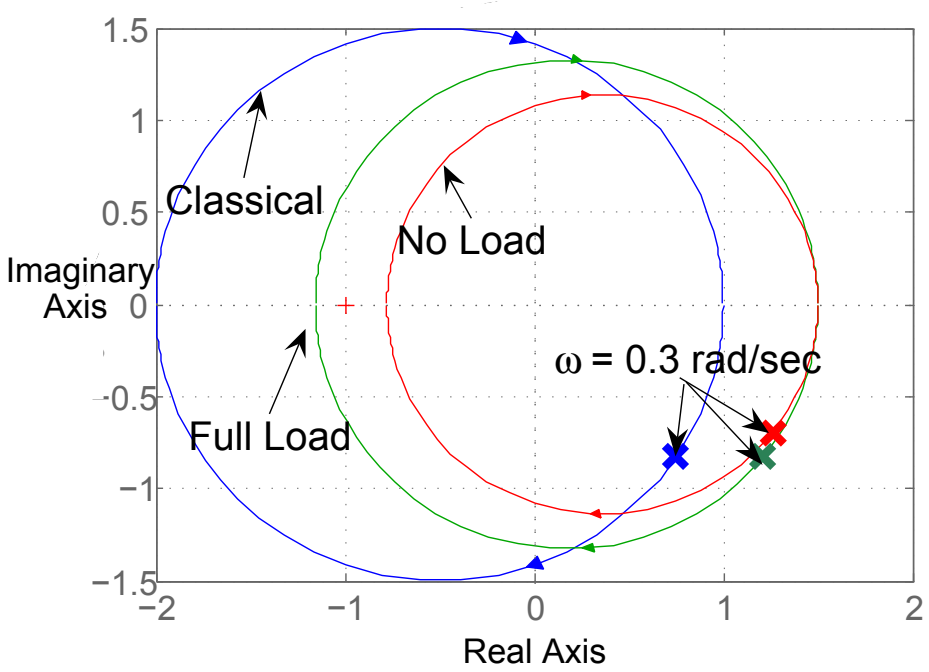


Figure 6.5: Frequency response loci of hydraulic turbine-penstock models

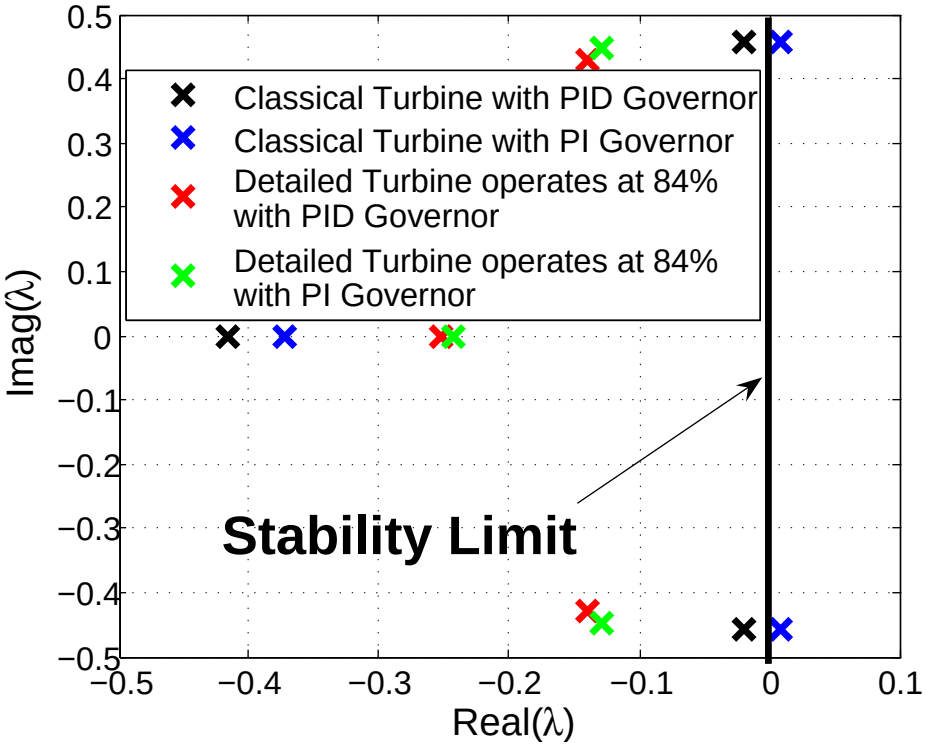


Figure 6.6: Eigenvalues trace for hydraulic system

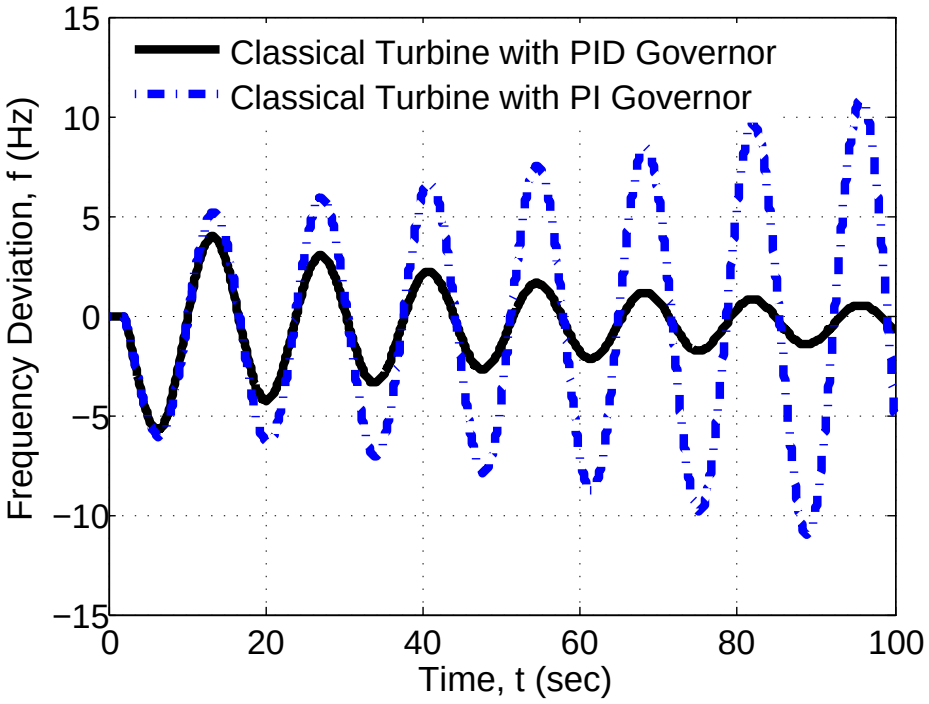


Figure 6.7: Frequency deviation time responses

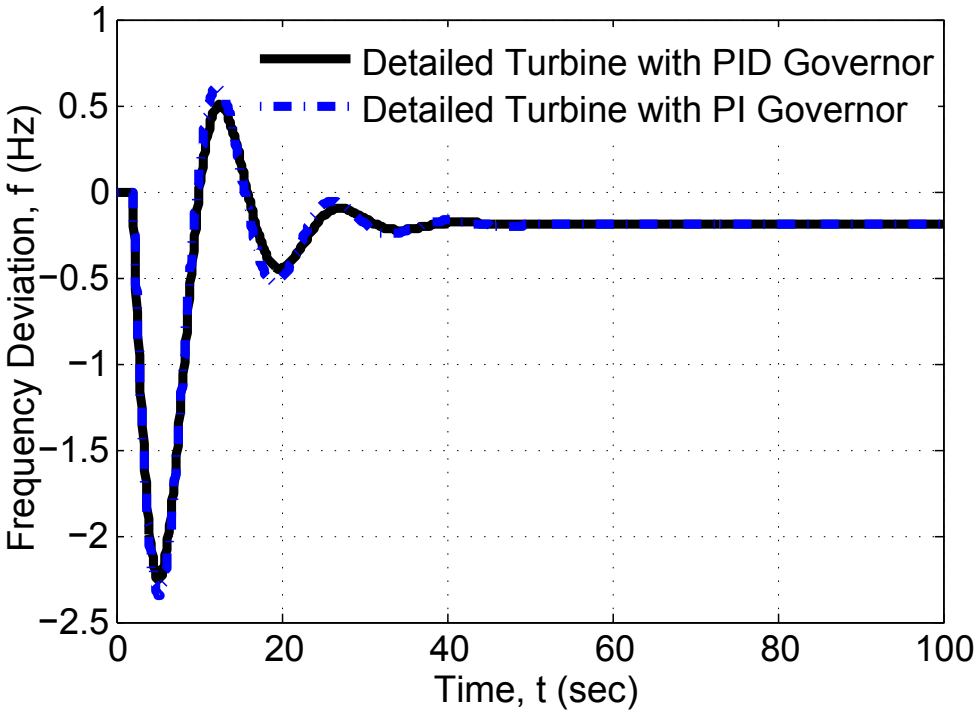


Figure 6.8: Frequency deviation time responses

## 6.4 Summary

In this chapter, the time domain analyses of the governing system subject to load disturbances are verified by frequency response methods as well as with the stability limit curves of the hydraulic system. It is concluded that the detailed modelling of power system components is vital to capture essential system dynamic behaviour. Also, it is observed that the PID and PI governors perform better when applied to a more realistic model. Furthermore, the inclusion of the derivative action in the governor aids in extending the system stability limit.

## References


[1] "Hydraulic turbine and turbine control models for system dynamic studies," *IEEE Trans. Power Syst.*, Vol. 7, no. 1, pp. 167-179, Feb 1992.

[2] P. Kundur. *Power System Stability and Control.* McGraw-Hill, 1994.

[3] L. N. Hannett, J. W. Feltes and B. Fardanesh, "Field tests to validate hydro turbine-governor model structure and parameters," *IEEE Trans. Power Syst.*, Vol. 9, no. 4, pp. 1744-1751, November 1994.

[4] J. M. Undrill and J. L. Woodward, "Nonlinear Hydro Governing Model and Improved Calculation for Determining Temporary Droop," *IEEE Trans. Power App. Syst.*, Vol. PAS-86, no. 4, pp. 443-453, April 1967.

[5] D. H. Thorne and E. F. Hill, "Field Testing and Simulation of Hydraulic Turbine Governor Performance," *IEEE Trans. Power App. Syst.*, Vol. PAS-93, no. 4, pp. 1183-1191, July 1974.

[6] "IEEE Guide for the Application of Turbine Governing Systems for Hydroelectric Generating Units," *IEEE Std 1207-2004*, pp. 1-121, 2004.

[7] R. C. Dorf, R. H. Bishop. *Modern Control Systems.* 10th ed., Pearson Education, Inc., 2005.

# Chapter 7

# Subsynchronous Torsional Behaviour of a Hydraulic Turbine-Generator Unit Connected to an HVDC System


### Abstract

Torsional interaction is an important phenomenon of concern when a turbine-generator (TG) unit is connected to a series compensated line or an high voltage direct current (HVDC) system. The subsynchronous torsional interaction (SSTI) may have significant impact on the hydraulic system due to the negative damping introduced by HVDC converter controls. This chapter investigates the SSTI behaviour of hydro TG units interconnected with an HVDC system for a varying generator-to-turbine inertia ratio. Case studies are carried out by changing the value of firing angle, applying a three-phase fault at the inverter bus and line switching at the rectifier ac system.

## 7.1 Introduction

The torsional interaction behaviour of the steam TG units have been reported in the literature, such as the shaft failures at the Mohave Generating Station (in Southern Nevada, USA) [1] and Square Butte (in North Dakota, USA) [2]. These SSTI are significant on steam units where significant level of analysis has been carried out. However, little information exists with regard to hydro systems.

The torsional mode of a Kaplan-type hydraulic unit is normally 10 Hz or less, whilst the torsional frequency for a Francis or Pelton wheel type hydraulic unit is in the range between 10 and 24 Hz, with an average around 18 Hz [3]. When the complement frequency of the electrical resonance frequency, $f_{comp}$ (i.e. $f_0 - f_{er}$) is approximately equal to the mechanical torsional mode, $f_n$ of the TG unit, while there is insufficient damping in the combined electro-mechanical systems, sustained shaft oscillations will appear.

A Kaplan type of hydraulic unit could possibly excite torsional interaction problem with HVDC as its torsional frequency is 10 Hz or less as reported in [3]. The HVDC converters contribute to the damping of the torsional oscillations of a TG unit depending on the frequency of oscillation. At low frequency, the converter provides negative damping. If the turbine modal damping $D_n$ is large enough to overcome the negative damping contributed by the converter, the torsional oscillations will be damped and subside to steady-state. The level and the frequency range of negative damping are dependent on the value of the firing angle and the dc power transfer [4].

In general, steam, gas and nuclear units are more susceptible to SSTI problem as they have multiple turbine masses and faster moving shafts which are more vulnerable to twisting compared to hydro units whose mechanical shafts are slow in motion and turbine-generator masses are large. Typically, the large inertia of the hydro generator provides inherent damping of torsional oscillations. However, this chapter aims to demonstrate that the hydro units with low generator-to-turbine inertia ratio $n$ would experience SSTI problem.

In this chapter, SSTI behaviour of a hydro TG unit (with varying generator-to-turbine

inertia ratio $n$) interconnected with an HVDC system is investigated. The time domain simulations are performed by changing the value of firing angle $\alpha$, applying three-phase fault at the inverter bus and incorporating line switching at the rectifier ac system.

## 7.2 Subsynchronous Torsional Interaction Phenomenon

Interactions between wide-bandwidth power controllers, such as HVDC converters, static var compensator (SVC) systems, power system stabilisers, and TGs has resulted in an acknowledgement of an extensive range of TG torsional interactions that are categorised as subsynchronous oscillations [5, 6].

Subsynchronous oscillation has been defined by the IEEE Subsynchronous Resonance Working Group as an electric power system condition where the electric network exchanges significant energy with a TG at one or more of the natural frequencies of the integrated system below the system synchronous frequency following a disturbance from equilibrium [5, 6].

The TG torsional oscillations cause the modulation of both the amplitude and phase of the rectifier side AC voltage for an HVDC system. The modulated voltage subsequently induces a voltage on the dc system commutating bus. With the commonly used equidistant firing angle control in modern HVDC system, a shift in voltage phase results in an equal shift in the firing angle. The variations in direct voltage, current and power will be resulted as a consequence of this firing angle modulation, as well as the alternating voltage amplitude modulation. The closed-loop current controller acts to rectify these differences. This is revealed as a change in generator electrical torque, resulting from the correction on the differences in direct voltage, current and power. If the phase lag between the change in shaft speed at torsional frequency, and the resulting change in electrical torque of the generator exceeds 90°, the torsional oscillations become unstable [7].

## 7.3 Modelling of Hydraulic System with an HVDC Link

The modelling of the system network includes the detailed representation of synchronous generator, exciter, hydraulic turbine-governor and torsional shaft system. The time domain simulations of an integrated system are investigated to study the SSTI behaviour of a hydraulic TG unit in the vicinity of an HVDC system.

### 7.3.1 Modelling of HVDC System

To represent the HVDC systems for power-flow and stability analyses, the following assumptions are made [7, 8]:

- The direct current $I_d$ is ripple-free.
- The ac systems at both the rectifier and the inverter compose of purely sinusoidal, constant frequency and balanced voltage sources behind balanced impedances.
- The converter transformers do not saturate.

The dynamic representation of the HVDC system as shown in Fig. 7.1 is developed as follows:

$$\dot{I}_{dr} = \frac{1}{L_d}\left(V_{dr} - R_d I_{dr} - V_{dm}\right) \tag{7.1}$$

$$\dot{I}_{di} = \frac{1}{L_d}\left(V_{dm} - R_d I_{di} - V_{di}\right) \tag{7.2}$$

$$\dot{V}_{dm} = \frac{1}{C_d}\left(I_{dr} - I_{di}\right) \tag{7.3}$$

$$V_{dr} = V_{d0r} cos\alpha - \frac{3}{\pi} X_{cr} B_r I_{dr} \tag{7.4}$$

$$V_{d0r} = \frac{3\sqrt{2}}{\pi} B_r T_r E_{acr} \tag{7.5}$$

$$V_{di} = V_{d0i}cos\gamma - \frac{3}{\pi}X_{ci}B_iI_{di} \tag{7.6}$$

$$V_{d0i} = \frac{3\sqrt{2}}{\pi}B_iT_iE_{aci} \tag{7.7}$$

where, $I_d$ is the direct current, $V_d$ is the DC voltage, $V_{dm}$ is the DC voltage on the dc line, $R_d$, $L_d$ and $C_d$ are the dc line resistance, inductance and capacitance respectively, $\alpha$ is the rectifier ignition delay angle, $\gamma$ is the inverter extinction advance angle, $R_c$ and $X_c$ are the equivalent commutating resistance and reactance respectively, $B$ is the number of bridges in series, $T$ is the transformer ratio, $E_{ac}$ is the AC line-to-line voltages, the subscripts $r$ and $i$ represent rectifier and inverter respectively, and subscript 0 denotes the initial operating condition.

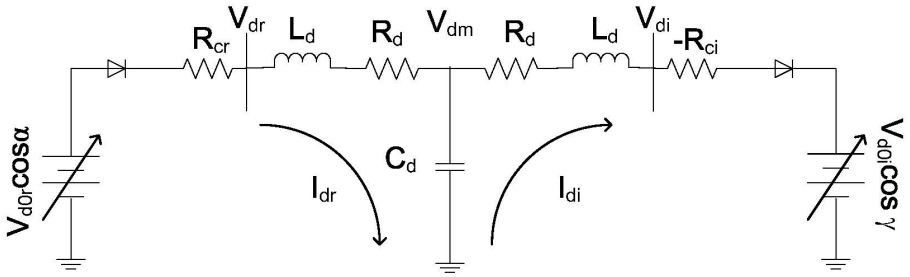


Figure 7.1: HVDC T-model transmission line

The rectifier subsystem of the HVDC system is operated in constant current (CC) control mode and the inverter subsystem is operated in constant extinction angle (CEA) control mode. The CC control of the rectifier will be modelled as a PI controller as shown in Fig. 7.2.

$$\alpha = \left(K_p + \frac{K_i}{s}\right)(I_{ord} - I_{dr}) \tag{7.8}$$

where $K_p$ = proportional gain, $K_i$ = integral gain, $I_{ord}$ = current order.

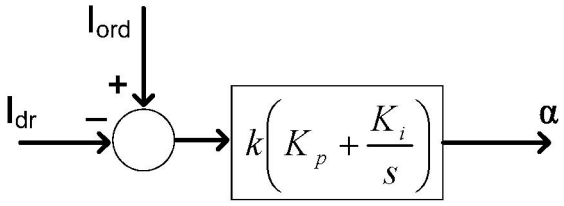


Figure 7.2: Constant current control of the rectifier

### 7.3.2 Modelling of AC Network

This subsection describes the modelling of a hydro unit together with its exciter, turbine-governor, and the torsional shaft model. The eigenvalue analysis is employed to determine the torsional frequency $f_n$ of the hydro unit.

#### 7.3.2.1 Hydraulic TG Unit

The salient pole synchronous machine model used in the analysis is the two-axis model. The IEEE alternator supplied rectifier excitation system (AC1A), the mechanical-hydraulic governor and a non-elastic water column turbine without surge tank are selected PSCAD library for developing the PSCAD model.

#### 7.3.2.2 Torsional Shaft Model

The linearised model of the hydraulic TG shaft system is represented based on a mass-spring-damping model as follows [7]:

$$\Delta\dot{\omega}_{gen} = -\frac{1}{2H_{gen}}\Delta P_e + \frac{D_{tg}}{2H_{gen}}\Delta\omega_{tur} + \frac{K_{tg}}{2H_{gen}}\Delta\delta_{tur} - \frac{D_{gen}+D_{tg}}{2H_{gen}}\Delta\omega_{gen} - \frac{K_{tg}}{2H_{gen}}\Delta\delta_{gen} \tag{7.9}$$

$$\Delta\dot{\omega}_{tur} = \frac{1}{2H_{tur}}\Delta P_m - \frac{D_{tur}+D_{tg}}{2H_{tur}}\Delta\omega_{tur} + \frac{D_{tg}}{2H_{tur}}\Delta\omega_{gen} - \frac{K_{tg}}{2H_{tur}}\Delta\delta_{tur} + \frac{K_{tg}}{2H_{tur}}\Delta\delta_{gen} \tag{7.10}$$

where, $\omega$ is the rotor speed, $H$ is the inertia constant, $D$ is the damping coefficient, $D_{tg}$ and $K_{tg}$ are the damping coefficient and spring constant between the turbine and the generator,

$\delta$ is the rotor angle, $P_m$ and $P_e$ are the mechanical and electrical powers respectively. Subscripts '*gen*' and '*tur*' represent generator and turbine respectively.

#### 7.3.2.3 Combined Network System

The combined ac system represented in a small-signal state-space model has the following expression:

$$\Delta\dot{x} = \left[A_{sys}\right]\Delta x + \left[B_{sys}\right]\Delta u \tag{7.11}$$

where, the ac system state variables are

$$\Delta x = [\Delta\omega_{gen}\ \Delta\delta_{gen}\ \Delta\psi_{fd}\ \Delta\psi_{1d}\ \Delta\psi_{2q}\ \Delta v_1 \Delta v_{cont}\ \Delta E_{fd}\ \Delta g\ \Delta T_m\ \Delta\omega_{tur}\ \Delta\delta_{tur}]^T \tag{7.12}$$

### 7.3.3 Interaction between AC/DC Systems

The SSTI behaviour of the hydraulic TG unit is analysed in conjunction with CIGRE first HVDC benchmark model.

The interaction equations, which describe the relationship between AC and DC systems, are as follows:

$$I_{acr} = \frac{\sqrt{6}}{\pi} I_{dr} B_r T_r \tag{7.13}$$

$$cos\phi_r \approx cos\alpha - \frac{X_{cr} I_d}{\sqrt{2} T_r E_{acr}} \tag{7.14}$$

where, $I_{ac}$ = the AC line current flowing through the converter transformer and $cos\phi$ = phase angle between fundamental line current and the line-to-neutral source voltage.

## 7.4 Analytical Methodologies

Torsional instability is normally caused by the control paths such as the supplementary damping control and the rectifier current control [7]. If the torsional frequency of the generator unit is low enough and lie within the negative damping frequency range of a normal HVDC operation, then there is a possibility for the unit to interact with the HVDC converter

controls and result in instability. Thus, it is important to have analytical methodologies for the different aspects of the SSTI problem.

### 7.4.1 Methods for SSTI Analysis

#### 7.4.1.1 Screening Tool

The Unit Interaction Factor (UIF) has been used widely as a screening tool to measure the influence of dc system controls on torsional stability. It computes the impact of the fast acting control loops of a dc system on torsional damping of a generator. This factor is expressed as follows [9, 10]:

$$UIF = \frac{MVA_{HVDC}}{MVA_{Gen}} \left(1 - \frac{SC_{Gout}}{SC_{Gin}}\right)^2 \tag{7.15}$$

where, $MVA_{HVDC}$ and $MVA_{gen}$ are the ratings of the HVDC system and the generator respectively, $SC_{Gin}$ and $SC_{Gout}$ are the short circuit capacities at the HVDC commutating bus with and without the generator respectively. The $MVA_{HVDC}/MVA_{Gen}$ ratio identifies the relative size of the HVDC system and the generator, while the term $(1 - SC_{Gout}/SC_{Gin})^2$ establishes the electrical coupling between the HVDC system and the generator [9].

This method identifies whether detailed studies are required; if UIF is 0.1 or greater, the system needs further investigation.

#### 7.4.1.2 Time Domain Analysis

PSCAD®/ EMTDC© is used as the tool for time domain analysis. It allows detailed representation of the integrated AC-DC system network. This analysis is useful for analysing the transient shaft torque oscillations due to SSTI.

### 7.4.2 Mitigation Methods

To overcome the SSTI problem in the vicinity of an HVDC system, a subsynchronous damping controller (SSDC) is normally included at a rectifier station to provide an additional

damping. However, this is not a subject matter of this chapter and hence, it will not be discussed herein.

## 7.5 Simulation Results

A hydraulic TG unit connected to an HVDC system shown in Fig. 7.3 is used as the study system for SSTI analysis. This study system consists of a 500 kV, 1000 MW monopolar DC link and a 1210 MVA hydraulic system, which represents the aggregated model of multiple hydro units. The HVDC system is represented by the CIGRE first HVDC benchmark model [11]. It is considered to operate at normal operation, i.e. the rectifier operates at CC control mode whilst the inverter operates at CEA control mode. The sensitivity of different factors such as the value of the firing angle $\alpha$ and the dc power transfer $P_{HVDC}$, for the possible initiation of SSTI problem, are investigated. Some of the specific case studies such as three-phase fault at the inverter commutating bus and line switching at the rectifier ac system are examined as well. The time domain simulations are conducted using PSCAD®/ EMTDC©.

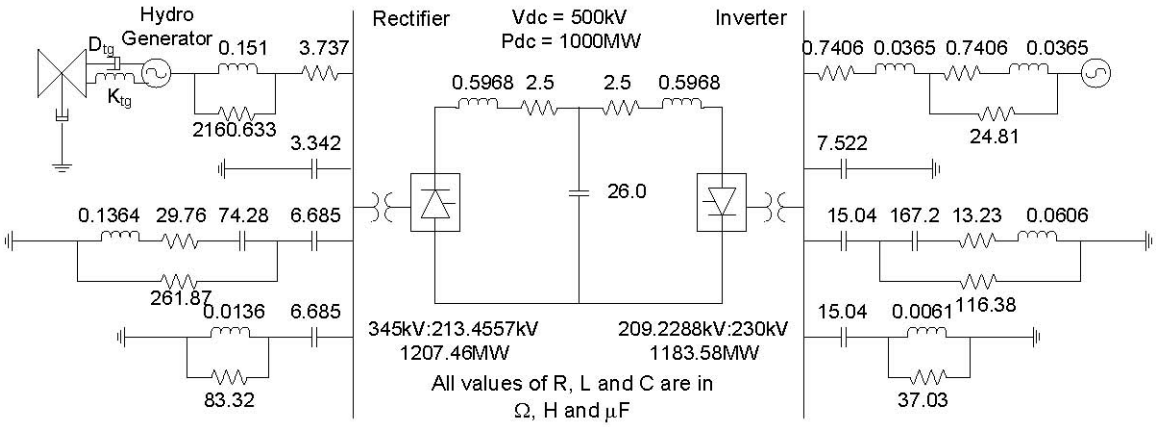


Figure 7.3: A hydro turbine-generator unit interconnected to CIGRE first HVDC benchmark model

### 7.5.1 Frequency Modulation and Eigenvalue Analysis

A preliminary study is carried out for a hydraulic TG unit interconnected with a constant voltage source with frequency modulation. The SSTI phenomenon is investigated for a lower frequency modulation band of 49 Hz $\geq f_m \geq$ 0.01 Hz, leading to a superimposed frequency range of 1 Hz $\leq f_i \leq$ 49.99Hz.

Fig. 7.4 shows the torsional torque deviation of a hydraulic TG unit with different generator-to-turbine inertia ratio $n$ for a superimposed frequency of 4 Hz $\leq f_i \leq$ 6 Hz. The inset shows the torsional torque deviation plot for frequency modulation in the range of 0 Hz $\leq f_i \leq$ 50 Hz. It is observed that the peak deviation occurs at a superimposed frequency $f_i$ of 5.4 Hz. This indicates that the system could possibly excite the torsional interaction when the complement of the system network resonance frequency $f_{comp}$ coincides with the torsional mechanical frequency $f_n$. The torsional mechanical frequency $f_n$ for a hydraulic system can be evaluated using eigenvalue analysis. A linearised model of the hydraulic system, including the salient pole synchronous machine, governor, turbine, exciter and the shaft model, has been developed. The eigenvalue analysis is used to determine the mechanical torsional modes with the inertia of each mass and the spring constant provided. The hydraulic units with lower inertia ratio $n$ indicate larger torsional torque deviation over a wide frequency range of interest.

Fig. 7.5 shows part of the eigenvalues for a hydraulic system. The pair of eigenvalues $\lambda =$ -0.04$\pm$ j33.95 has an oscillation frequency of 5.4034 Hz with a damping ratio of 0.0012; they are identified as the torsional modes. Another pair of eigenvalues $\lambda =$ -0.84$\pm$ j7.72 has an oscillation frequency of 1.2292 Hz with a damping ratio of 0.1075 and they are identified as local modes. The torsional modes appear to be the critical modes. The torsional frequency $f_n$ shows a strong agreement with the results obtained from the time domain analysis.

### 7.5.2 A Hydro Unit Interconnected with CIGRE first HVDC Benchmark Model

The preliminary study carried out in Section 7.5.1 has highlighted the possibility of torsional torque oscillation at the torsional frequency $f_n$ of the hydro unit (especially for hydro units

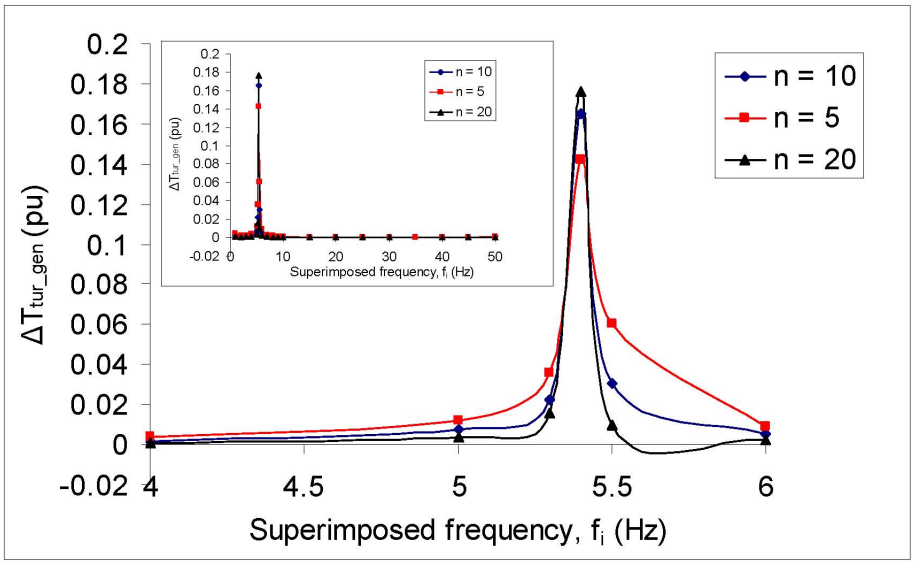


Figure 7.4: Torsional torque deviation of hydraulic turbine-generator unit with different generator-to-turbine inertia $n$ for a frequency range of interest

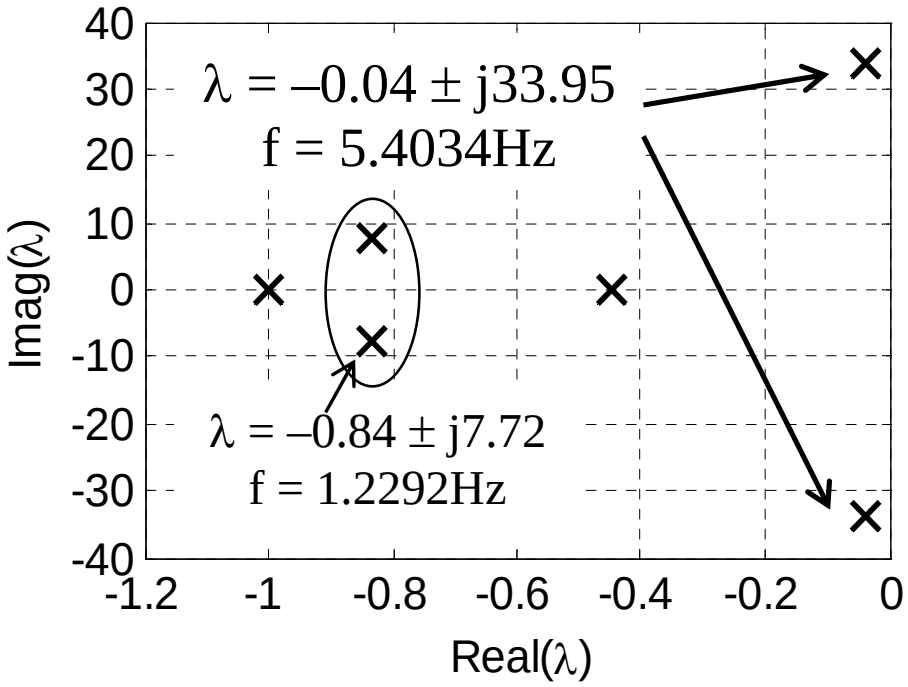


Figure 7.5: System eigenvalues of the ac system

with low $n$). The following case studies will demonstrate the SSTI behaviour of the hydraulic TG unit interconnected with the CIGRE first HVDC benchmark model shown in Fig. 7.3. The system is subjected to various disturbances such as change in firing angle $\alpha$ and dc power transfer $P_{HVDC}$, three-phase fault at the inverter bus and line switching at the rectifier bus.

#### 7.5.2.1 Effect of changing firing angle $\alpha$ and dc power transfer, $P_{HVDC}$

The fast acting control loops of HVDC converter station can result in SSTI. This phenomenon typically get initiated from control interactions [9]. Such fast response of the control loops can be simulated by changing the firing angle $\alpha$ or changing the dc power transfer $P_{HVDC}$. The response of $\alpha$ and $P_{HVDC}$ are closely-related, as $P_{HVDC} = V_d I_d$, where $V_d$ is function of $\alpha$ as indicated in (7.4).

Fig. 7.6 shows the TG torque and system frequency responses of the hydro units (with different $n$) for an increment of firing angle $\alpha$ from 21.25° to 24.375° at $t = 5$ sec. The corresponding change in DC power flow $P_{HVDC}$ is shown in Fig. 7.7. It is observed that the sustained TG torque oscillations are excited on the hydro units with the fast acting converter controller operation. The SSTI phenomenon is more pronounced for a hydro unit with a low value of $n$. This is due to the decrement of the modal damping at the torsional frequency $f_n$. The modal damping $D_n$ is represented as $D_n = n^2 D_{tur} + D_{tg}(1-1/n)^2$ [3] where $D_{tur}$ is the turbine damping coefficient and $D_{tg}$ is the damping coefficient between the turbine and the generator. The low value of $n$ subsequently reduces the modal decrement factor $\sigma_n$ and the log decrement $\delta_n$. Both $\sigma_n$ and $\delta_n$ are represented as $\sigma_n = \left[nD_{tur} + D_{tg}(1-1/n)^2\right]/4H$ and $\delta_n = \sigma_n/f_n$ [3]. System frequency is affected relatively when SSTI is resulted in. A supplementary control in terms of SSDC could provide an additional damping to overcome such SSTI problem.

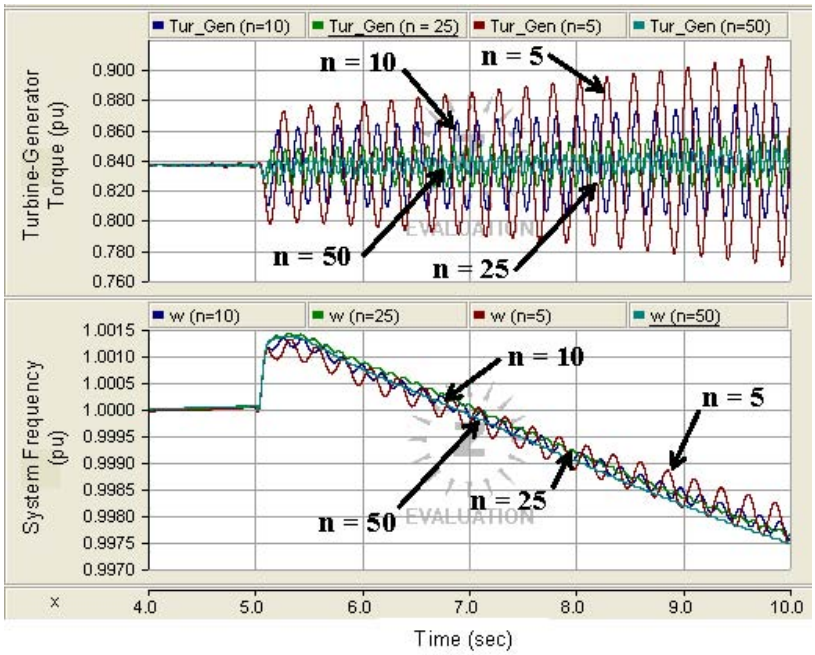


Figure 7.6: Turbine-generator torque and system frequency responses subject to the change in alpha ($\alpha$)

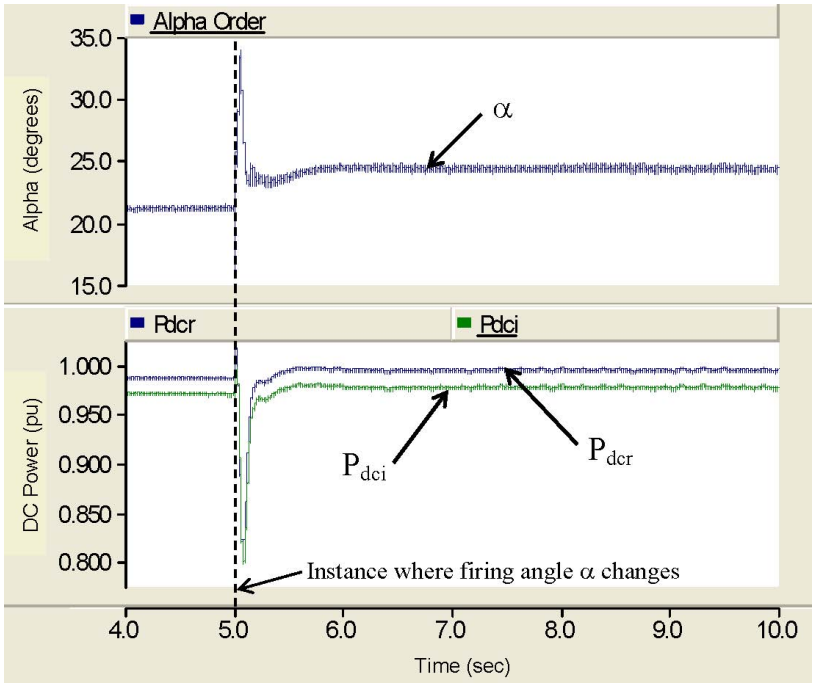


Figure 7.7: Firing angle and power transferred in dc link subject to the change in alpha ($\alpha$)s

#### 7.5.2.2 Three-phase fault at the inverter bus

A generator encounters a large number of switching operations throughout its lifetime, and such disturbances can excite undesired high levels of oscillatory shaft torques. The switching operations include line switching, system faults, fault clearance, etc. The cumulative shaft torsional stresses experienced by the unit may result in loss of fatigue life [7, 12].

Typically, three-phase faults can jeopardise the system stability, as well as the TG condition to a great extent. A five-cycle three-phase fault is applied on the inverter bus at $t = 5$ sec and the effect on the shaft system is analysed.

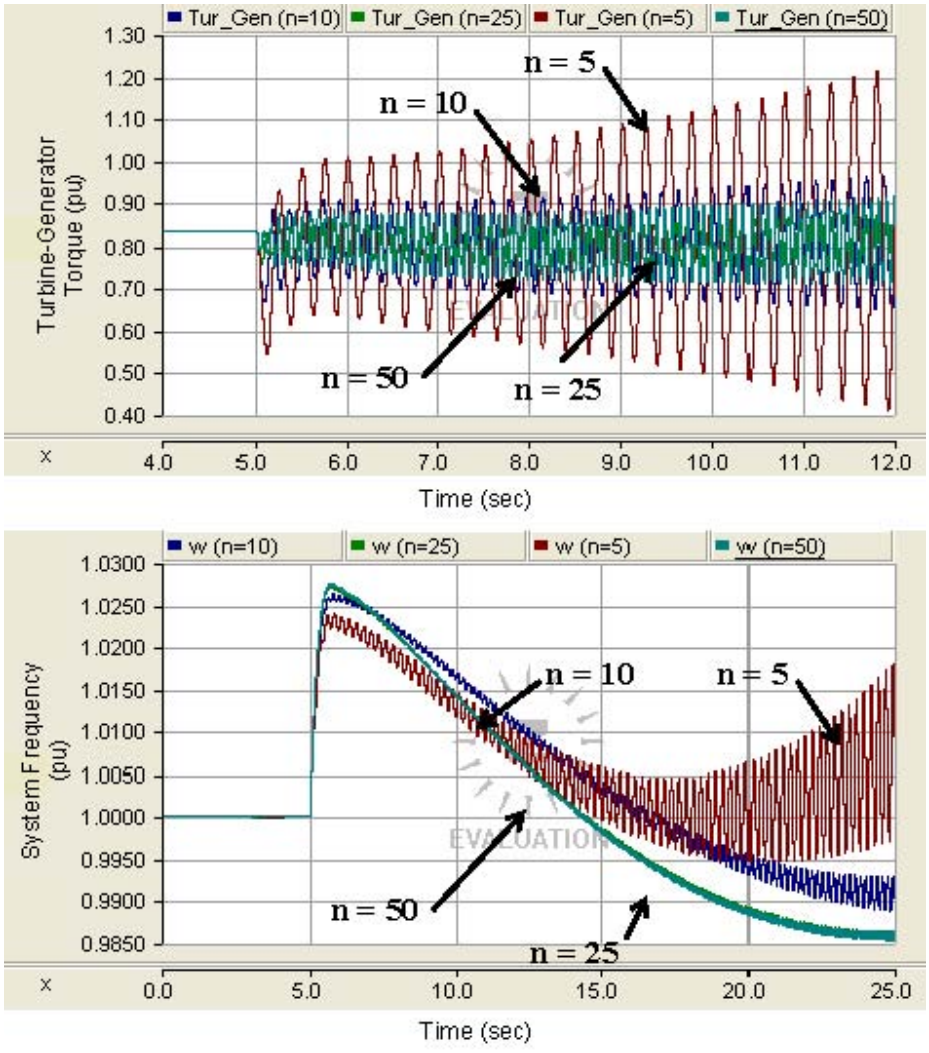


Figure 7.8: Turbine-generator torque and system frequency responses subject to 3 phase fault at inverter bus

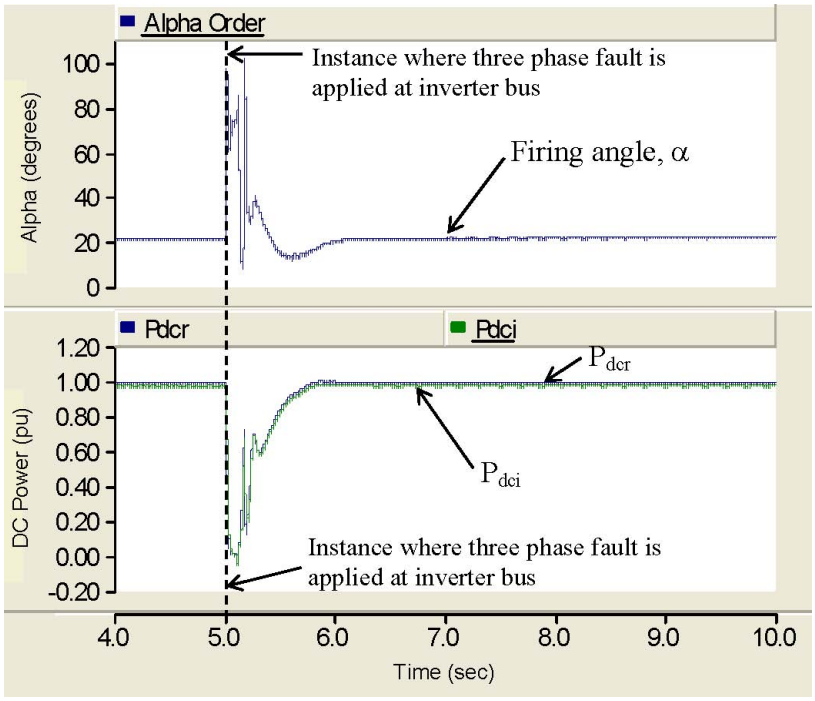


Figure 7.9: Firing angle and power transferred in dc link subject to 3 phase fault at inverter bus

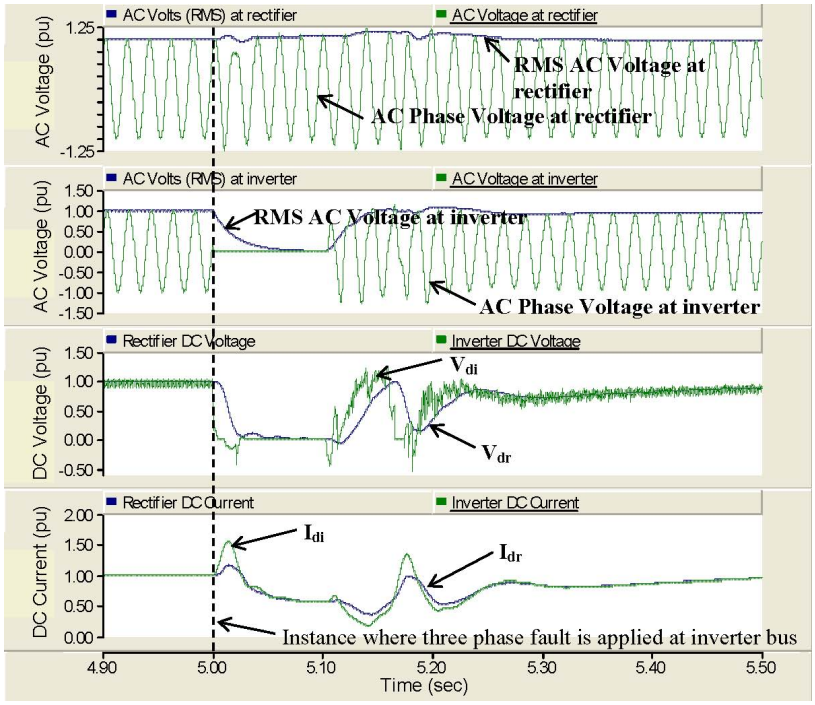


Figure 7.10: System responses subject to 3 phase fault at inverter bus

Figs. 7.8, 7.9 and 7.10 show the system response for a three-phase fault on the inverter bus. The torsional torque response shown in Fig. 7.8 demonstrates the likelihood of torsional oscillations on a hydro unit, especially for a low $n$ value. The responses of firing angle $\alpha$ and dc power transfer $P_{HVDC}$ are depicted in Fig. 7.9. The changes in dc voltage $V_d$ and dc current $I_d$ are shown in Fig. 7.10. The system settles down to a nominal state after clearing the fault.

#### 7.5.2.3 Line switching

Line switching is performed by switching the ac breaker, which connects the hydro unit to the HVDC system, to stimulate the torsional modes of shaft vibration. This represents the case study for the loss of the HVDC link and its impact on the hydro TG unit is examined. The switching operation is applied at $t = 5$ sec (by momentarily opening the breaker) and the system is reconnected back after 0.05 sec.

Similar to the previous studies, large shaft torsional vibrations are experienced when the hydro unit is disconnected from the HVDC link, especially on the small hydro unit as seen in Fig. 7.11. It is also observed that the system frequency goes beyond $\pm$ 5 %.

As seen in Fig. 7.12, the rectifier side ac system voltage drops down to as low as 0.2 pu. Thus, adequate protection schemes should be in place to avoid such deteriorating response from line switching event. Consequently, the dc voltage $V_d$ and the dc current $I_d$ drop down to a very low value, and this also results in the momentary drop out of the dc power flow.

The impact of the loss of HVDC system on the nearby TG unit has been analysed in an elementary manner. To represent a more realistic situation, HVDC line faults can be applied by executing the dc line protection and temporarily blocking one of the poles.

## 7.6 Summary

The torsional interaction behaviour of a hydraulic TG unit interconnected to an HVDC system has been studied in this chapter. In general, steam, gas and nuclear units are more susceptible to SSTI problem as they have multiple turbine masses and faster moving shafts

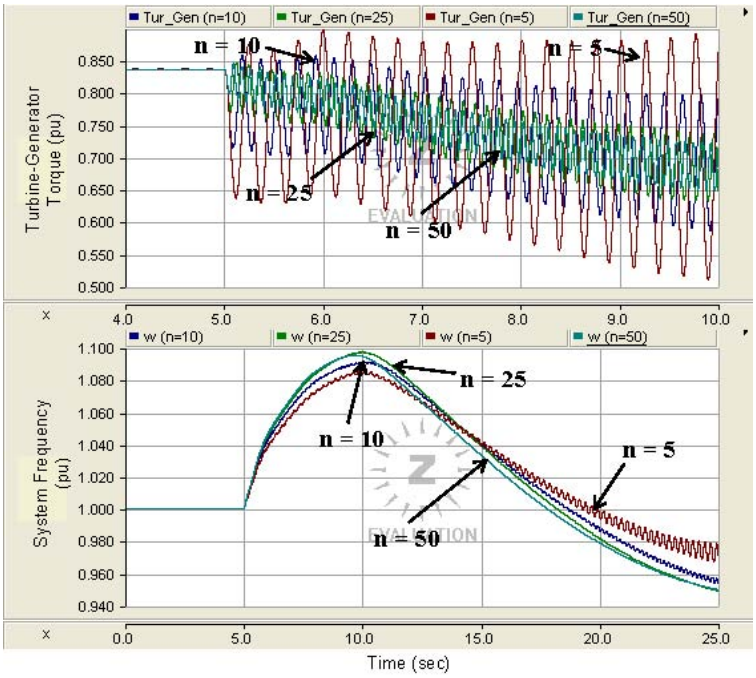


Figure 7.11: Turbine-generator torque and system frequency responses subject to line switching at rectifier side AC system

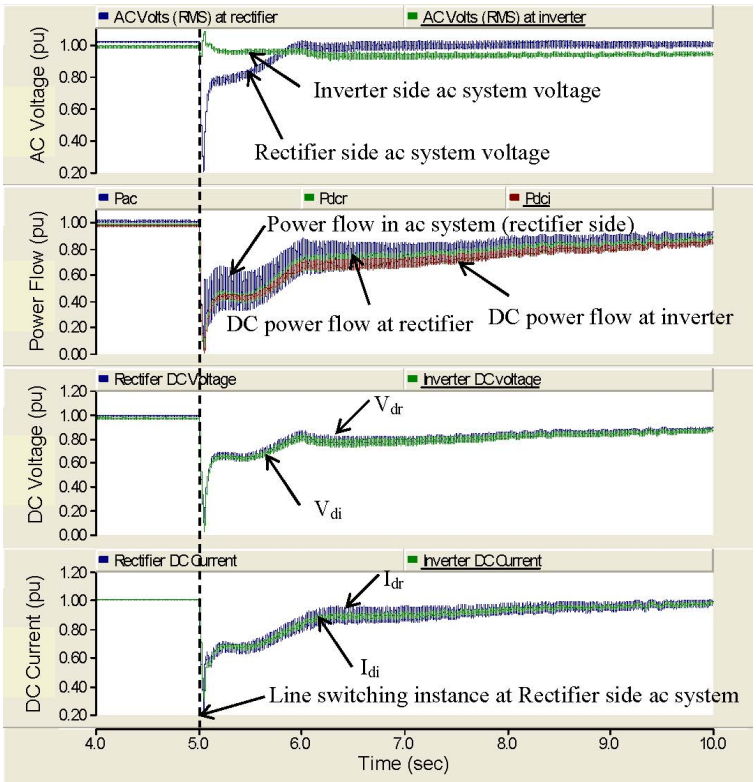


Figure 7.12: System responses subject to line switching at rectifier ac system

which are more vulnerable to twisting compared to hydro units whose mechanical shafts are slow in motion and turbine-generator masses are large. Typically, the large inertia of the hydro generator provides inherent damping of torsional oscillations. This chapter has demonstrated that the hydro units with a low generator-to-turbine inertia ratio $n$ have a potential to experience SSTI problem. This is due to the lack of damping at the torsional frequency $f_n$. The case studies have demonstrated the effects of change in firing angle $\alpha$, three-phase fault at the inverter commutating bus and line switching at the rectifier side ac system. The simulation results have revealed that the shaft vibration can be excited on a hydro unit, in conjunction with HVDC system.

## References


[1] R.G. Farmer, A.L. Schwalb, Eli Katz, "Navajo Project Report on Subsynchronous Resonance Analysis and Solutions," *IEEE Trans. Power App. Syst.*, Vol. PAS-96, no. 4, July/August 1977.

[2] M. Bahrman, E.V. Larsen, R.J. Piwko, H.S. Patel, "Experience with HVDC - Turbine-Generator Torsional Interaction at Square Butte," *IEEE Trans. Power App. Syst.*, Vol. PAS-99, No. 3, May/June 1980.

[3] G. Andersson, R. Atmuri, R. Rosenqvist, S. Torseng, "Influence of Hydro Units' Generator-to-Turbine Inertia Ratio on Damping of Subsynchronous Oscillations," *IEEE Trans. Power App. Syst.*, Vol. PAS-103, No. 8, August 1984.

[4] H. Bjorklund, K.E. Johansson, G. Liss, "Damping of Subsynchronous Oscillations in Systems containing Turbine Generators and HVDC Links," *Cigre* 14-01, 1980.

[5] IEEE Subsynchronous Resonance Working Group, "Proposed terms and definitions for subsynchronous oscillations," *IEEE Trans. Power App. Syst.*, Vol. PAS-99, No. 2, March/April 1980.

[6] IEEE Subsynchronous Resonance Working Group, "Terms, definitions and symbols for subsynchronous oscillations," *IEEE Trans. Power App. Syst.*, Vol. PAS-104, No. 6, June 1985.

[7] P. Kundur. *Power System Stability and Control.* McGraw-Hill, 1994.

[8] D.J. Kim, H.K. Nam and Y.H. Moon, "A Practical Approach to HVDC System Control for Damping Subsynchronous Oscillation Using the Novel Eigenvalue Analysis Program," *IEEE Trans. Power Syst.*, Vol. 22, No. 4, November 2007.

[9] *Torsional Interaction Between Electrical Network Phenomena and Turbine-Generator Shafts: Plant Vulnerability.* EPRI, Palo Alto, CA: 2006. 1013460.

[10] *Guide for Planning DC Links Terminating at AC Systems Locations Having Low Short-Circuit Capacities, Part I: AC/DC Interaction Phenomena*. CIGRE Working Group 14.07, June 1992.

[11] M. Szechtman, T. Wess, C.V. Thio, "First benchmark model for HVDC control studies," *Electra*, no. 135, pp. 54-73, Apr. 1991.

[12] J.S. Joyce, T. Kulig, D. Lambrecht, "Torsional Fatigue of Turbine-Generator Shafts Caused by Different Electrical System Faults and Switching Operations," *IEEE Trans. Power App. Syst.*, Vol. PAS-97, No. 5, Sept/Oct 1978.

# Chapter 8

# Dynamic Modelling of Hydroelectric Turbine-Generator Unit connected to an HVDC System for Small Signal Stability Analysis

**Abstract**

This chapter presents the linearised small-signal dynamic modelling of hydroelectric TG unit with CIGRE first HVDC benchmark system in the synchronously rotating $DQ$ reference frame for small-signal stability analysis. The interaction behaviour between the hydroelectric unit and the dynamics and control of HVDC system is investigated utilising eigen-analysis, participation factor analysis and by conducting sensitivity studies. The computation of eigenvalues and eigenvectors for small signal stability analysis provides an invaluable insight onto the power system dynamic behaviour by characterising the damping and frequency of the system oscillatory modes. The consequences of different operating con-

ditions, such as active and reactive power variations, the variation of generator-to-turbine inertia ratio, as well as the changes of HVDC constant current controller parameters on small-signal system stability are investigated.

## 8.1 Introduction

Since the 1920s, power system stability has been a vital aspect of secure system operation [1]. System stability is defined as the ability of a power system, for a given initial operating condition, to regain a state of operating equilibrium after being subjected to a disturbance [1, 2]. A system is said to be small signal stable if the power system is able to remain in synchronism under small disturbances. A disturbance is considered to be small if the linearisation of the equations that depict the corresponding response of the system is permitted for the purpose of analysis [2, 3].

The small signal stability issue generally occurs due to inadequate damping of power system oscillations [2]. The dynamic characteristics of the power system can be determined from small-signal analysis using linearisation approaches, and damping controllers can be designed based on the information provided on system oscillatory modes.

The formulation of the linearised small-signal state space model of the integrated AC-DC systems can be established by linearising each power system components individually, transforming input-output variables into common reference frames, and establishing interaction relationship between different power system components [4]. The developed linearised dynamic model is used to analyse the interaction behaviour between the hydroelectric unit and HVDC link by manipulating the operating conditions, generator-to-turbine inertia ratio and controller parameters; the consequences of such variations are depicted in the eigenvalue trajectories. Eigenvalue analysis is used to identify the stability modes and damping characteristics of the integrated system. The dominant modes will be used to identify system stability limit for different operating conditions, generator-to-turbine inertia ratio and HVDC constant current controller parameters.

For power system analysis, the electrical network is normally represented by means of

algebraic-equations in which inductances and capacitances are represented by their admittance at fundamental frequency. The dynamic representation of the electrical network based on linearised differential equations incorporated with linearised dynamic models of hydroelectric unit and HVDC system is applicable for the investigation of the high-frequency modes. The SSTI between turbine-generator torsional modes and the fast acting constant current controller of HVDC system may occur at high-frequency. The integrated linearised small-signal dynamic system developed in this chapter has included the dynamic representation of shaft model, which allows the investigation of SSTI phenomena.

The small signal stability analysis of HVDC and static var compensators with their controllers has been addressed in [5]. Three different modelling approaches for CIGRE first HVDC benchmark model, namely linear-continuous-detailed model, linear-continuous-simplified model and linear discrete system model have been presented in [6]. The development of a linear continuous time state model of the small-signal dynamics of an HVDC system using modularisation techniques is detailed in [4]. A parallel ac-dc power system has been represented with reference to a rotor rotating reference frame in [7] and the capabilities and limitation of the analog computer in providing solutions to electromechanical problems have been outlined in [8]. Linearised modelling of TG shaft dynamics and HVDC system has been presented in [9] and [10] for subsynchronous oscillation analysis.

The main purpose of this chapter is to present the modelling techniques, which depict the dynamic characteristics of hydroelectric TG unit and HVDC systems using linearised state space models. This allows the investigation of the small-signal stability aspects associated with the control interaction between the hydroelectric unit and the HVDC system at higher frequencies, using eigen-analysis. The chapter is structured as follows. Section 8.2 illustrates the analytical methodologies for small signal stability analysis. Section 8.3 describes the mathematical modelling of the hydroelectric unit and HVDC system, which includes detailed representation of governor, turbine, exciter, power system stabiliser (PSS), torsional shaft model, AC filter, electrical system, converter system and current controller. Section 8.4 elaborates the integrated study system involving hydroelectric power system

and CIGRE first HVDC benchmark model and simulation results are presented by applying small disturbances to the study system. The chapter is concluded in section 8.5.

## 8.2 Small-Signal Stability Analysis

This section elaborates the small signal stability analysis of a power system when subjected to small disturbances. Analytical methodologies used to determine the small signal stability are eigenanalysis, participation factors analysis and sensitivity analysis. Eigen properties such as damping ratio and oscillation frequency associated with system modes are revealed as well.

### 8.2.1 Eigenanalysis

The eigenvalues of the system are the values of $\lambda$ that fulfil the characteristic equation of system matrix $A_{sys}$:

$$det(\lambda I - A_{sys}) = 0 \tag{8.1}$$

The analysis of the eigen properties in matrix $A_{sys}$ reveals vital information on the system stability characteristics. A pair of eigenvalues is represented as $\lambda = \sigma \pm j\omega$, where its oscillation frequency and damping ratio are established as $f = \frac{\omega}{2\pi}$ and $\zeta = \frac{-\sigma}{\sqrt{\sigma^2+\omega^2}}$ respectively. System stability can be guaranteed if all the system eigenvalues lie onto left-half plane, i.e. $\mathrm{Re}(\lambda_i) < 0$ for all $i$ [2, 3].

### 8.2.2 Participation Factor Analysis

Participation matrix, which combines both left and right eigenvectors, is a non-dimensional scalar that measures the correlation between the state variables and the modes of a linear system. It implies the relative involvements of the respective states in the corresponding modes. This is described as [2, 3]:

$$P = [p_1,\ p_2\ \ldots\ p_n] \tag{8.2}$$

with $p_i = [p_{1i},\ p_{2i}\ \ldots p_{ni}]^T = [\phi_{1i}\psi_{i1},\ \phi_{2i}\psi_{i2}\ \ldots \phi_{ni}\psi_{in}]^T$ where, $\phi_{ki} = k^{th}$ entry of the right eigenvector $\phi_i$; and $\psi_{ik} = k^{th}$ entry of the left eigenvector $\psi_i$.

$\phi_{ki}$ evaluates the activity of the $k^{th}$ state variable in the $i^{th}$ mode, while $\psi_{ik}$ weighs the contribution of this activity to the mode [2].

## 8.3 Linearised State Space Models of Hydroelectric Turbine-Generator and HVDC Link

The formulation of the linearised state space model for the integrated system involves linearisation of each subsystem, transformation of input-output variables into common reference frames, and interconnection of the subsystems [4]. Similar techniques have been employed in this chapter for formulation of the system state equations. Integration of the subsystems can be carried out as the input-output of a subsystem can be the output-input of another subsystem. Note that the Park's components $f_{dq}$ and the Kron's components $f_{DQ}$ will be used conventionally throughout the chapter, where $f$ can be any variable. Subscripts $dq$ and $DQ$ are used to denote variables in rotor and synchronous reference frames, respectively.

### 8.3.1 Modelling of Hydroelectric Turbine-Generator

A three-phase salient pole synchronous machine, with its equivalent circuits of $dq$-axes as shown in Fig. 8.1, is modelled to represent the hydroelectric TG unit. The established linearised machine model has the following state-space representation:

$$\Delta\dot{x}_{hydro} = [A_{hydro}]\,\Delta x_{hydro} + [B_{hydro1}]\,\Delta E_{fd} + [B_{hydro2}]\,\Delta u_{hydro} \tag{8.3}$$

$$\Delta y_{hydro} = [C_{hydro}]\,\Delta x_{hydro} \tag{8.4}$$

where, $\Delta x_{hydro} = [\Delta\psi_d\ \Delta\psi_q\ \Delta\psi_{fd}\ \Delta\psi_{kd}\ \Delta\psi_{kq}]^T$, $\Delta u_{hydro} = [\Delta v_d\ \Delta v_q]^T$, $\Delta y_{hydro} = [\Delta i_d\ \Delta i_q]^T$, $A_{hydro}$, $B_{hydro}$ and $C_{hydro}$ are the state, control or input and output matrices respectively for a hydro unit. $E_{fd}$ is the field voltage, $\psi_d$ and $\psi_q$ are the stator flux linkages per second, $\psi_{fd}$, $\psi_{kd}$ and $\psi_{kq}$ are rotor flux linkages per second for a field winding and damper windings

repectively, $v_{dq}$ and $i_{dq}$ are voltages and currents in $dq$ reference frame respectively.

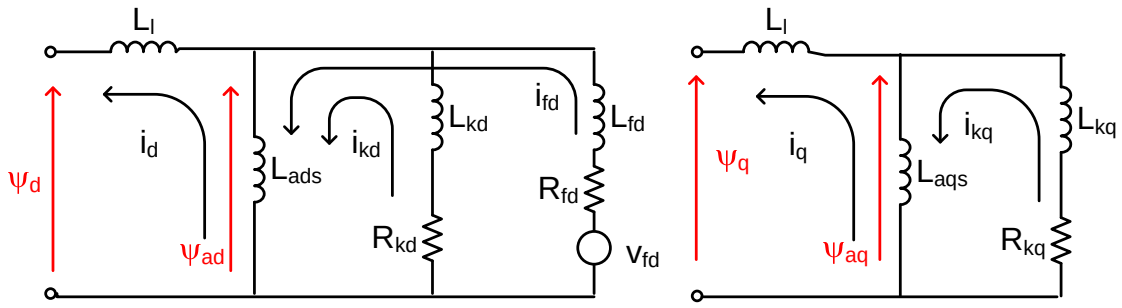


Figure 8.1: Equivalent circuits of $dq$-axes for hydroelectric unit

### 8.3.2 Modelling of Mechanical System

The linearised model of the hydroelectric torsional shaft system is represented based on a mass-spring-damping model as follows:

$$\Delta\dot{x}_{shaft} = [A_{shaft}]\Delta x_{shaft} + [B_{shaft}]\Delta u_{shaft} \tag{8.5}$$

$$\Delta y_{shaft} = [C_{shaft}]\Delta x_{shaft} \tag{8.6}$$

where, $\Delta x_{shaft} = [\Delta\omega_{gen}\ \Delta\omega_{tur}\ \Delta\delta_{gen}\ \Delta\delta_{tur}]^T$, $\Delta y_{shaft} = [\Delta\omega_{gen}\ \Delta\delta_{gen}]^T$, $\Delta u_{shaft} = [\Delta P_m\ \Delta P_e]^T$, $A_{shaft}$, $B_{shaft}$, $C_{shaft}$ are the state, control or input and output matrices respectively for the mechanical system. $\omega$ and $\delta$ are the rotor speed and angle. $P_m$ and $P_e$ are the mechanical and electrical powers respectively. Subscripts '$gen$' and '$tur$' represent generator and turbine respectively.

### 8.3.3 Modelling of Electrical System

The linearised representation of the excitation system (exciter and PSS) and governor-turbine can be expressed as:

$$\Delta\dot{x}_e = [A_e]\Delta x_e + [B_e]\Delta u_e \tag{8.7}$$

$$\Delta y_e = [C_e]\Delta x_e + [D_e]\Delta u_e \tag{8.8}$$

where, $x_e$, $y_e$, $u_e$ are the state, output and input vectors of the excitation and governor-turbine system, $A_e$, $B_e$, $C_e$ and $D_e$ are the state, control or input, output and feedforward matrices respectively for the excitation and governor-turbine system.

The AC side filters can be represented in terms of a shunt capacitor with reactance $X_{Cfilter}$. The state space representation of the rectifier side AC system (in terms of $DQ$ components of different variables) can be expressed as follows:

$$\Delta \dot{x}_N = [A_N]\Delta x_N + [B_N]\Delta u_N \tag{8.9}$$

$$\Delta y_N = [C_N]\Delta x_N \tag{8.10}$$

where, $\Delta x_N = [\Delta v_D \ \Delta v_Q]^T$, $\Delta y_N = [\Delta v_D \ \Delta v_Q]^T$, $\Delta u_N = [\Delta i_D \ \Delta i_Q \ \Delta i_{hvdcD} \ \Delta i_{hvdcQ}]^T$, $A_N$, $B_N$, $C_N$ are the state, control or input and output matrices respectively for the electrical system. $v_D$, $v_Q$ are the bus voltages represented in $DQ$ reference frame at the rectifier ac side, $i_{DQ}$ and $i_{hvdcDQ}$ are generator and HVDC currents in $DQ$ reference frame respectively.

The currents $i_{CDQ}$ flowing through the ac filter at rectifier side are decided by the power system components connected to the bus. Hydroelectric unit is connected directly to the bus, and an HVDC link as well in this study system. Thus, generator and HVDC currents are the inputs to the system.

$$\Delta i_{CDQ} = \Delta i_{DQ} - \Delta i_{hvdcDQ} \tag{8.11}$$

### 8.3.4 Modelling of HVDC System

The HVDC system can be represented in terms of a T-model as shown in Fig. 8.2. The linearisation of the dynamic equations for the HVDC system including the constant current (CC) controller of rectifier, yields equations (8.12), (8.13) and (8.14). The CC controller has a phase-locked loop (PLL) associated to it, which provides a more stable operation [10]. The phase lag resulting from PLL is represented by $\alpha_{PLL}$. The dynamics of CC and PLL are depicted in Fig. 8.3.

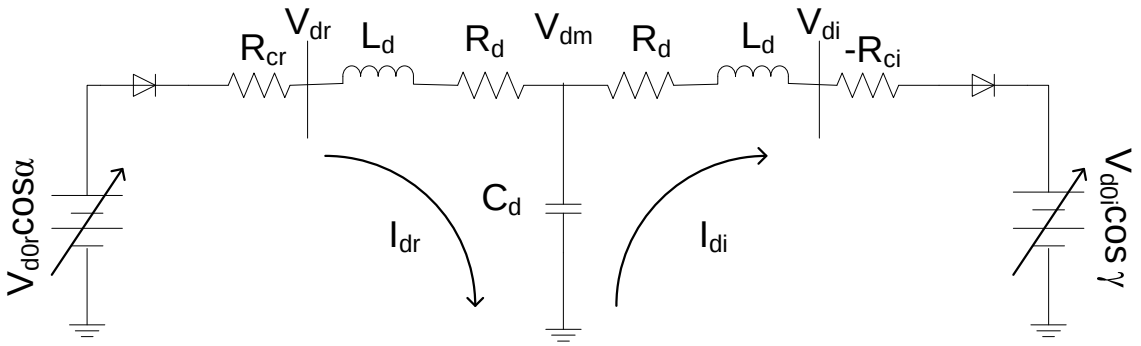


Figure 8.2: HVDC system

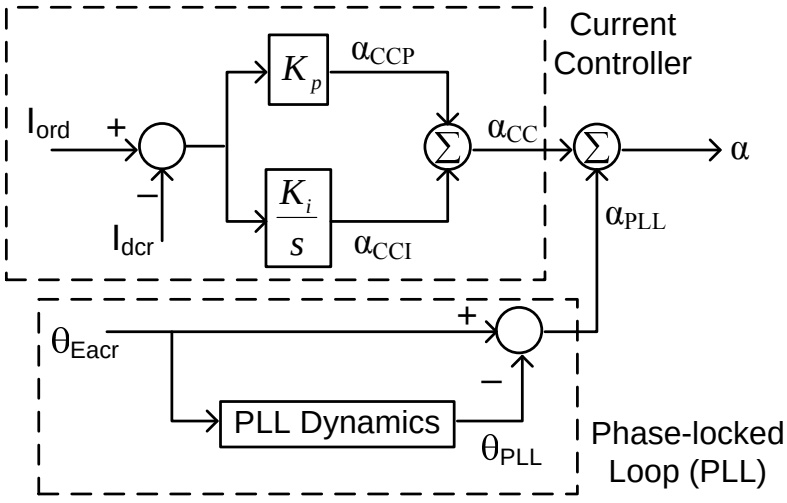


Figure 8.3: Converter control

$$\Delta\dot{x}_{hvdc} = [A_{hvdc}]\Delta x_{hvdc} + [B_{hvdc1}]\Delta u_{hvdc1} + [B_{hvdc2}]\Delta u_{hvdc2} + [B_{hvdc3}]\Delta u_{hvdc3} \tag{8.12}$$

$$\Delta y_{hvdc1} = [C_{hvdc1}]\Delta x_{hvdc} + [D_{hvdc11}]\Delta u_{hvdc1} + [D_{hvdc12}]\Delta u_{hvdc2} \tag{8.13}$$

$$\Delta y_{hvdc2} = [C_{hvdc2}]\Delta x_{hvdc} + [D_{hvdc21}]\Delta u_{hvdc1} + [D_{hvdc23}]\Delta u_{hvdc3} \tag{8.14}$$

where, $\Delta x_{hvdc} = [\Delta I_{dcr}\ \Delta I_{dci}\ \Delta V_{dcm}\ \Delta\alpha_{CCI}\ \Delta\theta_{PLL}]^T$, $\Delta u_{hvdc1} = [\Delta I_{ord}\ \Delta\gamma]^T$, $\Delta u_{hvdc2} = [\Delta V_{acr}\ \Delta\theta_{Vacr}]^T$, $\Delta u_{hvdc3} = [\Delta V_{aci}\ \Delta\theta_{Vaci}]^T$, $\Delta y_{hvdc1} = [\Delta I_{acr}\ \Delta\theta_{Iacr}]^T$, $\Delta y_{hvdc2} = [\Delta I_{aci}\ \Delta\theta_{Iaci}]^T$, $A_{hvdc}$, $B_{hvdc}$, $C_{hvdc}$ and $D_{hvdc}$ are the state, control or input, output and feedforward matrices respectively for the HVDC system. $I_{dc}$ is the direct current, $V_{dcm}$ is the DC voltage on the dc line, $\alpha_{CCI}$ is the rectifier angle output from the integral controller, $\theta_{PLL}$ is the PLL output angle, $I_{ord}$ is the reference current, $\gamma$ is the inverter extinction advance angle, $V_{ac}$ and $\theta_{Vac}$ are the AC line-to-line voltages and the phasor associated at the converter bus, $I_{ac}$ and $\theta_{Iac}$ are the AC line current flowing through the converter transformer and its associated phasor, subscripts $r$ and $i$ represent rectifier and inverter respectively.

### 8.3.5 Interface Between AC and DC Systems

The linearised state space model for each subsystem has been represented individually as shown in subsections 8.3.1, 8.3.2, 8.3.3 and 8.3.4. The linearised representation of the ac-dc interaction equations, as in equations (8.15) and (8.16), highlights the small-signal inter-relationship between ac and dc systems as shown below:

$$\Delta I_{acr} = \frac{\sqrt{6}}{\pi} B_r T_r \Delta I_{dcr} \tag{8.15}$$

$$\Delta\phi_{acr} = -\frac{X_{cr} I_{dcr0}}{\sqrt{2} T_r V_{acr0}^2 sin(\phi_{acr0})}\Delta V_{acr} + \frac{sin(\alpha_0)}{sin(\phi_{acr0})}\Delta\alpha + \frac{X_{cr}}{\sqrt{2} T_r V_{acr0} sin(\phi_{acr0})}\Delta I_{dcr} \tag{8.16}$$

where, $B$ = number of bridges in series, $T$ = transformer ratio, $\phi_{ac}$ = phase angle between fundamental line current and the line-to-neutral source voltage, $X_c$ = commutating reactance, $\alpha$ = ignition delay angle, subscript $r$ represents the rectifier-side and subscript 0

denotes the initial operating condition.

Since each subsystem is represented in a different reference frame, it is important to transform all the variables into common reference frame before the integration of different subsystems. The linearised transformation between variables in $DQ$ reference frame and polar coordinates is shown in equation (8.17).

$$\begin{bmatrix} \Delta f_D \\ \Delta f_Q \end{bmatrix} = \begin{bmatrix} sin\theta_{fac0} & f_{ac0}cos\theta_{fac0} \\ cos\theta_{fac0} & -f_{ac0}sin\theta_{fac0} \end{bmatrix} \begin{bmatrix} \Delta f_{ac} \\ \Delta\theta_{fac} \end{bmatrix} \tag{8.17}$$

The linearised transformation from synchronously rotating reference frame to rotor reference frame is expressed in equation (8.18) [11]. The relationship among variables in rotor, synchronous reference frames and polar coordinates is illustrated in Fig. 8.4.

$$\begin{bmatrix} \Delta f_d \\ \Delta f_q \end{bmatrix} = \begin{bmatrix} cos\delta_0 & sin\delta_0 \\ -sin\delta_0 & cos\delta_0 \end{bmatrix} \begin{bmatrix} \Delta f_D \\ \Delta f_Q \end{bmatrix} + \begin{bmatrix} \Delta f_{q0} \\ -\Delta f_{d0} \end{bmatrix} \Delta\delta \tag{8.18}$$

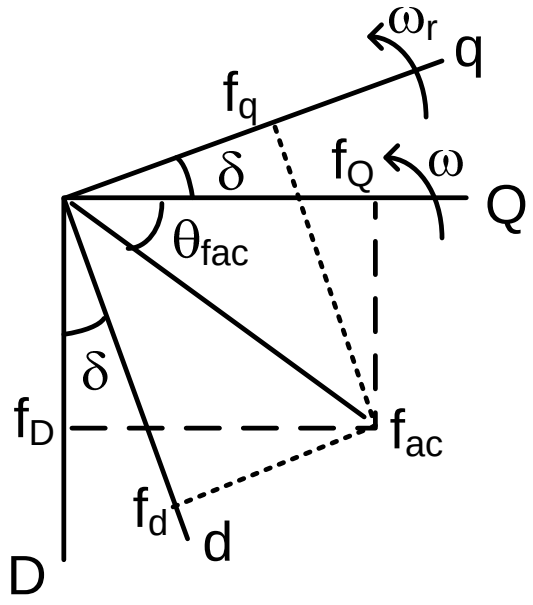


Figure 8.4: Phasor diagram of the relationship among variables in $dq$, $DQ$ reference frames and polar coordinates

## 8.4 Simulation Results

A hydroelectric TG unit connected to an HVDC system (shown in Fig. 8.5), presented in Chapter 7 will be used as the study system for small signal stability analysis in this Chapter. As mentioned in Chapter 7, this study system comprises of a 500 kV, 1000 MW monopolar DC link and a 1210 MVA hydroelectric system. The HVDC system is represented by the CIGRE first HVDC benchmark model. It is assumed that the rectifier operates at CC control mode whilst the inverter operates at constant extinction angle (CEA) control mode.

The hydroelectric unit on the rectifier ac side composes of turbine-generator, governor, excitation system, PSS and shaft system. The overall system comprises of 30 state variables.

Analytical methodologies, such as eigen-analysis, participation factor and sensitivity analyses, are utilised to investigate the interaction behaviour between the hydroelectric unit and the dynamics and control of HVDC system. The consequences of different operating conditions, such as active and reactive power variations, as well as the variations of generator-to-turbine inertia ratio $n$ and the changes of HVDC constant current controller parameters $K_p$ and $K_i$ on small-signal stability are investigated in this chapter.

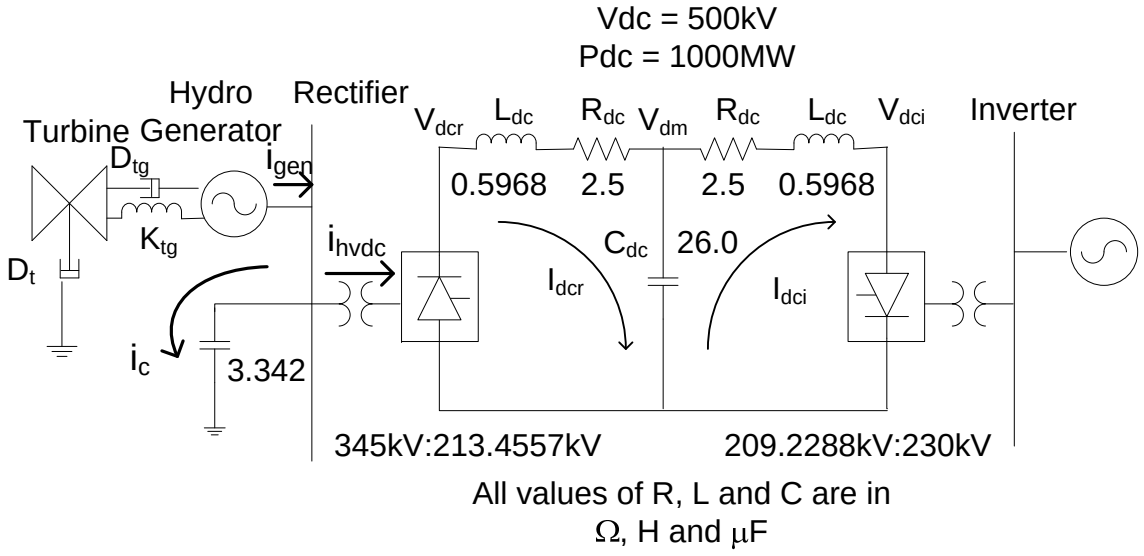


Figure 8.5: A hydro turbine-generator unit interconnected to CIGRE first HVDC benchmark model

### 8.4.1 Eigenvalue and Participation Factor Analyses for Initial Operating Condition

This subsection reveals the eigenvalues of each subsystem individually and for an interconnected system at an initial operating condition. The eigenvalue analysis distinctively allows the investigation of how each power system component influences the overall system eigenvalues. Tables 8.1 and 8.2 shows the eigenvalues of hydroelectric unit and HVDC system independently. The eigenvalue modes 5 and 6 of hydroelectric unit are the local plant mode of oscillation, which has an oscillation frequency of 2.0475 Hz and a damping ratio of 0.0699. The modes 1, 2 and 3, 4 in Table 8.2 represent the dynamics of the HVDC link while mode 5 represents the time constant of the PLL.

Some of the selective eigenvalues for the integrated system are shown in Table 8.3. Modes 12 and 13 are the torsional modes of the hydroelectric unit, and they are critically damped but are generally stable. This corresponds to a hydroelectric system with generator-to-turbine inertia ratio $n$ of 10. Such torsional modes have an oscillation frequency of 6.22 Hz.

Figs. 8.6, 8.7 and 8.8 show the participation factor analysis on hydroelectric unit, HVDC system and the overall system respectively. This analysis reveals the relative involvements of the respective states in the corresponding modes. The participation factor analysis on the overall system as seen in Fig. 8.8 shows that state variables 24 and 25 contribute the most onto mode 20 associated with the exciter. The next highest contribution is from state variable 24 onto mode 3 associated with the hydro unit. State variables 24 and 25 are voltage variables of PSS. This suggests that PSS has a considerable effects onto modes 3 and 20.

Table 8.1: Eigenvalues of Hydroelectric Unit

| Mode | Real($\lambda$) | Imag($\lambda$) | $f$ (Hz) | Damping ratio, $\sigma$ |
|---|---|---|---|---|
| 1,2 | -12.49 | $\pm$ j313.49 | 49.8935 | 0.0398 |
| 3 | -50.09 | j0.00 | 0.00 | 1.0000 |
| 4 | -47.10 | j0.00 | 0.00 | 1.0000 |
| 5,6 | -0.90 | $\pm$ j12.86 | 2.0475 | 0.0699 |
| 7 | -0.55 | j0.00 | 0.00 | 1.0000 |

Table 8.2: Eigenvalues of HVDC System

| Mode | Real($\lambda$) | Imag($\lambda$) | $f$ (Hz) | Damping ratio, $\sigma$ |
|---|---|---|---|---|
| 1,2 | -38.23 | $\pm$ j346.91 | 55.2129 | 0.1095 |
| 3,4 | -35.08 | $\pm$ j69.47 | 11.0568 | 0.4507 |
| 5 | -25.00 | j0.00 | 0.00 | 1.0000 |

Table 8.3: Selective Eigenvalues of the Interconnected System

| Mode | Real($\lambda$) | Imag($\lambda$) | $f$ (Hz) | Damping ratio, $\sigma$ |
|---|---|---|---|---|
| 1 | -1.000 | j0.0 | 0.00 | 1.000 |
| 2,3 | -13.854 | $\pm$ j2292.5 | 364.86 | 0.006 |
| 4,5 | -16.980 | $\pm$ j1607.0 | 255.76 | 0.011 |
| 6,7 | -38.275 | $\pm$ j346.8 | 55.20 | 0.110 |
| 8 | -111.396 | j0.0 | 0.00 | 1.000 |
| 9,10 | -35.146 | $\pm$ j69.5 | 11.06 | 0.451 |
| 11 | -52.430 | j0.0 | 0.00 | 1.000 |
| 12,13 | -0.000 | $\pm$ j39.1 | 6.22 | 0.000 |
| 14 | -36.698 | j0.0 | 0.00 | 1.000 |
| 15 | -34.392 | j0.0 | 0.00 | 1.000 |
| 16,17 | -13.133 | $\pm$ j14.7 | 2.35 | 0.665 |
| 18 | -28.515 | j0.0 | 0.00 | 1.000 |
| 19 | -29.412 | j0.0 | 0.00 | 1.000 |
| 20 | -25.000 | j0.0 | 0.00 | 1.000 |

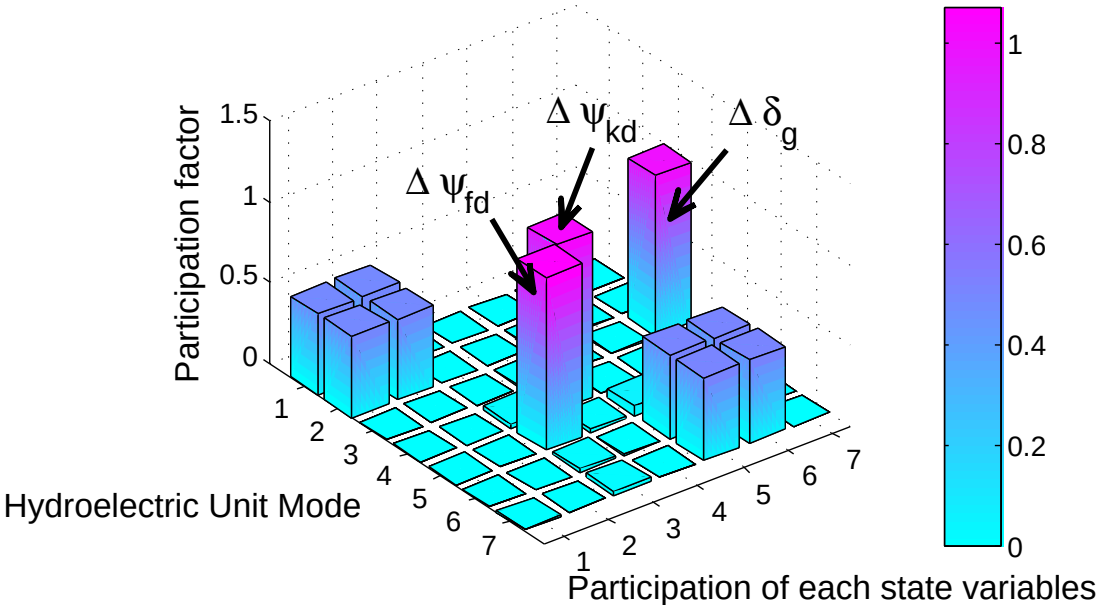


Figure 8.6: Participation factor analysis on hydroelectric unit

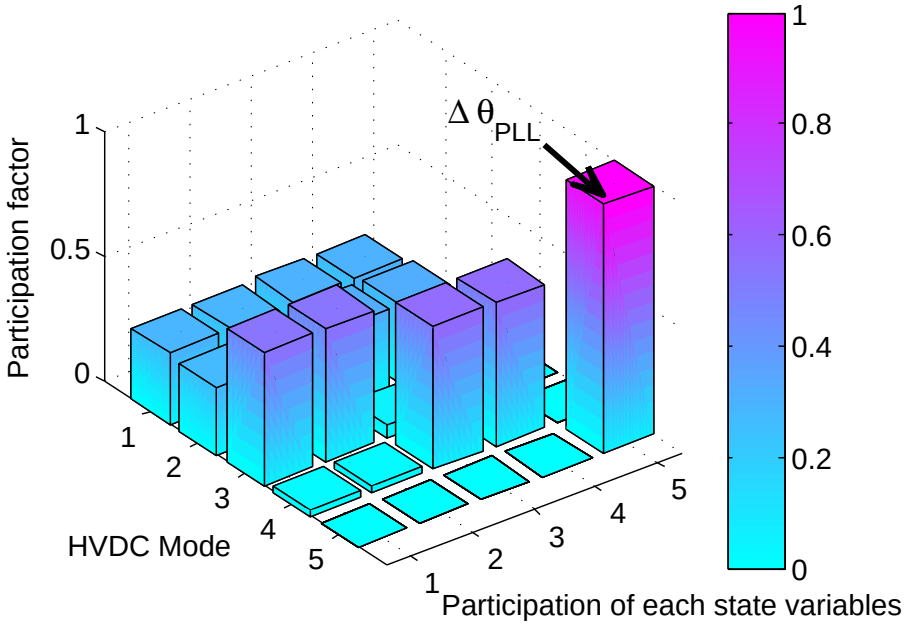


Figure 8.7: Participation factor analysis on HVDC system

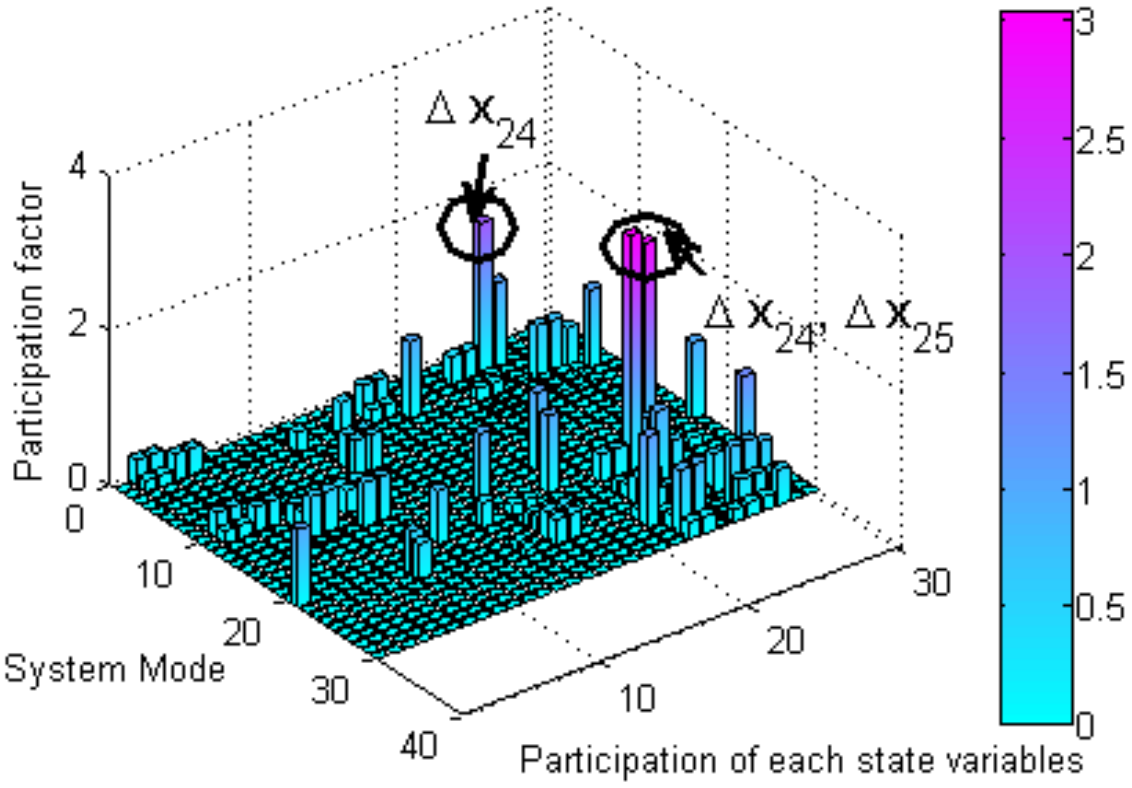


Figure 8.8: Participation factor analysis on overall system

### 8.4.2 Sensitivity Analysis for Different Operating Conditions

Different operating conditions have considerable effects on system small-signal stability. In reality, small disturbances always occur in a power system, such as small variations of load and generation. Thus, it is important to investigate the influence of system operating conditions on the overall small-signal stability. In this study, the system is subjected to active ($P$) and reactive power ($Q$) changes and system least stable modes will be used as an indicator for stability. Two cases have been considered: isolated hydroelectric system and interconnected hydroelectric system with HVDC system.

Simulation results for influence of $PQ$ variations on system small-signal stability for isolated and interconnected operations are shown in Figs. 8.9 and Fig. 8.10 respectively. In an isolated operation, the local plant mode (swing mode) oscillations are used as the stability indicator. The torsional modes are used as the stability indicator for interconnected operation as they appears to be the critical modes in the system. It is observed in Fig. 8.9 that the swing mode is not affected substantially by the $PQ$ variations. It is well-damped for both leading and lagging power factor conditions. However, the swing mode frequency increases slightly for an increment of active power. On the contrary, the critical modes of the overall system are sensitive to the $PQ$ changes as seen in Fig. 8.10. For low $P$ injection into the system, it is more susceptible to instability due to insufficient damping and the negative damping introduced by HVDC converter controls. Increase in $Q$ may result in instability.

The torsional modes of the system appear to be system critical mode. Damping controller can be designed based on the information provided on system oscillatory modes, and incorporated to provide more damping into the system.

### 8.4.3 Effects of Different Generator-to-Turbine Inertia Ratio

It has been demonstrated in the earlier studies [12] that the hydro units with a low generator-to-turbine inertia ratio $n$ would experience SSTI problem, which is due to the lack of damping at the torsional frequency $f_n$. This subsection illustrates the consequences of $n$

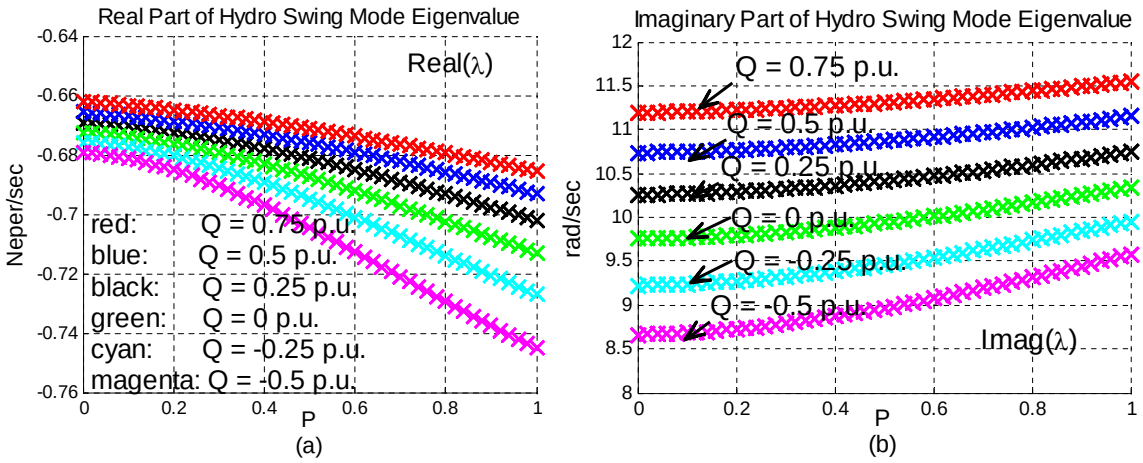


Figure 8.9: Swing mode for hydroelectric unit subject to $PQ$ variation

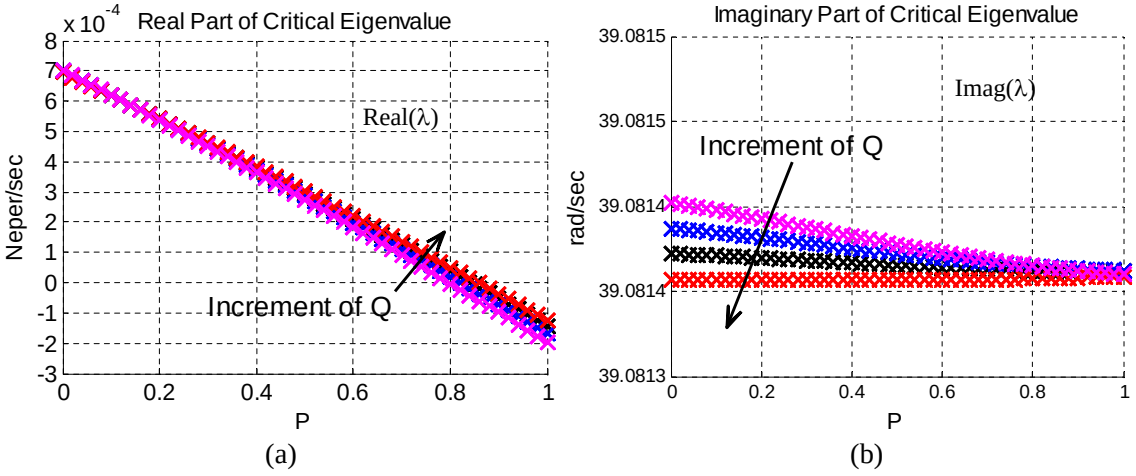


Figure 8.10: Critical mode of overall system subject to $PQ$ variation

variation on the small-signal stability. In this study, generator inertia $H_{gen}$ is 3.0 sec and remains the same for all $n$ values. It is the turbine inertia $H_{tur}$ that varies throughout the studies. Fig. 8.11 shows that with an increasing value of $n$, torsional modes tend to shift more to the stable region. However, at $n = 30$, the damping begins to reduce (indicated by the reduction of torsional modes real part). The increment of $n$ does improve the damping of the torsional modes. The simulation results also indicate that the hydro unit connected in the close vicinity of the HVDC system can possibly experience SSTI problem as the torsional modes for the integrated system have relatively low damping due to the negative damping introduced by CC controller. This can be evidently seen in Table 8.4.

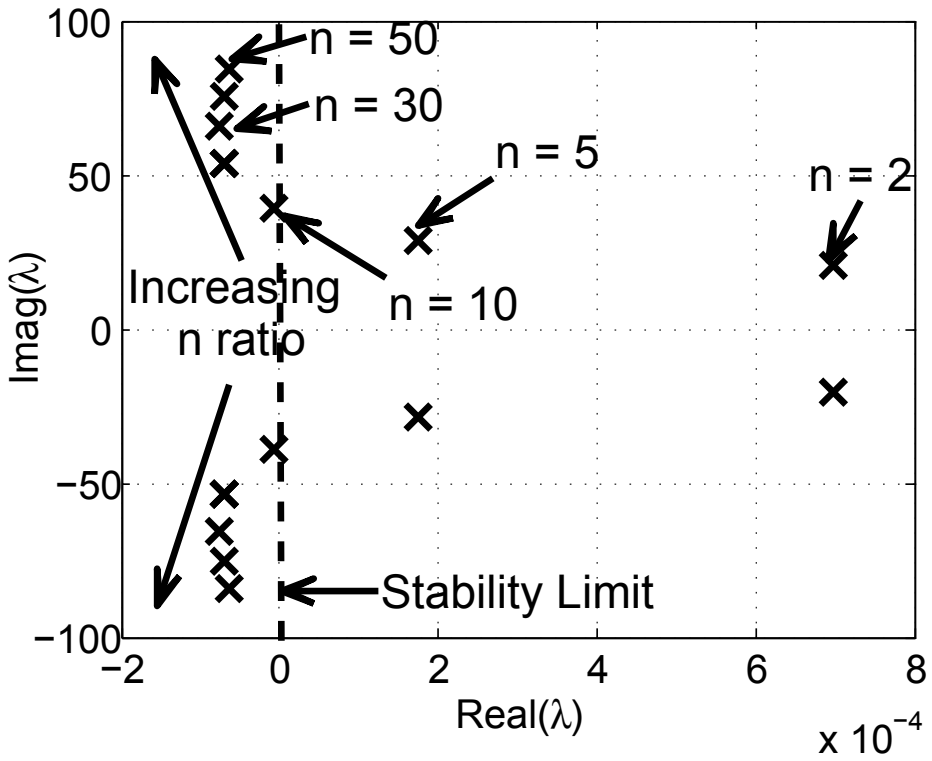


Figure 8.11: Torsional modes of the hydroelectric unit subject to variation of generator-to-turbine inertia ratio ($n$)

### 8.4.4 Effects of Constant Current Controller Parameters

The level and the frequency range of negative damping for the ac-dc system are dependent on the value of the firing angle [12]. Thus, the variation of HVDC constant current controller

Table 8.4: System Torsional Modes for Different Generator-to-Turbine Inertia Ratio ($n$)

| $n$ | Real($\lambda$) | Imag($\lambda$) | $f$ (Hz) | Damping ratio, $\sigma$ |
|---|---|---|---|---|
| 2 | 6.9907e-4 | ± j20.404 | 3.247 | -3.4261e-5 |
| 5 | 1.7341e-4 | ± j28.862 | 4.594 | -6.0082e-6 |
| 10 | -6.2582e-6 | ± j39.080 | 6.220 | 1.6014e-7 |
| 20 | -7.0500e-5 | ± j54.000 | 8.594 | 1.3056e-6 |
| 30 | -7.5738e-5 | ± j65.609 | 10.442 | 1.1544e-6 |
| 40 | -7.0400e-5 | ± j75.450 | 12.008 | 9.3307e-7 |
| 50 | -6.2438e-5 | ± j84.153 | 13.393 | 7.4196e-7 |

parameters, $K_p$ and $K_i$ on small-signal stability are also examined in this study. Fig. 8.12 shows the trajectory of the critical system mode, which is identified as the torsional mode, subject to the variation of HVDC constant current controller parameters $K_p$ and $K_i$ at rectifier side. It is observed that the damping of the system critical mode can be improved utilising a low value of $K_p$ and $K_i$. The mode has less damping with an increment value of $K_p$. It is seen in Fig. 8.12(b) that with $K_p$ less than 8.5, all values of $K_i$ ranged from 10 - 100 will result in a stable system.

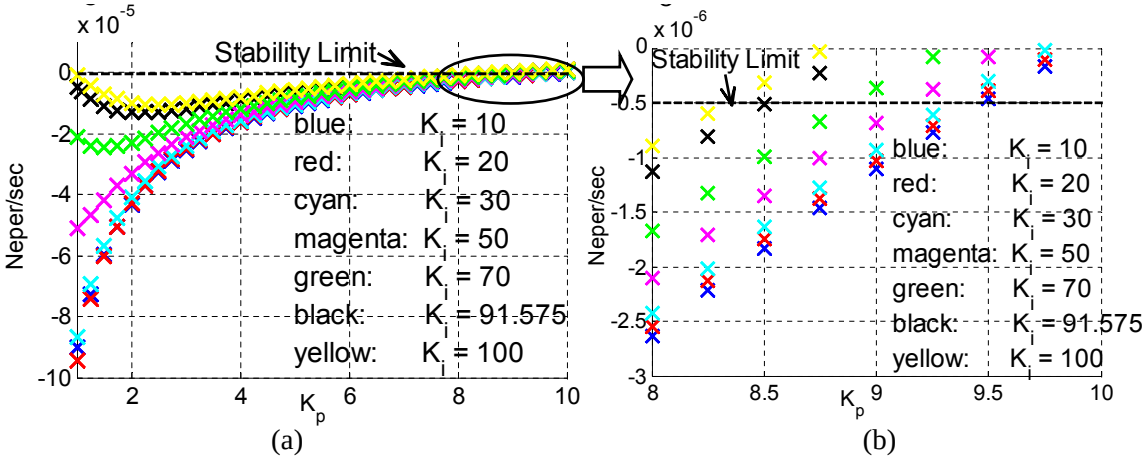


Figure 8.12: Critical mode of overall system subject to constant current PI controller variation

## 8.5 Summary

This chapter presents a linearised small-signal dynamic model of hydroelectric system connected to an HVDC system. The eigenvalue analysis has been used as an analytical tech-

nique for small signal stability analysis of a sample hydroelectric system connected to CIGRE first HVDC benchmark model. The dynamic system response for different operating conditions, generator-to-turbine inertia ratio and HVDC constant current controller parameters has been investigated. The modal analysis for varying $P$ and $Q$ generation demonstrates that the swing mode of the isolated hydro operation does not get affected substantially. On the contrary, the critical modes of the integrated system, identified as torsional modes, are sensitive to the $P$ and $Q$ variations and HVDC constant current controller parameters. It has also been demonstrated that the hydro units with low generator-to-turbine inertia ratio may experience SSTI problem due to dominant negative damping imposed by HVDC converter controls.

## References


[1] IEEE/CIGRE Joint Task Force on Stability Terms and Definitions, "Definition and Classification of Power System Stability," *IEEE Trans. Power Syst.*, Vol. 19, No. 2, pp. 1387-1401, May 2004.

[2] P. Kundur. *Power System Stability and Control.* McGraw-Hill, 1994.

[3] Y.C. Choo, K.M. Muttaqi, M. Negnevitsky, "Evaluation of small signal stability of a power system," *Australian Journal of Electrical and Electronics Engineering*, Vol. 4, No. 3, 2008.

[4] C. Osauskas, A. Wood, "Small-Signal Dynamic Modeling of HVDC Systems," *IEEE Trans. Power Del.*, Vol. 18, No. 1, pp. 220-225, January 2003.

[5] S. Arabi, G.J. Rogers, D.Y. Wong, P. Kundur, M.G. Lauby, "Small Signal Stability Program Analysis of SVC and HVDC in AC Power Systems," *IEEE Trans. Power Syst.*, Vol. 6, No. 3, pp. 1147-1153, August 1991.

[6] D. Jovcic, "Control of High Voltage DC and Flexible AC Transmission Systems," *PhD Thesis*, The University of Auckland, December 1999.

[7] H.A. Peterson, P.C. Krause, "A Direct- and Quadrature-Axis Representation of a Parallel AC and DC Power System," *IEEE Trans. Power App. Syst.*, Vol. PAS-85, No. 3, pp. 210-225, March 1966.

[8] H.A. Peterson, P.C. Krause, J.F. Luini, C.H. Thomas, "An Analog Computer Study of a Parallel AC and DC Power System," *IEEE Trans. Power App. Syst.*, Vol. PAS-85, No. 3, pp. 191-209, March 1966.

[9] K.R. Padiyar. *Analysis of Subsynchronous Resonance in Power Systems.* Kluwer Academic Publishers, 1999.

[10] D.J. Kim, H.K. Nam and Y.H. Moon, "A Practical Approach to HVDC System Control for Damping Subsynchronous Oscillation Using the Novel Eigenvalue Analysis Program," *IEEE Trans. Power Syst.*, Vol. 22, No. 4, pp. 1926-1934, November 2007.

[11] P.C. Krause. *Analysis of Electric Machinery.* McGraw-Hill, 1986.

[12] Y.C. Choo, A.P. Agalgaonkar, K.M. Muttaqi, S. Perera, M. Negnevitsky, "Subsynchronous Torsional Behaviour of a Hydraulic Turbine-Generator Unit Connected to a HVDC System," *Proceedings of Australasian Universities Power Engineering Conference (AUPEC 2008)*, Sydney, New South Wales, 14-17 December, 2008.

# Chapter 9

# Subsynchronous Torsional Interaction Behaviour of Wind Turbine-Generator Unit Connected to an HVDC System


### Abstract

Utilisation of wind energy to generate electricity has attracted considerable attention worldwide, and is rapidly-growing. The integration of large wind farms with HVDC transmission network could be one of the preferred options for supplying bulk power over a long distance. Since HVDC rectifier stations with constant current control may introduce negative damping on the nearby generating units, it is important to identify the torsional interaction characteristics between turbine-generator units and the HVDC systems over a frequency range of interest. However, very little related information exists in regard to wind turbine-generators. This chapter presents the electromagnetic transient time domain analysis to investigate the possible SSTI phenomenon of fixed-speed (induction machine based) wind turbine-generator (WTG) unit interconnected to a CIGRE first HVDC benchmark system.

Electrical disturbances, such as three-phase short circuit fault at the inverter station and DC power flow change are simulated to examine the possible dynamic interactions of the WTG unit. Simulation studies are conducted using PSCAD®/EMTDC©.

## 9.1 Introduction

The grid integration of wind resources is rapidly-growing all over the world due to its environmental benefits [1, 2]. In 2013, global renewable electricity generation grew to nearly 5,070 TWh and accounted for almost 22% of total power generation worldwide [3, 4]. This development inexorably integrates WTGs into the electrical network in a large scale, thereby posing numerous challenges to all parties concerned.

WTG units exhibit different characteristics compared to steam and hydro units, which typically feature high turbine inertia and low shaft stiffness between the turbine and generator rotor [2, 5]. These characteristics result in a lightly damped, low frequency torsional shaft mode oscillations, wherein the turbine (hub and blades) swings coherently against the generator [6]. It is also demonstrated in [6] that the soft shaft mode can be excited by random wind variations, which results in large oscillatory fluctuations in the shaft torques and the electrical power. Prospective interactions of WTG units connected to a series-compensated line and an HVDC link are discussed in [7]. The performance issues related to the dynamic characteristics of both conventional induction generators and doubly-fed induction machine based wind turbines are also discussed. However, SSTI between the wind farm and the HVDC system was not investigated thoroughly.

The undesirable interactions between the HVDC terminal and the 11.5 Hz torsional mode of an electrically-close turbine-generator unit were noted during the field tests conducted at Square Butte in North Dakota, USA [8]. Subsequently, it was revealed that the HVDC rectifier stations with constant current control may introduce negative damping on the nearby generating units [8]. A current-controlled voltage-source converter, located electrically close to the generator may also introduce negative damping in the certain frequency range and proper design of current controller may nullify the possibility of negative damp-

ing [9]. SSTI characteristics can possibly be observed when a WTG unit is connected in the close vicinity of the HVDC system. ABB has conducted comprehensive system studies for integrating large wind farms in the American electricity network, especially in the close vicinity of HVDC [10]. However, little information exists in the literature in regard to the SSTI behaviour of an individual WTG unit connected to HVDC system. The objective of this chapter is to model a WTG system, including the dynamics of the blade and shaft systems, connected to an HVDC system for SSTI analysis.

The chapter is structured as follows: Section 9.2 outlines the fixed-speed induction machine based WTG modelling, which includes blade dynamics, shaft model and induction generator model. Section 9.3 demonstrates the perturbation analysis for a WTG unit for an investigation of the possible dynamic interactions. Section 9.4 briefly describes the SSTI phenomenon when a turbine-generator is connected in the vicinity of an HVDC system. A study system involving a WTG unit interconnected to a CIGRE first HVDC benchmark system is presented in Section 9.5. The time domain simulation studies using PSCAD®/EMTDC© and frequency spectrum analysis are used to investigate the SSTI behaviour of WTG unit for electrical disturbances on HVDC system and the results are presented in Section 9.6. Section 9.7 concludes the chapter.

## 9.2 Wind Turbine-Generator Model

The modelling aspects related to wind energy capturing mechanism, torsional shaft system, the induction machine and the electrical network are presented in this section. The MOD-2 type WTG model is used for the wind system representation in PSCAD®/EMTDC©.

### 9.2.1 Blade Dynamics

The power extraction from wind and associated mechanical torque can be mathematically represented as follows [11, 12]:

$$P = \frac{1}{2}\rho A v_w^3 C_p(\lambda, \beta) \tag{9.1}$$

$$T = \frac{P}{\omega_m} \tag{9.2}$$

where $P$ = wind power in watts, $\rho$ = air density in kg/m$^3$, $A$ = area swept by wind blade in m$^2$, $\upsilon_w$ = wind speed in m/s, $\lambda$ = tip speed ratio, $\beta$ = blade pitch angle in degrees, $C_p$ = power coefficient, $T$ = torque in Nm, $\omega_m$ = turbine mechanical speed in rad/s.

The power coefficient $C_p$ is a function of both $\lambda$ and $\beta$, and is generally nonlinear. The approximate expressions for nonlinear blade dynamics are as follows [12]:

$$\omega_h = \frac{\omega_m}{GR} \tag{9.3}$$

$$\lambda = \frac{2.237 \upsilon_w}{\omega_h} \tag{9.4}$$

$$C_p = \frac{1}{2}(\lambda - 0.022\beta^2 - 5.6)e^{-0.17\lambda} \tag{9.5}$$

where $\omega_h$ is a hub speed in m/s and GR is a gear ratio.

A power coefficient versus tip speed ratio ($C_p$ – $\lambda$) characteristic curve for a typical MOD-2 type WTG is shown in Fig. 9.1 for a wind speed of 15 m/s with different blade pitch angles.

### 9.2.2 Shaft Model

The mechanical shaft system of a WTG unit generally comprises of a turbine, low-speed shaft, gearbox, high-speed shaft and generator rotor. It can be represented as a mass-spring-damper system as shown in Fig. 9.2 [2, 6]. The inertia of the blades are represented as a lumped inertia. The inertia of the high speed shaft aggregates the individual inertias of both gearbox and generator, assuming the high speed shaft to be rigid. The inertia of

the low speed shaft is shared between hub and gearbox [6].

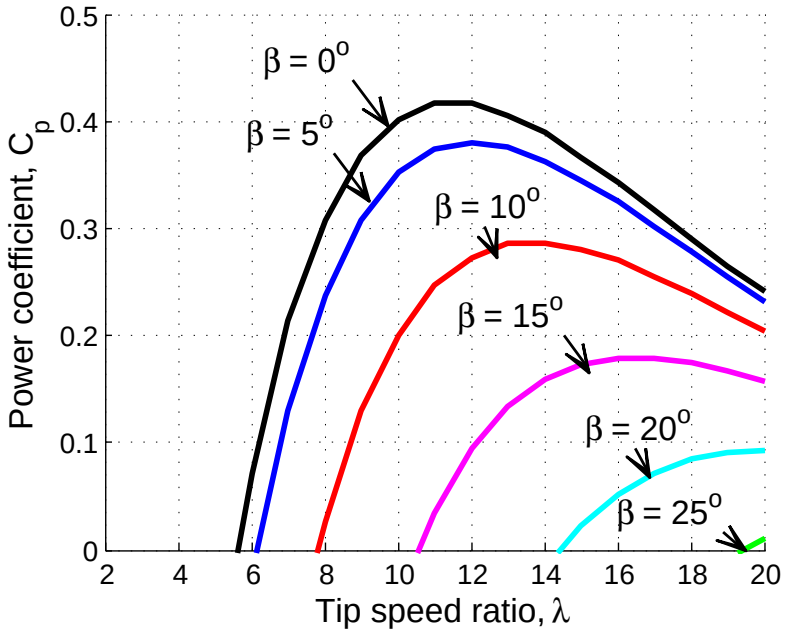


Figure 9.1: Power coefficient vs tip speed ratio characteristic of a MOD-2 type WTG for different pitch angles

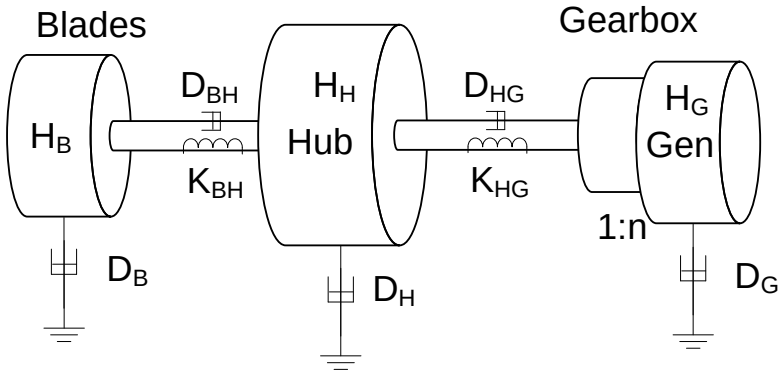


Figure 9.2: Mass-spring-damper shaft model of WTG unit

The mechanical shaft system of a WTG unit is represented based on a mass-sping-damper system as follows [6, 13]:

$$2H_i s\Delta\omega_i = \Delta T_i + \Delta T_{ij} - \Delta T_{jk} - D_i\Delta\omega_i \tag{9.6}$$

$$\Delta T_{ij} = K_{ij}(\Delta\theta_i - \Delta\theta_j) + D_{ij}(\Delta\omega_i - \Delta\omega_j) \tag{9.7}$$

where $s$ is the Laplace operator, $\omega$ and $\theta$ are the rotor speed and angle respectively, $H_i$ is the inertia constant of mass $i$, $T_i$ is the external torque applied on mass $i$, $D_i$ is the damping coefficient of mass $i$, $T_{ij}$, $K_{ij}$ and $D_{ij}$ are the torsional torque, spring constant and damping coefficient between masses $i$ and $j$ respectively. A WTG shaft model with typical values of inertia constants and spring constants, in accordance with Fig. 9.2 is as shown in Table 9.1. This tabulated data is used for SSTI analysis presented in this chapter. Typically, torsional frequencies of oscillation ($f_n$) for the WTG shaft model can be calculated as follows [14]:

$$f_n = \frac{1}{2\pi}\sqrt{-\frac{b}{2} \pm \frac{\sqrt{b^2 - 4c}}{2}} \tag{9.8}$$

where

$$\begin{aligned} b &= -\left[K_{BH}\left(\frac{1}{2H_B} + \frac{1}{2H_H}\right) + K_{HG}\left(\frac{1}{2H_H} + \frac{1}{2H_G}\right)\right] \\ c &= K_{BH}K_{HG}\frac{(H_B + H_H + H_G)}{2^2 H_B H_H H_G} \end{aligned}$$

and subscripts $G$, $H$ and $B$ in the expressions for '$b$' and '$c$' refer to generator, hub and blade masses respectively. Accordingly, it is observed that the torsional frequencies for the WTG shaft system under consideration are 0.6086 Hz and 4.9818 Hz respectively.

Table 9.1: Shaft Model of WTG Unit [6]

| $H_B$ (s) | $H_H$ (s) | $H_G$ (s) | $K_{BH}$ (pu/el.rad) | $K_{HG}$ (pu/el.rad) |
|---|---|---|---|---|
| 9.1150 | 0.4764 | 1.0455 | 2.7410 | 0.0904 |

### 9.2.3 Induction Generator Model

A fixed-speed induction machine of fourth order is used to represent the WTG unit, and its voltage and current relationship in the synchronously-rotating reference frame can be

expressed as [15]:

$$v^e = Z_{im} i^e \tag{9.9}$$

where $v^e = [v^e_{qs} \;\; v^e_{ds} \;\; v'^e_{qr} \;\; v'^e_{dr}]^{-1}$, $i^e = [i^e_{qs} \;\; i^e_{ds} \;\; i'^e_{qr} \;\; i'^e_{dr}]^{-1}$; subscripts '$s$' and '$r$' represent the stator and rotor side variables respectively, while superscript ''$e$' refers to the transformation of rotor side variables into the stator side using the rotor-to-stator turns ratio. $Z_{im}$ is the induction machine internal impedance matrix.

## 9.3 Perturbation Analysis For A WTG Unit

The perturbation analysis is conducted to examine the WTG response at different frequencies. The grid side voltage signal is perturbed at different modulated frequencies as shown in Fig. 9.3. It can be expressed mathematically as follows:

$$v_{ac} \;\; = \;\; [\omega_b + msin(\omega_m t)] V_p cos(\omega_b t) \tag{9.10}$$

where $\omega_b$ is the base frequency in rad/s, $m$ is the magnitude of the speed deviation, $\omega_m$ is the frequency of oscillation of the rotor speed in rad/s, $t$ is the time and $V_p$ is the peak voltage.

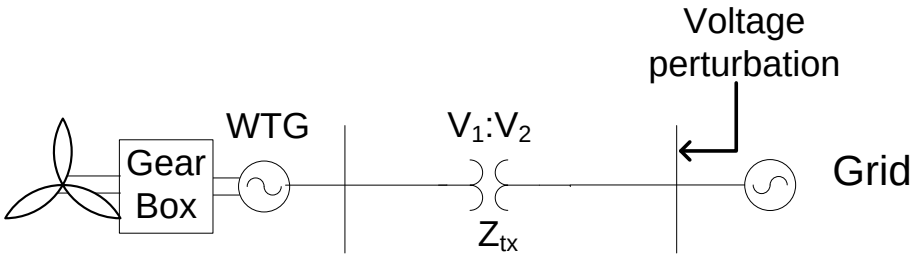


Figure 9.3: AC voltage perturbation onto WTG unit

A typical time response of the bus voltage for a modulated frequency $f_m$ is as shown in Fig. 9.4(a). The corresponding representative frequency spectrum of the AC voltage is shown in Fig. 9.4(b). It can be seen that the AC voltage oscillates at fundamental ($f_{fund}$),

sub- ($f_{sub}$) and super-($f_{super}$) synchronous frequencies as a consequence of the frequency modulation.

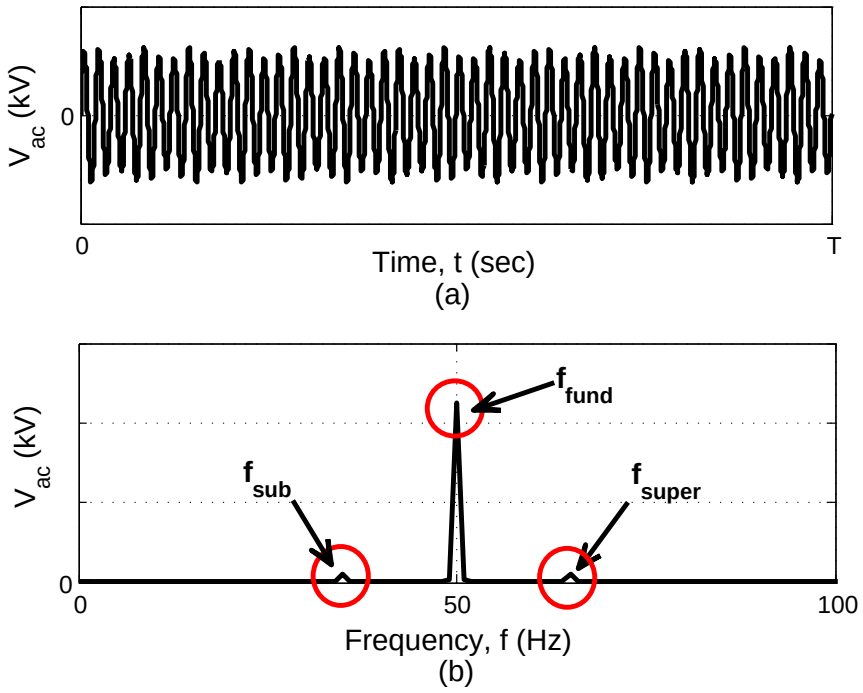


Figure 9.4: (a) Time response and (b) frequency spectrum of AC voltage at a modulated frequency, $f_m$ of 15 Hz

It is also envisaged that the voltage perturbation at different modulated frequencies may instigate torsional modes of a WTG unit. The possible dynamic interaction of the WTG unit can be investigated by examining the resulting deviation in blade-hub and hub-generator torques (mechanical torques) of the WTG unit. It may very well depict the WTG response under network disturbances. The simulation results for frequency spectrum analysis of a typical WTG unit are presented in Section 9.6.1.

## 9.4 Subsynchronous Torsional Interaction For A Machine Connected To HVDC System

SSTI phenomenon for the WTG connected to an HVDC system is elaborated in this section with the assumptions that the generator is directly connected to the HVDC system and the

commutating voltage and phase angle at the rectifier station are in accordance with those at the generator internal bus [16].

The machine side AC voltage is oscillating sinusoidally at different frequency components, namely fundamental frequency $f_b$, subsynchronous frequency $f_b - f_m$ and supersynchronous frequency $f_b + f_m$ as a consequence of torsional oscillations. It can be also looked at as an amplitude and phase modulation of AC voltage. This results in current oscillations over the HVDC link depending on the effective impedance of the HVDC system [16]. The subsynchronous and supersynchronous frequency components of the AC current are subsequently induced in the AC system and hence it is apparent that the electromagnetic torque consists of sub- and super- synchronous frequency components. Typically, negative damping torque results from the subsynchronous frequency currents whilst positive damping torque is provided by the supersynchonous frequency currents [16].

The HVDC system can be represented in terms of a T-model as shown in Fig. 9.5. An aggregated wind system, including the wind energy capturing mechanism and the torsional shaft system, has been connected to the HVDC system in parallel to the connection of an infinite bus and an AC filter at the rectifier station as seen in Fig. 9.5. The constant current (CC) controller is normally installed at the rectifier station with a phase-locked loop (PLL) to ensure a stable system operation. The system equations to depict the operation of the HVDC system including the rectifier side CC controller are as follows [13, 17]:

$$sI_{dr} = \frac{V_{dr} - R_d I_{dr} - V_{dm}}{L_d} \tag{9.11}$$

$$sI_{di} = \frac{V_{dm} - R_d I_{di} - V_{di}}{L_d} \tag{9.12}$$

$$sV_{dm} = \frac{I_{dr} - I_{di}}{C_d} \tag{9.13}$$

$$\alpha = (K_p + \frac{K_i}{s})(I_{ord} - I_{dr}) + \alpha_{PLL} \tag{9.14}$$

where $I_d$ is the DC current, $V_d$ is the DC voltage, $V_{dm}$ is the DC voltage on the dc line, $R_d$, $L_d$ and $C_d$ are the dc line resistance, inductance and capacitance respectively, $\alpha$ is the rectifier firing angle, $K_p$ and $K_i$ are the proportional and integral gains, $I_{ord}$ is the reference

current and $\alpha_{PLL}$ is the phase lag resulting from PLL. The subscripts $r$ and $i$ represent rectifier and inverter side variables respectively. The characteristics of the CC controller and PLL are illustrated in Fig. 9.6. Fig. 9.6 shows that the phase angle of the rectifier side AC voltage $\theta_{Eacr}$ has an effect on the firing angle $\alpha$ with equidistant pulse control. PLL is associated to the controller to synchronise firing angle to the AC voltage [16].

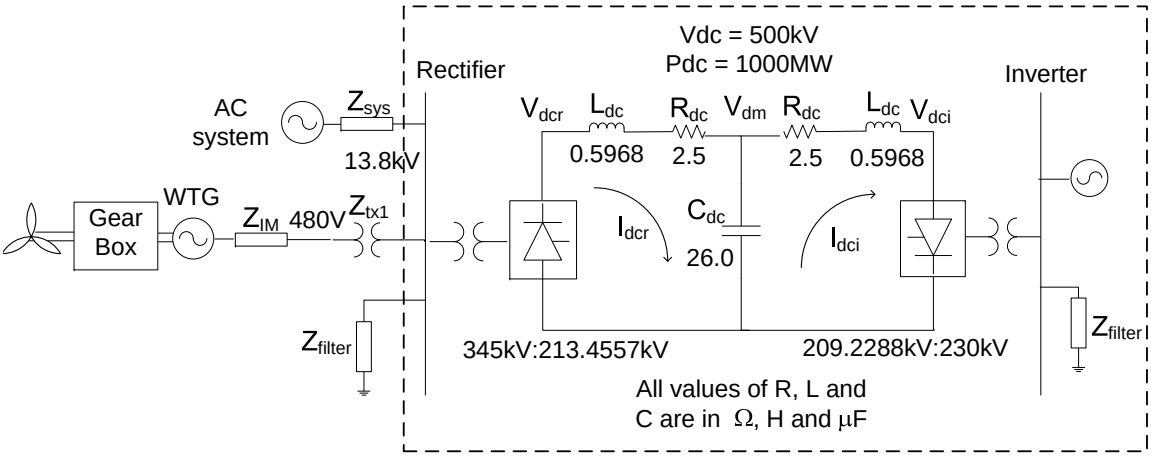


Figure 9.5: PSCAD®/EMTDC© simulated WTG unit connected to an HVDC system

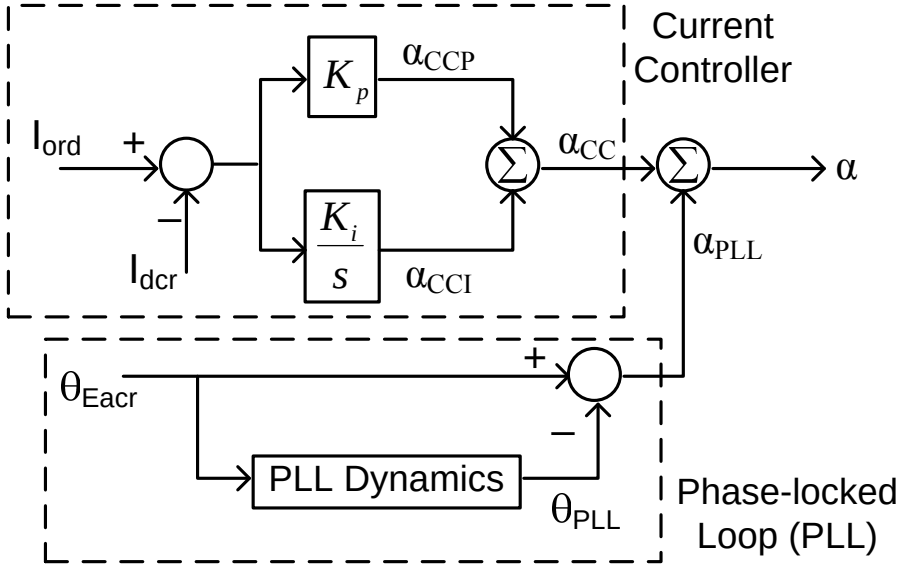


Figure 9.6: Converter control at the rectifier station

## 9.5 Study System

A WTG unit of 1 MVA capacity with a rated voltage of 480 V is directly connected to the HVDC system as shown in Fig. 9.5. The time domain simulation studies are conducted in PSCAD®/EMTDC© to examine SSTI behaviour of a WTG unit for voltage perturbation and network disturbances. The data for the WTG unit is as provided in Table 9.2. The collector system, rated at a voltage of 13.8 kV, connects the WTG unit and a 345 kV AC system grid through a 13.8/345 kV transformer. The WTG unit has a blade pitch angle controller of proportional-integral (PI) type, as seen in Fig. 9.7. In case of a high wind speed condition, the blade pitch angle will be activated and is adjusted to ensure a delivery of the rated power. The pitch angle is varied utmost at the rate of 3° – 10° per second determined by the capacity of the wind turbine [18].

The simulation studies are carried out using fixed-speed induction machine based WTG. To operate the induction machine within the range of 0.98-0.99 lagging power factor, supplementary reactive support is required [7, 19]. A local capacitor bank is usually connected at the machine terminal and the rating of the bank is selected to give unity power factor at rated conditions [20]. In this study, it is assumed that the reactive power requirement of the machine has been met by the grid.

The HVDC system is represented by the CIGRE first HVDC benchmark model, with the monopolar DC link rated at 500 kV and 1000 MW [21]. It is considered that the HVDC system operates at normal conditions, i.e. the rectifier operates at CC control mode whilst the inverter operates at constant extinction angle (CEA) control mode.

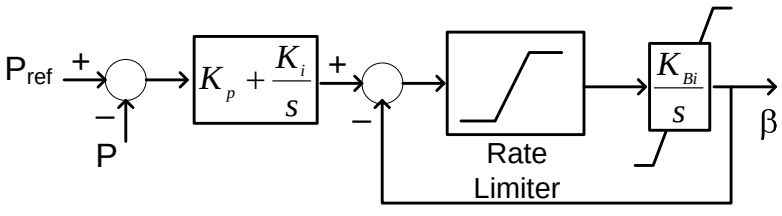


Figure 9.7: Blade pitch angle controller

Table 9.2: WTG Unit Parameters

| System quantities | Values |
|---|---|
| Rated speed of machine output | 314.1593 rad/s |
| Wind speed, $\upsilon_w$ | 15 m/s |
| Gear Ratio, $GR$ | 55 |
| Rotor blade radius, $R$ | 20.0 m |
| Rotor blade swept area, $A$ | 1256.6 $m^2$ |
| Number of poles, $p$ | 6 |
| Gear box efficiency, $G_{eff}$ | 97% |
| Machine rated MVA, $G_{MVA}$ | 1.0 MVA |
| Initial pitch angle, $\beta$ | 0° |
| Air density, $\rho$ | 1.229 $kg/m^3$ |

## 9.6 Simulation Results

Sustained torsional oscillations could be resulted if the complement of the system resonance frequency is close to the mechanical torsional mode frequency and that the combined electromechanical system lacks in system damping [22]. The main focus of the chapter is to investigate the effect of fast-acting control loop associated with the current controller at the rectifier station, which could possibly excite torsional oscillations on the nearby generator. PSCAD®/EMTDC© simulated model is used to investigate the SSTI interactions of a WTG unit connected to HVDC system.

Simulated line fault on the HVDC system and sinusoidal modulation of the HVDC terminal at the torsional resonant frequency can excite the torsional modes of shaft oscillation [23]. Hence, different case scenarios with the application of the disturbances on the HVDC side, such as three-phase to ground fault at the inverter station and 25% decrement in the rated DC power flow are considered for SSTI investigation on a WTG unit by conducting time domain simulation studies.

### 9.6.1 Frequency Spectrum Analysis for a WTG unit

Perturbation analysis is conducted to investigate the oscillatory response of a WTG unit for different frequency injections. The grid side voltage is perturbed to depict network disturbances. The resulting dynamic interactions in blade-hub and hub-generator torques

(mechanical torques) of the WTG unit are examined for an injection of different modulated frequency, $f_m$. The PSCAD®/EMTDC© simulated circuit for voltage perturbation is shown in Fig. 9.8.

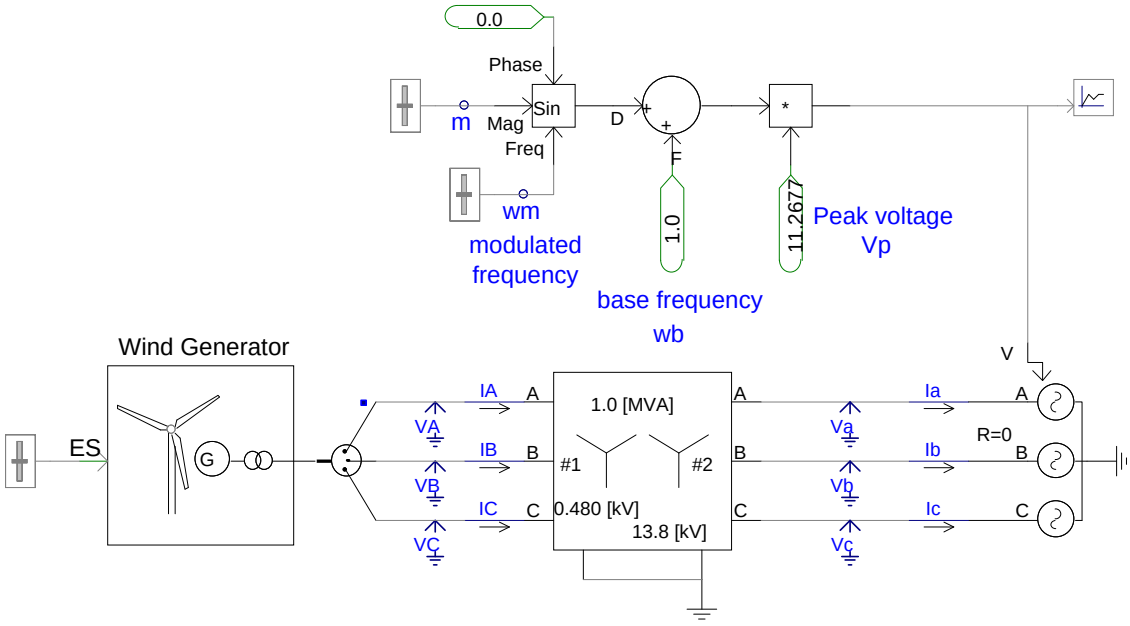


Figure 9.8: PSCAD®/EMTDC© simulated test system for perturbation analysis

The terminal voltage as shown in Fig. 9.8 is modulated at 5 Hz and 10 Hz. The corresponding time domain and frequency domain responses of blade-hub and hub-generator torques, as well as the machine speed are illustrated in Figs. 9.9, 9.10 and 9.11 respectively. The responses of the WTG unit without any frequency modulation are also presented for comparative analysis.

It is seen in Fig. 9.9(a) that the blade-hub torque response at a modulated frequency of 10 Hz does not change appreciably as compared to the torque response without any modulation. Fig. 9.9(b) illustrates that the torsional mode (with a torsional frequency $f_n$ = 4.98 Hz) will be excited for a modulated frequency of 10 Hz, but it is of very small value of 0.03 p.u. However, when the terminal voltage is modulated at 5 Hz, growing oscillations will be evidently seen as shown in Fig. 9.9(c). Fig. 9.9(d) demonstrates that the torsional mode will be excited when the voltage is modulated at 5 Hz, i.e. close to the torsional mode

of the WTG unit. It is observed that the blade-hub torque experience oscillatory response of 0.24 p.u. at 4.98 Hz.

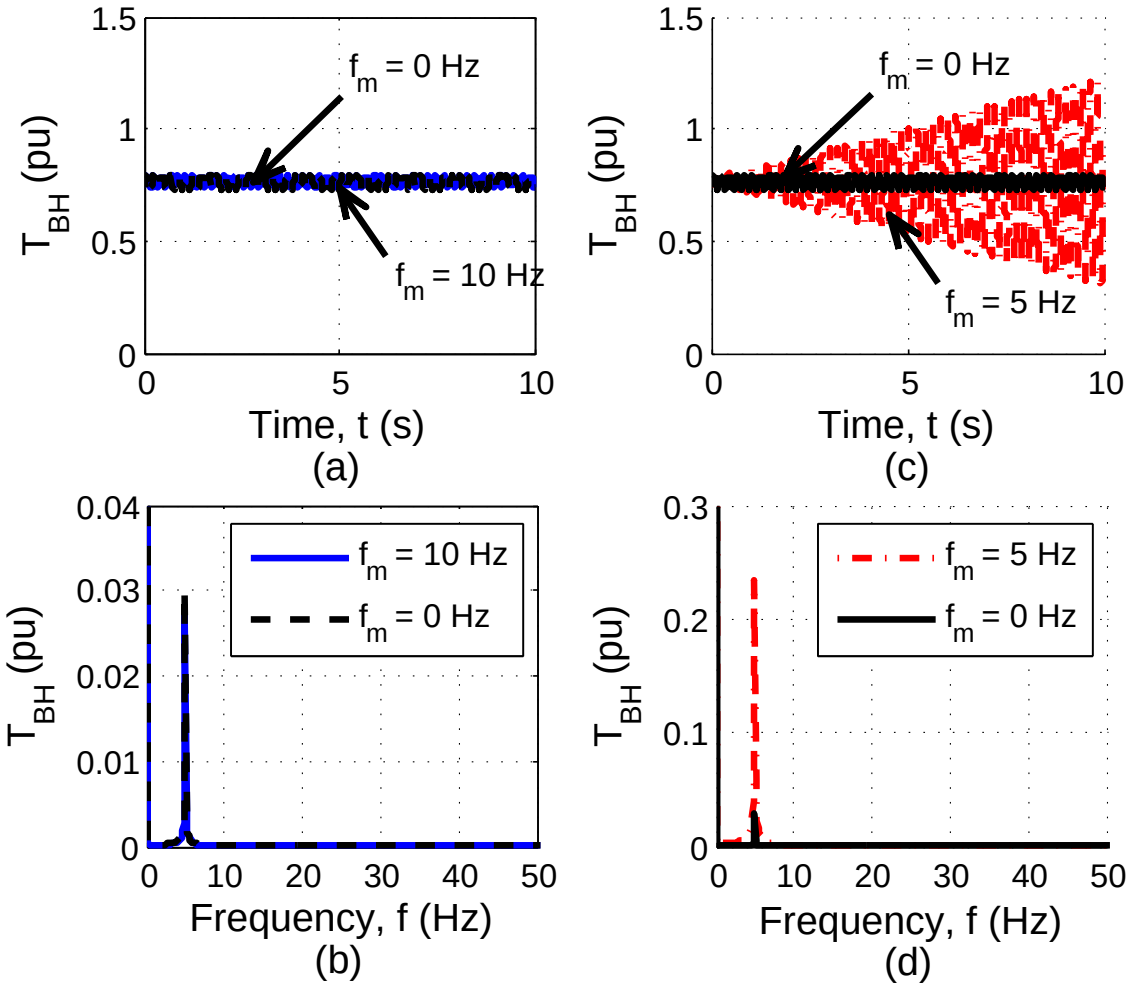


Figure 9.9: Time response and frequency spectrum of blade-hub torque at a modulated frequency

Similar time domain and frequency domain responses are observed for a hub-generator torque as demonstrated in Fig. 9.10. The growing oscillations in the hub-generator torque can be predominantly seen for a modulated frequency of 5 Hz as shown in Fig. 9.10(c), whilst the hub-generator torque settles down for a modulated frequency of 10 Hz as shown in Fig. 9.10(a). It can be evidently seen in Figs. 9.10(b) and 9.10(d) that the torsional mode oscillation at 10 Hz is of very small value (i.e. 0.00098 p.u.), compared to the one at a modulated frequency of 5 Hz (i.e. 0.0095 p.u.).

The machine speed oscillates at a larger value when the network side voltage is modulated at a frequency close to the torsional mode of the WTG unit. Accordingly, it can be seen in Figs. 9.11(a) and 9.11(c) that the speed deviation at a modulated frequency of 5 Hz is of larger magnitude as that of the one at a modulated frequency of 10 Hz. The torsional mode, however, has insignificant contribution to the rotor speed deviation as seen in Figs. 9.11(b) and 9.11(d).

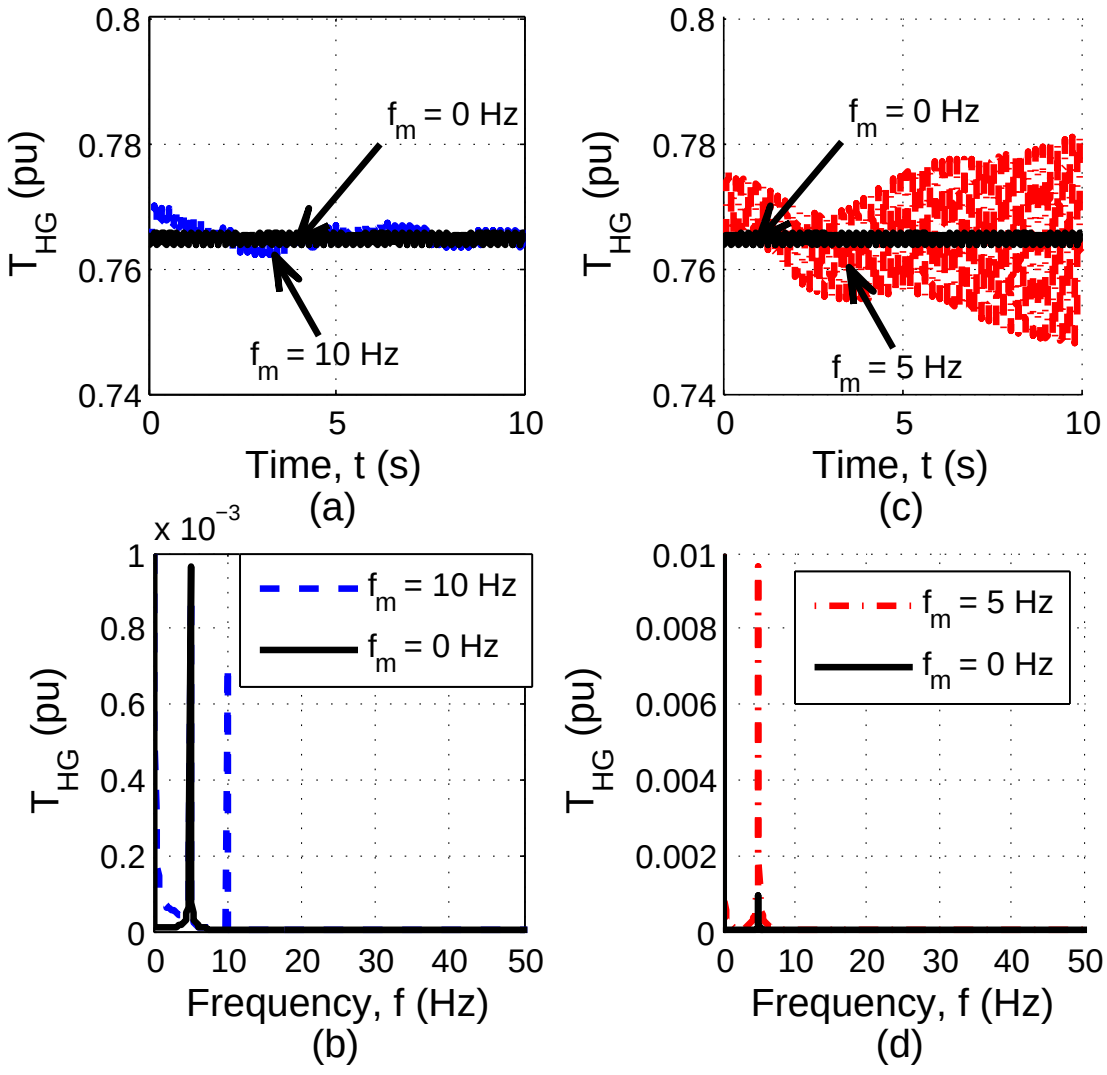


Figure 9.10: Time response and frequency spectrum of hub-generator torque at a modulated frequency

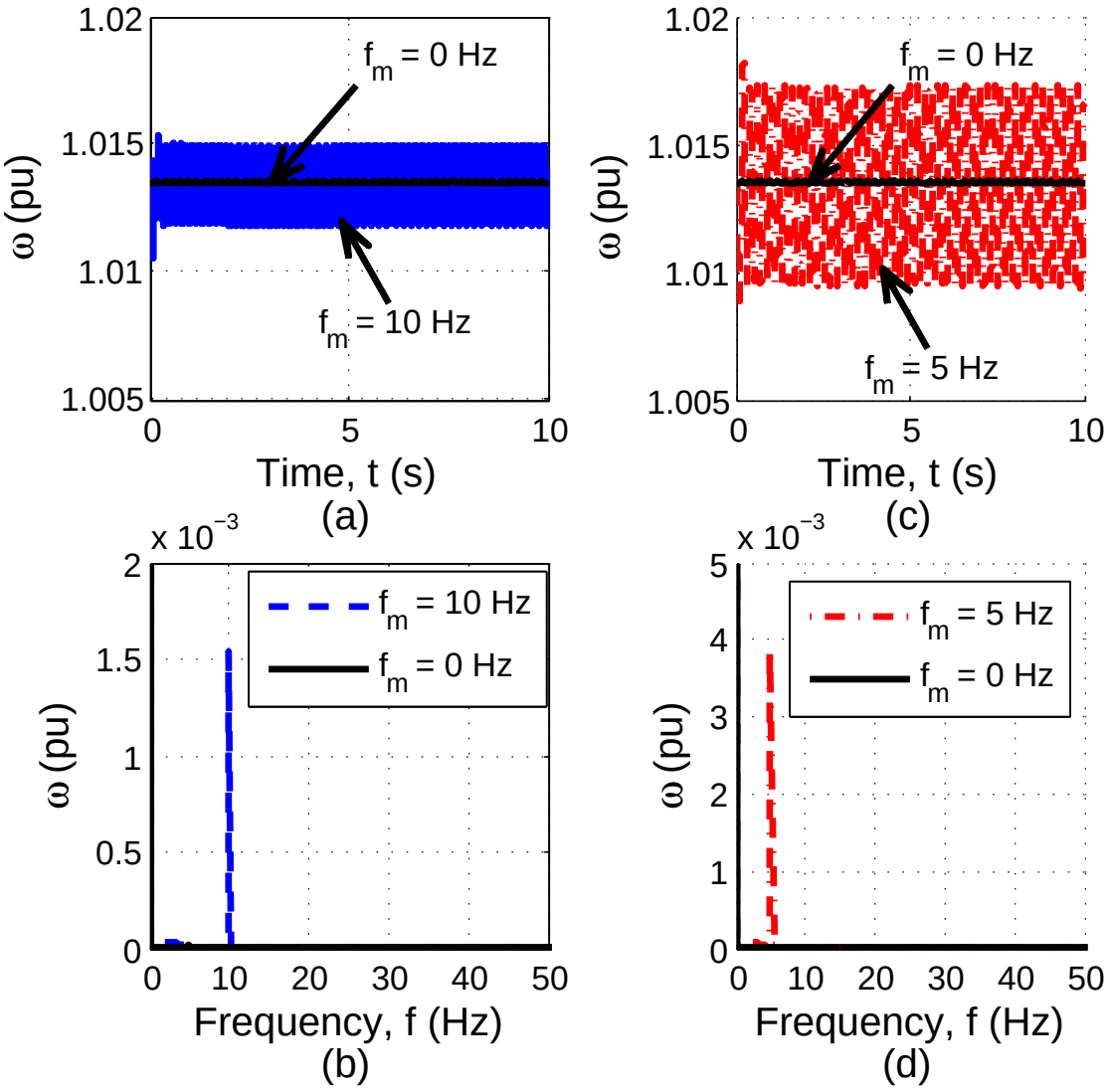


Figure 9.11: Time response and frequency spectrum of machine speed at a modulated frequency

### 9.6.2 WTG Response to Network Disturbances

Two case scenarios are now considered to investigate the SSTI behaviour of the WTG unit when connected in the close vicinity of HVDC system, i.e. a three-phase to ground fault at inverter station and a DC power flow reduction.

#### 9.6.2.1 Three-phase to ground fault at the inverter station

The interaction behaviour of the WTG unit of 1 MVA capacity has been examined by applying a three-phase to ground fault of 5 cycles on the inverter station at $t = 5$ s. The time domain simulation plot and the frequency spectrum for the blade-hub torsional torque ($T_{BH}$) and the hub-generator torsional torque ($T_{HG}$) of a WTG unit are shown in Figs. 9.12 – 9.15 for a three-phase to ground fault on the inverter side.

Figs. 9.12 and 9.13 show the corresponding time domain responses of the blade-hub and hub-generator torques with reference to the inverter side fault. Figs. 9.12(a) and 9.13(a) show the time domain responses in the time range of 0 – 100 s whilst Figs. 9.12(b) and 9.13(b) give a better illustration on the responses for a shortened time frame of 90 s $\leq t \leq$ 100 s. The oscillatory transient responses at 5 s as seen in Figs. 9.12(a) and 9.13(a) are due to the application of the three-phase to ground fault. The transient responses subside to steady-state as soon as the fault is cleared after 0.1 s. The oscillatory response of the blade-hub torque is of larger value (with a torque deviation of 0.07 p.u.) as seen in Fig. 9.12(b) compared to the hub-generator torque response in Fig. 9.13(b) (with a torque deviation of 0.002 p.u.).

It is seen in Figs. 9.14 and 9.15 that the oscillatory fluctuations of 4.98 Hz occur in both blade-hub and hub-generator torques when a three-phase to ground fault is applied at the inverter station. Some of the other low-frequency components of very small magnitude also appear in the blade-hub and hub-generator torques. Fig. 9.14 highlights a large oscillatory mode of 4.98 Hz with the torque deviation of 0.034 p.u. in the blade-hub torque. Fig. 9.15 demonstrates small oscillatory mode of 4.98 Hz in the hub-generator torque with a torque deviation of 0.0011 p.u.

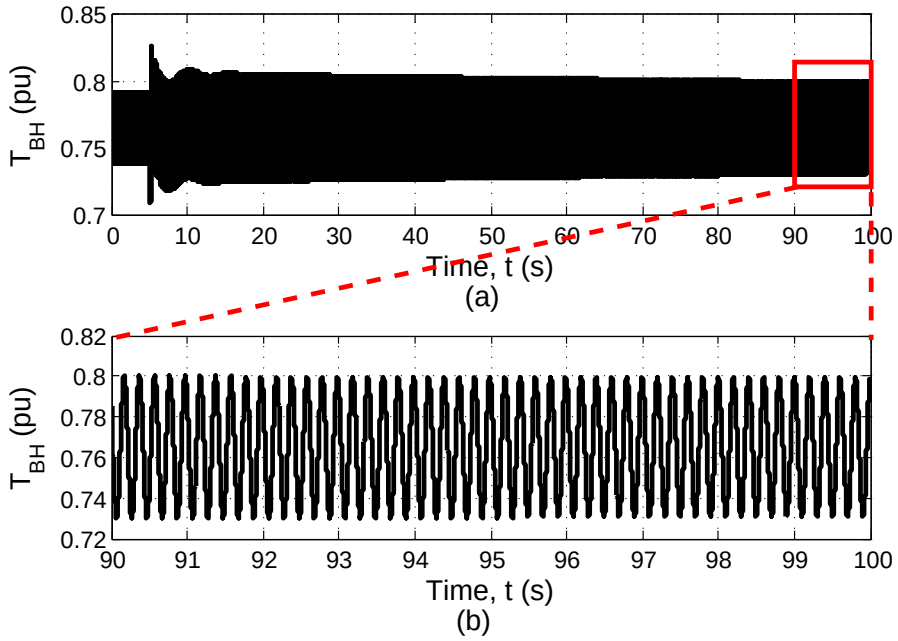


Figure 9.12: Time domain response of blade-hub torque for a three phase fault at the inverter station

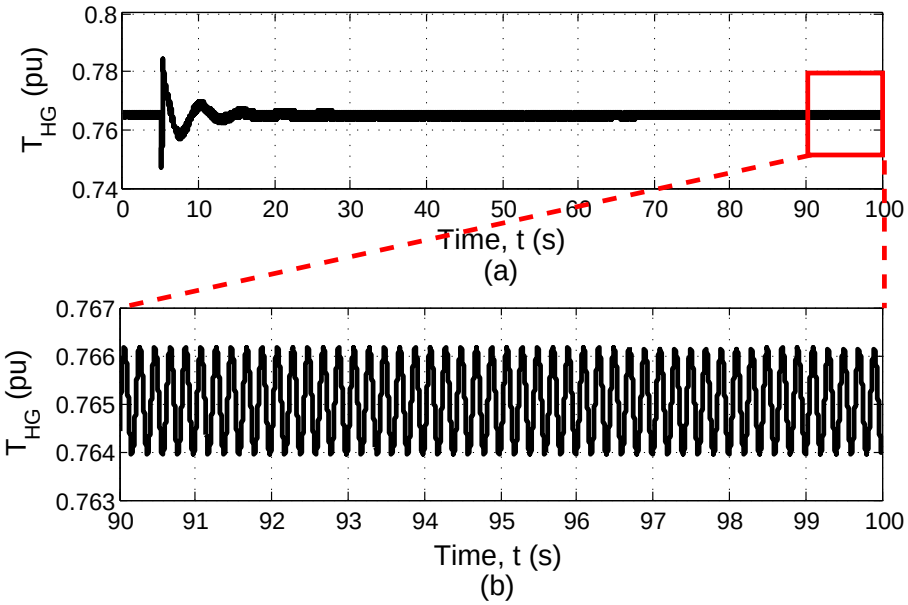


Figure 9.13: Time domain response of hub-generator torque for a three phase fault at the inverter station

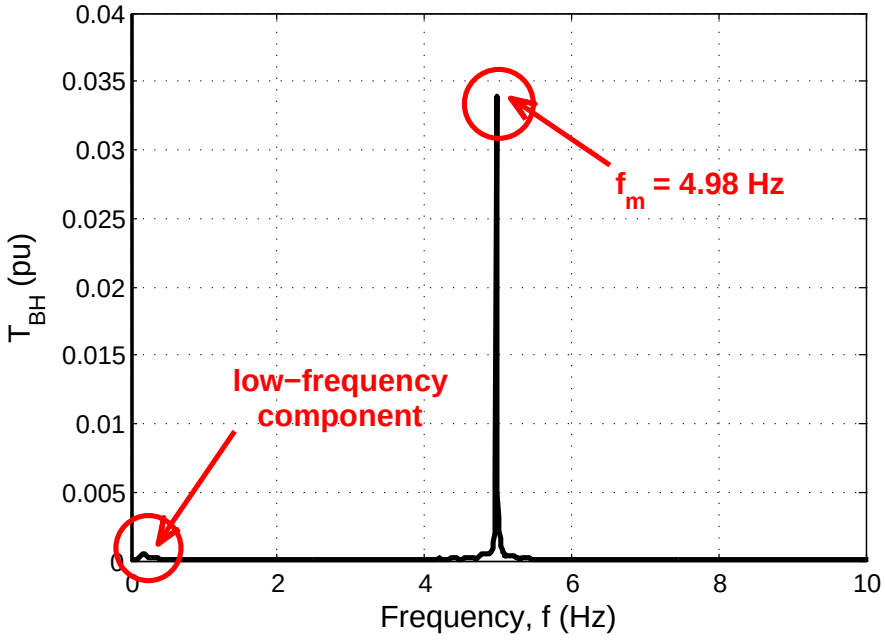


Figure 9.14: Frequency spectrum of blade-hub torque for a three phase fault at the inverter station

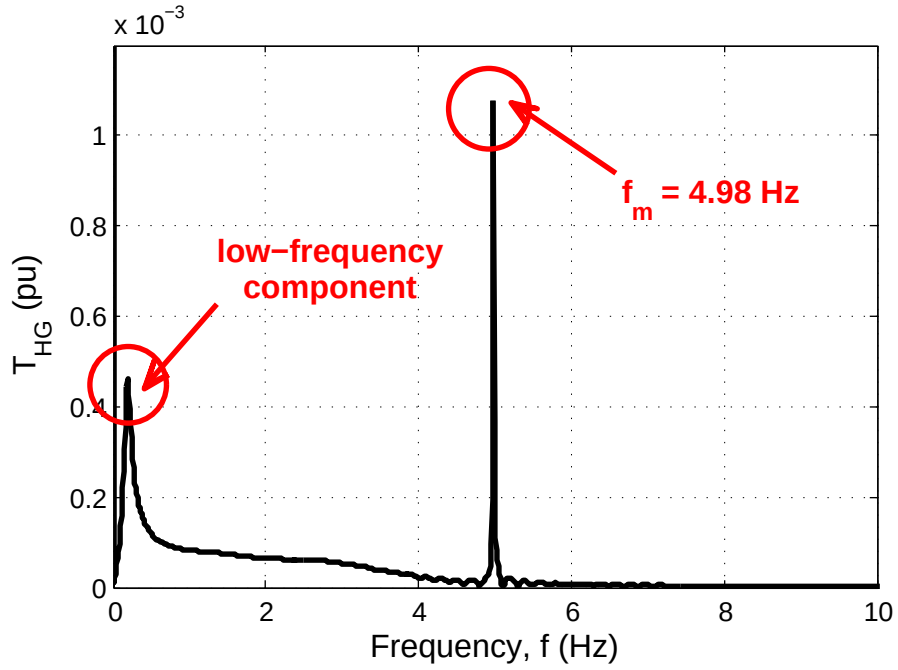


Figure 9.15: Frequency spectrum of hub-generator torque for a three phase fault at the inverter station

The time domain responses of the machine speed and the electromagnetic torque output of the WTG unit for an inverter side fault are illustrated in Figs. 9.16 and 9.17 respectively. Figs. 9.16(a) and 9.17(a) show the entire time domain responses of the machine speed and electromagnetic torque for 0 s $\leq t \leq$ 100 s, and oscillatory transient responses at 5 s is resulted from the application of the three-phase to ground fault at the inverter station. It is observed that the machine speed and the electromagnetic torque settle down very quickly after the disturbance at the inverter station. However, sustained oscillations from the disturbances result which can be seen in Figs. 9.16(b) and 9.17(b) respectively, in the shortened time range of 90 – 100 s.

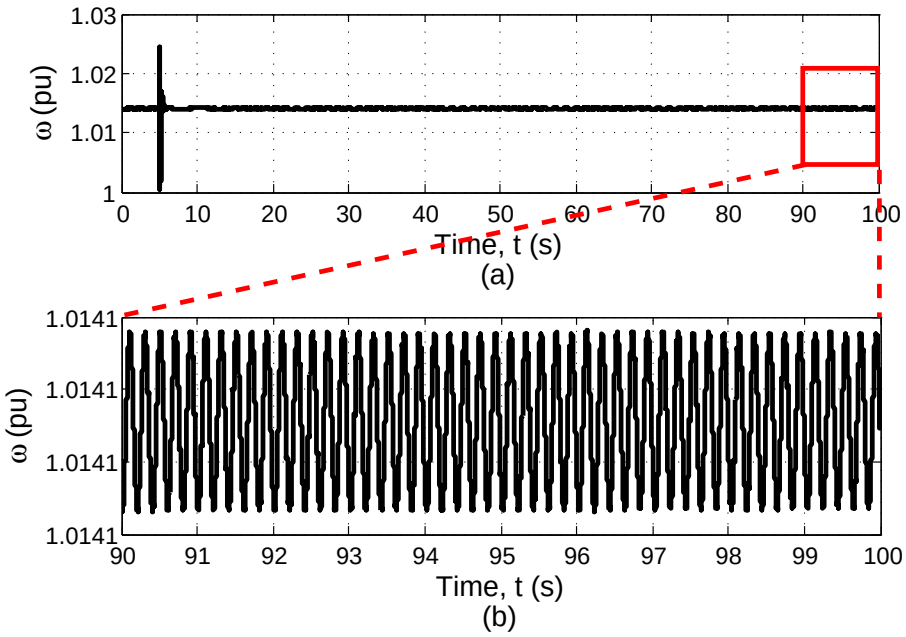


Figure 9.16: Time domain response of electrical speed for a three phase fault at the inverter station

### 9.6.2.2 Change in DC Power Flow

The behaviour of WTG unit is investigated by decreasing the DC power flow by 25%, i.e. from 1000MW to 750MW. The resulting time domain simulation plot and the frequency spectrum of the blade-hub torque $T_{BH}$ and hub-generator torque $T_{HG}$ are depicted in Figs. 9.18 – 9.21.

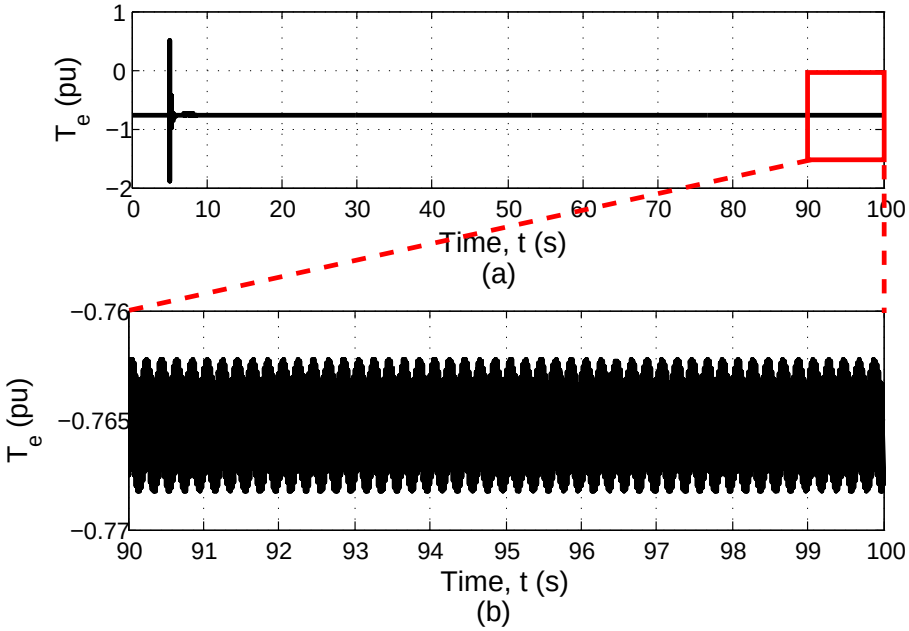


Figure 9.17: Time domain response of electromagnetic torque for a three phase fault at the inverter station

Figs. 9.18 and 9.19 illustrate the time domain responses of the blade-hub and the hub-generator torques resulting from a DC power flow change at $t = 5$ s. Figs. 9.18(a) and 9.19(a) show the entire time domain responses in the time range of 0 – 100 s whereas Figs. 9.18(b) and 9.19(b) depict torque responses in the shortened time range of 90 s $\leq t \leq$ 100 s. The oscillatory transient responses at 5 s as seen in Figs. 9.18(a) and 9.19(a) are due to the sudden change in DC power flow from 1000 MW to 750 MW. The blade-hub torque deviation as seen in Fig. 9.18(b) is of larger amplitude ($\approx$ 0.0375 p.u.) compared to the hub-generator torque deviation, which is of approximately 0.0011 p.u. as depicted in Fig. 9.19(b). The responses of blade-hub and hub-generator torques settle down after the reduction in the DC power flow, however the sustained oscillatory response can be seen throughout the simulation. The oscillatory time responses of the torsional torques in Figs. 9.18 and 9.19 contain numerous low-frequency components resulting from the change in DC power transfer. This is illustrated in Fig. 9.20 where the blade-hub torque component at 4.98 Hz dominates other low-frequency components and have a value of 0.018 p.u. On the other hand, the hub-generator torque has a lower value of 0.000625 p.u. at 4.98 Hz as

shown in Fig. 9.21.

The time domain response of machine speed is shown in Fig. 9.22. It can be seen that the electromagnetic torque fluctuation is between -0.7625 p.u. to -0.7675 p.u. in case of an inverter side fault as shown in Fig. 9.17 while the same is between -0.762 p.u. to -0.767 p.u. for a change in DC power flow as shown in Fig. 9.23. The transient responses resulted in Figs. 9.22(a) and 9.23(a) at 5 s are due to the sudden DC power flow reduction from 1000 MW to 750 MW.

The simulation results emphasise that there could be torsional oscillations in a WTG unit when it is connected in the close-vicinity of an HVDC system. The small frequency components of torsional torques are observed in a WTG unit due to the large turbine inertia, low generator inertia and low shaft stiffness. It is realised that the modelling of the shaft system will play key role in the SSTI analysis. It is also observed that the oversimplification of the shaft model may not adequately represent the torsional dynamics and the simulation results may be erroneous.

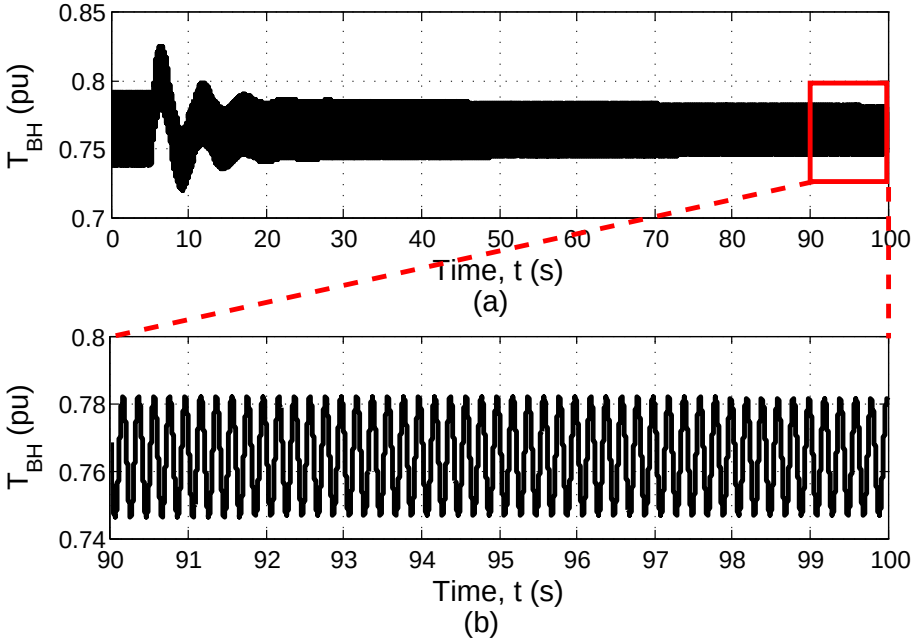


Figure 9.18: Time domain response of blade-hub torque for 25% decrement of DC power transfer

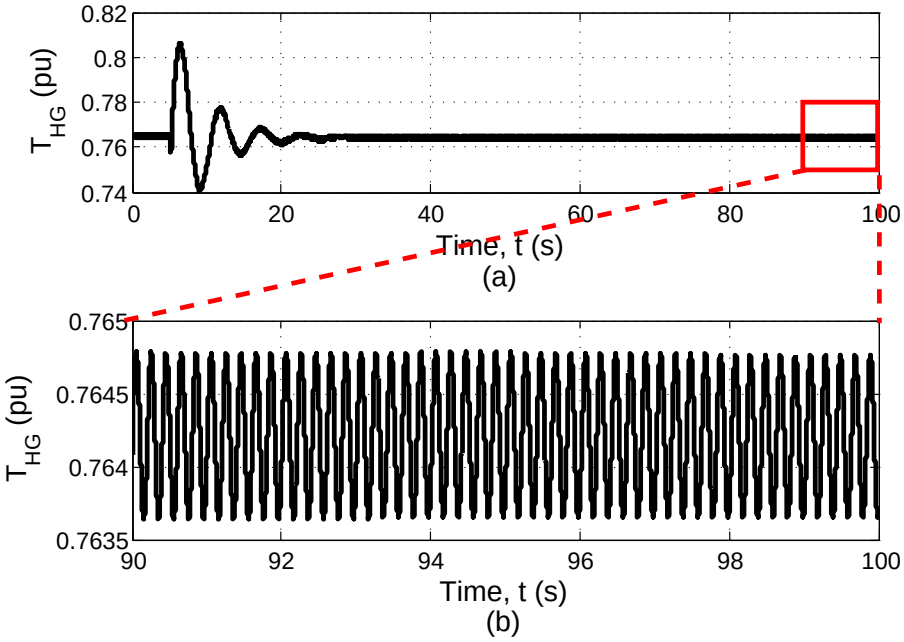


Figure 9.19: Time domain response of hub-generator torque for 25% decrement of DC power transfer

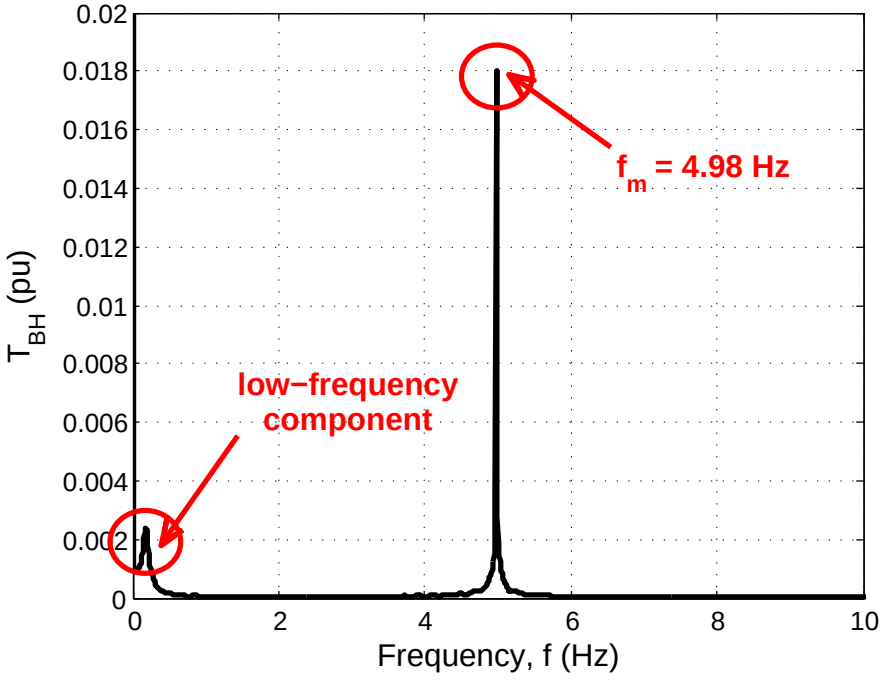


Figure 9.20: Frequency spectrum of blade-hub torque for 25% decrement of DC power transfer

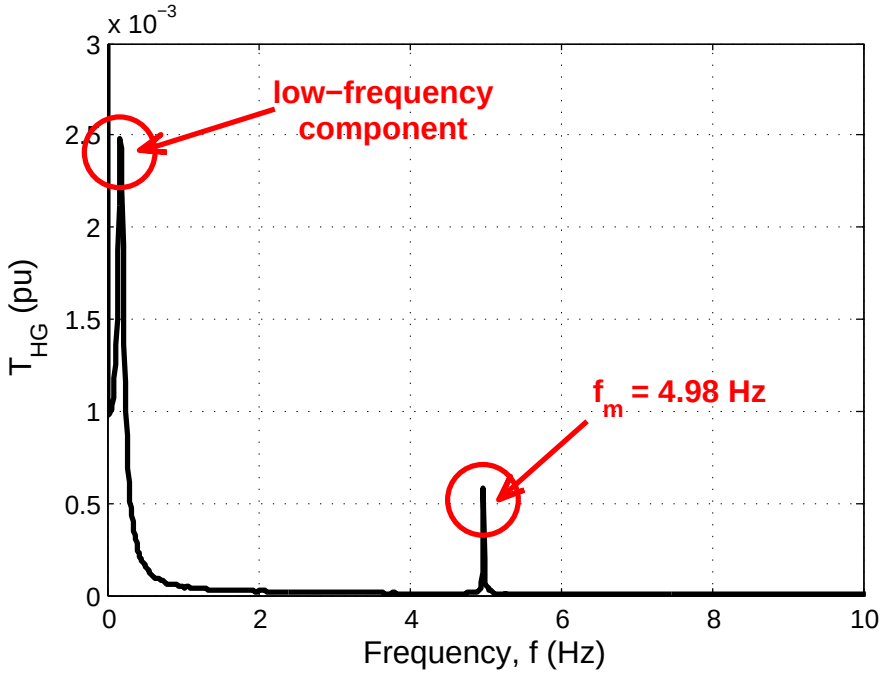


Figure 9.21: Frequency spectrum of hub-generator torque for 25% decrement of DC power transfer

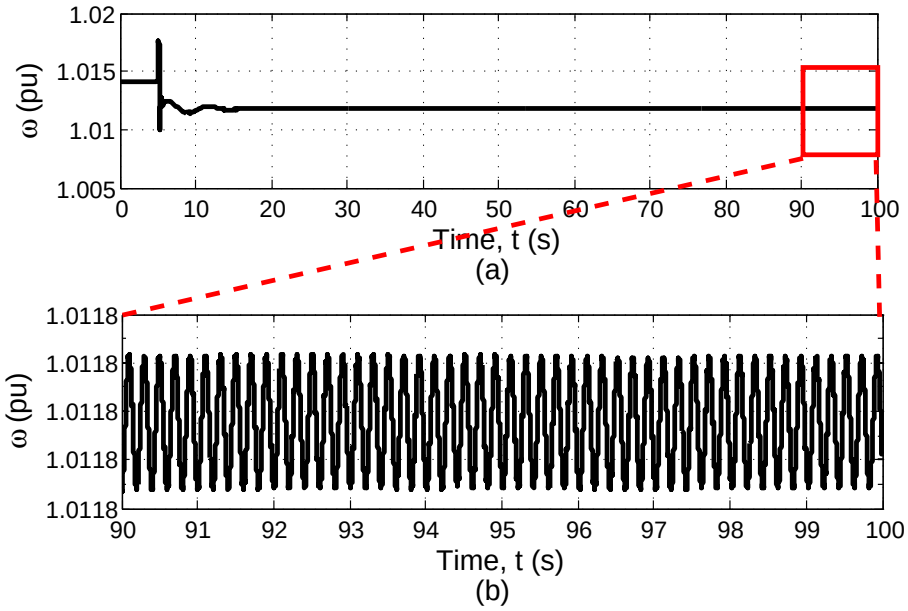


Figure 9.22: Time domain response of electrical speed for 25% decrement of DC power transfer

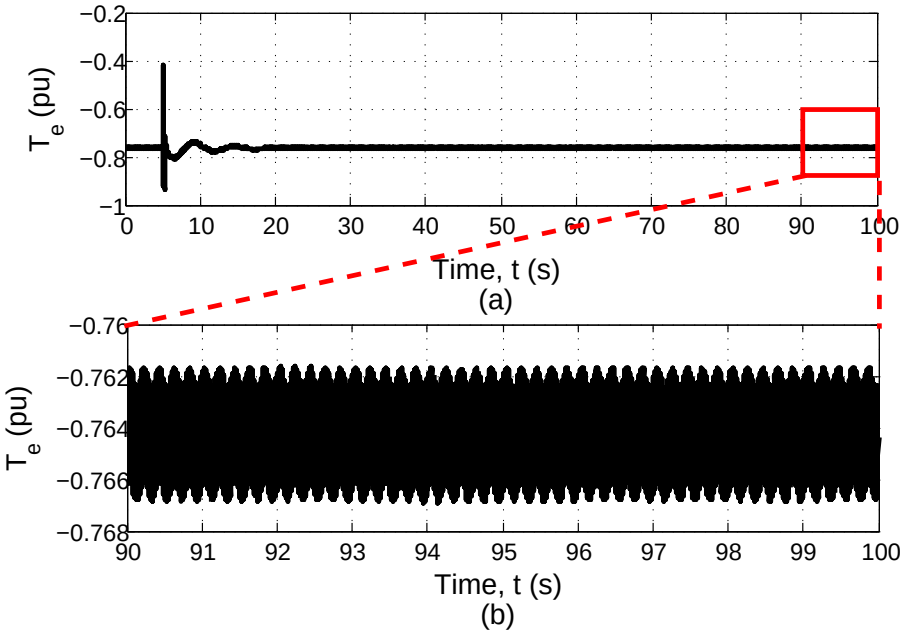


Figure 9.23: Time domain response of electromagnetic torque for 25% decrement of DC power flow

## 9.7 Summary

This chapter investigates the SSTI behaviour of a fixed-speed induction machine based WTG unit using time domain simulation studies conducted in PSCAD®/EMTDC© environment. The perturbation analysis has been conducted for a WTG unit to analyse the time response and frequency spectrum of different torque components at modulated frequencies. It is observed that there will be growing torque oscillations if the modulated frequency is close to the torsional mode of a WTG unit and the combined electromechanical system lacks damping. The torsional mode will be excited with the significant deviation in the torque components. In order to examine the effect of negative damping being introduced by the rectifier side current control of an HVDC system, the time domain simulation studies are conducted for a WTG unit interconnected to a CIGRE first HVDC benchmark system. The subsynchronous torsional behaviour of a WTG unit has been investigated under two case scenarios highlighting network disturbances i.e. a three-phase to ground fault at the inverter station and change in DC power flow. It is observed that the low-frequency tor-

sional mode will be excited for a WTG unit connected in the close vicinity of an HVDC system. The resulting oscillatory fluctuations in the blade-hub torque of a WTG unit are substantially high in comparison with the one in the hub-generator torque for the specified electrical disturbances. The torsional torques may eventually settle down after a certain time interval, however, the sustained torsional oscillations may result in fatigue damage and reduce the fatigue life of the mechanical shaft system.

## References


[1] A. Tabesh, R. Iravani, "Small-signal dynamic model and analysis of a fixed-speed wind farm - a frequency response approach," *IEEE Trans. Power Del.*, Vol. 21, No. 2, pp. 778–787, April 2006.

[2] S. K. Salman, A.L.J. Teo, "Windmill modeling consideration and factors influencing the stability of a grid-connected wind power-based embedded generator," *IEEE Trans. Power Syst.*, Vol. 18, No. 2, pp. 793–802 May 2003.

[3] Commodity Market Monthly, accessed 1 Mar 2015. URL `http://www.imf.org/external/np/res/commod/pdf/monthly/091114.pdf`

[4] Karel Beckman, Global renewable energy at the cross-roads, accessed 1 Mar 2015. URL `http://www.energypost.eu/global-renewable-energy-cross-roads/`

[5] E.N. Hinrichsen, P.J. Nolan, "Dynamics and stability of wind turbine generators," *IEEE Trans. Power App. Syst.*, Vol. PAS-101, No. 8, pp. 2640–2648, August 1982.

[6] O. Wasynczuk, D.T. Man, J.P. Sullivan, "Dynamic behavior of a class of wind turbine generators during random wind fluctuations," *IEEE Trans. Power App. Syst.*, Vol. PAS-100, No. 6, pp. 2837–2845, June 1981.

[7] P. Pourbeik, R.J. Koessler, D.L. Dickmander, W. Wong, "Integration of large wind farms into utility grids (part 2 - performance issues)," *Proc. of IEEE Power Engineering Society General Meeting*, pp. 1520-1525, 2003.

[8] M. Bahrman, E.V. Larsen, R.J. Piwko, H.S. Patel, "Experience with HVDC - turbine-generator torsional interaction at square butte," *IEEE Trans. Power App. Syst.*, Vol. PAS-99, No. 3, pp. 966-975, May/June 1980.

[9] L. Harnefors, "Analysis of Subsynchronous Torsional Interaction With Power Electronic Converters," *IEEE Trans. Power Syst.*, Vol. 22, no. 1, pp. 305-313, Feb. 2007.

[10] ABB Experience in the analysis of wind farms and their interconnection to utility grids, accessed 1 May 2010. URL `http://www05.abb.com/global/scot/scot221.nsf/veritydisplay/952ce63c8e46f738c1256fda003b4d69`

[11] S. Heier. *Grid Integration of Wind Energy Conversion Systems.* John Wiley & Sons, 1998.

[12] P. M. Anderson, A. Bose, "Stability simulation of wind turbine systems," *IEEE Trans. Power App. Syst.*, Vol. PAS-102, No. 12, pp. 3791–3795, December 1983.

[13] P. Kundur. *Power System Stability and Control.* McGraw-Hill, 1994.

[14] O. Anaya-Lara, N. Jenkins, J. Ekanayake, P. Cartwright, M. Hughes. *Wind Energy Generation Modelling and Control.* John Wiley & Sons, 2009.

[15] P.C. Krause, O. Wasynczuk, S. D. Sudhoff, *Analysis of Electric Machinery.* The Institute of Electrical and Electronics Engineers, Inc., New York, 1995.

[16] K.R. Padiyar *Analysis of Subsynchronous Resonance in Power Systems.* Kluwer Academic Publishers, 1999.

[17] Y.C. Choo, A.P. Agalgaonkar, K.M. Muttaqi, S. Perera, M. Negnevitsky, "Subsynchronous torsional behaviour of a hydraulic turbine-generator unit connected to a HVDC system, " *Proc. of Australasian Universities Power Engineering Conf. (AUPEC 2008)*, Sydney, New South Wales, 14th – 17th December 2008.

[18] T. Ackermann. *Wind Power in Power Systems.* John Wiley & Sons, 2005.

[19] R.K. Varma, S. Auddy, Y. Semsedini, "Mitigation of subsynchronous resonance in a series-compensated wind farm using FACTS controllers," *IEEE Trans. Power Del.*, Vol. 23, No. 3, pp. 1645–1654, July 2008.

[20] S.M. Muyeen, M.H. Ali, R. Takahashi, T. Murata, J. Tamura, "Damping of blade-shaft torsional oscillations of wind turbine generator system," *Electric Power Components and Systems*, 36:2, pp. 195–211, 2008.

[21] M. Szechtman, T. Wess, C.V. Thio, "First benchmark model for HVDC control studies," *Electra*, no. 135, pp. 54–73, Apr. 1991.

[22] IEEE Subsynchronous Resonance Working Group, "Proposed terms and definitions for subsynchronous oscillations," *IEEE Trans. Power App. Syst.*, Vol. PAS-99, No. 2, pp. 506–511, March/April 1980.

[23] K. Mortensen, E.V. Larsen, R.J. Piwko, "Field tests and analysis of torsional interaction between the coal creek turbine-generators and the CU HVDC system," *IEEE Trans. Power App. Syst.*, Vol. PAS-100, No. 1, pp. 336-344, Jan. 1981.

# Chapter 10

# Analysis of Subsynchronous Torsional Interaction of HVDC System Integrated Hydro Units with Small Generator-to-Turbine Inertia Ratios


### Abstract

The constant current controllers at HVDC rectifier stations and the outer loops which set the reference to the current controller have potential to introduce negative damping on the nearby generating units. It is therefore vital to investigate the torsional interaction behaviour between TG units and the HVDC systems over a frequency range of interest. In this chapter, SSTI phenomenon for hydroelectric TG units with small generator-to-turbine inertia (GTI) ratios interconnected to an HVDC system has been investigated. The sensitivity of different system parameters, such as generating capacity and loading, DC power flow, AC network strength and current controller gains, towards electrical damping

contribution is also examined. Hydro units with different shaft systems are examined for SSTI proneness by conducting perturbation analysis. The impact of hydroelectric TG units with different GTI ratios has also been examined by applying a three-phase to ground fault at the rectifier station. Simulation studies have been carried out in PSCAD®/EMTDC© environment. Due to lack of modal damping with relatively low decrement factor and logarithmic decrement, sustained and growing TG torque oscillations are noted for certain operating conditions of hydro units with small GTI ratios interconnected with an HVDC system.

## 10.1 Introduction

SSTI between a steam TG unit and an HVDC system received deliberate attention especially after the field tests at Square Butte, North Dakota, USA revealed the undesirable interactions between the HVDC terminal and an electrically-close TG unit [1]. The increasing complexity of the electrical network as well as the stressed system conditions under various contingencies demand dynamic interaction studies from stability perspective.

To date, various research aspects associated with SSTI behaviour of turbogenerators have been reported in the literature. However, limited number of research studies have been conducted for hydroelectric TG units, especially in the close vicinity of HVDC systems, due to the fact that the high inherent GTI ratios of hydro units enhance the modal damping at torsional frequencies, thereby minimising the risk of sustained torsional oscillations [2]. Unlike Francis and Pelton wheels, Kaplan units could be more prone to SSTI due to their torsional frequencies within the negative damping frequency range of normal DC operation [3]. Authors of [3] have also indicated that the hydroelectric TG units with a low GTI ratio may be susceptible to SSTI problem. However, thorough investigations for different system conditions are required to depict the realistic behaviour of hydroelectric TG units connected to HVDC systems. Moreover, it is very important to investigate the hydroelectric TG response for network side perturbations and the effect of negative damping posed by an HVDC current controller and the outer loops which set the reference to the

current controller. This is because there could be certain network conditions such as close association of an HVDC system with a hydroelectric unit with small GTI ratio, wherein the negative damping introduced by the HVDC current controller and the outer loops which set the reference to the current controller may trigger sustained torsional oscillations on the shaft of the machine [3].

The complex torque coefficients method has been proposed in [4, 5] for SSTI analysis of TG sets. The interaction phenomenon for the electrical and the mechanical systems has been explained in [4] while the applicability of the proposed approach on a test network is presented in [5]. Complex torque analysis computes the change in electromagnetic torque in terms of synchronising and damping torque components [4, 6]. It facilitates the formulation of state-space model and transfer function representation of each power system component [6]. The system stability can be assured if the electrical damping is positive for the requisite frequency range of interest. The proof of the positive-net-damping stability criterion has been presented in [7] using the Nyquist criterion. The clarification has also been made in [7] that the net damping should be assessed for the open-loop resonances, as well as for low frequencies where the loop gain goes beyond unity.

The multi-infeed HVDC interactions have been analysed in [8] using small-signal analysis and verified with the aid of PSCAD®/EMTDC©. The application of frequency-domain analysis for investigating SSTI between synchronous machine and a current-controlled voltage source converter (VSC) has been demonstrated in [6]. The subsynchronous resonance characteristic of the VSC-based HVDC using damping torque analysis, eigenvalue analysis, and transient simulation studies has been investigated in [9]. The performance indices to assess torsional damping and system susceptibility to experience torsional oscillations have been presented in [10]. The evaluation and enhancement of small signal stability of a renewable-energy-based electricity distribution system have been detailed in [11] while hydrokinetic-energy-conversion systems, which consists of a number of cascaded stages, are studied in [12, 13]. The development of high performance control systems for an HVDC converter connected to a weak AC network is described in [14].

A sustained subsynchronous power oscillation, however, was observed within the normal frequency range of hydropower unit torsional modes during a startup test of an electrical island in the Nordic power system although hydroelectric units are not known to be relatively susceptible to SSTI [15]. It was noted that self-excitation may happen due to the induction generator effect regardless of the inertia ratio and the mechanical damping if the electrical network size is small. This stability criterion is governed by the total effective resistance of the electrical system at the resonance frequency. Turbine damping and the inertia ratio are the most vital factors which decide the stability condition close to the stability boundary [15].

This chapter aims to investigate SSTI phenomenon for HVDC system integrated hydro units under different system conditions. Damping torque analysis has been carried out to determine the degree of sensitivity of system parameters, such as hydroelectric unit with different power output capacities and loading levels, varying power flows through a DC link, different levels of AC system strength and current controller gains towards electrical damping contribution. Perturbation analysis is conducted to assess the dynamic response of a hydroelectric unit with different GTI ratios.

The chapter is structured as follows. Section 10.2 describes the system model. Section 10.3 describes the modal analysis of a hydroelectric TG unit. Section 10.4 outlines the effect of HVDC constant current controller on electrical damping and illustrates the methodology to investigate system stability. The hydroelectric unit integrated to CIGRE first HVDC benchmark system has been used as a test case and presented in Section 10.5. Simulation results are presented in Section 10.6. The chapter is concluded in Section 10.7.

## 10.2 System Model

For representing the system model involving generator, HVDC system and AC system, the dynamic characteristics of the power system, described by a set of first order non-linear differential-algebraic equations, are linearised at an equilibrium point [16]. The overall system dynamics are represented in the synchronously rotating $dq$ reference frame fixed in

the rotor.

### 10.2.1 Linearised Synchronous Machine Model

A three-phase salient pole synchronous machine is modeled in detail to represent the hydroelectric TG unit. The equivalent circuits of $dq$-axes are shown in Figs. 10.1(a) and (b) respectively. The rotor of a hydroelectric unit normally comprises of a field winding and an armortisseur (damper) winding on the direct axis and a damper winding on the quadrature axis. The linearised machine model has the following state-space representation [16, 17]:

$$\begin{bmatrix} \Delta\dot{\psi}_d \\ \Delta\dot{\psi}_q \\ \Delta\dot{\psi}_{fd} \\ \Delta\dot{\psi}_{kd} \\ \Delta\dot{\psi}_{kq} \\ \Delta\frac{\dot{\omega}_r}{\omega_s} \\ \Delta\dot{\delta}_r \end{bmatrix} = \begin{bmatrix} A_{sm} \end{bmatrix} \begin{bmatrix} \Delta\psi_d \\ \Delta\psi_q \\ \Delta\psi_{fd} \\ \Delta\psi_{kd} \\ \Delta\psi_{kq} \\ \Delta\frac{\omega_r}{\omega_s} \\ \Delta\delta_r \end{bmatrix} + \begin{bmatrix} B_{sm} \end{bmatrix} \begin{bmatrix} \Delta v_d^e \\ \Delta v_q^e \\ \Delta v_{fd}'^r \\ \Delta v_{kd}'^r \\ \Delta v_{kq}'^r \end{bmatrix} \tag{10.1}$$

where, the state vector of the synchronous machine comprises of state variables $d$- and $q$- axes stator flux linkages per second ($\psi_d$ and $\psi_q$), rotor flux linkages per second for a field winding ($\psi_{fd}$) and for $d$- and $q$- axes damper windings ($\psi_{kd}$ and $\psi_{kq}$), rotor speed ($\omega_r$), nominal frequency ($\omega_s$) and rotor angle ($\delta_r$). The input vector comprises of $d$- and $q$- axes voltage referred to the synchronous rotating reference frame ($v_d^e$ and $v_q^e$) and voltages referred to a reference frame fixed in the rotor ($v_{fd}'^r$, $v_{kd}'^r$ and $v_{kq}'^r$). $A_{sm}$ is the state matrix and $B_{sm}$ is the input matrix. Appendix A details the small-signal state space modelling of the individual power system subsystems. The components of the state matrix and the input matrix are presented in the appendix.

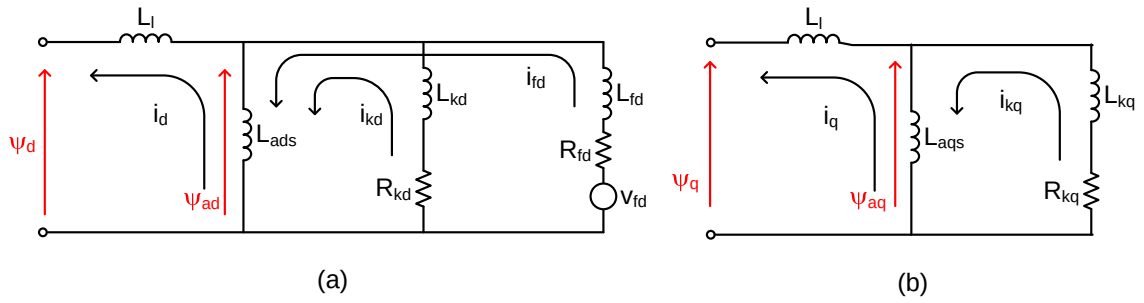


Figure 10.1: Equivalent circuits of $dq$-axes for synchronous machine

### 10.2.2 Linearised HVDC System

The T-model of an HVDC system, as shown in Fig. 10.2, has a linearised, state-space formulation as follows:

$$\begin{bmatrix} \Delta\dot{I}_{dr} \\ \Delta\dot{I}_{di} \\ \Delta\dot{V}_{dm} \end{bmatrix} = \begin{bmatrix} -\frac{R_d}{L_d} & 0 & -\frac{1}{L_d} \\ 0 & -\frac{R_d}{L_d} & \frac{1}{L_d} \\ \frac{1}{C_d} & -\frac{1}{C_d} & 0 \end{bmatrix} \begin{bmatrix} \Delta I_{dr} \\ \Delta I_{di} \\ \Delta V_{dm} \end{bmatrix} + \begin{bmatrix} \frac{1}{L_d} & 0 \\ 0 & -\frac{1}{L_d} \\ 0 & 0 \end{bmatrix} \begin{bmatrix} \Delta V_{dr} \\ \Delta V_{di} \end{bmatrix} \tag{10.2}$$

where, the three state variables are the dc-side currents at rectifier and inverter stations ($I_{dr}$ and $I_{di}$) and the capacitor voltage at the middle point of the DC transmission line ($V_{dm}$). The two inputs are the direct voltages at rectifier and inverter stations ($V_{dr}$ and $V_{di}$) respectively.

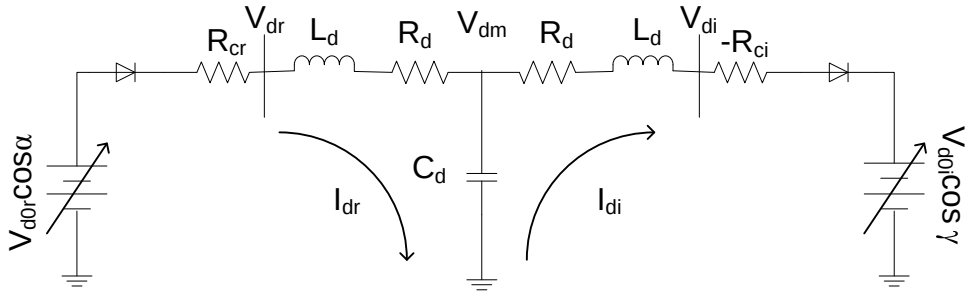


Figure 10.2: HVDC T-model transmission line

The direct voltage and current can be manipulated by controlling the internal voltages ($V_{d0r}\cos\alpha$ and $V_{d0i}\cos\gamma$). $V_{d0r}$ and $V_{d0i}$ refer to the ideal no-load direct voltages at rectifier

and inverter stations respectively, $\alpha$ is the ignition delay angle and $\gamma$ is the extinction advance angle [16].

### 10.2.3 Linearised AC Electrical Network

An electrical network comprises of an impedance connected in series with the generator ($Z_{SM}$), an ac system connected in parallel to the generator ($Z_{sys}$) and filter impedance ($Z_{filter}$).

The impedances, in general, have the following representation in the $dq$-reference frame [17]:

$$Z = \begin{bmatrix} R + sL & -\omega_s L \\ \omega_s L & R + sL \end{bmatrix} \tag{10.3}$$

where, $R$ is the resistance and $L$ is the inductance.

Accordingly, the $dq$ component of voltage can be expressed as:

$$\Delta V_{dq} = [Z_{SM} + (Z_{sys}^{-1} + Z_{filter}^{-1})^{-1}]\Delta I_{dq} \tag{10.4}$$

### 10.2.4 Interface between AC and DC Systems

The linearised state-space model for each subsystem has been represented individually as shown in Subsections 10.2.1, 10.2.2 and 10.2.3. The linearised representation of the ac-dc interaction equations derived from the power balance equation, as in (10.5), highlights the small-signal inter-relationship between ac and dc systems as shown below:

$$\begin{bmatrix} \Delta i_{acr} \\ \Delta \phi_{acr} \end{bmatrix} = \begin{bmatrix} 0 & 0 & \frac{\sqrt{6}}{\pi} B_r T_r \\ x_{acdc1} & \frac{\sin \alpha_0}{\sin \phi_{acr0}} & x_{acdc2} \end{bmatrix} \begin{bmatrix} \Delta v_{acr} \\ \Delta \alpha \\ \Delta I_{dr} \end{bmatrix} \tag{10.5}$$

where, $x_{acdc1} = -\frac{X_{cr} I_{dr0}}{\sqrt{2} T_r v_{acr0}^2 \sin \phi_{acr0}}$ and $x_{acdc2} = \frac{X_{cr}}{\sqrt{2} T_r v_{acr0} \sin \phi_{acr0}}$, $i_{ac}$ = RMS value of the alternating current at fundamental frequency, $\phi_{ac}$ = phase angle between fundamental line

current and the line-to-neutral source voltage, $v_{ac}$ = line-to-line voltage of an ac system, $B$ = number of bridges in series, $T$ = transformer ratio, $X_c$ = commutating reactance, subscript $r$ represents the rectifier-side and subscript 0 denotes the initial operating condition.

Since each subsystem has been represented in a different reference frame, all the variables need to be transformed into common reference frame before the integration of different subsystems.

## 10.3 Modal Analysis of a Hydroelectric Turbine-Generator Unit

The mechanical shaft system of a hydroelectric TG unit typically consists of three rotor masses, which are turbine, generator and exciter. It can be represented as a lumped mass-spring-damper system. The torsional oscillations can be mathematically represented by the equation of motion [18]:

$$2H\ddot{\theta} + D\dot{\theta} + K\theta = T \tag{10.6}$$

where $H$ is the diagonal matrix of inertia constant for all three masses, $D$ and $K$ are tridiagonal symmetric matrices of damping coefficient and spring stiffness respectively. $\theta$ is the vector of rotor angle whilst $T$ is the vector of the externally applied torque.

Modal analysis can be performed on the system represented by (10.6) with the substitution of $\theta = Q\theta_m$ as modal angle transformation and premultiplication of $Q^t$, where $Q$ is the transformation matrix, $Q^t$ is the transpose of $Q$ and $\theta_m$ is the modal angle [18].

$$2Q^tHQ\ddot{\theta}_m + Q^tDQ\dot{\theta}_m + Q^tKQ\theta_m = Q^tT \tag{10.7}$$

Equation (10.7) can be rewritten as follows:

$$2H_m\ddot{\theta}_m + D_m\dot{\theta}_m + K_m\theta_m = Q^tT \tag{10.8}$$

where $H_m$, $D_m$ and $K_m$ denote the modal inertia, damping coefficient and shaft stiffness

matrices respectively. Equation (10.8) is in decoupled form, wherein $H_m$, $D_m$ and $K_m$ matrices are in diagonal form with the proper selection of $Q$.

Consider a two-mass hydroelectric unit with turbine and generator rotor. The modal inertia ($H_m$), modal damping coefficient ($D_m$), decrement factor ($\sigma_m$) and logarithmic decrement ($\delta_m$) for the torsional mode ($f_n$) of the modal system can be represented as follows [3, 18]:

$$H_m = GTI\,(H_{tur} + H_{gen}) \tag{10.9}$$

$$D_m = GTI^2 D_{tur} + D_{tg}(GTI + 1)^2 \tag{10.10}$$

$$\sigma_m = \frac{D_m}{4H_m} \tag{10.11}$$

$$\delta_m = \frac{\sigma_m}{f_n} \tag{10.12}$$

where GTI is the generator-to-turbine inertia ratio and the subscripts '*gen*' and '*tur*' refer to generator and turbine respectively, and '*tg*' refers to turbine-generator.

For a high GTI ratio, the modal inertia of the shaft system is large as indicated by (10.9). This large modal inertia subsequently reduces the decrement factor of the electrical damping ($\sigma_e$), which is described as follows [9]:

$$\sigma_e = \frac{D_e}{4H_m} \tag{10.13}$$

where $D_e$ is the electrical damping coefficient.

The inherent mechanical modal torsional damping may become adequate to counteract the effect of negative damping posed by HVDC current-controller. A thorough investigation of this particular aspect has been conducted in this chapter for a hydroelectric generator connected to an HVDC system.

Torsional interactions are principally a transient torque phenomenon, and they arise as a result of normal switching operations and faults. Significant torque oscillations at torsional frequencies are caused by a switching incident on the transmission system [19].

If the complement of the system resonance frequency is close to the mechanical torsional mode frequency and the combined electro-mechanical system lacks in system damping, then it may result in sustained or growing torsional oscillations in torque and subsequently result in instability [20].

System SSTI stability can be determined by system modal decrement factor or logarithmic decrement as indicated by (10.11) and (10.12). The pictorial representation of the decrement factor is shown in Fig. 10.3 for a variation of turbine damping ($D_{tur}$) and generator-to-turbine inertia ratio. The hydroelectric unit may experience SSTI instability with sustained or growing torque oscillations for any combination of $D_{tur}$ and the GTI ratio that falls below the stability boundary as shown in Fig. 10.3. The decrement factor plot also depends on $D_{tg}$ as seen in (10.10), and for a higher $D_{tg}$, the system modal damping will be greatly improved. Accordingly, a wide range of turbine-generator damping has also been accounted in this chapter to analyse its impact on modal damping.

## 10.4 Effect of HVDC Constant Current Controller on Electrical Damping

This section discusses the effect of HVDC current controller on electrical damping for a hydro machine connected to an HVDC system. It is assumed that the commutating voltage and phase angle at the rectifier station of an HVDC system are strongly dependent on the generator internal bus [18].

Consider that the generator rotor is oscillating sinusoidally at a constant speed of $\omega_s$:

$$\omega_r = \omega_s + m\sin(\omega_m t) \tag{10.14}$$

where, $\omega_r$ is the rotor speed in rad/sec, $\omega_s$ is the nominal frequency in rad/sec, $m$ is the magnitude of the speed deviation, $\omega_m$ is the frequency of oscillation of the rotor speed in rad/sec, and $t$ is the time in sec.

With the changes in internal flux linkages neglected, the voltage induced in the armature of a generator is composed of three components, which are 1) nominal frequency ($\omega_s$), 2)

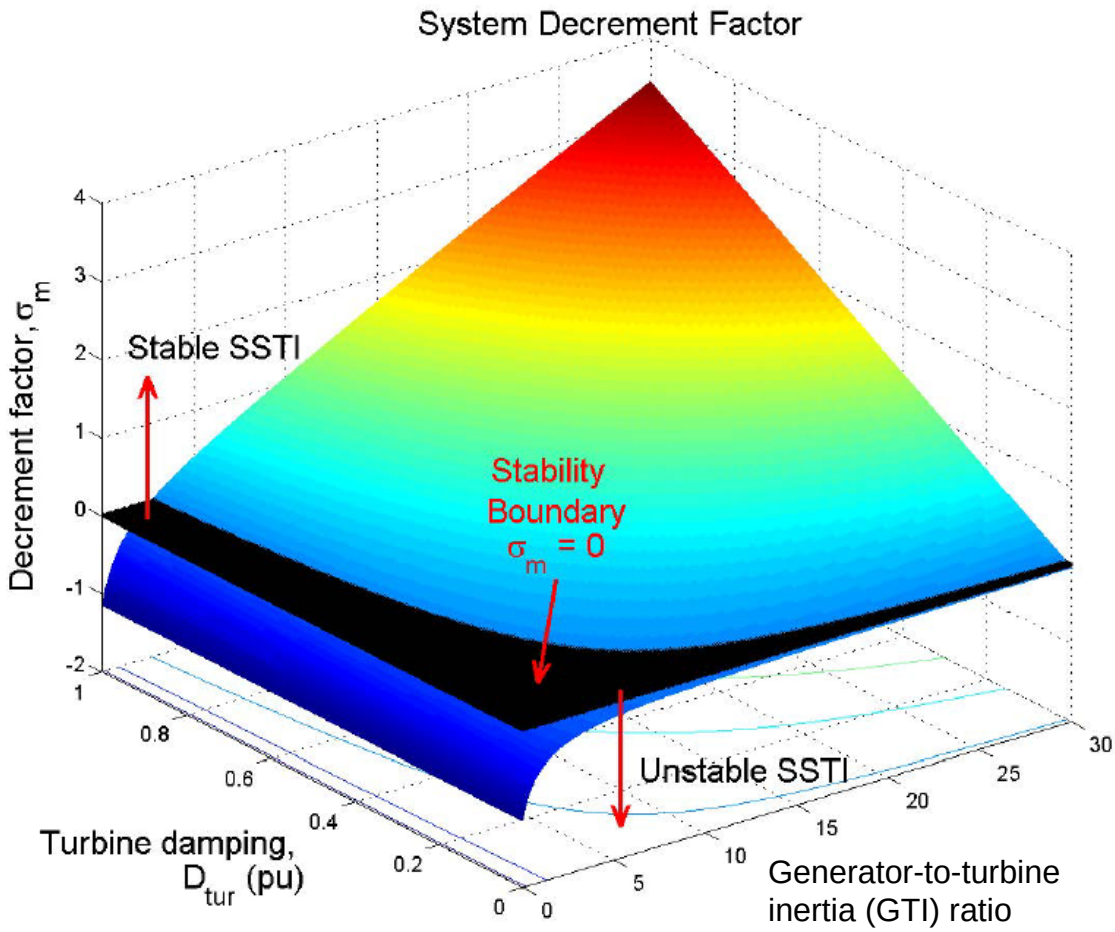


Figure 10.3: System modal decrement factor in determining SSTI stability

subsynchronous frequency ($\omega_s - \omega_m$), and 3) supersynchronous frequency ($\omega_s + \omega_m$) as seen in (10.15).

$$v_{ac} = V_p \cos(\omega_s t) - \frac{mV_p}{2} \sin(\omega_s - \omega_m)t + \frac{mV_p}{2} \sin(\omega_s + \omega_m)t \tag{10.15}$$

where $V_p$ is the amplitude of the fundamental ac voltage.

The HVDC system is considered to operate at normal conditions, i.e. the rectifier operates in constant current (CC) control mode and the inverter operates in constant extinction angle (CEA) control mode. Both CC and CEA controllers are based on proportional and integral (PI) logic to adjust the firing angle at rectifier and inverter stations respectively. The linearised PI controller operation at the rectifier station can be represented as follows:

$$\Delta\alpha = \left(K_p + \frac{K_i}{s}\right) \Delta I_{dc} \tag{10.16}$$

where, $\Delta$ represents small deviations, $\alpha$ is the rectifier firing angle, $K_p$ and $K_i$ are the proportional and integral gains respectively, $s$ is the Laplace transform variable and $I_{dc}$ is the dc-side current.

The linearised dc-side current of an HVDC system can be represented as follows [8, 21]:

$$L_{dc}\frac{d\Delta i_{dc}}{dt} + R_{dc}\Delta i_{dc} = \Delta v_{dc} = \Delta v_{dcr} - \Delta v_{dci} \tag{10.17}$$

where, $i_{dc}$ is the dc-side current, $v_{dcr}$ and $v_{dci}$ are the direct voltage at rectifier and inverter respectively. $L_{dc}$ is the DC line inductance and $R_{dc}$ is the DC line resistance.

Assuming that the system on the inverter side is a relatively strong system, its voltage is held approximately constant by CEA control, where $\Delta v_{dci} = 0$ (i.e. $\Delta v_{dc}$ will be equal to $\Delta v_{dcr}$). Thus, the HVDC load can be described in s-domain as follows:

$$\Delta I_{dc} = Z^{-1}_{hvdc}(s)\Delta V_{dc} \tag{10.18}$$

where $V_{dc}$ is the direct voltage and $Z_{hvdc}$ is the DC line impedance, which can be represented as $R_{dc} + sL_{dc}$.

The average direct voltage is represented as follows [8, 16]:

$$V_{dc} = \frac{3\sqrt{2}}{\pi} B_r T_r V_{acr} \cos\alpha \tag{10.19}$$

where, $B_r$ and $T_r$ are the number of bridges in series, and the transformer turns ratio at the rectifier station respectively, and $V_{acr}$ is the line-to-line AC voltage.

Linearisation of (10.19) yields the representation of the direct voltage with respect to the changes in rotor speed ($\Delta\omega_r$) and rectifier firing angle ($\Delta\alpha$) as follows:

$$\Delta V_{dc} = \frac{3\sqrt{2}}{\pi} B_r T_r V_{acr0} (\cos\alpha_0 \Delta\omega_r - \sin\alpha_0 \Delta\alpha) \tag{10.20}$$

where, $V_{acr0}$ is the initial AC voltage, $\alpha_0$ is the initial rectifier firing angle and $\Delta V_{acr} = V_{acr0}\Delta\omega_r$.

Substituting (10.20) into (10.18), and by considering a PI type current controller operation at the rectifier station as described by (10.16), the dc-side current change can be expressed with respect to the change in rotor speed as follows:

$$\frac{\Delta I_{dc}(s)}{\Delta\omega_r(s)} = \frac{Z^{-1}_{hvdc}(s)\frac{3\sqrt{2}}{\pi} B_r T_r V_{acr0} \cos\alpha_0}{1 + Z^{-1}_{hvdc}(s)\frac{3\sqrt{2}}{\pi} B_r T_r V_{acr0} \sin\alpha_0 \left(K_p + \frac{K_i}{s}\right)} \tag{10.21}$$

The current flowing into AC system ($i_{ac}$) is related to the dc-side current ($I_{dc}$) by the following equation that expresses the AC-DC interaction [16, 18].

$$i_{ac} = \frac{\sqrt{6}}{\pi} B_r T_r I_{dc} \cos(\omega_s t - \alpha) \tag{10.22}$$

Linearisation of (10.22) yields the small-signal inter-relationship between AC and DC sys-

tems of an HVDC system, as described below:

$$\Delta i_{ac} = \frac{\sqrt{6}}{\pi} B_r T_r \cos(\omega_s t - \alpha)\Delta I_{dc} + \frac{\sqrt{6}}{\pi} B_r T_r I_{dc0} \sin(\omega_s t - \alpha)\Delta\alpha \tag{10.23}$$

where, $I_{dc0}$ is the initial dc-side current.

The linearised ac-side current representation as in (10.23) can be rewritten as follows using (10.14) and (10.16):

$$\Delta i_{ac} = \frac{\sqrt{6}}{\pi} B_r T_r \left| \frac{\Delta I_{dc}}{\Delta \omega_r}(\omega_m) \right| m\{\sin B \cos A - \frac{K_i I_{dc0}}{\omega_m} \sin A \cos B + K_p I_{dc0} \sin A \sin B\} \tag{10.24}$$

where, $A = \omega_s t - \alpha$, $B = \omega_m t + \phi$ and $\frac{\Delta I_{dc}}{\Delta \omega_r}(j\omega_m) = \left| \frac{\Delta I_{dc}}{\Delta \omega_r}(\omega_m) \right| \angle\phi(\omega_m)$.

The representation of (10.24) in terms of the subsynchronous ($\omega_{sub}$) and supersynchronous ($\omega_{super}$) frequency components of the AC current can be illustrated as follows:

$$\Delta i_{ac} = \frac{\sqrt{6}}{2\pi} B_r T_r \left| \frac{\Delta I_{dc}}{\Delta \omega_r}(\omega_m) \right| m[x - y + z] \tag{10.25}$$

where,

$$\begin{aligned} x &= \left(1 - \frac{K_i I_{dc0}}{\omega_m}\right) \sin\left(\omega_{super} t - \alpha + \phi\right), \\ y &= \left(1 + \frac{K_i I_{dc0}}{\omega_m}\right) \sin\left(\omega_{sub} t - \alpha - \phi\right), \\ z &= K_p I_{dc0} \left[\cos\left(\omega_{sub} t - \alpha - \phi\right) - \cos\left(\omega_{super} - \alpha + \phi\right)\right]. \end{aligned}$$

The electromagnetic torque ($T_e$) can be represented as:

$$\Delta T_e = \frac{V_{acr} \Delta i_q}{\omega_r} \tag{10.26}$$

where $V_{acr}$ is the commutating voltage at the rectifier bus and $i_q$ is the $q$-axis current. The electromagnetic power ($V_{acr}\Delta i_q$) is the power at synchronous speed. This electromagnetic

power is equal to the electromagnetic torque with the assumption that $\omega_r = 1.0$ pu. It is thus obvious that the electromagnetic torque consists of sub- and super- synchronous frequency components.

A damping torque analysis is used in this chapter to identify the contribution made by the network towards the electrical damping of the generator unit of interest. As discussed earlier, perturbation of the rotor speed will be reflected on the stator terminal voltage, causing the current to oscillate depending on the network impedance as seen from the generator perspective [22]. The sequence components of stator currents contain sub- and super- synchronous frequency components. This results in a change in electrical torque at a modulated frequency ($\omega_m$).

The combined AC and HVDC system as seen in Fig. 10.4 is used to illustrate the damping torque analysis.

The electrical torque deviation can be obtained by disabling the rotor dynamics associated with the generator unit (i.e. neglecting the mechanical torque deviations) [6, 22], and applying a sinusoidal small speed perturbation ($\Delta\omega_r$). The rotor speed to electrical torque transfer function ($G_e$) can be computed by repeating this procedure for the frequency range of interest. The mathematical expression for $G_e$ can be given as:

$$\frac{\Delta T_e}{\Delta \omega_r}(j\omega) = |G_e(\omega)| \angle \phi_{Ge}(\omega) \tag{10.27}$$

where, $\phi_{Ge}$ is the relative phase angle.

The electrical damping can be plotted against the modulated frequency to depict the amount of electrical damping contribution from the electrical network, and thereby determining the system stability. The system is considered to be stable if the electrical damping is positive and associated phase angle lies between $+90^\circ$ and $-90^\circ$.

To calculate the electrical damping at the modulated frequency, the rotor speed and the electromagnetic torque signals are passed through a narrow-bandpass filter (with high quality factor) to extract the frequency components of interest. The 2nd-order mid-pass filter is

used for extracting the related frequency component. The effective electrical damping ($D_e$) and synchronising coefficient ($S_e$) can be calculated as follows [1, 22]:

$$D_e(\omega) = \Re\{G_e(s)\} = |G_e(\omega)| \cos\phi_{Ge} \tag{10.28}$$

$$S_e(\omega) = \Im\{G_e(s)\} = |G_e(\omega)| \sin\phi_{Ge} \tag{10.29}$$

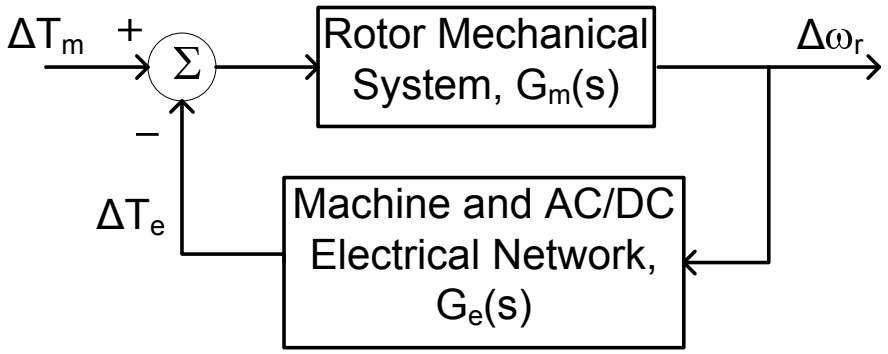


Figure 10.4: Electrical and mechanical systems diagram

## 10.5 Test Case

A hydroelectric turbine-generator unit connected to an HVDC system, with a parallel connection of an AC system is shown in Fig. 10.5. This is used as test case for damping torque analysis with a monopolar DC link rated at 500 kV, 1000 MW connected to a hydroelectric unit. Hydroelectric units with rated capacities of 500 MVA, 840 MVA and 1000 MVA are considered for detailed investigation. The data for 500 MVA hydroelectric unit are obtained from [17]. The 840 MVA and 1000 MVA hydroelectric generators are represented by Sanxia generator data given in [23].

The HVDC system is represented by the CIGRE first HVDC benchmark model [24]. It is considered that the HVDC system operates with CC control mode on the rectifier side and CEA control mode on the inverter side as shown in Fig. 10.6. Accordingly, HVDC system can be represented as load, where the inverter side voltage is assumed to be constant.

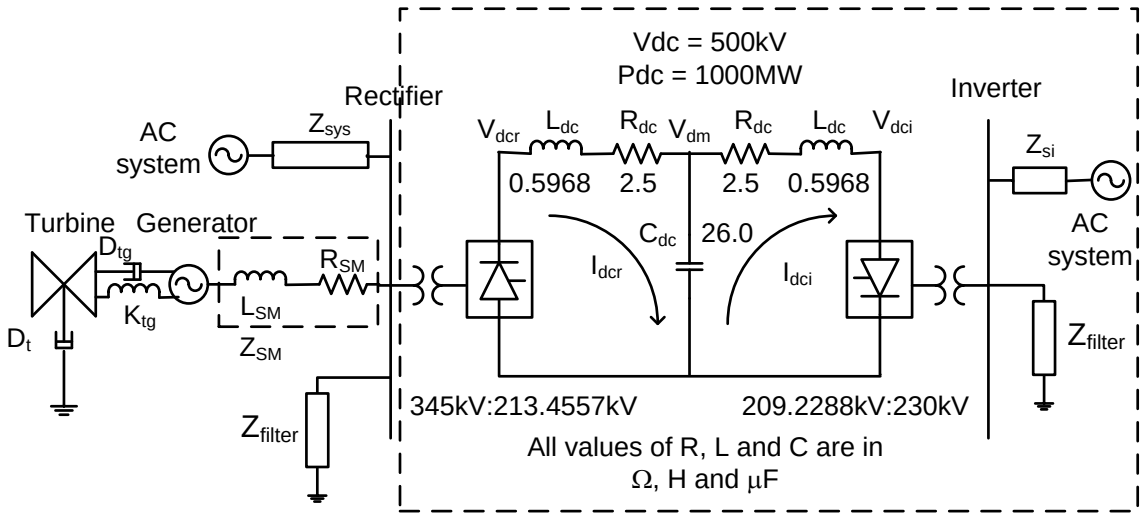


Figure 10.5: Hydroelectric unit connected to an HVDC system

The dc-side current is kept constant by varying the firing angle ($\alpha$) at the rectifier station. The rectifier controller mode will be changed to constant ignition angle (CIA) control mode if the minimum firing angle $\alpha_{min}$ is hit, as no further direct voltage increment is allowed. For small signal analysis, it is assumed that the converter controllers are operating close to the normal operating conditions without changing the controller modes.

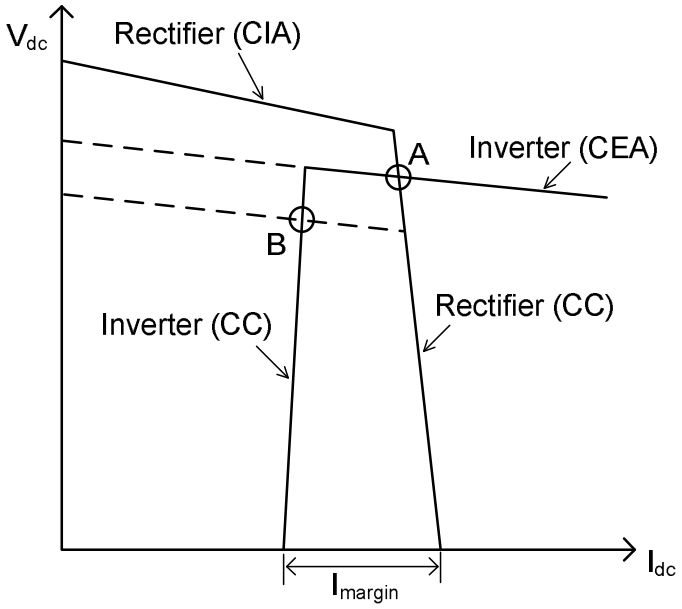


Figure 10.6: Converter control steady state characteristics

Both CC and CEA controllers are based on the PI logic to adjust the firing angle at the rectifier and inverter stations respectively. The difference between measured dc-side current and the current order is used as an input to the CC controller, whilst the difference between measured extinction angle and the extinction angle order is used as an input to the CEA controller as illustrated in Figs. 10.7(a) and 10.7(b) respectively.

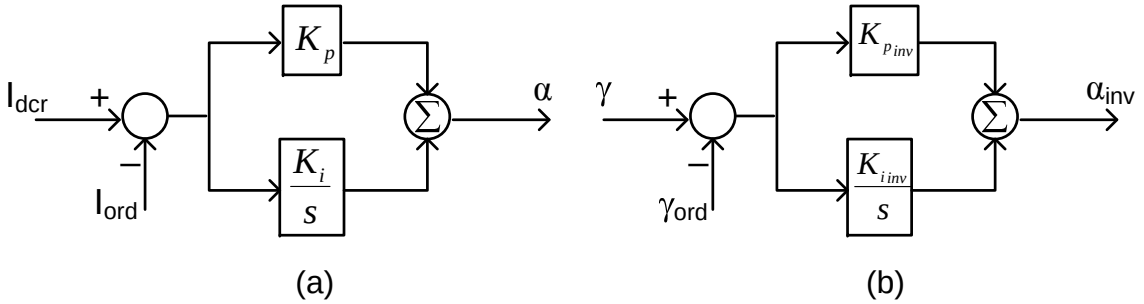


Figure 10.7: HVDC control modes: (a) Constant current controller at rectifier station (b) Constant extinction angle controller at inverter station

The rest of the AC systems on the rectifier and inverter sides have been modeled as AC grid equivalents with equivalent Thevenin impedances of $Z_{sys}$ and $Z_{si}$ respectively (as shown in Fig. 10.5). Accordingly, the system strength of the parallel AC network on the rectifier side can be determined based on $Z_{sys}$, which is inversely proportional to the short circuit ratio (SCR). In the simulation study, $Z_{sys}$ is assumed to be very high so as to depict the worse case scenario, where the electrical damping of the interconnected AC-DC system is contributed solely by the HVDC system. In this chapter, the AC system with short circuit ratios (SCRs) of $2.5\angle 84^\circ$ and $10\angle 75^\circ$ is considered to represent the weak and strong system respectively [24].

## 10.6 Simulation Results

The interaction behaviour of an HVDC system with a nearby generator is investigated through sensitivity analysis. It identifies the system parameters at different operating conditions, that may result in instability or pose negative damping.

Extensive simulation studies have been conducted to examine the amount of the electri-

cal damping for the interconnected AC-DC system within the frequency range of interest. Different scenarios as highlighted below have been investigated:

- Hydroelectric unit with different power output capacities ($S_{hydro}$),
- Hydroelectric unit with different loading levels ($P_{hydro}$),
- Varying power flows through a DC link ($P_{dc}$),
- Different levels of AC system strength ($Z_{sys}$), and
- Different current controller gains.

The following subsections demonstrate the perturbation analysis as a screening tool to investigate the effect of negative damping, contributed inherently by the current controller operation at the HVDC rectifier station, on hydroelectric turbine-generator units. It is assumed that the firing angle at the rectifier station varies between 15 to 20 degrees.

### 10.6.1 Perturbation analysis from machine side (mechanical system perturbation)

A PSCAD®/EMTDC© simulated model is used for damping torque analysis as described in Section 10.4. A small sinusoidal perturbation of rotor speed ($\Delta\omega_r$) of $0.01\sin(\omega_m t)$ is introduced on the synchronous machine by disabling the rotor dynamics. The resulted electromagnetic torque deviation ($\Delta T_e$) is measured and the magnitude and phase angle of electrical damping ($D_e$) are also calculated for the frequency range of interest. The system stability can be determined from the electrical damping and phase angle plots. Torsional interactions between the hydroelectric unit and HVDC system are investigated through sensitivity analysis at different operating conditions for 0 Hz $\leq f_m \leq$ 50 Hz.

Fig. 10.8(a) shows the time response of the generator internal bus voltage resulting from a modulated frequency ($f_m$) of 10 Hz. Frequency spectrum of the AC voltage as seen in Fig. 10.8(b) illustrates that fundamental ($f_{fund}$), sub- ($f_{sub}$) and super-($f_{super}$) synchronous frequency components exist when the rotor speed is modulated at 10 Hz, with extra frequency components possibly arising as a result of multiple armature reaction.

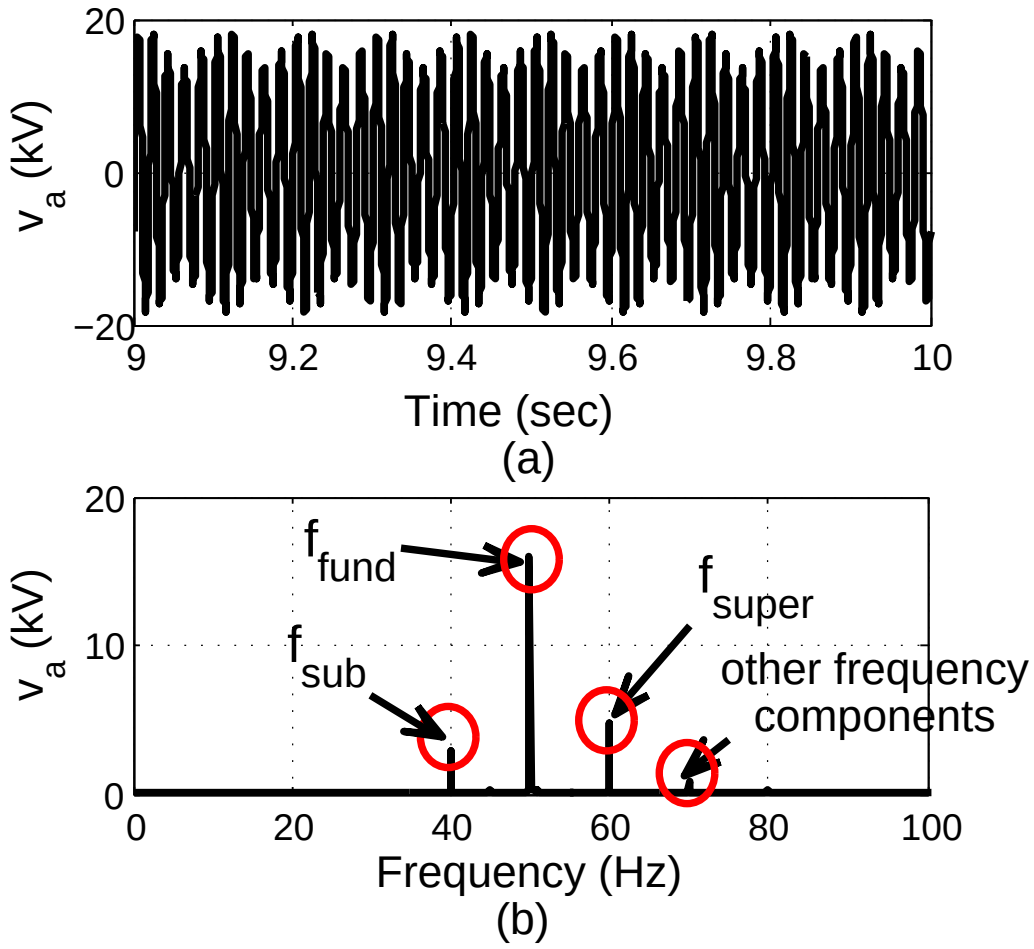


Figure 10.8: (a) Time response and (b) Frequency spectrum of AC voltage at a modulated frequency, $f_m$ of 10 Hz

#### 10.6.1.1 Hydroelectric unit with different power output capacities

The electrical damping plots for a hydroelectric TG unit connected in parallel with a weak AC network (SCR of 2.5∠84°), and with the rated DC power transfer, are shown in Fig. 10.9(a). It is assumed that the hydroelectric unit operates at 0.85 power factor lagging. It is observed that the negative damping exists for a frequency range of 4 Hz $\leq f_m \leq$ 9 Hz. The torsional frequency of a hydroelectric TG unit falls well within the frequency range where the negative damping persists. This suggests that the current controller of the rectifier can possibly destabilise the torsional interaction. However, if the mechanical damping exceeds the electrical damping in magnitude, the system could be stable. Modal analysis will be elaborated later to further evaluate the possible SSTI behaviour of the hydroelectric unit with an HVDC system.

The system electrical damping for a hydroelectric TG unit connected in parallel with a strong AC network (SCR of 10∠75°), with the rated DC power transfer and the rated generator loading, is greatly enhanced as shown in Fig. 10.9(b). A much higher amount of positive electrical damping is provided for most of the frequency range of interest. Thus, SSTI is highly unlikely to be observed on any hydroelectric unit when a strong AC network is connected in parallel to the rectifier station.

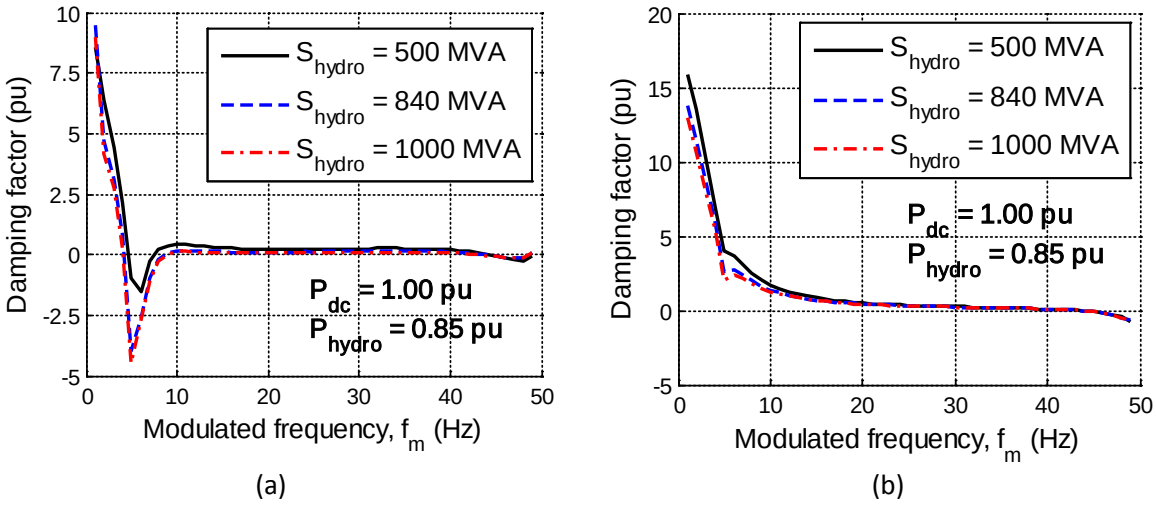


Figure 10.9: Electrical damping for a hydroelectric turbine-generator unit with (a) a weak AC link in parallel (b) a strong AC link in parallel

#### 10.6.1.2 Hydroelectric unit with different loading ($P_{hydro}$)

Hydroelectric units operating at different loading levels, i.e. $P_{hydro}$ = 0.75 pu, 0.5 pu and 0.25 pu, are investigated. Figs. 10.10(a) – (c) highlight the electrical damping contribution for hydroelectric units with different capacities and loadings, connected in parallel with a weak AC system interconnected to the HVDC system. It is shown in Fig. 10.10(c) that the hydroelectric unit of 1000 MVA experiences electrical damping of −4.5 pu for 0.85 pu loading. Similarly, electrical damping contribution from the network increases to −1.5 pu for 0.25 pu loading.

Negative electrical damping contributions for hydroelectric units of 500 MVA and 840 MVA are observed in Fig. 10.10(a) and (b) respectively. The hydroelectric units of 840 MVA and 500 MVA experience electrical damping of −4 pu and −1.5 pu for 0.85 pu loading under normal operation.

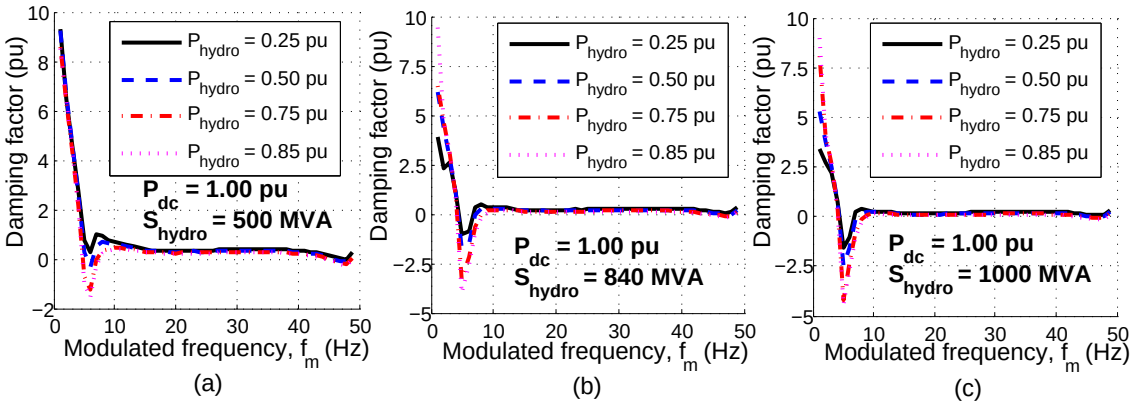


Figure 10.10: Electrical damping for a hydroelectric turbine-generator unit with a weak parallel AC network connection and different generator loadings, $P_{hydro}$ and capacities, $S_{hydro}$

#### 10.6.1.3 DC line operating at different power flow ($P_{dc}$)

Simulation results presented in Figs. 10.11(a)–(c) show that the system is more susceptible in imposing negative damping when the DC line is operating at a higher level of power flow. In fact, positive damping has been provided for the frequency range of interest when the DC power flow ($P_{dc}$) is 0.5 pu and 0.25 pu for all hydroelectric units of different capacity

and loading. It can be summarised that for a hydroelectric unit connected in parallel with a weak AC system integrated to the HVDC system, the overall contribution of the electrical damping increases with low DC power transfer.

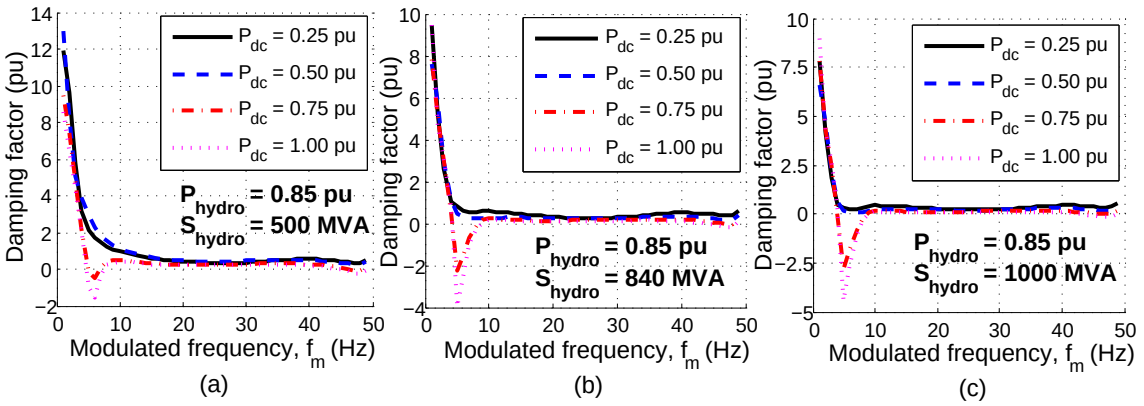


Figure 10.11: Electrical damping for a hydroelectric turbine-generator unit with a weak parallel AC network connection and varying DC power flow

### 10.6.1.4 Sensitivity analysis of current controller gains on electrical damping

The torsional interactions between the generator unit and the HVDC system are highly sensitive to the current controller gains. The effect of the rectifier current controller gains ($K_p$ and $K_i$) onto the electrical damping is examined. The sensitivity of the current controller integral gain ($K_i$) on the electrical damping with proportional gain ($K_p$) set to 1.0989 is demonstrated in Fig. 10.12(a), whereas Fig. 10.12(b) presents the sensitivity of the proportional gain ($K_p$) on the electrical damping with $K_i$ set to 91.58 for $0 < f_m \leq 50$ Hz.

It is observed that the frequency range in which the negative damping persists varies with the change in $K_i$ as shown in Fig. 10.12(a). The effect of $K_i$ on the damping contribution is predominant when the torsional mode of 6.3 Hz is selected for the study as seen in Fig. 10.13(a) with a fixed value of $K_p$. It is observed in Fig. 10.12(b) that the negative damping exists for a frequency range of 4 Hz $\leq f_m \leq$ 9 Hz for most of the $K_p$ values with $K_i$ set to 91.58. The torsional mode of a hydro unit falls well within the frequency range where the negative damping persists. The decrease in $K_p$ results in a large contribution of negative damping.

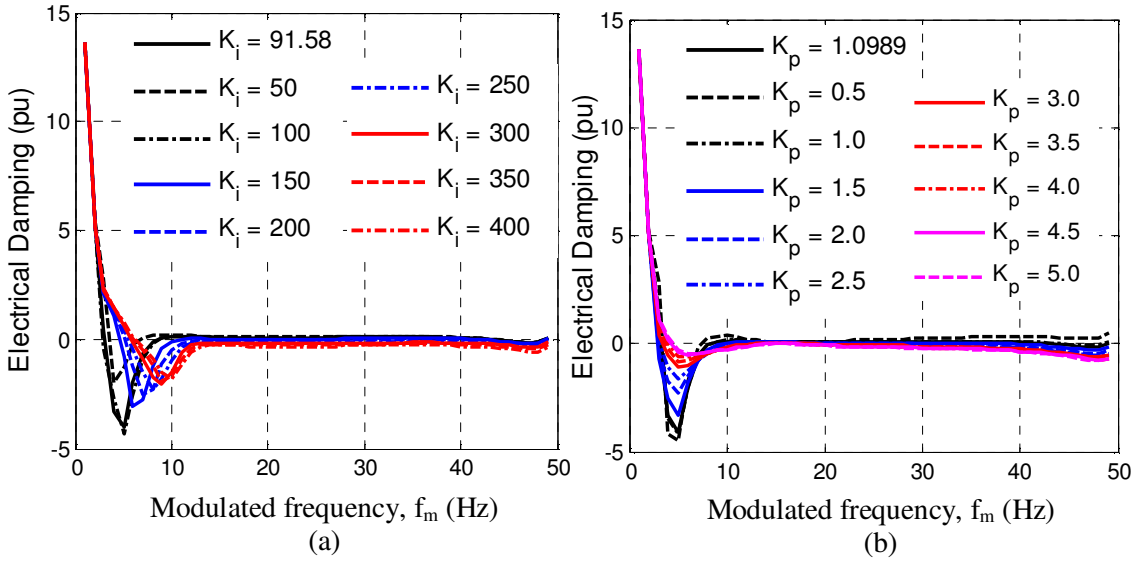


Figure 10.12: Sensitivity analysis of current controller (a) $K_i$ and (b) $K_p$ gains on electrical damping

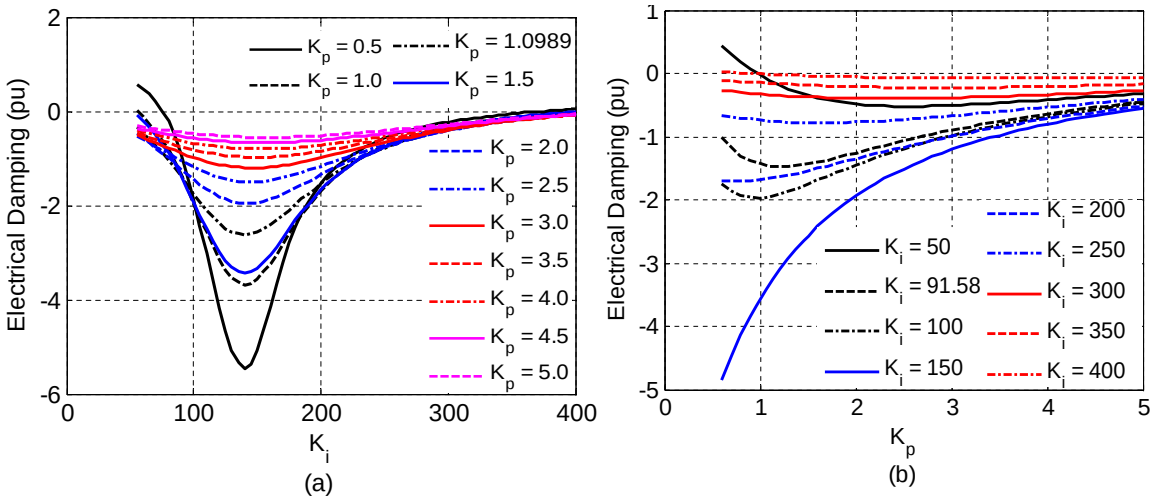


Figure 10.13: Sensitivity analysis of current controller (a) $K_i$ and (b) $K_p$ gains on electrical damping for the torsional mode of hydro unit $f_n = 6.3$ Hz

The dependency of $K_i$ and $K_p$ on the electrical damping for the torsional mode ($f_n$) of 6.3 Hz can be evidenced in Figs. 10.13(a) and (b). Fig. 10.13(a) shows the electrical damping as a function of $K_i$ for different values of $K_p$. The torsional mode experiences the least damping when $K_i$ is 150. The electrical damping can be improved by increasing $K_p$.

The electrical damping presented as a function of $K_p$ for different values of $K_i$ is demonstrated in Fig. 10.13(b). As seen in the figure, the electrical damping contribution is consistent for $K_p$ variation with a high value of $K_i$. For a low value of $K_i$ (i.e. $K_i = 50$), positive electrical damping is obtained for the torsional mode for low values of $K_p$ (i.e. $K_p \leq 1$). However, increase in $K_p$ results in a decrement in electrical damping, and the mode becomes unstable.

### 10.6.2 Perturbation analysis from AC network side (electrical system perturbation)

Voltage perturbation at different modulated frequency ($f_m$) is applied at the terminal bus to depict the perturbation arising from HVDC system operation (network side perturbation). The perturbation is mathematically expressed in (10.15). The resulting deviation in the TG torque (mechanical torque) of the hydroelectric unit is then measured for different modulated frequencies. The TG torque signal is further passed through the bandpass filter so as to extract the frequency component of interest.

The torsional data for hydroelectric units presented in Table 10.1 is derived from [3] and is used for torsional interaction studies reported in this chapter. Perturbation signal ($\Delta\omega_r$) of 0.1 pu is applied so as to depict the severe faults at the generator terminal. Fig. 10.14 shows the resulting deviation in TG torque of the hydroelectric units, rated at 500 MVA, 840 MVA and 1000 MVA with different shaft parameters (as given in Table 10.1), for 0 Hz $\leq f_m \leq$ 12 Hz. As seen, TG torque oscillations can be excited at torsional frequency of the mechanical shaft.

The three shaft systems under investigation have the torsional frequencies ($f_n$) of 8.6, 6.3 and 7.2 Hz. These torsional frequencies fall between 4−9 Hz, where the electrical damping contribution from the system is negative as discussed in the previous Section. TG torque

deviations are found to be 1.0 pu, 1.5 pu and 0.6 pu for a 500 MVA hydroelectric unit with shaft system 1, 2 and 3 respectively. For hydroelectric units rated at 840 MVA and 1000 MVA, the resulting TG torque deviations are less than 0.5 pu for all shaft systems under consideration.

Table 10.1: Hydroelectric Torsional Shaft System Data

| Shaft | 1 | 2 | 3 |
|---|---|---|---|
| Speed (rpm) | 136.4 | 100 | 115.4 |
| $H_{gen}$ (s) | 4.54 | 2.16 | 2.29 |
| $H_{tur}$ (s) | 0.22 | 0.26 | 0.22 |
| GTI | 20.5 | 8.2 | 10.6 |
| $f_n$ (Hz) | 8.6 | 6.3 | 7.2 |

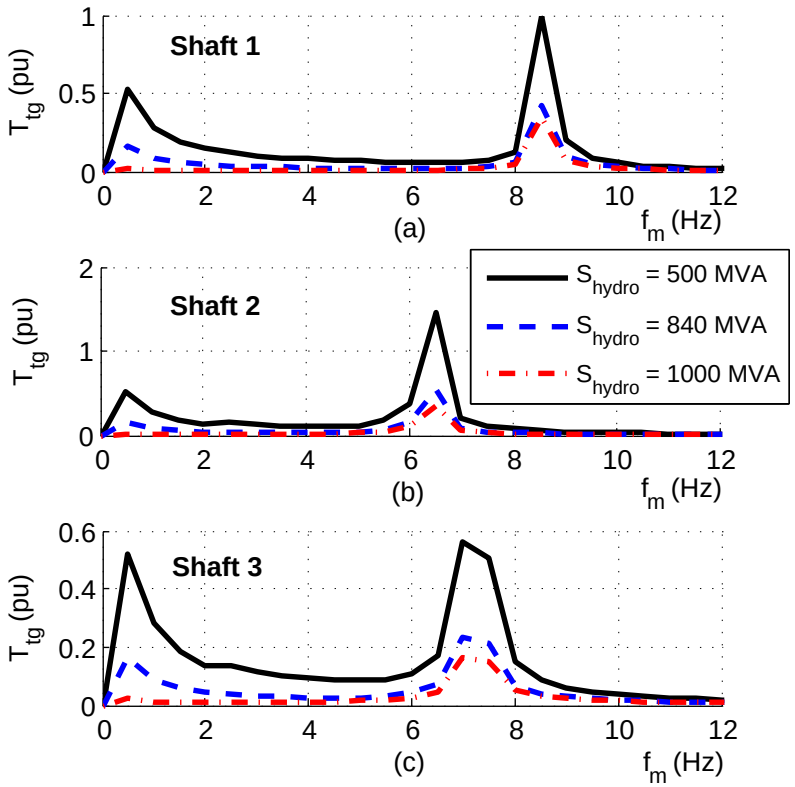


Figure 10.14: Turbine-generator torque vs modulated frequency

This screening analysis demonstrates that TG torque can be excited at the torsional frequency on a hydroelectric unit. It is vital to carry out further investigations especially using time domain simulations.

### 10.6.3 Time Domain Analysis

Subsections 10.6.1 and 10.6.2 have presented the perturbation analysis for investigating the potential SSTI phenomenon. This subsection further examines the SSTI behaviour of hydroelectric units with different shaft systems (as given in Table 10.1), for a sample network depicted in Fig. 10.5, through time domain simulation studies conducted using PSCAD®/EMTDC©. Hydroelectric units rated at 500 MVA, 840 MVA and 1000 MVA are considered for the investigation. It is assumed that the hydroelectric unit and DC line are operating at rated condition, i.e. $P_{hydro} = 0.85$ pu and $P_{dc} = 1.0$ pu. Moreover, the firing angle ($\alpha$) varies between 15° and 20°.

#### 10.6.3.1 Three-phase to ground fault at the rectifier station

As per IEEE Std C50.12-2005, the initial steady-state voltage at the generator bus is set to be at 1.05 pu before applying electrical perturbation. A three-phase to ground fault is applied at the rectifier station at $t = 0.5$ sec, and is cleared in 3 cycles, i.e. 0.06 sec for a 50 Hz system. A three-phase to ground fault at the rectifier station is considered as worst case scenario, and will have greater impact on the generator unit due to the electrically-close distance between the unit and the rectifier station.

This disturbance was noted to induce small voltage fluctuations between the frequency range of 35 Hz $\leq f \leq$ 65 Hz. There are still other frequency components present in the voltage fluctuations, but they are of relatively small magnitude. The mechanical torsional mode frequency ($f_n$) falls well-within the complement of the system resonance frequency range ($f_m = f_b - f_{sub}$ or $f_{super} - f_b$). This complement frequency range is between 0 Hz $\leq f_m \leq$ 15 Hz.

Figs. 10.15 – 10.17 show the TG torque for hydroelectric units with capacities of 500 MVA, 840 MVA and 1000 MVA associated with shaft system 1, 2 and 3 respectively for a three-phase to ground fault at the rectifier station. The total simulation time of 150 sec is considered. Insets have been included in the figures to demonstrate the oscillation frequency of the response for the snapshot of 0.4 sec. It is observed that the sustained TG

torque oscillations are present due to the occurrence of the three-phase fault in most of the cases. However, the oscillating TG torque for the hydroelectric unit of 500 MVA (with shaft systems 2 and 3) eventually settles down, as seen in Figs. 10.15(b) and (c), while Figs. 10.16(b), 10.17(b) and 10.17(c) demonstrate the cases of growing oscillations in TG torque for the hydroelectric unit of 840 MVA capacity associated with shaft system 2, and 1000 MVA hydroelectric unit with shaft systems 2 and 3. It is seen in Fig. 10.17(a) that the oscillations grow slowly even with a high GTI ratio of 20.5.

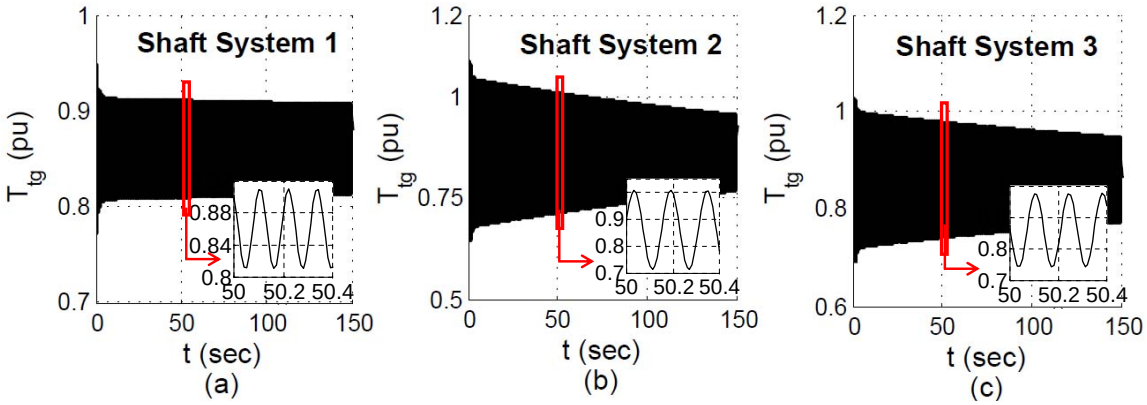


Figure 10.15: TG torque response of 500 MVA hydro unit for three-phase to ground fault at the rectifier station

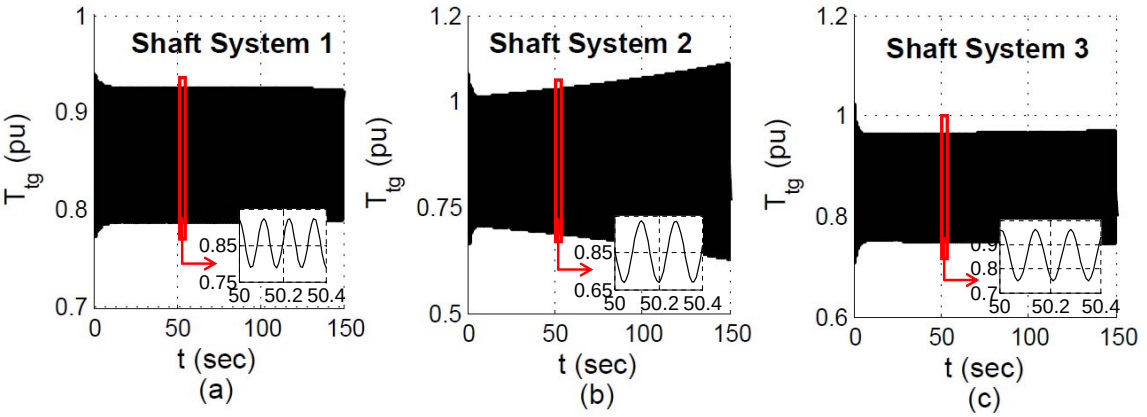


Figure 10.16: TG torque response of 840 MVA hydro unit for three-phase to ground fault at the rectifier station

The corresponding frequency spectrums of the TG torque are shown in Fig. 10.18(i). These figures demonstrate the contribution from the torsional modes towards the TG torque

oscillation, and also suggest that the TG torque deviation is the highest when the hydroelectric TG unit has the lowest GTI ratio. From the system studies, the second shaft system presented in Table 10.1 has the lowest GTI of 8.2, followed by the third shaft system with a ratio of 10.6 and lastly, the first shaft system having the GTI value of 20.5. The corresponding TG torque deviation for hydroelectric unit with first shaft system in service is the least (i.e. $< 0.05$ pu). It is also observed that the TG torque deviation is higher when a hydroelectric unit of higher capacity is in operation. As shown in Fig. 10.18(ii), it is noted that the torsional modes of hydroelectric units with shaft systems under investigation have very little contribution to the rotor speed deviation $\Delta\omega_r$. It is noted that $\Delta\omega_r$ is less than 0.35 rad/sec for hydroelectric unit associated with shaft system 2 while $\Delta\omega_r$ is less than 0.04 rad/sec for hydroelectric unit with shaft system 1.

Figs. 10.19 – 10.21 illustrate the time responses of the rotor speed oscillations for hydroelectric units of capacities ($S_{hydro}$) 500 MVA, 840 MVA and 1000 MVA associated with shaft system 1, 2 and 3. The rotor speed oscillation eventually damps down for most cases as shown in Figs. 10.19 – 10.21, however, there are cases where the rotor speed oscillation grows, leading to the system instability as seen in Figs. 10.20(b), 10.21(b) and 10.21(c).

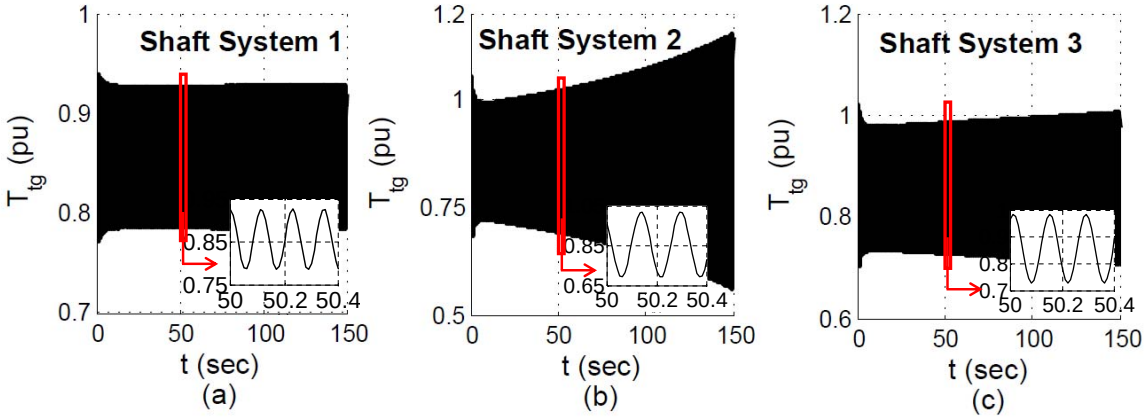


Figure 10.17: TG torque response of 1000 MVA hydro unit for three-phase to ground fault at the rectifier station

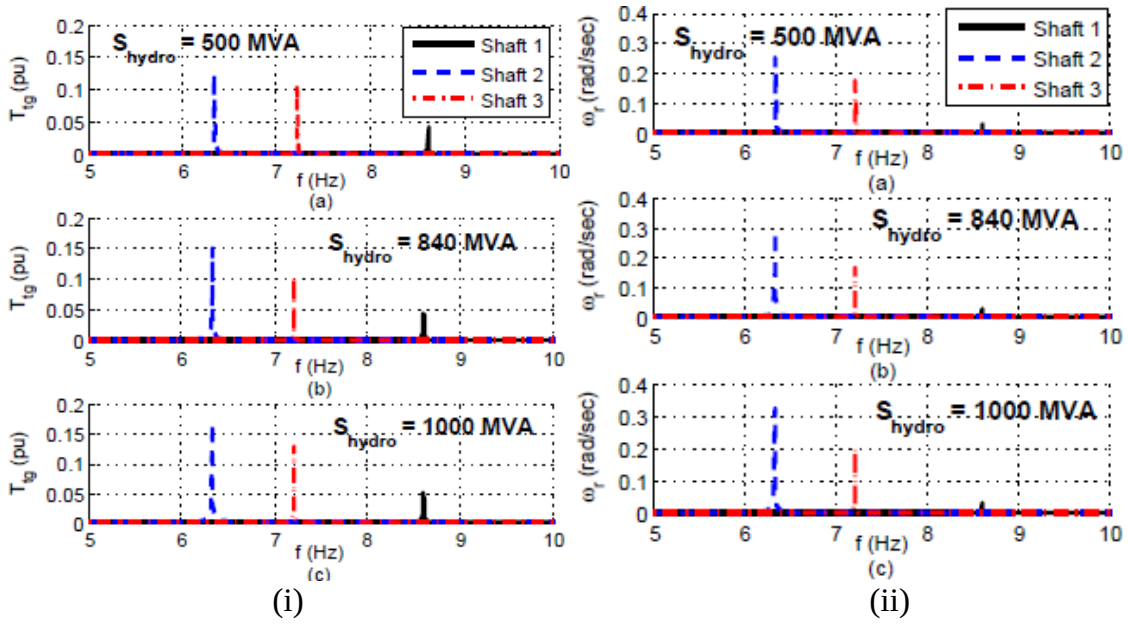


Figure 10.18: Frequency spectrum of (i) TG torque (ii) Rotor speed of hydroelectric unit for a three-phase to ground fault at the rectifier station

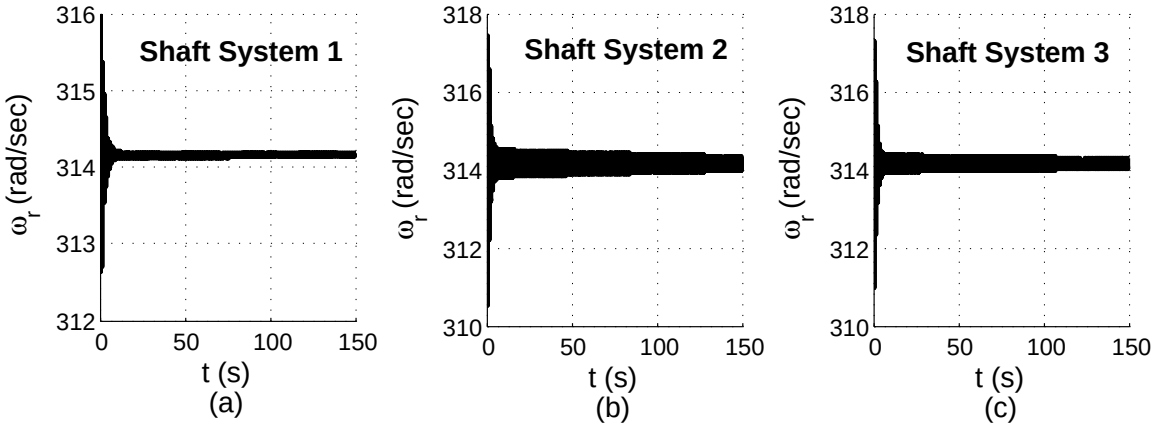


Figure 10.19: Rotor speed response of 500 MVA hydro unit for three-phase to ground fault at the rectifier station

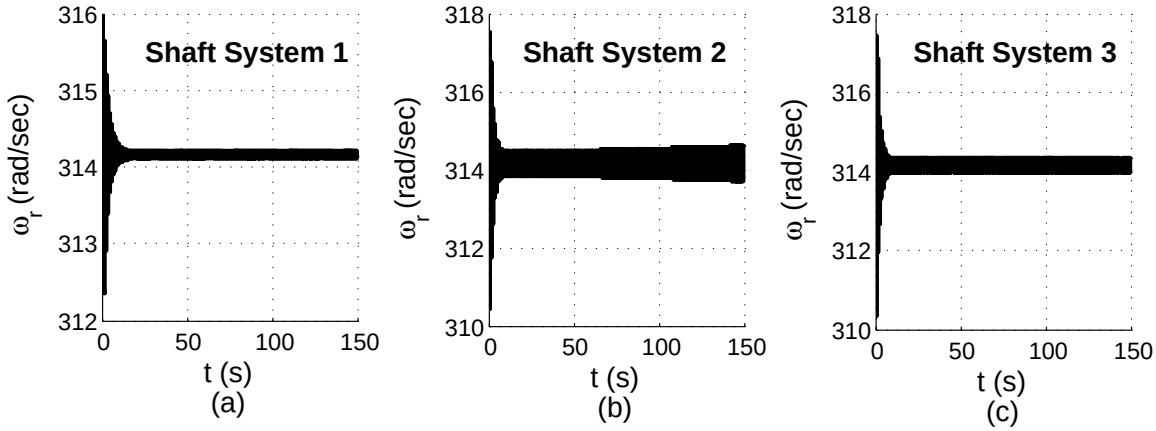


Figure 10.20: Rotor speed response of 840 MVA hydro unit for three-phase to ground fault at the rectifier station

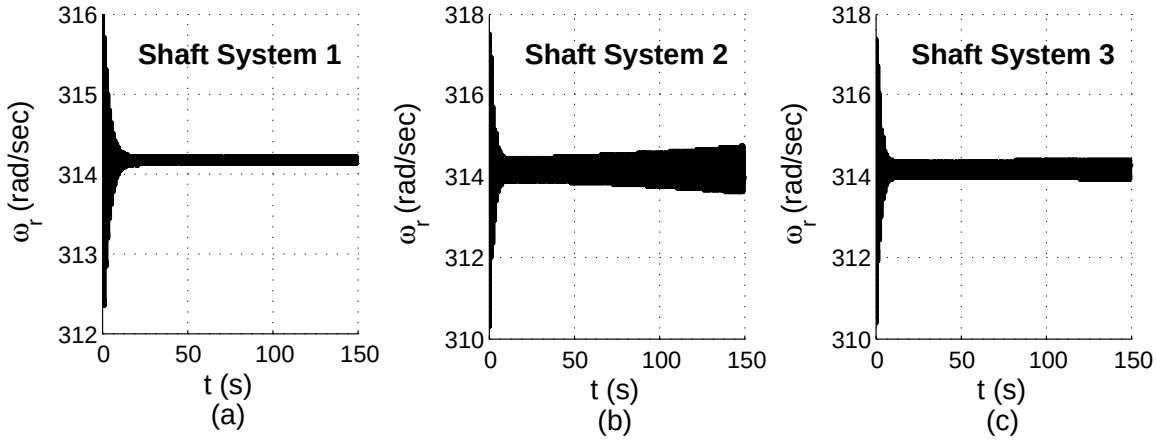


Figure 10.21: Rotor speed response of 1000 MVA hydro unit for three-phase to ground fault at the rectifier station

#### 10.6.3.2 Step change applied on the current controller

SSTI is generally resulted from the interaction of a TG unit with fast acting controllers of power system components. The hydro unit's responses are observed with a step change applied on the current controller. Similar results as that subjected to a three-phase to ground fault are obtained. The TG torque responses of 500 MVA, 840 MVA and 1000 MVA hydro units for a step change on the current controller are shown in Figs. 10.22 – 10.24 respectively. Insets have been included in the figures to demonstrate the oscillation frequency of the response for the snapshot of 0.4 sec. The corresponding rotor speed responses of the hydroelectric units are given in Figs. 10.25 – 10.27. Growing TG torque oscillations are expected for the hydro units with higher capacities (840 MVA and 1000 MVA) associated with shaft systems 2 and 3, which have low GTI ratios of 8.2 and 10.6 respectively. These are evidenced in Figs. 10.23(b), 10.23(c), 10.24(b) and 10.24(c).

The decrement factor of the integrated hydroelectric unit and an HVDC system is demonstrated in Fig. 10.28 as a function of GTI ratio and turbine damping ($D_{tur}$) for turbine-generator damping ($D_{tg}$) between 0 pu and 1.0 pu. The generator inertia ($H_{gen}$) of 2.158 sec is considered. The worst electrical damping factor of $-4.5$ pu has been taken into account in order to obtain the respective modal damping, decrement factor and logarithmic decrement of the integrated AC-DC system.

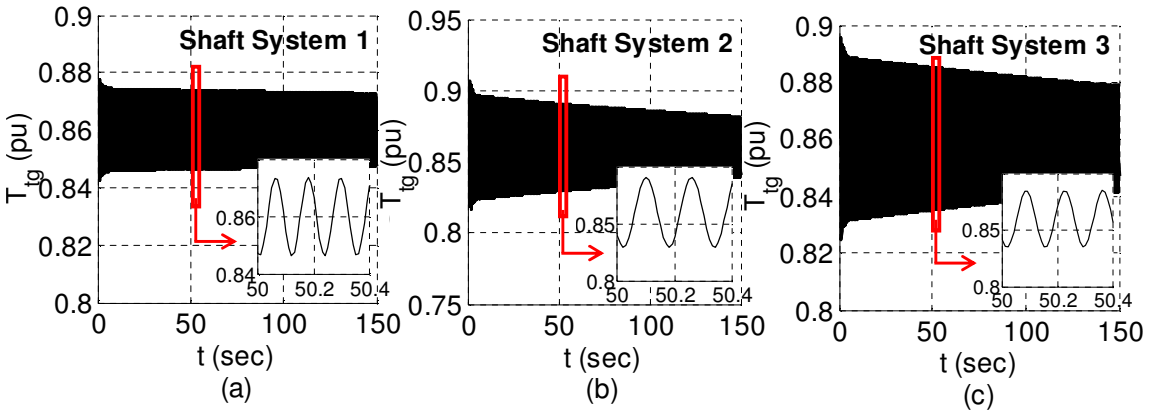


Figure 10.22: TG torque response of 500 MVA hydro unit for a step change applied on the current controller

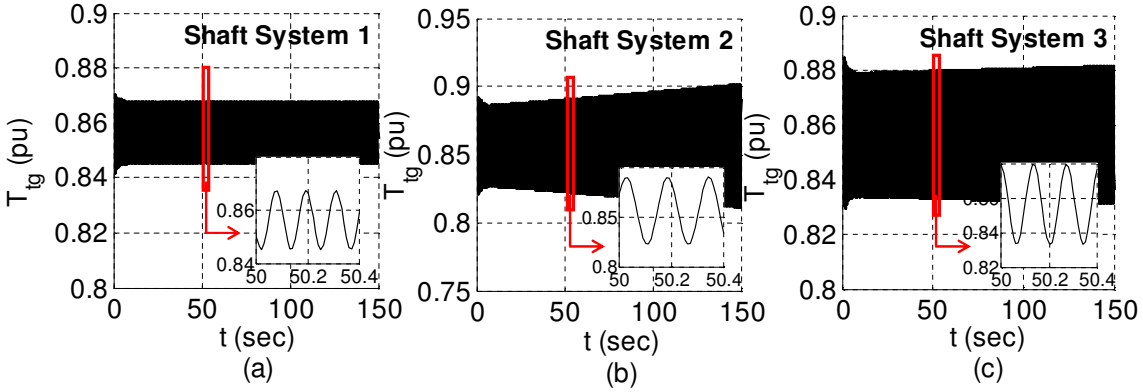


Figure 10.23: TG torque response of 840 MVA hydro unit for a step change applied on the current controller

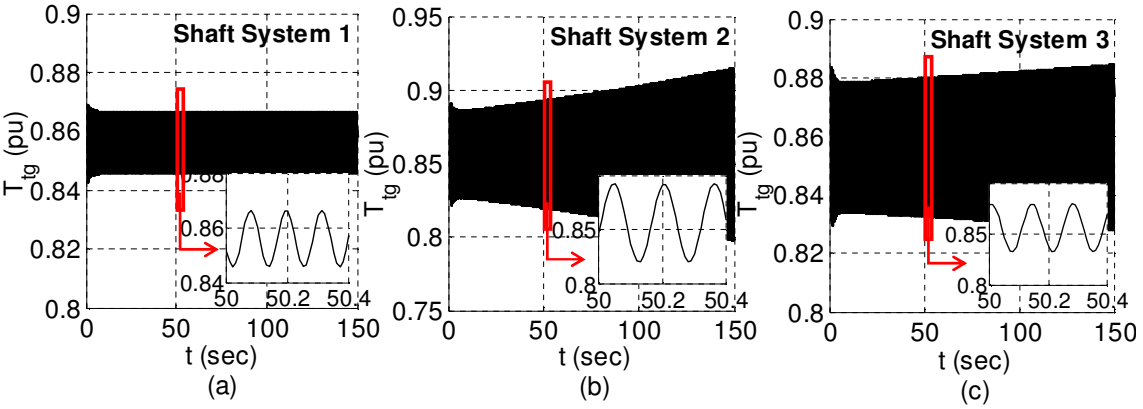


Figure 10.24: TG torque response of 1000 MVA hydro unit for a step change applied on the current controller

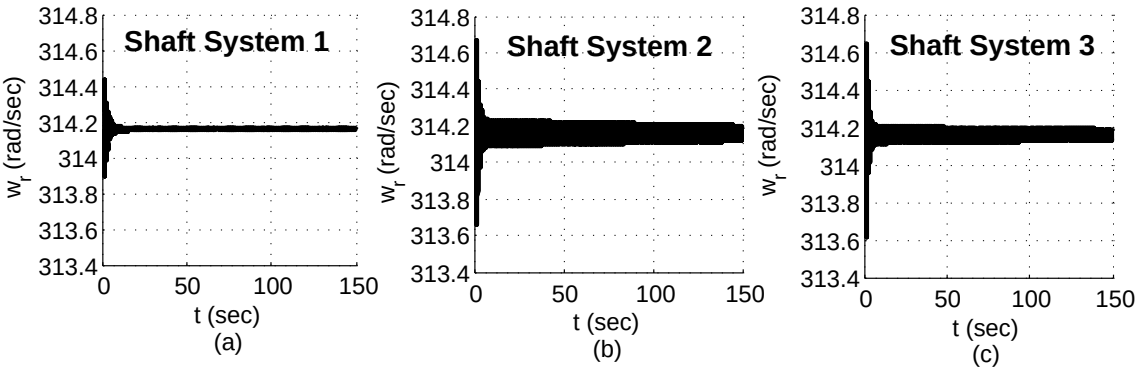


Figure 10.25: Rotor speed response of 500 MVA hydro unit for a step change applied on the current controller

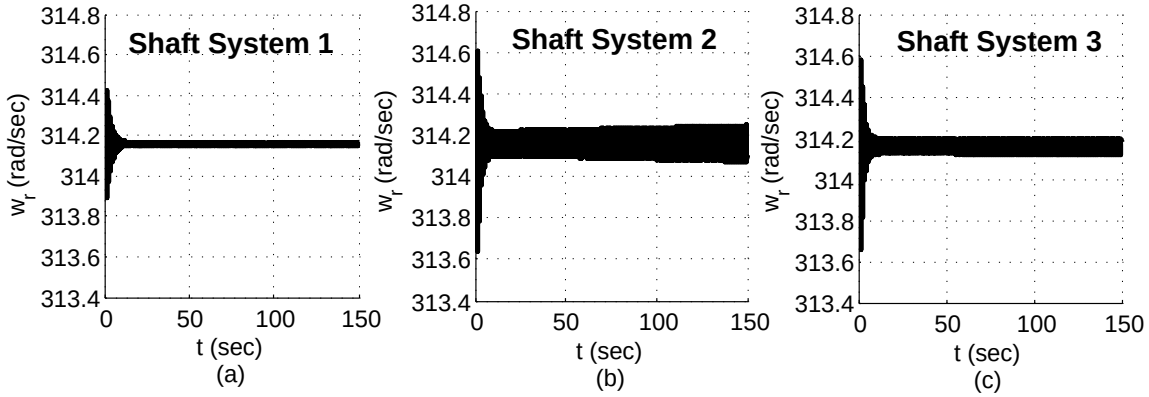


Figure 10.26: Rotor speed response of 840 MVA hydro unit for a step change applied on the current controller

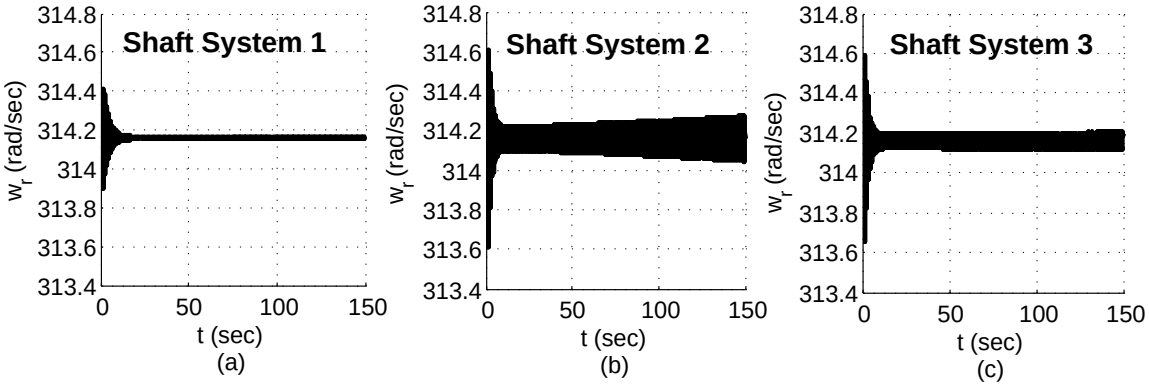


Figure 10.27: Rotor speed response of 1000 MVA hydro unit for a step change applied on the current controller

It is observed in Fig. 10.28 that the decrement factor of the integrated system becomes negative for a low GTI ratio of hydroelectric TG unit when $D_{tg} = 1.0$ pu. This may result in sustained or growing subsynchronous oscillations. Fig. 10.29 presents the side view of the system decrement factor, with a clearer view shown in the inset. The decrement factor becomes negative when GTI $< 1$ as seen in Fig. 10.29. If $D_{tg}$ is negligible ($D_{tg} \approx 0$ pu), there may be a system, with different combination of GTI ratio and $D_{tur}$, experiencing SSTI. This is shown in Fig. 10.28, as indicated by a stability boundary of $\sigma_m = 0$. For a system with any combination of $D_{tur}$ and GTI that falls below the indicative stability boundary, the system experiences unstable SSTI phenomenon.

As shown in Fig. 10.29, the negative system decrement factor is observed for all GTI values with $D_{tg} = 0$ pu, which suggests that the system may experience SSTI instability even when a hydroelectric unit with higher GTI ratio is in operation. The growing subsynchronous oscillations in TG torque, as seen in Figs. 10.17(b), 10.17(c), 10.24(b) and 10.24(c) for a 1000 MVA hydroelectric unit operating close to the HVDC system, are due to lack of modal damping in the system with a relatively low value of modal decrement factor.

#### 10.6.3.3 Damping improvement by subsynchronous damping controller

Subsynchronous damping controller (SSDC), constituting a washout filter, a SSDC gain block and a lead-lag phase compensator, as seen in Fig. 10.30 can be designed and incorporated to the current controller of the rectifier to overcome the torsional interaction between the TG unit and the HVDC system. The phase characteristics of SSDC can be designed properly to compensate any phase lead/lag between the current controller input and the generator electrical torque, so as to provide positive damping at the required frequency range [21, 25]. The frequency response between the constant current controller input and the generator electrical torque, to determine the phase compensation required, can be obtained with the assumption that the generator angle is maintained constant. A washout filter, which is a high pass filter, is also included to remove the steady speed variations [25].

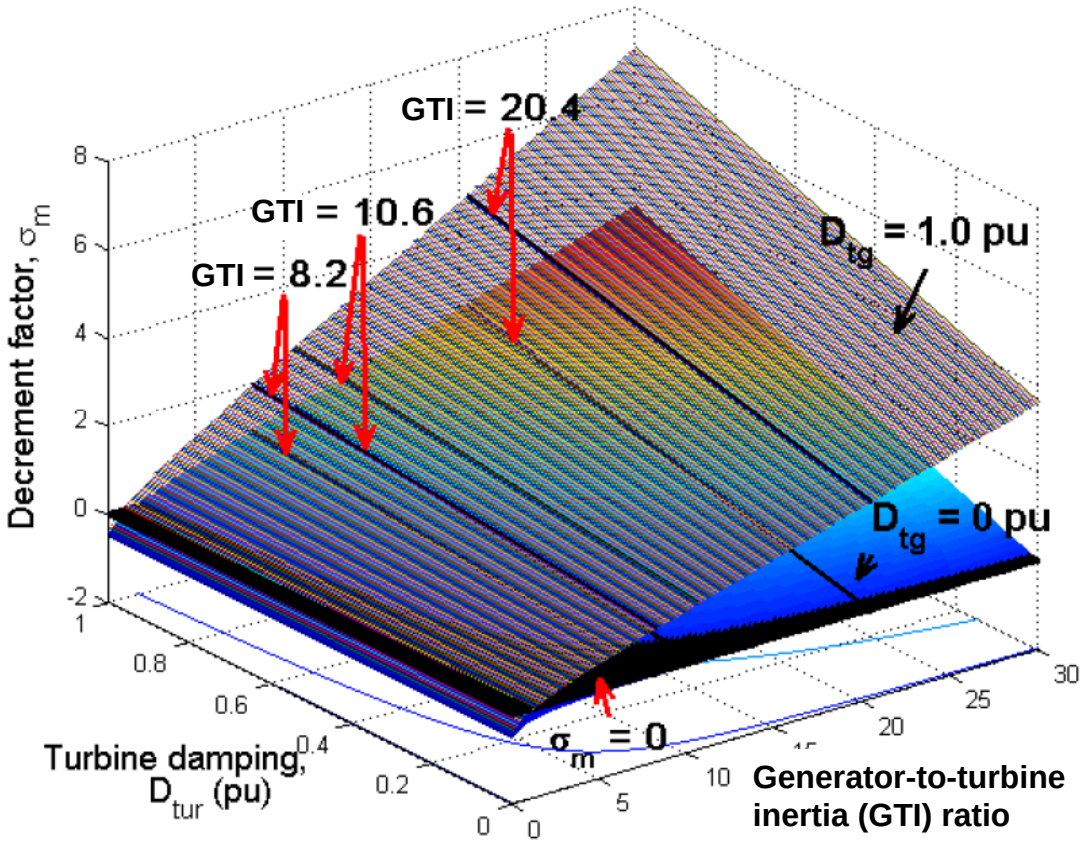


Figure 10.28: Decrement factor of the integrated hydroelectric unit and an HVDC system

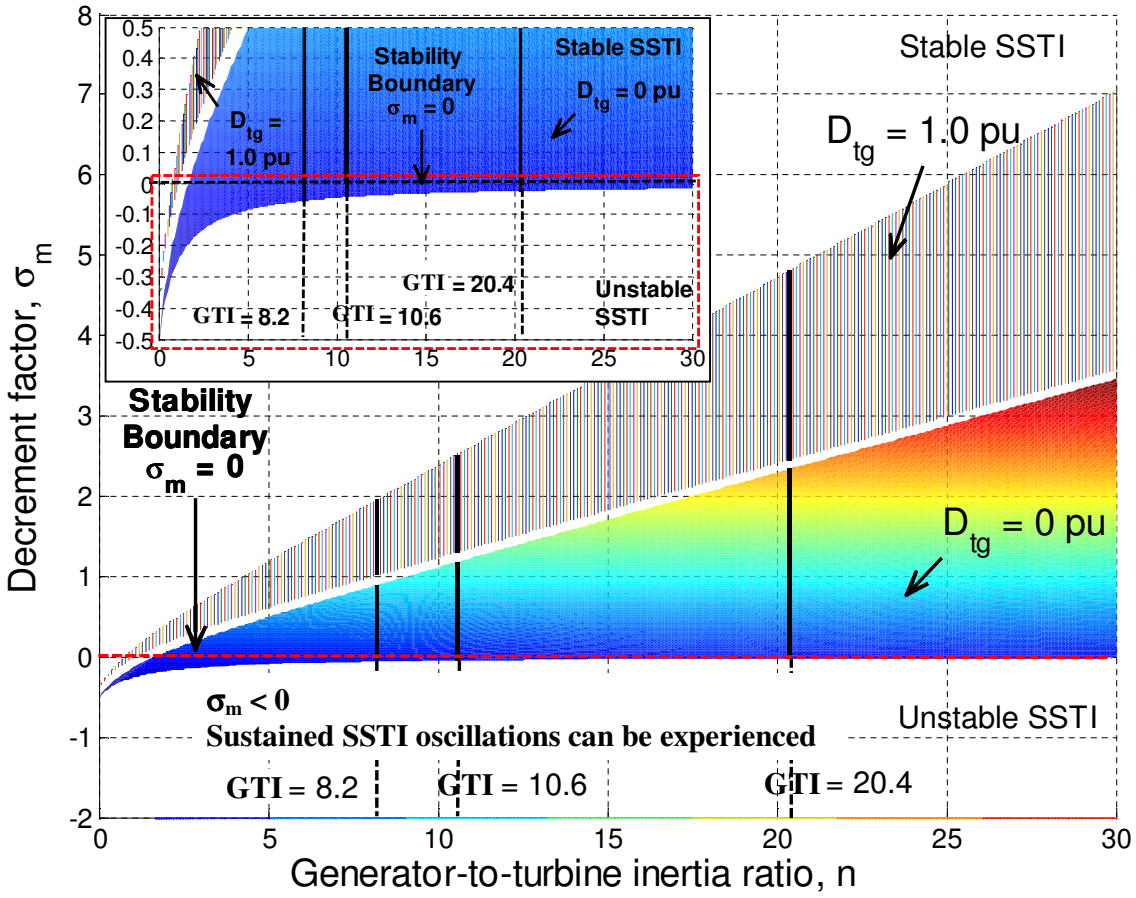


Figure 10.29: Decrement factor with respect to generator-to-turbine inertia ratio for a hydro unit connected to HVDC

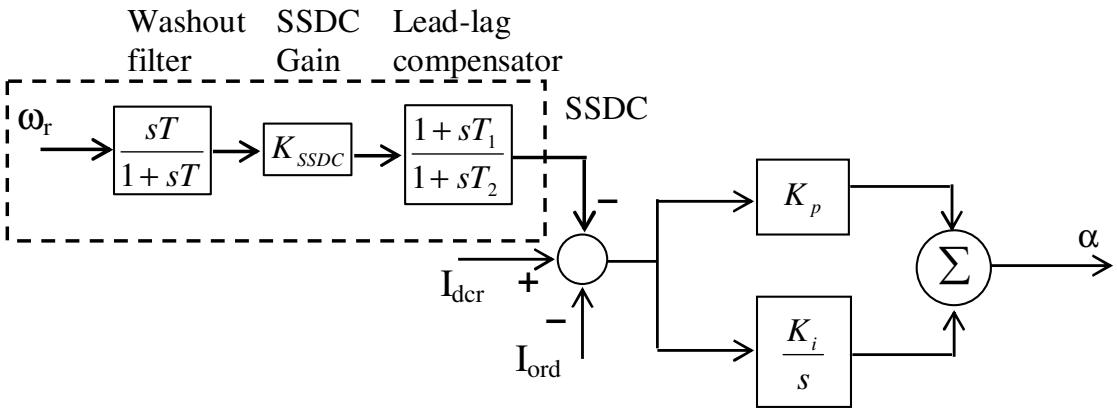


Figure 10.30: Constant current controller with SSDC at rectifier station

It is noted that the torsional interactions between the HVDC controls and the hydro TG shaft system predominantly exist for the largest hydroelectric unit of 1000 MVA capacity with a small GTI ratio, where the turbine modal damping may not be sufficient to counteract the negative damping introduced by the HVDC current controller. Accordingly, a typical SSDC has been incorporated to demonstrate the mitigation of SSTI between the largest hydroelectric unit and the HVDC system at vulnerable torsional frequencies.

It is demonstrated that the TG torque deviation is critical for the largest hydro unit with the shaft system 2 (GTI ratio of 8.2). A typical SSDC is designed to improve the damping of the torsional mode for this machine. The improvement in TG torque response for a three-phase to ground fault at rectifier station when a SSDC is incorporated can be seen in Fig. 10.31(a). The corresponding rotor speed response is shown in Fig. 10.31(b). The system with no SSDC results in growing oscillations in TG torque and rotor speed responses as evidenced in Figs. 10.17(b) and 10.21(b) respectively. With the incorporation of a SSDC into the system, it is observed that the TG torque oscillations have subsequently been damped out and the system remains stable.

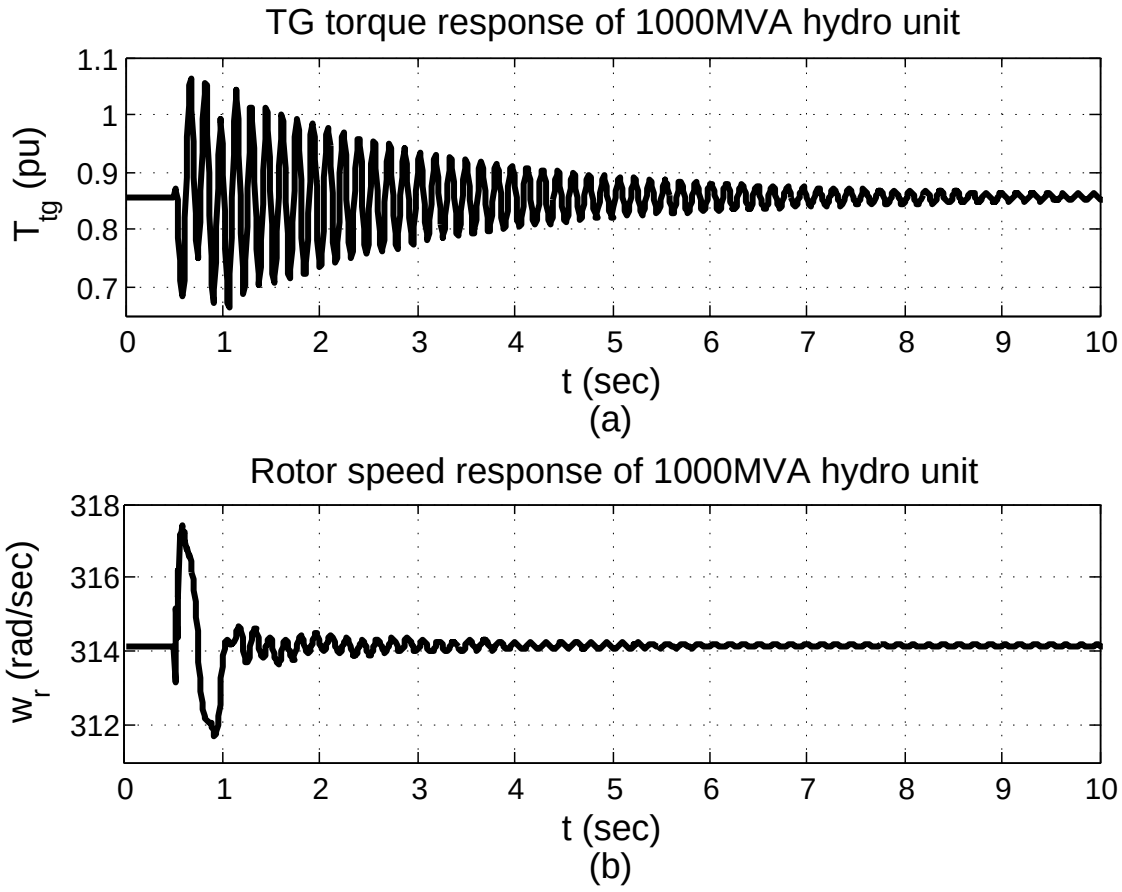


Figure 10.31: (a) TG torque response and (b) Rotor speed response of 1000MVA hydro unit for three-phase to ground fault at the rectifier station with SSDC incorporated in CC controller at rectifier

## 10.7 Summary

This chapter has investigated SSTI for a hydroelectric TG unit connected to an HVDC system under different operating conditions. Damping torque analysis has been conducted to examine the SSTI. Sensitivity analysis has revealed that a system with a higher hydroelectric generator loading, higher DC power transfer or a weak AC link is more susceptible to SSTI instability. It is found that the torsional frequency of a hydroelectric TG unit may fall well-within the frequency range of the negative damping introduced by the HVDC current controller. The modal torsional damping may be sufficient to diminish the negative damping effect posed by the HVDC current controller with a relatively high value of generator-to-turbine inertia ratio. It is also observed that the hydroelectric TG units may experience instability for large disturbances such as three-phase to ground fault at the rectifier station. Sustained and growing TG torque oscillations are noted for some operating conditions, for which the rotor speed oscillations may grow, resulting in system instability. SSTI phenomenon is predominant for an HVDC system integrated hydroelectric unit with low generator-to-turbine inertia ratio due to deficiency in modal damping.

## References


[1] M. Bahrman, E. V. Larsen, R. J. Piwko H. S. Patel, "Experience with HVDC-Turbine-Generator Torsional Interaction at Square Butte," *IEEE Trans. Power App. Syst.*, Vol. PAS-99, No. 3, pp. 966-975, May 1980.

[2] K. Clark, "Overview of Subsynchronous Resonance Related Phenomena," in *Proc. 2012 IEEE PES Transmission and Distribution Conf. and Exposition (T&D)*, pp. 1-3, 2012.

[3] G. Andersson, R. Atmuri, R. Rosenqvist, and S. Torseng, "Influence of Hydro Units' Generator-to-Turbine Inertia Ratio on Damping of Subsynchronous Oscillations," *IEEE Trans. Power App. Syst.*, Vol. PAS-103, No. 8, pp. 2352-2361, Aug 1984.

[4] I. M. Canay, "A Novel Approach to the Torsional Interaction and Electrical Damping of the Synchronous Machine Part I: Theory," *IEEE Trans. Power App. Syst.*, Vol. PAS-101, No. 10, pp. 3630-3638, Oct 1982.

[5] I. M. Canay, "A Novel Approach to the Torsional Interaction and Electrical Damping of the Synchronous Machine Part II: Application to an arbitrary network," *IEEE Trans. Power App. Syst.*, Vol. PAS-101, No. 10, pp. 3639-3647, Oct 1982.

[6] L. Harnefors, "Analysis of Subsynchronous Torsional Interaction With Power Electronic Converters," *IEEE Trans. Power Syst.*, Vol. 22, No. 1, pp. 305-313, Feb 2007.

[7] L. Harnefors, "Proof and Application of the Positive-Net-Damping Stability Criterion," *IEEE Trans. Power Syst.*, Vol. 26, No. 1, pp. 481-482, Feb 2011.

[8] C. Karawita, and U. D. Annakkage, "Multi-Infeed HVDC Interaction Studies Using Small-Signal Stability Assessment," *IEEE Trans. Power Del.*, Vol. 24, No. 2, pp. 910-918, Apr 2009.

[9] N. Prabhu and K. R. Padiyar, "Investigation of Subsynchronous Resonance With VSC-Based HVDC Transmission Systems," *IEEE Trans. Power Del.*, Vol. 24, No. 1, pp. 433-440, Jan 2009.

[10] A. Tabesh and R. Iravani, "Frequency-response analysis of torsional dynamics," *IEEE Trans. Power Syst.*, Vol. 19, No. 3, pp. 1430-1437, Aug 2004.

[11] S. Dahal, N. Mithulananthan, and T. Saha, "Assessment and Enhancement of Small Signal Stability of a Renewable-Energy-Based Electricity Distribution System," *IEEE Trans. Sustain. Energy*, Vol. 3, No. 3, pp. 407-415, July 2012.

[12] M. Khan, M. Iqbal, and J. Quaicoe, "Effects of Efficiency Nonlinearity on the Overall Power Extraction: A Case Study of Hydrokinetic-Energy-Conversion Systems," *IEEE Trans. Energy Convers.*, Vol. 26, No. 3, pp. 911-922, Sept. 2011.

[13] M. Khan, M. Iqbal, and J. Quaicoe, "Dynamics of a vertical axis hydrokinetic energy conversion system with a rectifier coupled multi-pole permanent magnet generator," *IET Renew. Power Gen.*, Vol. 4, No. 2, pp. 116-127, March 2010.

[14] J. O'Reilly, A. Wood, C. Osauskas, "Frequency domain based control design for an HVDC converter connected to a weak ac network," *IEEE Trans. Power Del.*, Vol. 18, No. 3, pp. 1028-1033, July 2003.

[15] J. Bladh, P. Sundqvist, and U. Lundin, "Torsional Stability of Hydropower Units Under Influence of Subsynchronous Oscillations," *IEEE Trans. Power Syst.*, Vol. 28, No. 4, pp. 3826-3833, Nov. 2013.

[16] P. Kundur. *Power System Stability and Control.* McGraw-Hill, 1994.

[17] P. C. Krause, O. Wasynczuk, S. D. Sudhoff, *Analysis of Electric Machinery.* New York, NY, USA: IEEE Press, 1995.

[18] K. R. Padiyar. *Analysis of Subsynchronous Resonance in Power Systems.* Norwell, MA, USA: Kluwer, 1999.

[19] Torsional interaction between electrical network phenomena and turbine-generator shafts: plant vulnerability, EPRI, Tech Rep., 2006.

[20] IEEE Subsynchronous Resonance Working Group, "Proposed Terms and Definitions for Subsynchronous Oscillations," *IEEE Trans. Power App. Syst.*, Vol. PAS-99, No. 2, pp. 506-511, Mar 1980.

[21] D. J. Kim, H. K. Nam, and Y. H. Moon, "A Practical Approach to HVDC System Control for Damping Subsynchronous Oscillation Using the Novel Eigenvalue Analysis Program," *IEEE Trans. Power Syst.*, Vol. 22, No. 4, pp. 1926-1934, Nov 2007.

[22] P. Pourbeik, A. Bostrom, and B. Ray, "Modeling and application studies for a modern static var system installation," *IEEE Trans. Power Del.*, Vol. 21, No. 1, pp. 368-377, Jan 2006.

[23] [Online]. Available: http://www.hydroconsult.de/content.php?action=forum

[24] M. Szechtman, T. Wess, and C. V. Thio, "First benchmark model for HVDC control studies," *Electra*, no. 135, pp. 54-73, Apr. 1991.

[25] C. Karawita and U. D. Annakkage, "HVDC-Generator-Turbine Torsional Interaction Studies Using A Linearized Model With Dynamic Network Representation," in *Proc. Int. Conf. Power Systems Transients (IPST2009)*, 2009.

# Chapter 11

# Conclusions and Recommendations for Future Work

## 11.1 Conclusions

This thesis has investigated the dynamic interactions of the hydroelectric TG unit when connected in close vicinity of HVDC system. The development of the small-signal stability model to analyse the dynamic interactions of the hydroelectric TG unit and the HVDC system has been presented. As our research focuses on the electrical and electromechanical behaviours of hydroelectric unit, thus, only salient pole machine representation is described in the thesis. Stator transients have been included in the formulation of the synchronous machine for detailed analysis. The dynamics of all AC network elements, including transmission lines, transformers, loads, filters and etc, have also been encountered for detailed analysis, especially when HVDC and SSTI are of interest, where the frequency of interest is larger. The conventional steady-state representation of the system network only allows for the electromechanical oscillation analysis, and it will not be adequate for HVDC and SSTI analysis.

Chapter 2 has investigated the transient stability of the power system when subjected to large disturbances. Various transient stability assessments have been used to evaluate the

transient stability of SMIB system and multimachine system. It has demonstrated a comparative study of the different techniques in assessing transient stability. The effectiveness of the assessments compared to the conventional TD approach has been illustrated.

Chapter 3 has further investigated the small-signal stability of a power system when subjected to small disturbances using different techniques, these include eigenvalue analysis, participation factors analysis and transient security assessment using transient security index. Participation factors determine the dominant state variables associated with the mode (eigenvalues). This allows the determination of an optimal site to install a power system stabiliser for Hopf bifurcation control in the critical mode.

Stability of a hydroelectric system governed by a PID controller has been studied in Chapter 4. It is important to control and maintain the overall system frequency to ensure satisfactory operation of the power system. System frequency relies heavily on the generation/load balance; any frequency deviation resulted from active power imbalance will initiate the response of the governor, to restore the frequency in accordance with the permanent speed droop settings of the units. An optimum setting for a governor will result in a desired transient response with least speed deviation and faster restoration to conventional speed when subject to a step load change. Frequency response methods has been utilised to determine the stability criterion to govern an isolated hydroelectric system as well as relative stability of the hydroelectric system. Procedure in adjusting the system gains to improve the relative stability has also been presented.

Detailed representation of hydroelectric turbine-penstock has been presented in Chapter 5. Frequency response analysis as well as transient response analysis has been performed to evaluate the effects of the detailed modelling of the turbine-penstock to the stability analyses and the dynamic performances. The classical ideal lossless representation of the hydroelectric turbine, used widely in the past for governor stability studies, may not be adequate for satisfactory fast response and stable operation of governor studies as this model is suitable for small perturbations around the initial operating condition, and approximates to the practical turbine characteristics at low frequencies only. Rather, a more accurate

modelling of the turbine-penstock characteristics is desired to capture and depict the essential dynamic performances at higher frequencies for wide variety of system analyses. The optimum parameters suggested for the PID governor based on the conventional turbine-penstock model do not result in an optimum response when applied to a system with a more detailed turbine-penstock represented. It is suggested that the water hammer effects as well as the friction effects have to be modelled carefully to allow a more accurate and reliable analysis in system dynamics to be performed.

Chapter 6 further concluded that the detailed modelling of power system components is vital to capture essential system dynamic behaviour. The PID and PI governors have been observed to perform better when applied to a more realistic model. Accurate modelling of hydroelectric governor-turbines is essential to characterise and diagnose the system response during an emergency situation. The inclusion of the derivative action in the governor aids in extending the system stability limit.

This thesis has mainly focussed on the torsional interaction, an important phenomenon of concern when a TG unit is connected to a series compensated line or an HVDC system, and has been described in Chapter 7. In general, steam, gas and nuclear units are more susceptible to SSTI problem as they have multiple turbine masses and faster moving shafts which are more vulnerable to twisting compared to hydro units whose mechanical shafts are slow in motion and turbine-generator masses are large. Typically, the large inertia of the hydro generator provides inherent damping of torsional oscillations. However, it is demonstrated that the hydro units with a low GTI ratio $n$ would experience SSTI problem. This is due to the lack of damping at the torsional frequency $f_n$. The simulation results have revealed that the shaft vibration can be excited on a hydro unit, in conjunction with HVDC system

Chapter 8 extended the studies in Chapter 7 by presenting the linearised small-signal dynamic modelling of hydroelectric TG unit with CIGRE first HVDC benchmark system in the synchronously rotating $D$-$Q$ reference frame for small-signal stability analysis. The interaction behaviour between the hydroelectric unit and the dynamics and control of HVDC

system is investigated utilising eigen-analysis, participation factor analysis and conducting sensitivity studies. The computation of eigenvalues and eigenvectors for small signal stability analysis provides an invaluable insight onto the power system dynamic behaviour by characterising the damping and frequency of the system oscillatory modes. The consequences of different operating conditions, such as active and reactive power variations, the variation of GTI ratio, as well as the changes of HVDC constant current controller parameters on small-signal system stability have been investigated. The modal analysis for varying $P$ and $Q$ generation demonstrates that the swing mode of the isolated hydro operation does not get affected substantially. On the contrary, the critical modes of the integrated system, identified as torsional modes, are sensitive to the $P$ and $Q$ variations and HVDC constant current controller parameters. It has also been demonstrated that the hydro units with low GTI ratio may experience SSTI problem due to dominant negative damping imposed by HVDC converter controls.

Utilisation of wind energy to generate electricity has attracted considerable attention worldwide, and is rapidly-growing. The integration of large wind farms with HVDC transmission network could be one of the preferred options for supplying bulk power over a long distance. Since HVDC rectifier stations with constant current control may introduce negative damping on the nearby generating units, it is important to identify the torsional interaction characteristics between TG units and the HVDC systems over a frequency range of interest. However, very little related information exists in regard to wind turbine-generators. Chapter 9 has presented the electromagnetic transient time domain analysis to investigate the possible SSTI phenomenon of fixed-speed (induction machine based) WTG unit interconnected to a CIGRE first HVDC benchmark system. The perturbation analysis has been conducted for a WTG unit to analyse the time response and frequency spectrum of different torque components at modulated frequencies. Growing torque oscillations have been observed if the modulated frequency is close to the torsional mode of a WTG unit and the combined electromechanical system lacks damping. The torsional mode will be excited with the significant deviation in the torque components. The resulting oscillatory fluctuations

in the blade-hub torque of a WTG unit are substantially high in comparison with the one in the hub-generator torque for the specified electrical disturbances. The torsional torques may eventually settle down after a certain time interval, however, the sustained torsional oscillations may result in fatigue damage and reduce the fatigue life of the mechanical shaft system.

The constant current controllers at HVDC rectifier stations and the outer loops which set the reference to the current controller have potential to introduce negative damping on the nearby generating units. It is therefore vital to investigate the torsional interaction behaviour between TG units and the HVDC systems over a frequency range of interest. In Chapter 10, extensive investigations have been carried out to examine the SSTI phenomenon of hydroelectric TG units connected to an HVDC system under different operating conditions using damping torque analysis. Sensitivity analysis has revealed that a system with a higher hydroelectric generator loading, higher DC power transfer or a weak AC link is more susceptible to SSTI instability. Hydro units with different shaft systems are examined for SSTI proneness by conducting perturbation analysis. The impact of hydroelectric TG units with different GTI ratios has also been examined by applying a three-phase to ground fault at the rectifier station. The torsional frequency of a hydroelectric TG unit may fall well-within the frequency range of the negative damping introduced by the HVDC current controller. The modal torsional damping may be sufficient to diminish the negative damping effect posed by the HVDC current controller with a relatively high value of GTI ratio. The hydroelectric TG units may experience instability for large disturbances such as three-phase to ground fault at the rectifier station. Sustained and growing TG torque oscillations have been noted for some operating conditions, for which the rotor speed oscillations may grow, resulting in system instability. SSTI phenomenon is predominant for an HVDC system integrated hydroelectric unit with low GTI ratio due to deficiency in modal damping with relatively low decrement factor and logarithmic decrement.

## 11.2 Recommendations for Future Work

The work presented in this thesis is mainly concentrated on the development of an analytical method in investigating the stability aspect, in particular, SSTI behaviour of a hydroelectric turbine-generator unit connected to an HVDC system.

The dynamic interactions of the power system can be analysed using the developed small-signal model. Future research can be conducted by extending this small-signal model to include other dynamic power system components to further investigate the dynamic interactions in the power system. General directions for future work are provided below:

- Chapter 9 has investigated the SSTI behaviour of a fixed-speed induction machine based wind turbine-generator unit using time domain simulation studies conducted in PSCAD®/EMTDC© environment. The grid integration of wind resources is rapidly-growing all over the world. This development inexorably integrates WTGs into the electrical network in a large scale, thereby posing numerous challenges to all parties concerned. The generating mechanisms for WTG, for example, variable-speed or doubly-fed induction generators, permanent magnet generators and induction generators together with the controllers could possibly exhibit different characteristics and dynamic interactions. SSTI between the WTGs and the HVDC system could be further investigated through incorporating the dynamic characteristics of different type WTGs into the small-signal stability model.

- The developed small-signal model can be further extended to a combined model which represents both conventional synchronous generator (for example, hydroelectric TGs) and WTGs for SSTI analysis with HVDC system. Both SSTI of hydroelectric TGs and WTGs with HVDC system can be further analysed by considering their dynamic characteristics. An offshore wind farm can be included to study its dynamic characteristics associated with the HVDC system.

- The developed combined small-signal model which represents both conventional synchronous generator and WTGs can be further extended to multi-machine system,

which include a variety of TGs, such as steam and gas TGs, to investigate their dynamic characteristics and SSTI with HVDC system in the power system.

- The small-signal model with the voltage-source converter (VSC) type HVDC system can be further expanded to develop a multi-terminal HVDC (MTDC) transmission system. There is an increasing interest in the MTDC system in today's advanced power systems. This MTDC system can be developed similarly to the approach used in this thesis in developing the two-terminal HVDC system. Further investigation is required to analyse the interactions of the TGs with this MTDC system. Furthermore, a continue research can be carried out to investigate the dynamic interactions between this MTDC system and the multi-machine system, which includes a variety of TGs, such as hydroelectric unit, WTGs, steam and gas TGs.

- The guidelines for a generic SSDC design have been presented in Chapter 10. The robust design methodologies for supplementary subsynchronous damping controller (SSDC) to provide sufficient positive damping in improving the dynamic performance of the ac/dc system and to overcome the negative damping produced inherently by DC current control at the rectifier can be further investigated. A study approach in obtaining the optimum gain for SSDC would be beneficial.

# Appendix A

# Linearised Models

## A.1 Linearised Synchronous Machine Model

The representation of a three-phase salient pole synchronous machine is generally of $5^{th}$ order for conventional stability analysis with stator transients neglected. The rotor of the salient pole synchronous machine comprises of a field winding and an armortisseur (damper) winding on the direct axis and a damper winding on the quadrature axis. This detailed model of synchronous machine is designated as model (2.1), where the first number indicates the number of windings on $d$-axis and the second number indicates the number of windings on $q$-axis [1]. Its equivalent circuits of $dq$-axes are shown in Fig. A.1(a) and (b). A round rotor synchronous machine can be easily represented by incorporating an additional $kq$ winding in $q$-axis, which yields a $6^{th}$ order representation.

Hydroelectric TGs are salient pole machines. Steam and gas TGs are round (or cylindrical) machines. Our research focuses on the electrical and electromechanical behaviours of hydroelectric unit, thus, only salient pole machine representation is described in the thesis. Stator transients have been included in the formulation of the synchronous machine for detailed analysis; this yields $7^{th}$ order model for salient pole machine, and $8^{th}$ order model for round rotor machine (with two additional differential equations for the stator flux components in dq axes included). The linearised state space model of a synchronous machine

is formulated with the assumptions that the stator current flowing out of the terminal is positive.

The established linearised machine model has the following state-space representation [1, 2, 3]:

$$\begin{bmatrix} \Delta\dot{\psi}_d \\ \Delta\dot{\psi}_q \\ \Delta\dot{\psi}_{fd} \\ \Delta\dot{\psi}_{kd} \\ \Delta\dot{\psi}_{kq} \\ \Delta\frac{\dot{\omega}_r}{\omega_b} \\ \Delta\dot{\delta}_r \end{bmatrix} = \begin{bmatrix} A_{sm11} & A_{sm12} & A_{sm13} & A_{sm14} & 0 & A_{sm16} & A_{sm17} \\ A_{sm21} & A_{sm22} & 0 & 0 & A_{sm25} & A_{sm26} & A_{sm27} \\ A_{sm31} & 0 & A_{sm33} & A_{sm34} & 0 & 0 & 0 \\ A_{sm41} & 0 & A_{sm43} & A_{sm44} & 0 & 0 & 0 \\ 0 & A_{sm52} & 0 & 0 & A_{sm55} & 0 & 0 \\ A_{sm61} & A_{sm62} & A_{sm63} & A_{sm64} & A_{sm65} & A_{sm66} & 0 \\ 0 & 0 & 0 & 0 & 0 & A_{sm76} & 0 \end{bmatrix} \begin{bmatrix} \Delta\psi_d \\ \Delta\psi_q \\ \Delta\psi_{fd} \\ \Delta\psi_{kd} \\ \Delta\psi_{kq} \\ \Delta\frac{\omega_r}{\omega_b} \\ \Delta\delta_r \end{bmatrix} + \begin{bmatrix} B_{sm11} & B_{sm12} & 0 & 0 & 0 \\ B_{sm21} & B_{sm22} & 0 & 0 & 0 \\ 0 & 0 & B_{sm33} & 0 & 0 \\ 0 & 0 & 0 & B_{sm44} & 0 \\ 0 & 0 & 0 & 0 & B_{sm55} \\ 0 & 0 & 0 & 0 & 0 \\ 0 & 0 & 0 & 0 & 0 \end{bmatrix} \begin{bmatrix} \Delta v_d^e \\ \Delta v_q^e \\ \Delta v_{fd}'^r \\ \Delta v_{kd}'^r \\ \Delta v_{kq}'^r \end{bmatrix} \tag{A.1}$$

where, the seven state variables are $d$- and $q$- axes stator flux linkages per second ($\psi_d$ and $\psi_q$), rotor flux linkages per second for a field winding ($\psi_{fd}$) and for $d$- and $q$- axes damper windings ($\psi_{kd}$ and $\psi_{kq}$), rotor speed ($\omega_r$), nominal frequency ($\omega_s$) and rotor angle ($\delta_r$). The five inputs are $d$- and $q$- axes voltage referred to the synchronous rotating reference frame ($v_d^e$ and $v_q^e$) and voltages referred to a reference frame fixed in the rotor ($v_{fd}'^r$, $v_{kd}'^r$ and $v_{kq}'^r$).

The components of the synchronous machine state matrix $A_{sm}$ and the input matrix $B_{sm}$ are given as follows:

$$
\begin{aligned}
A_{sm11} &= \frac{r_s}{D_d}\left(X'_{fd}X'_{kd} - X^2_{md}\right) & A_{sm34} &= -\frac{r_{fd}}{D_d}\left(X_dX_{md} - X^2_{md}\right)\\
A_{sm12} &= \frac{\omega_r}{\omega_b} & A_{sm41} &= -\frac{r_{kd}}{D_d}\left(X_{md}X'_{fd} - X^2_{md}\right)\\
A_{sm13} &= \frac{r_s}{D_d}\left(-X_{md}X'_{kd} + X^2_{md}\right) & A_{sm43} &= -\frac{r_{kd}}{D_d}\left(X_dX_{md} - X^2_{md}\right)\\
A_{sm14} &= \frac{r_s}{D_d}\left(-X_{md}X'_{fd} + X^2_{md}\right) & A_{sm44} &= -\frac{r_{kd}}{D_d}\left(-X_dX'_{fd} + X^2_{md}\right)\\
A_{sm16} &= \psi_{q0} & A_{sm52} &= -\frac{r_{kq}X_{mq}}{D_q}\\
A_{sm17} &= v^r_{q0} & A_{sm55} &= \frac{r_{kq}X_q}{D_q}\\
A_{sm21} &= -\frac{\omega_r}{\omega_b} & A_{sm61} &= \frac{-i_{q0}+\psi_{q0}m_{d11}}{2H\omega_b}\\
A_{sm22} &= \frac{r_sX'_{kq}}{D_q} & A_{sm62} &= \frac{i_{d0}-\psi_{d0}m_{q11}}{2H\omega_b}\\
A_{sm25} &= \frac{-r_sX_{mq}}{D_q} & A_{sm63} &= \frac{\psi_{q0}m_{d12}}{2H\omega_b}\\
A_{sm26} &= -\psi_{d0} & A_{sm64} &= \frac{\psi_{q0}m_{d13}}{2H\omega_b}\\
A_{sm27} &= -v^r_{d0} & A_{sm65} &= \frac{-\psi_{d0}m_{q12}}{2H\omega_b}\\
A_{sm31} &= \frac{-r_{fd}}{D_d}\left(X_{md}X'_{kd} - X^2_{md}\right) & A_{sm66} &= \frac{-K_d}{2H\omega_b}\\
A_{sm33} &= \frac{-r_{fd}}{D_d}\left(-X_dX'_{kd} + X^2_{md}\right) & A_{sm76} &= 1
\end{aligned}
$$

$$
\begin{aligned}
B_{sm11} &= cos\delta_0 & B_{sm33} &= \frac{r_{fd}}{X_{md}}\\
B_{sm12} &= sin\delta_0 & B_{sm44} &= 1\\
B_{sm21} &= -sin\delta_0 & B_{sm55} &= 1\\
B_{sm22} &= cos\delta_0
\end{aligned}
$$

$$
\begin{aligned}
m_{d11} &= \frac{1}{D_d}\left(X'_{fd}X'_{kd} - X^2_{md}\right) & m_{q11} &= \frac{X'_{kq}}{D_q}\\
m_{d12} &= \frac{1}{D_d}\left(-X_{md}X'_{kd} + X^2_{md}\right) & m_{q12} &= \frac{-X_{mq}}{D_q}\\
m_{d13} &= \frac{1}{D_d}\left(-X_{md}X'_{fd} + X^2_{md}\right) & m_{q21} &= \frac{X_{mq}}{D_q}\\
m_{d21} &= \frac{1}{D_d}\left(X_{md}X'_{kd} - X^2_{md}\right) & m_{q22} &= \frac{-X_q}{D_q}\\
m_{d22} &= \frac{1}{D_d}\left(-X_dX'_{kd} + X^2_{md}\right) & D_d &= X^2_{md}\left(X_d - 2X_{md} + X'_{fd} + X'_{kd}\right) - X_dX'_{fd}X'_{kd}\\
m_{d23} &= \frac{1}{D_d}\left(X_dX_{md} - X^2_{md}\right) & D_q &= -X_qX'_{kq} + X^2_{mq}\\
m_{d31} &= \frac{1}{D_d}\left(X_{md}X'_{fd} - X^2_{md}\right)\\
m_{d32} &= \frac{1}{D_d}\left(X_dX_{md} - X^2_{md}\right)\\
m_{d33} &= \frac{1}{D_d}\left(-X_dX'_{fd} + X^2_{md}\right)
\end{aligned}
$$

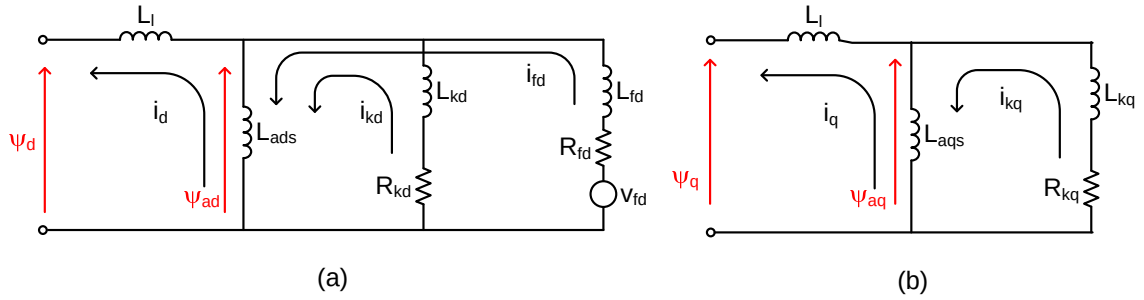


Figure A.1: Equivalent circuits of dq-axes for hydroelectric unit

## A.2 Linearised Mechanical System

The linearised model of the hydroelectric torsional shaft system is represented based on a mass-spring-damping model as seen in Fig. A.2. With the exciter mass neglected, the torsional shaft system of a hydroelectric unit generally comprises of turbine and generator masses, and it can be mathematically described as follows:

$$\begin{bmatrix} \Delta\dot{\omega}_g \\ \Delta\dot{\delta}_g \\ \Delta\dot{\omega}_t \\ \Delta\dot{\delta}_t \end{bmatrix} = \begin{bmatrix} -\frac{D_g+D_{tg}}{2H_g} & -\frac{K_{tg}}{2H_g} & \frac{D_{tg}}{2H_g} & \frac{K_{tg}}{2H_g} \\ \omega_b & 0 & 0 & 0 \\ \frac{D_{tg}}{2H_t} & \frac{K_{tg}}{2H_t} & -\frac{D_t+D_{tg}}{2H_t} & -\frac{K_{tg}}{2H_t} \\ 0 & 0 & \omega_b & 0 \end{bmatrix} \begin{bmatrix} \Delta\omega_g \\ \Delta\delta_g \\ \Delta\omega_t \\ \Delta\delta_t \end{bmatrix} + \begin{bmatrix} 0 & -\frac{1}{2H_g} \\ 0 & 0 \\ -\frac{1}{2H_t} & 0 \\ 0 & 0 \end{bmatrix} \begin{bmatrix} \Delta T_m \\ \Delta T_e \end{bmatrix} \tag{A.2}$$

where, the four state variables are the generator rotor speed and angle ($\omega_g$ and $\delta_g$) and turbine rotor speed and angle ($\omega_t$ and $\delta_t$), the two inputs are mechanical and electrical torques ($T_m$ and $T_e$).

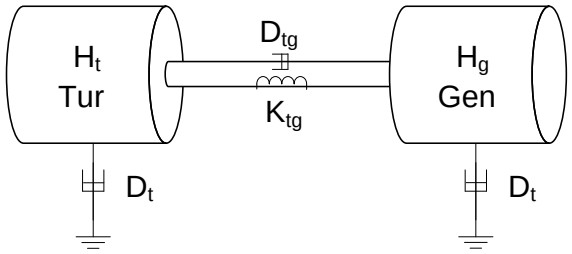


Figure A.2: Mass-spring-damper mass

Equation (A.2) describes a state-space representation of a two-masses shaft system, and it can be easily extended to include more masses in the state-space representation.

## A.3 Linearised AC Electrical Network System

The dynamics of all AC network elements, including transmission lines, transformers, loads, filters and etc, will need to be encountered for detailed analysis, especially when HVDC and SSTI are of interest. The conventional steady state representation of the system network only allows for the electromechanical oscillation analysis, but it will not be adequate for HVDC and SSTI analysis. This section explains the linearised modelling of the AC electrical network, including their dynamic effects.

Consider an electrical network of a series resistance $R$ and an inductive reactance $X_L$, the electrical network can be represented in $DQ$-synchronously rotating reference frame as follows:

$$\begin{bmatrix} \Delta\dot{i}_D \\ \Delta\dot{i}_Q \end{bmatrix} = \begin{bmatrix} -\frac{\omega R}{X_L} & \omega \\ -\omega & -\frac{\omega R}{X_L} \end{bmatrix} \begin{bmatrix} \Delta i_D \\ \Delta i_Q \end{bmatrix} + \begin{bmatrix} \frac{\omega}{X_L} & 0 \\ 0 & \frac{\omega}{X_L} \end{bmatrix} \begin{bmatrix} \Delta v_D \\ \Delta v_Q \end{bmatrix} \tag{A.3}$$

where, the two state variables are the electrical network currents in $DQ$-synchronously rotating reference frame ($i_D$ and $i_Q$) and the two output variables are the electrical network voltages in $DQ$-synchronously rotating reference frame ($v_D$ and $v_Q$).

## A.4 Linearised HVDC System

The analytical modelling of an HVDC system has been demanding due to the inherently nonlinear characteristics of the DC converter. The complexity of the HVDC system modelling involves modelling of the 12-pulse Graetz converter bridge, phase locked oscillator (PLO), firing and valve blocking controls and firing angle $\alpha$ and extinction angle $\gamma$ measurements, as well as the RC snubber circuits for each thyristor. For small-signal stability analysis, some assumptions are made to represent the linearised HVDC system. The three-phase ac systems are assumed to be balanced at fundamental frequency and higher order harmonics have been neglected [4].

### A.4.1 Converter model

The converters perform ac-dc and dc-ac conversion and comprises of valve bridges and transformer with tap changers. The direct voltage considering commutation overlap and ignition delay is given by the equation as follows:

$$V_{dr} = \frac{3\sqrt{2}}{\pi} B_r T_r V_{acr} cos\alpha - \frac{3}{\pi} X_{cr} B_r I_{dr} \quad (A.4)$$

$$V_{di} = \frac{3\sqrt{2}}{\pi} B_i T_i V_{aci} cos\beta + \frac{3}{\pi} X_{ci} B_i I_{di} \quad (A.5)$$

where, $V_{ac}$ is the line-to-line voltage of an ac system, $B$ = number of bridges in series, $T$ = transformer ratio, $I_d$ = direct current, $X_c$ = commutating reactance, $\alpha$ is the ignition delay angle, $\beta$ is the ignition advance angle, subscripts $r$ and $i$ represent the rectifier-side and inverter side respectively.

Linearisation of (A.4) and (A.5) yields the representation of the direct voltage at rectifier and inverter stations with respect to the changes in rotor speed ($\Delta\omega_r$), rectifier firing angle ($\Delta\alpha$), ignition advance angle ($\Delta\beta$) and direct current at rectifier and inverter stations ($\Delta I_{dr}$ and $\Delta I_{di}$) as follows:

$$\Delta V_{dr} = \frac{3\sqrt{2}}{\pi} B_r T_r V_{acr0} (\cos\alpha_0 \Delta\omega_r - \sin\alpha_0 \Delta\alpha) - \frac{3}{\pi} X_{cr} B_r \Delta I_{dr} \quad (A.6)$$

$$\Delta V_{di} = \frac{3\sqrt{2}}{\pi} B_i T_i V_{aci0} (\cos\beta_0 \Delta\omega_r - \sin\beta_0 \Delta\beta) + \frac{3}{\pi} X_{ci} B_i \Delta I_{di} \quad (A.7)$$

where, $V_{acr0}$ and $V_{aci0}$ is the initial AC voltage at rectifier and inverter stations respectively, $\alpha_0$ is the initial rectifier firing angle, $\beta_0$ is the initial ignition advance angle, $\Delta V_{acr} = V_{acr0}\Delta\omega_r$ and $\Delta V_{aci} = V_{aci0}\Delta\omega_r$.

### A.4.2 DC Transmission Line Model

The T-model HVDC system as shown in Fig. A.3 has a linearised, state-space formulation as given in (A.8).

$$\begin{bmatrix} \Delta\dot{I}_{dr} \\ \Delta\dot{I}_{di} \\ \Delta\dot{V}_{dm} \end{bmatrix} = \begin{bmatrix} -\frac{R_d}{L_d} & 0 & -\frac{1}{L_d} \\ 0 & -\frac{R_d}{L_d} & \frac{1}{L_d} \\ \frac{1}{C_d} & -\frac{1}{C_d} & 0 \end{bmatrix} \begin{bmatrix} \Delta I_{dr} \\ \Delta I_{di} \\ \Delta V_{dm} \end{bmatrix} + \begin{bmatrix} \frac{1}{L_d} & 0 \\ 0 & -\frac{1}{L_d} \\ 0 & 0 \end{bmatrix} \begin{bmatrix} \Delta V_{dr} \\ \Delta V_{di} \end{bmatrix} \tag{A.8}$$

where, the three state variables are the dc-side currents at rectifier and inverter stations ($I_{dr}$ and $I_{di}$) and the capacitor voltage at the middle point of the DC transmission line ($V_{dm}$). The two inputs are the direct voltages at rectifier and inverter stations ($V_{dr}$ and $V_{di}$) respectively.

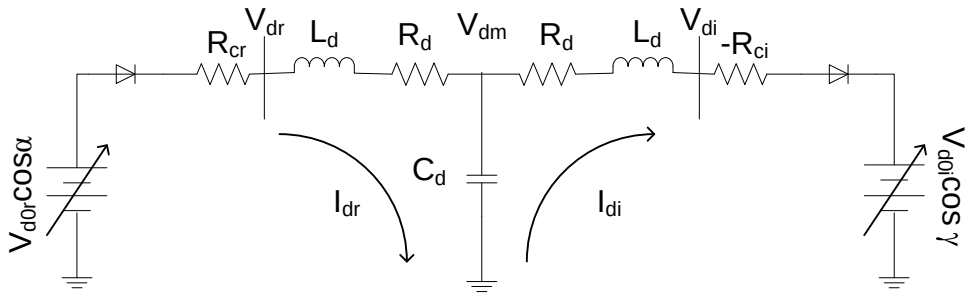


Figure A.3: HVDC T-Model Transmission Line

### A.4.3 HVDC Controllers

The HVDC system is considered to operate at normal conditions, i.e. the rectifier operates in CC control mode whilst the inverter operates in CEA control mode as shown in Fig. A.4. It is assumed that the converter controllers are operating close to the normal operating conditions without changing the controller modes for small signal analysis.

Both CC and CEA controllers are based on proportional and integral logic to adjust the firing angle at rectifier and inverter stations respectively. The difference between measured dc-side current and the current order is used as an input to the CC controller, whilst the difference between measured extinction angle and the extinction angle order is used as an input to the CEA controller as illustrated in Figs. A.5(a) and A.5(b).

The state-space formulation of the CC controller at rectifier station and its respective

change in the firing angle are given in the following:

$$\Delta\dot{x}_{cc} = K_i\left(\Delta I_{dr} - \Delta I_{ord}\right) \tag{A.9}$$

$$\Delta\alpha = K_p\left(\Delta I_{dr} - \Delta I_{ord}\right) + \Delta x_{cc} \tag{A.10}$$

where, $\alpha$ = firing angle at rectifier station, $K_p$ = proportional gain, $K_i$ = integral gain, $I_{ord}$ = current order.

As for the CEA controller at inverter station, its state-space representation and the respective change in the firing angle are as follows:

$$\Delta\dot{x}_{cea} = K_i\left(\Delta\gamma - \Delta\gamma_{ord}\right) \tag{A.11}$$

$$\Delta\alpha_{inv} = K_p\left(\Delta\gamma - \Delta\gamma_{ord}\right) + \Delta x_{cea} \tag{A.12}$$

where, $\alpha_{inv}$ = firing agle at inverter station, $\gamma_{ord}$ = extinction angle order.

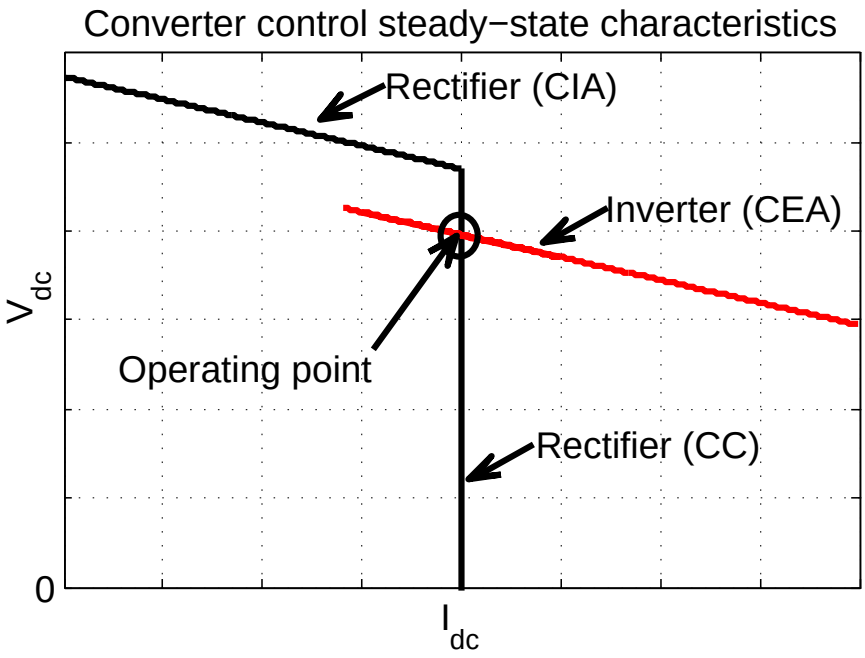


Figure A.4: Converter control steady state characteristics

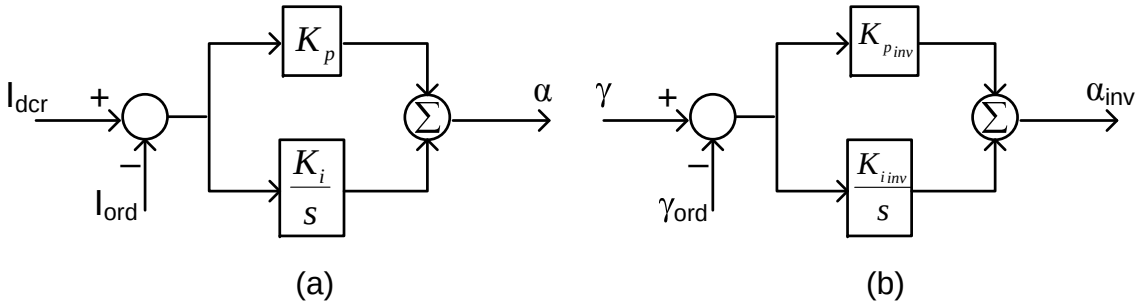


Figure A.5: Constant Current Control of the Rectifier

### A.4.4 Phase Locked Oscillator

The block diagram of the phase locked oscillator (PLO), used in the 6-pulse bridge component as shown in Fig. A.6, is of the DQZ type. The three major components comprise of an error signal calculator, PI controller and voltage-controlled oscillator (VCO) [4].

The PLO is based on the phase vector technique. This technique exploits trigonometric multiplication identities to form an error signal, which speeds up or slows down the VCO in order to match the phase between the ac voltage and PLO output. The input to the PLO is the phase angle component of the ac bus voltage in the synchronous reference frame. The output signal $\theta_{PLO}$ generated is a ramp synchronised to the ac voltage. The error signal of the phase between the ac voltage and PLO output is passed through the PI controller to obtain the angular frequency error, which is then added to the nominal frequency $\omega_0$. The subsequent frequency is integrated to acquire the phase angle. The integrator, representing the VCO operation, is necessary so to allow the PLO to trace changes in the ac bus voltage frequency with zero steady-state error [4, 5].

All PLO schemes have their own controller with two adjustable parameters. The benefit of having two additional controller gains is that they can be applied to optimise the system stability, and possibly to overcome the stability issues by adjusting the controller parameters [6].

The small-signal state-space representation of the PLO model is given in (A.13). The resulting phase angle from the PLO, i.e. $\theta_{PLO}$, is added to the desired firing angle $\alpha_{cc}$ to

acquire the firing instant $\alpha$ as seen in Fig. A.7.

$$\begin{bmatrix} \Delta\dot{x}_{PLO} \\ \Delta\dot{\theta}_{PLO} \end{bmatrix} = \begin{bmatrix} 0 & -K_{iPLO}V_p^2 \\ 1 & -K_{pPLO}V_p^2 \end{bmatrix} \begin{bmatrix} \Delta x_{PLO} \\ \Delta\theta_{PLO} \end{bmatrix} + \begin{bmatrix} K_{iPLO}V_p^2 \\ K_{pPLO}V_p^2 \end{bmatrix} \begin{bmatrix} \Delta\delta \end{bmatrix} \tag{A.13}$$

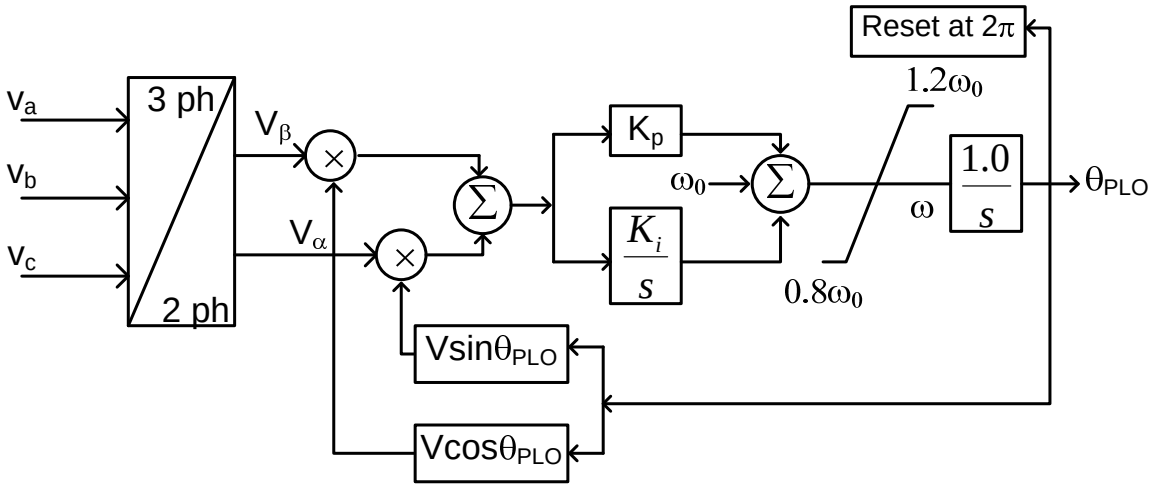


Figure A.6: Phase Locked Oscillator

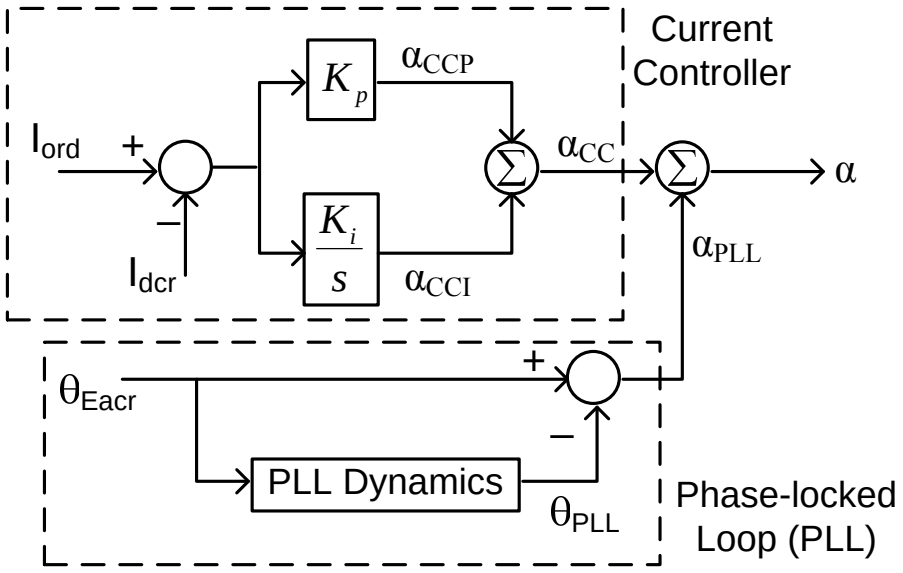


Figure A.7: Converter control at the rectifier station

### A.4.5 Interface Between AC and DC Systems

The linearised state space model for each subsystem has been represented individually as shown in subsections A.1, A.2, A.3 and A.4. These linearised models of the subsystems can be combined together to obtain the overall small-signal state space model of the electrical network system. The linearised representation of the ac-dc interaction equations derived from the power balance equation, as in (A.14), highlights the small-signal inter-relationship between ac and dc systems as shown below:

$$\begin{bmatrix} \Delta i_{acr} \\ \Delta \phi_{acr} \end{bmatrix} = \begin{bmatrix} 0 & 0 & \frac{\sqrt{6}}{\pi} B_r T_r \\ x_{acdc1} & \frac{\sin \alpha_0}{\sin \phi_{acr0}} & x_{acdc2} \end{bmatrix} \begin{bmatrix} \Delta v_{acr} \\ \Delta \alpha \\ \Delta I_{dr} \end{bmatrix} \tag{A.14}$$

where, $x_{acdc1} = -\frac{X_{cr} I_{dr0}}{\sqrt{2} T_r v_{acr0}^2 \sin \phi_{acr0}}$ and $x_{acdc2} = \frac{X_{cr}}{\sqrt{2} T_r v_{acr0} \sin \phi_{acr0}}$, $i_{ac}$ = RMS value of the alternating current at fundamental frequency, $\phi_{ac}$ = phase angle between fundamental line current and the line-to-neutral source voltage, $v_{ac}$ = line-to-line voltage of an ac system, $B$ = number of bridges in series, $T$ = transformer ratio, $X_c$ = commutating reactance, subscript $r$ represents the rectifier-side and subscript 0 denotes the initial operating condition.

Since each subsystem has been represented in a different reference frame, all the variables need to be transformed into common reference frame before the integration of different subsystems.

The linearised transformation between variables in $DQ$ reference frame and polar coordinates is shown in (A.15).

$$\begin{bmatrix} \Delta f_D \\ \Delta f_Q \end{bmatrix} = \begin{bmatrix} sin\theta_{fac0} & f_{ac0} cos\theta_{fac0} \\ cos\theta_{fac0} & -f_{ac0} sin\theta_{fac0} \end{bmatrix} \begin{bmatrix} \Delta f_{ac} \\ \Delta \theta_{fac} \end{bmatrix} \tag{A.15}$$

The linearised transformation from synchronously rotating reference frame to rotor reference frame is expressed in (A.16) [1]. The relationship among variables in rotor, synchronous

reference frames and polar coordinates is illustrated in Fig. A.8.

$$\begin{bmatrix} \Delta f_d \\ \Delta f_q \end{bmatrix} = \begin{bmatrix} cos\delta_0 & sin\delta_0 \\ -sin\delta_0 & cos\delta_0 \end{bmatrix} \begin{bmatrix} \Delta f_D \\ \Delta f_Q \end{bmatrix} + \begin{bmatrix} \Delta f_{q0} \\ -\Delta f_{d0} \end{bmatrix} \Delta\delta \tag{A.16}$$

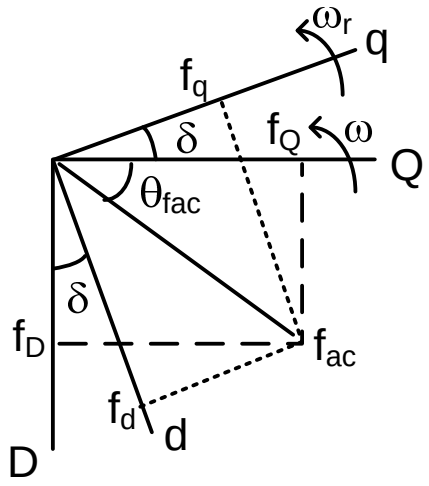


Figure A.8: Phasor diagram of the relationship among variables in $dq$, $DQ$ reference frames and polar coordinates

## References


[1] P. C. Krause, O. Wasynczuk, and S. D. Sudhoff. *Analysis of Electric Machinery.* The Institute of Electrical and Electronics Engineers, Inc., New York, 1995.

[2] Y. C. Choo, A. P. Agalgaonkar, K. M. Muttaqi, S. Perera, and M. Negnevitsky. Dynamic modelling of hydroelectric turbine-generator unit connected to a HVDC system for small signal stability analysis. In *Australasian Universities Power Engineering Conference, 2009. AUPEC 2009.*, pages 1 –6, 27-30 2009.

[3] K. R. Padiyar. *Analysis of Subsynchronous Resonance in Power Systems.* Kluwer Academic Publishers, 1999.

[4] C. Osauskas, A. Wood, "Small-signal dynamic modeling of HVDC systems," *IEEE Trans. Power Del.*, Vol. 18, No. 1, pp. 220-225, January 2003.

[5] V. K. Sood, V. Khatri and H. Jin, "Performance assessment using EMTP of two gate firing units for HVDC converters operating with weak AC systems," *IPST95 - International conference on power system transients*, Lisbon, pp. 517 – 522, 3–7 September 1995.

[6] Dragan Jovcic, Nalin Pahalawaththa and Mohamed Zavahir, "Analytical modelling of HVDC-HVAC systems," *IEEE Trans. Power Del.*, Vol. 14, No. 2, April 1999.

[7] Dong-Joon Kim, Hae-Kon Nam, and Young-Hwan Moon. A practical approach to hvdc system control for damping subsynchronous oscillation using the novel eigenvalue analysis program. 22(4):1926 –1934, November 2007.